UNIVERSITÀ
DEGLI STUDI
DI PADOVA

UNIVERSITÀ DEGLI STUDI DI PADOVA

Sede Amministrativa: Università degli Studi di Padova

Dipartimento di Ingegneria Industriale

CORSO DI DOTTORATO DI RICERCA IN INGEGNERIA INDUSTRIALE

INDIRIZZO: INGEGNERIA MECCANICA, CHIMICA E DEI MATERIALI

CICLO XXIX

Feasibility of producing Ti6Al4V biomedical parts through sheet forming processes at elevated temperature

Coordinatore del corso: Ch.mo Prof. Paolo Colombo

Supervisore: Ch.mo Prof. Stefania Bruschi

Dottorando: Beatrice Valoppi

A.A: 2016/2017

Table of contents

Abstract

Over the last years, the aging population and people more active in sports have been correlated to an increasing demand of prostheses and biomedical implants, most of which are made of Ti6Al4V alloy, since it assures elevated corrosion resistance, good mechanical properties and biocompatibility.

In the hip replacement, the acetabulum in the pelvis is replaced by a Ti6Al4V acetabular cup, which is currently manufactured through Additive Manufacturing (AM) technologies and machining operations. Nevertheless, this process presents some critical drawbacks in the production of acetabular cups characterized by a high surface-to-thickness ratio, such as the elevated distortions in AM and the significant waste of material in machining operations to reach the final shape.

Therefore, the alternative idea suggested and investigated in this PhD project is the application of sheet forming processes to be carried out at elevated temperature to increase the limited formability that Ti6Al4V shows at room temperature.

Aiming at identifying the proper working conditions, the research work focused on three main topics, namely (i) the investigation of the material behaviour and biomedical properties to address the forming issue and assure a good osseointegration process at the implant-bone interface, respectively; (ii) the modelling of material rheology and ductility; (iii) the manufacturing of a prototype.

Following this approach, because a review of literature showed that Ti6Al4V has been mostly investigated at low strain rates typical of the superplastic regime, the material behaviour was first explored in a wide range of temperatures and moderate strain rates, pointing out the relations between the mechanical and microstructural properties. Based on these results, the process conditions necessary to address the forming issue were identified, since higher temperatures higher ductility. However, the preservation of the material bioactivity, which was enhanced through the application of different surface treatments, was found to limit the forming temperature to a maximum value.

The research work on the material modelling raised from the increasing interest of the industrial and scientific communities on the use of Finite-Element (FE)

models to numerically assess the manufacturing process. In this context, the Ti6Al4V flow stress behaviour was modelled applying the well-known Johnson-Cook and Arrhenius-type constitutive models, while great efforts were addressed to propose a new model able to describe the ductility of Ti6Al4V sheet in a wide range of temperatures and stress states. With this aim, the original Johnson-Cook fracture strain criterion was modified to incorporate a quadratic function of the stress triaxiality and Lode parameter, whose coupled effect was recently recognized to have a significant role in predicting the fracture occurrence also in more complex stress states. On the other hand, a quadratic function of the temperature was introduced to represent the transformation related ductility inherent in the two phase (α/β phases) titanium alloy Ti6Al4V at elevated temperatures.

Finally, Incremental Sheet Forming (ISF) process was chosen to manufacture the biomedical part because, according to literature, ISF technique is suitable for small volume batches and high customized sheet metal parts, as the case of biomedical implants. Different variants of ISF process were electrically-assisted to manufacture difficult-to-form Ti6Al4V sheets, and their results were evaluated in terms of final shape and surface characteristics, the latter playing a key role in the biological phenomena at the basis of the osseointegration process.

In addition, within the same manufacturing topic, a variant of ISF process was selected to investigate the fracture phenomenon and provide a deeper understanding of the relations between the process mechanics and the fracture occurrence.

Sommario

Durante gli ultimi anni, l'invecchiamento della popolazione e il crescente interesse per le attività sportive sono stati accompagnati da un aumento della richiesta di protesi e componenti biomedicali, la maggior parte dei quali viene prodotta in lega di titanio Ti6Al4V, vista la sua elevata resistenza alla corrosione, le buone proprietà meccaniche e la sua biocompatibilità.

Nella protesi d'anca, l'acetabolo è sostituito da una coppa acetabolare in Ti6Al4V, che è attualmente prodotta per Additive Manufacturing e operazioni di tornitura. D'altra parte, nella produzione di coppe acetabolari caratterizzate da un elevato rapporto tra superficie e spessore, questo processo presenta degli svantaggi, come le elevate distorsioni nelle operazioni di Additive Manufacturing e il significativo spreco di materiale nella tornitura per raggiungere la geometria desiderata.

Pertanto, l'idea alternativa suggerita e valutata in questo progetto di dottorato è l'applicazione di processi di formatura delle lamiere, che devono però essere condotti ad alta temperatura per aumentare la formabilità limitata del Ti6Al4V a temperatura ambiente.

Allo scopo di individuare le migliori condizioni di processo, il lavoro di ricerca si è concentrato su tre temi principali, (i) l'indagine del comportamento del materiale e delle proprietà biomedicali per assicurare rispettivamente l'ottenimento del componente e il processo di osseo-integrazione all'interfaccia osso-impianto; (ii) la modellazione della reologia e della duttilità del materiale; (iii) la fabbricazione di un prototipo.

Seguendo questo approccio, visto che un'analisi della letteratura ha mostrato che il Ti6Al4V è stato principalmente studiato a basse velocità di deformazione, tipiche del regime superplastico, il comportamento del materiale è stato studiato in un ampio range di temperature a velocità di deformazione moderate, evidenziando in particolare le relazioni tra le proprietà meccaniche e quelle microstrutturali. Sulla base di questi risultati, le condizioni di processo necessarie per formare il componente sono state identificate, dal momento che maggiori temperature corrispondono ad una maggiore duttilità del materiale. D'altra parte, la temperatura

di formatura deve essere limitata per preservare la bioattività del materiale, che è stata dimostrata essere migliorata attraverso l'applicazione di differenti trattamenti di modifica superficiale.

Il lavoro di ricerca relativo alla modellazione del comportamento del materiale in differenti condizioni di processo è legato al crescente interesse delle comunità industriali e scientifiche all'uso di modelli agli elementi finiti per valutare il processo produttivo. In questo contesto, la reologia delle lamiere in Ti6Al4V è stata descritta utilizzando il criterio di Johnson-Cook e un'equazione tipo-Arrhenius, mentre notevoli sforzi sono stati indirizzati alla proposta di un nuovo modello in grado di descrivere la duttilità delle lamiere in Ti6Al4V in diversi stati tensionali e all'interno di un vasto range di temperature. A tal fine, il criterio di frattura di Johnson-Cook è stato modificato incorporando una funzione quadratica della triassialità e del parametro di Lode, il cui effetto congiunto è stato recentemente riconosciuto avere un ruolo significativo nel prevedere la frattura anche in stati di sollecitazione più complessi. D'altra parte, una funzione quadratica della temperatura è stata introdotta nel modello per rappresentare il fatto che la duttilità del materiale è correlata alla trasformazione insita nelle due fasi α e β del Ti6Al4V a temperature elevate.

In conclusione, il processo di formatura incrementale (Incremental Sheet Forming process, ISF) è stato individuato per produrre il componente acetabolare visto che, sulla base dell'analisi della letteratura, questo processo è adatto a piccoli lotti di produzione e a componenti altamente personalizzati, come il caso degli impianti biomedicali. Diverse varianti del processo di formatura incrementale sono state elettricamente assistite per incrementare la temperatura di formatura, sfruttando così il relativo incremento della duttilità del Ti6Al4V. I risultati sono stati poi valutati in termini di accuratezza geometrica e caratteristiche superficiali, essendo quest'ultime fondamentali per i fenomeni biologici alla base del processo di osseo-integrazione dell'impianto.

Sempre all'interno di questo ambito, il fenomeno di frattura in una particolare variante di processo è stato poi analizzato per individuare le relazioni tra lo stato tensionale che si verifica durante il processo e il fenomeno stesso della rottura.

1 Chapter

Introduction

Over the last decades, the use of lightweight titanium alloys has been widely promoted by different industries for many technological applications, thanks to their high strength-to-weight ratio, elevated corrosion resistance and good biocompatibility [1]. Among titanium alloys, Ti6Al4V represents more than 50% of the total titanium usage [2] and it is the most widely employed for the production of load bearing surgical implants [3], [4]. Indeed, because of an aging population and people more active in sports, prosthesis is becoming a very high-demand item, thus increasing the value of its global market. As an example, the market of knee and hip prosthesis reached EUR 9 billion in 2011, with about 58% of the market in the USA, 23% in Europe and 19% in Asia [5].

In the hip replacement, the acetabulum in the pelvis is replaced by an artificial acetabular cup, which is made of Ti6Al4V and characterized by a thickness of about 3 mm as shown in Figure 1-1a, coupled with a polyethylene insert through a tight fit.

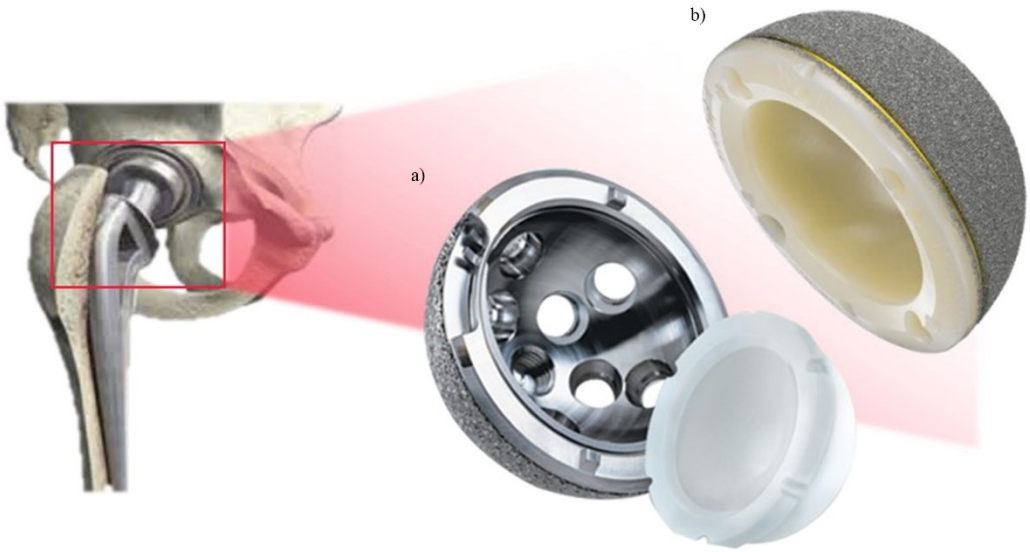

Figure 1-1. Representation of the hip replacement and the details of the two types of acetabular cups, a) modular cups and b) monobloc cups [courtesy of Eurocoating and Mathys].

The manufacturing process currently used to produce these acetabular cups is divided into two steps, involving the Additive Manufacturing (AM) technologies, which can produce rough surfaces to assure a successful osseointegration [6], [7], followed by machining operations in the internal surface [8]. However, the production of new concept of acetabular cups, consisting of Ti6Al4V shells pressed against a polyethylene monobloc (Figure 1-1b), presents some drawbacks, as the elevated distortions experienced in AM and the significant waste of material in the machining operations to reach the final shape.

Figure 1-2. Ti6Al4V shell characterized by a high surface-to-thickness ratio [courtesy of Eurocoating].

An alternative route to produce such parts, characterized by a high surface-to-thickness ratio as shown in Figure 1-2, is represented by sheet forming processes. However, the limited formability of Ti6Al4V at room temperature [9], [10] forces the forming operations to be carried out at elevated temperatures, thus reducing in the meantime the material springback [11] and improving the final geometric accuracy of the formed component.

To successfully implement this idea, the choice of the proper parameters and the need for the design and optimization of the process requires a comprehensive knowledge of the material behaviour, but also the use of Finite-Element (FE) models, which are helpful in predicting the process outcomes.

Starting with the first requirement, the material characterization carried out within the PhD project investigates the Ti6Al4V flow stress behaviour, the microstructural and anisotropic features, as well as the post-deformation mechanical properties, as a function of temperature and strain rate. Indeed, the thermo-mechanical cycle applied to the sheet during hot forming operations

influences the Ti6Al4V microstructural features [12], thus controlling the material mechanical properties [13], but it also affects the anisotropic characteristics, being the latter function of the material lattice and the orientation of its elementary cells [14].

It is worth to note that these analyses, which are performed under tensile conditions at moderate strain rates in a wide range of temperatures, spanning from room temperature to 900°C, allows filling a gap in literature about the behaviour of Ti6Al4V sheets. Indeed, while many papers are devoted to the evaluation of the material characteristics under compression conditions using bulk samples [1], [15]–[17], the analysis of Ti6Al4V sheets is mostly carried out in the warm temperature range and at very low strain rates, characteristics of the superplastic regime [18]–[20].

Regarding the necessity to assess the process numerically, the reliability of the simulation strongly depends on the accurate modelling of the material rheology, but also on the good prediction of the fracture onset, which has recently become one of the main focuses of the metal forming community [21].

Nowadays, the most common practise to predict the failure in sheet forming operations, at both academic and industrial level, is the method of the Forming Limit Diagrams (FLDs) [22]. However, because each FLD depends on different factors, such as sheet thickness, temperature and strain rate, the prediction of failure in a wide range of process conditions, which are typical of hot sheet forming processes, requires great experimental efforts when using this method. Therefore, the necessity to overcome this disadvantage pushed the PhD project to develop an alternative method, based on fracture criteria, which considers the ductile fracture sensitivity to temperature and strain rate, as they play a key role when the forming processes are performed at elevated temperature, but also the effects of the stress state in terms of both stress triaxiality and Lode parameter. Indeed, the influence of the Lode parameter was recently introduced in the characterization of the ductile failure behaviour [23] since, together with the stress triaxiality, allows predicting the fracture occurrence in more complex stress states [24].

However, besides the characterization and the modelling of the material behaviour, the proposal of hot sheet forming process as a candidate method to manufacture Ti6Al4V acetabular shell has to consider also the issues related to the biological interaction of the biomedical part with the human body. In this context,

it is important to underline that the surface of the implant highly influences its interaction with the biological environment, since some biological phenomena, as osseointegration, absorption of proteins and adhesion of osteoblasts, strongly depend on surface roughness, chemical composition and wettability properties [25], [26]. Therefore, different thermo-electro-chemical methods were applied to tailor the surface characteristics of Ti6Al4V sheets, and the resulting properties were evaluated in terms of surface roughness and material bioactivity, which is the ability of the part to react with the biological environment determining a successful or vain osseointegration process. Afterwards, considering the forming issue related to the industrial case, the influence of the sample surface modification on the alloy forming and post-forming characteristics was investigated, being these analyses mandatory to prove the feasibility of using sheet forming processes at elevated temperature for the production of the Ti6Al4V part.

In the end, a prototype of the acetabular shell was produced applying different variants of the Incremental Sheet Forming (ISF) process, which is suitable for the manufacturing of low-volume customized sheet metal parts, as the case of biomedical implants, because of its die-less nature and the consequent high flexibility and low set-up cost. However, to face the challenge of forming the difficult-to-form Ti6Al4V, because of its limited formability at room temperature [27], all the processes were electrically-assisted to increase the forming temperature. Afterwards, the formed parts were analysed in terms of geometric accuracy and post-deformation properties, focusing on the material micro-hardness and microstructure, but also on the surface roughness, which is related to the biomedical aspect of the part.

In addition, within the same manufacturing topic, a collaboration with the Northwestern University was initiated to investigate the fracture phenomenon in Double-Sided Incremental Forming (DSIF) strategy, thus providing a deeper understanding of the relations between the DSIF process mechanics and the fracture occurrence.

The objective of this work is to investigate the feasibility of producing Ti6Al4V acetabular shells by sheet forming processes at elevated temperature, as an alternative route to AM and machining operations. With this aim, the thesis is organised based on the following four aspects:

(i) the material characteristics as a function of the process parameters, namely strain rate and temperature;
(ii) the modelling of the material rheology and ductility, the latter considering, not only the temperature and strain rate, but also the effects of the stress triaxiality and Lode parameter, which, according to literature, are recognized to be significant factors in the description of the ductile fracture behaviour;
(iii) the methods used to modify the surface characteristics of Ti6Al4V sheets with the aim of increasing its biomedical properties;
(iv) the production of a prototype.

The thesis is divided into seven chapters. The first one provides an introduction on the industrial problem and the scientific aspects of the research project, describing the approach used to achieve the final objective and pointing out the main topics, fully analysed in the following parts of the thesis. The second chapter presents a comprehensive review of the literature, focusing on (i) the state of art related to the material characterization and modelling, (ii) the scientific knowledge about the properties required for the biomedical implants to assure a good bone-implant interaction and, finally, (iii) the existing studies concerning the sheet forming processes. Afterwards, the experimental tests performed to investigate the material behaviour in different testing conditions and the resulting data are described in the third chapter. The fourth one is related to the material modelling, which includes the modelling of the material rheology and ductility. Chapter 5, concerning the biomedical aspect of the research work, illustrates the methods applied to modify the surface characteristics and presents their effects in the material biomedical and mechanical properties. Finally, while the sixth chapter reports the results related to the application of the incremental forming process, focusing on the production of a prototype and on the analysis of the fracture

phenomenon, the last one presents the main conclusions of the entire research project.

2 Chapter

Literature review

The use of titanium alloys is widely distributed in a wide range of industries for different technological applications, spanning from aeronautical components, thanks to their potential high temperature resistance and strength-to-weight ratio [12], [28], to biomedical parts, because of their favourable biocompatibility, corrosion resistance and mechanical properties [29]. Indeed, titanium and its alloys are used in joint replacement, trauma system and dental implants, as reported for example in Figure 2-1 [30]. Among these materials, the most widely used titanium alloy for these biomedical components is the Ti6Al4V alloy [5], [31].

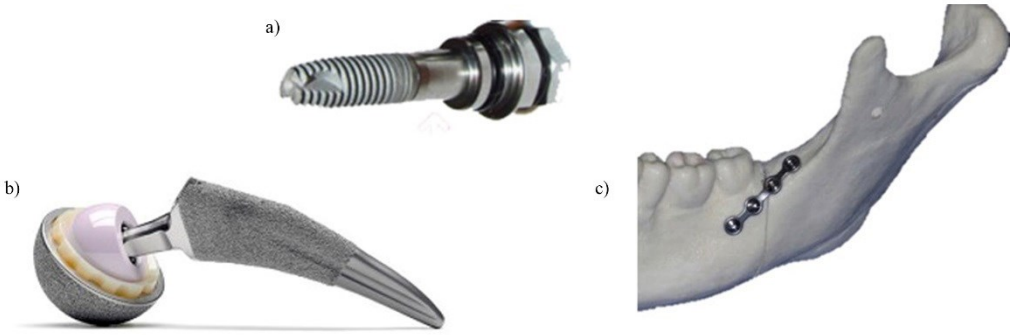

Figure 2-1. a) Dental implant [32], b) hip prosthesis [33], c) fixation system on the mandibular angle fracture [34].

2.1 Ti6Al4V

2.1.1 Crystallographic characteristics

Titanium is characterized by two allotropes, namely the alpha (α) and the beta phase (β). The α phase, characterized by the Hexagonal Close-Packed (HCP) crystal structure, is stable until 898°C, at which the allotropic transformation occurs, thus obtaining the Body-Centered Cubic (BCC) β phase, stable from this temperature to the melting one, as depicted in Figure 2-2.

Based on the crystal structures of the two phases, the HCP α phase, which is characterized by limited slip taking place on the basal planes, provides for high yield stress but limited ductility, whereas the toughness of this phase depends on its grain size. On the other hand, the BCC β phase allows a larger number of active slip planes, resulting in higher ductility but lower yield stress (almost 1/3 that of the α phase).

Because the phase volume fraction depends on the starting composition, the related mechanical properties of titanium alloys can be tailored varying the percentage of the alloying elements, which play a fundamental role in promoting the α or the β phase by raising or decreasing the transition temperature, respectively. Based on this, the alloying elements are classified as α and β-stabilizer, respectively.

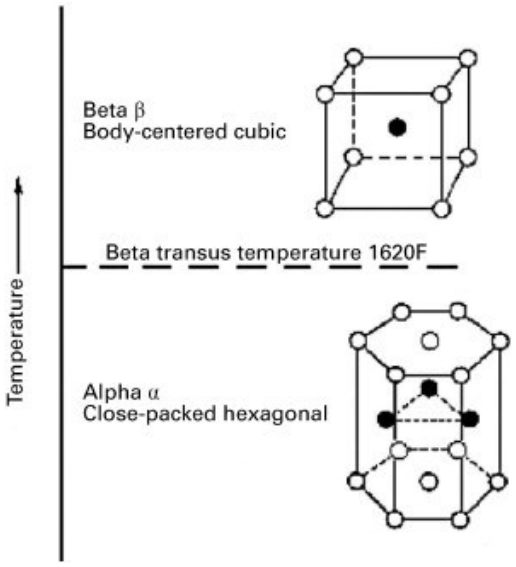

Figure 2-2. Crystal structures of titanium [35].

Among the $\alpha + \beta$ alloys, in which the two phases coexist at room temperature, Ti6Al4V is one of the most investigated [36]. It results from the balance between the most important alloying elements, i.e. the α-stabilizer aluminium (Al), and the vanadium (V), which is the β-stabilizer. In Ti6Al4V alloy, the two phases coexist until the β-transus temperature, which is equal to 995±15°C [12], [28].

2.1.2 Material sensitivity to temperature

At room temperature, Ti6Al4V has $\alpha + \beta$ structure with about 8-12% β volume fraction with the rest being α phase. As the temperature is raised, the volume fraction of β increases slightly up to 600°C, but, between 600°C and 900°C,

the volume fraction of β increases rapidly [37], [38], as it can be seen in Figure 2-3. The same figure includes also a plot of the β fraction as function of temperature as well as the associated microstructural states at selected temperatures. The volume fraction of the β phase can be estimated by fitting a simplified model to the experimental data, yielding a curve shown in Figure 2-3 that can be approximated as [39]:

$$f^{\beta} = \left[0.18 + 0.82 \cdot e^{-0.012 \cdot (1268 - T)}\right]. \quad (2\text{-}1)$$

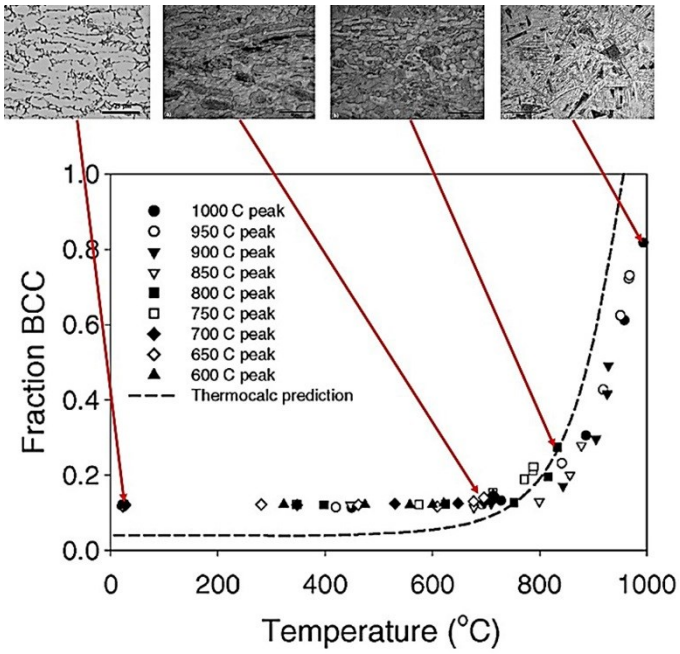

Figure 2-3. Ti6Al4V fraction of β-phase as a function of temperature, and representative microstructure at few selected temperatures [37], [38].

Since the flow stress of β phase is about 1/3 that of α phase, the aforementioned phase change as a function of temperature has profound influence on the flow behaviour of the titanium alloy, leading for example Johnson and Cook [40] to introduce a non-dimensional temperature parameter, named homologous temperature (T^*), in the their constitutive equation (Eq. (2-2)). However, the flow softening can be represented in the J-C flow stress criterion replacing its original flow stress multiplier dependent on the homologous temperature ($h(T^{*m})$ in Eq. (2-2)) with a quadratic function [41], as reported in Eq. (2-3).

$$\sigma = f(\varepsilon) \cdot g(\varepsilon^*) \cdot h(T^{*m}) \quad (2\text{-}2)$$

$$h(T^{*m}) = [1 - (T^*)^m] = \left[7.19 \cdot 10^{-5}\, T^{*2} - 0.02\, T^* + 1.64\right] \quad (2\text{-}3)$$

Since the flow stress is strongly dependent on temperature, we would expect material ductility to be also a strong function of temperature.

In addition to flow stress, other physical properties of Ti6Al4V are strongly dependent on temperature, as, for example, the heat capacity (C_p) that, expressed in J/(kg K), is given by a quadratic function of temperature in the range 5°C to 871°C (below β-transus) [42]:

$$C_p = 5559.77 - 0.1473\,T + 0.00042949\,T^2\,. \qquad (2\text{-}4)$$

2.1.3 Anisotropic features

The crystallographic texture of Ti6Al4V, in particular the HCP structure of the α phase for its low symmetry, induces an inherent anisotropy in its physical and mechanical properties [43], [44]. The rolling process, making the textures more pronounced in titanium sheets, gives rise to strong mechanical properties anisotropy and has a detrimental influence also on the other properties, such as fatigue, creep, working and shaping behaviours [45]. Therefore, because large anisotropies can induce different flow stress and springback depending on the deformation direction [14], the selection of the proper manufacturing process for the production of components made of Ti6Al4V has to take into account also this property.

The reduction of anisotropy in the mechanical properties can be advantageous for increasing the formability, pushing the research to investigate different methods aimed at addressing this issue. It was found that the application of forming processes and/or thermal treatments allow varying the material anisotropic characteristics, acting on the material crystallographic textures which are recognized to influence the anisotropy of tensile properties [14].

Nakai et al. [14], investigating another $\alpha + \beta$ alloy, i.e. Ti9, attributed the anisotropy in tensile properties to the formation of strong crystallographic texture, namely the alignment of the c-axis of the α hexagonal elementary cell with the direction perpendicular to the rolling one (T-texture). Aiming at reducing this anisotropy, the authors [14] analysed the effect of different heat treatments on the crystallographic texture, concluding that a decrease of T-texture, correspondent to the reduction of material anisotropy, was promoted by an increase of the heat-treatment temperature. The effect of the increasing temperature on the reduction of the texture intensity was proved also in [46] for Ti6Al4V bars deformed under various conditions.

Usually, the material anisotropy is quantified through two main parameters, namely the normal average anisotropy, $\bar{R}$ (Eq. (2-5)), and the planar anisotropy, ΔR (Eq. (2-6)). While the first determines thinning behaviour of sheet metals during stretching, the other one exhibits different behaviour in various planar directions.

$$\bar{R} = \frac{r_0 + 2r_{45} + r_{90}}{4} \tag{2-5}$$

$$\Delta R = \frac{r_0 - 2r_{45} + r_{90}}{2} \tag{2-6}$$

The coefficients r_i are the Lankford coefficients, which quantifies the variation of the plastic behaviour with the direction, namely 0, 45 and 90° with respect to the rolling direction as shown in Figure 2-4a. They are defined in terms of the true strains that the specimen undergoes in tension, as reported in Eq. (2-7),

$$r_i = \frac{\varepsilon_w}{\varepsilon_t}, \tag{2-7}$$

where the true strain in the width (ε_w) and thickness (ε_t) directions are illustrated in Figure 2-4b.

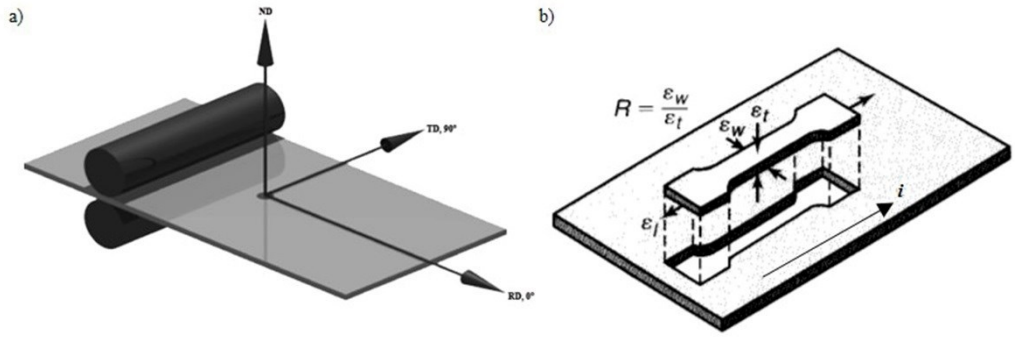

Figure 2-4. a) Axis of the rolled sheet metal: ND: Normal Direction, TD: Transverse Direction (90°), RD: Rolling Direction (0°) [47]. b) Strains on a tensile-test specimen removed from a piece of sheet metal in direction *i*. These strains are used in determining the normal and planar anisotropy of the sheet metal [48].

2.1.4 Microstructural characteristics

The most important microstructural parameter determining the mechanical properties for the $\alpha + \beta$ Ti6Al4V alloy is its α-colony size. With decreasing colony size, yield strength, ductility, micro-crack propagation resistance are improved, whereas the macro-crack propagation resistance and fracture toughness are

improved by larger α-colony size. The α-colony size depends on heating rate, cooling rate from the β-phase field and the evolving β grain size [37].

As a consequence, different microstructural characteristics and a variety of microstructures, ranging from lamellar to equiaxed $\alpha + \beta$ [12], [49], can be obtained controlling the processing parameters of both plastic working operations and heat treatments [46], [50].

The lamellar microstructure, which is formed after slow cooling when deformation or heat treatment takes place at a temperature in the single-phase β-field above the β-transus temperature, consists of α-lamellae within β phase grains (Figure 2-5a). An acicular or fine-lamellar (needle-like) microstructure is instead obtained quenching the material from temperatures higher than the β-transus, resulting in α' martensite.

On the other hand, the equiaxed microstructure, formed after deformation in the $\alpha + \beta$ field, consists of globular α phase dispersed in β phase matrix (Figure 2-5b) [50].

The thermal cycle applied to Ti6Al4V during hot forming operations in different testing conditions, influencing the material microstructural features, controls also the material mechanical properties and behaviour [51]. Indeed, while a lamellar microstructure shows high fatigue crack propagation resistance and high fracture toughness, the equiaxed one guarantees improvements in strength, ductility and fatigue life [13]. On this basis, the analysis of the material microstructure sensitivity to the process parameters becomes mandatory to obtained the desired mechanical properties in the final component.

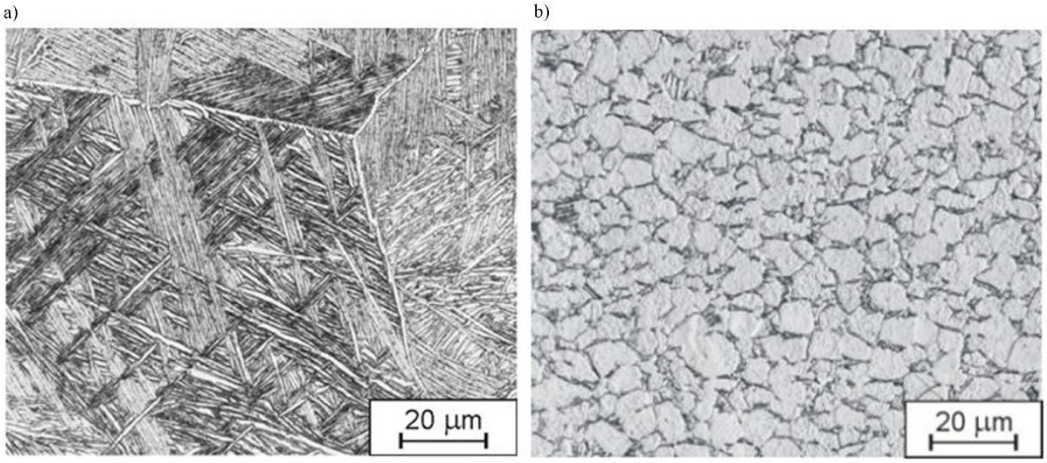

Figure 2-5. Microstructure of Ti6Al4V alloy: a) lamellar; b) equiaxed [52].

2.2 Material modelling

In addition to the microstructural analysis, the choice of the proper parameters to obtain the desired characteristics in the final component demands also the investigation of the Ti6Al4V formability, for which the stress-strain relations [9] and the fracture behaviour are the fundamental information.

However, beside the experimental results, the use of Finite Element (FE)-based simulation packages in the optimization of the industrial process requires the development of constitutive models, which accurately describe the material rheology and fracture behaviour as a function of the process parameters, thus enhancing the reliability of the simulation.

2.2.1 Modelling of material rheology

Considering first the analysis and the modelling of the material rheology, Kotkunde et al. [13] focused on the investigation of the Ti6Al4V flow stress behaviour under tensile conditions in the medium temperature range, spanning from 50 to 400°C, at strain rates ranging from 10^{-5} to 10^{-2} s^{-1}, as represented in Figure 2-6.

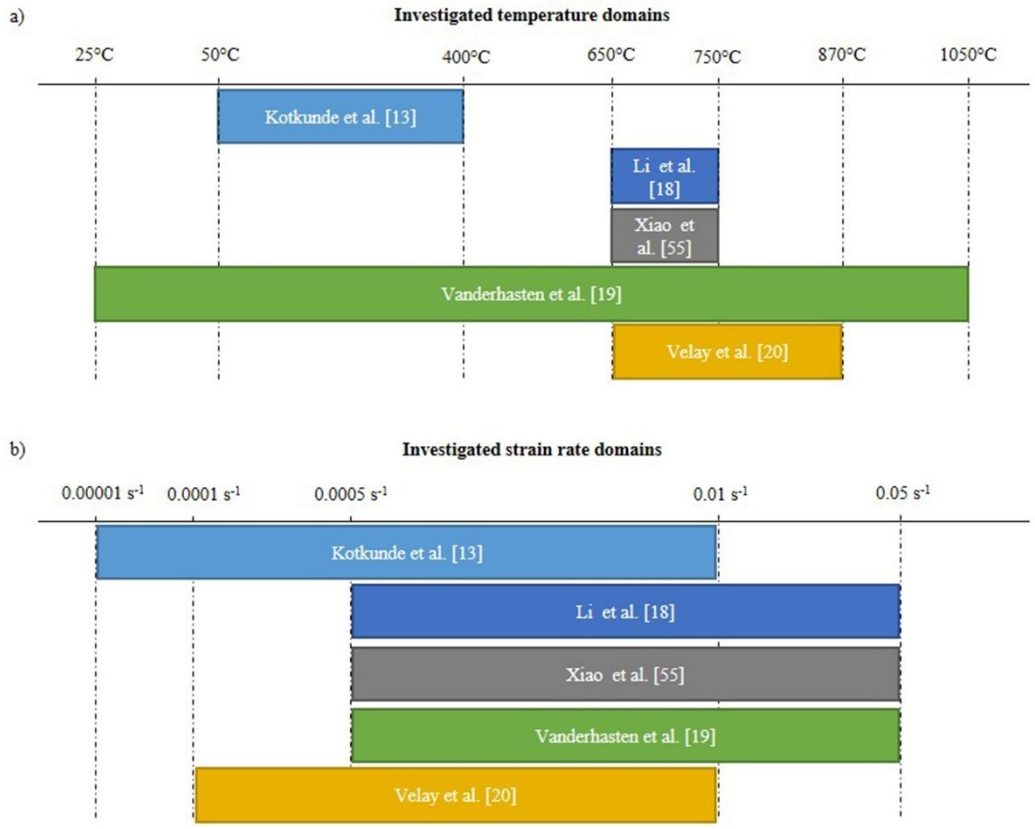

Figure 2-6. Schematic representation of the temperature and strain rate domains investigated in literature for Ti6Al4V under tensile conditions.

In these testing conditions, the prediction of the flow stress behaviour was done using different constitutive models, as the ones based on the Johnson-Cook criterion and Arrhenius-type equation [13], [53].

Li et al. [18] investigated the constitutive behaviour of the alloy in a higher temperature domain (650°C-750°C) compared to the previous one, but at still low strain rates ($5 \cdot 10^{-4}$-$5 \cdot 10^{-2}$ s^{-1}), close to the ones characteristics of the superplastic regime [54]. The true stress-strain curves in the same testing conditions were obtained also by Xiao et al. [55], founding that the flow stress decreased with the increase of the temperature and decrease of strain rate. Afterwards, based on the experimental data, the Arrhenius-type equation was calibrated to characterize the hot deformational behaviour, which resulted to be influenced by strain, strain rate and temperature.

The same values of strain rates used by Xiao et al. [55], but a wider range of temperatures, spanning from room temperature to 1050°C, were explored in the work by Vanderhasten et al. [19], where the tensile properties of Ti6Al4V were characterized through the Norton-Hoff equation in different temperature domains, as reported for example in Figure 2-7. To note that the model was modified introducing a grain size related factor, which is particularly significant in modelling the superplastic behaviour [19], [56].

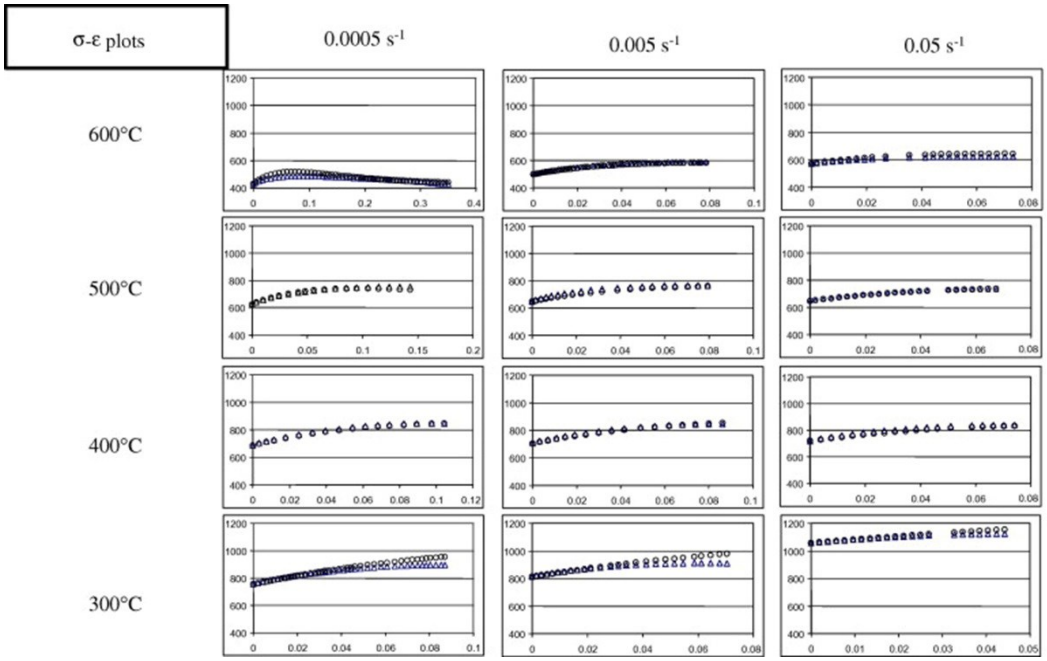

Figure 2-7. Comparison between the experimental and predicted σ–ε charts by applying Norton-Hoff model for tensile test carried out at different temperatures and strain rates [19].

The grain size effect was introduced also in the model proposed by Velay et al. [20], where the Ti6Al4V flow stress behaviour was analysed between 650°C and 870°C, at strain rates ranging from 10^{-4} to 10^{-2} s^{-1}.

Based on this literature review, and as it can be seen in the schematic representation of Figure 2-6, the previous studies were devoted to describe the constitutive behaviour of Ti6Al4V sheets under tensile conditions in the warm and elevated temperature range, but only at low strain rates.

However, in case of forming processes which guarantee a higher productivity than superplastic forming, the material behaviour is differently influenced by the higher strain rate values. Several papers can be found related to the Ti6Al4V constitutive modelling at elevated temperature and strain rate, but all of them refer to forging operations, where the material is subjected to compression.

Indeed, while Lee et. al. [57] examined the mechanical behaviour under compression conditions in a wide range of temperatures (25°C-1100°C) and elevated strain rates ($5 \cdot 10^{2}$-$3 \cdot 10^{3}$ s^{-1}) by means of the compressive split-Hopkinson bar technique, Majorell et al. [1] focused on an intermediated strain rate range (10^{-3}–10 s^{-1}), but still under various testing temperatures (377°C -1067°C).

Included in the aforementioned testing range [1], as it can be seen in Figure 2-8, there is also the paper by Luo et al. [17], in which the flow stress decreased with increasing temperature, while the strain rate sensitivity coefficient *m* was found to rise. A maximum value of *m* was obtained at a deformation temperature close to the β-transus one.

A smaller range of strain rates was instead considered in the papers by Ding et al. [15] and Lee et Lin [16], in which the mechanical behaviour of the titanium alloy under compression conditions was investigated in two different temperature ranges, namely 850°C–1050°C in [15] and 25°C–500°C in [16], as represented in Figure 2-8.

Therefore, based on the previous analysis and considering that the sheet deformation mostly occurs by tensile forces rather than by compression [58], very few papers deal with the constitutive behaviour of Ti6Al4V sheet deformed in tensile conditions under a wide range of temperatures and moderate strain rates [59], suggesting the need for further investigations.

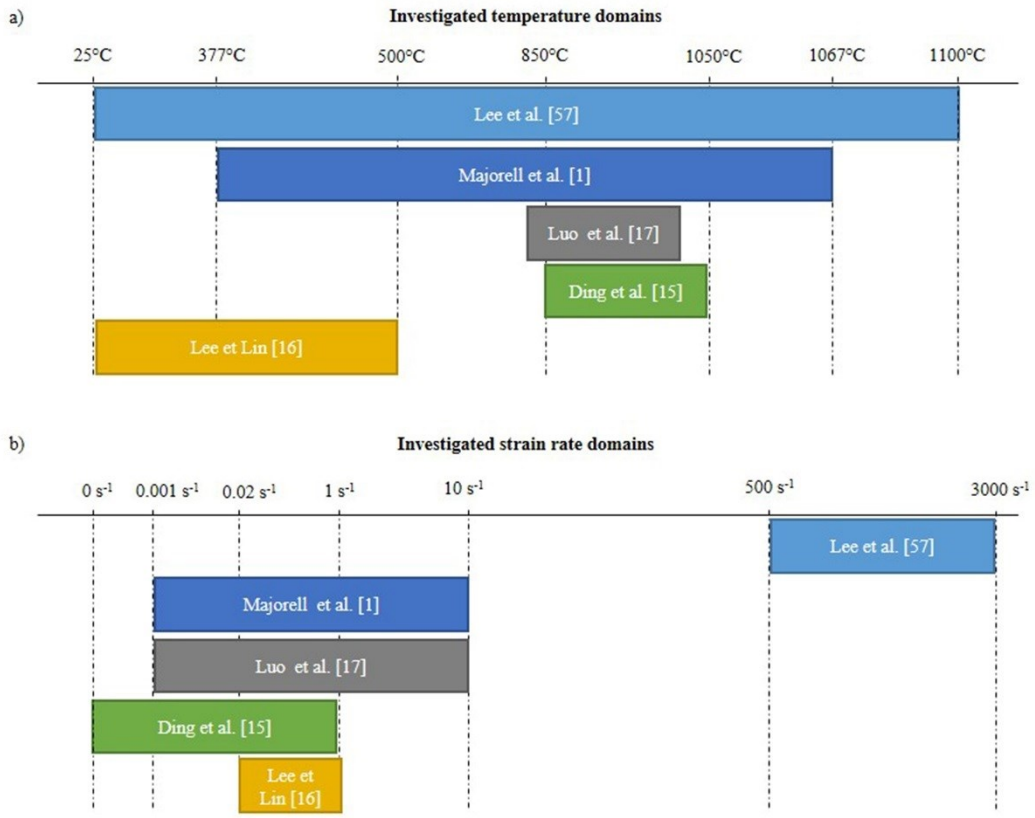

Figure 2-8. Schematic representation of the temperature and strain rate domains investigated in literature for Ti6Al4V under compression conditions.

Among the constitutive models, which describe the relations of the dynamic material properties with process parameters, the Johnson-Cook (J-C) model [40], based on the phenomenological theory, is one of the most widely used because of its simple calibration procedure and limited number of material constants [13]. The J-C equation is reported in Eqs. (2-8) and (2-9), where $f(\varepsilon)$, $g(\dot{\varepsilon}^*)$ and $h(T^*)$ are functions of the strain, strain rate and temperature respectively. The J-C model has been applied to take into account the effect of temperature and strain rate on the flow stress of different materials [13], but the fact that their influence is considered mutually independent reduces its prediction accuracy [60]. The Johnson-Cook model was reported to be inaccurate in predicting the material behaviour at very high strain rates, as in the case of machining [13].

$$\sigma = (A + B\varepsilon^n)(1 + C \ln \dot{\varepsilon}^*)(1 - T^{*m}) \tag{2-8}$$

$$\sigma = [f(\varepsilon)] \cdot [g(\dot{\varepsilon}^*)] \cdot [h(T^*)] \tag{2-9}$$

On the other hand, the Arrhenius-type model (Eq. (2-10)) requires a more complex procedure for the identification of its constants, but it allows a more effective coupling of the effect of strain rate and temperature on the flow stress

through the Zener-Hollomon parameter, *Z*, which is represented by Eq. (2-11) [60], [61]. This parameter was introduced by Zener and Hollomon [62] as a factor of temperature compensation, to express the fact that the internal strain rate of the material is controlled by heat activation process during high-temperature plastic deformation [60].

$$\sigma = \frac{1}{\alpha}\ln\left\{\left(\frac{Z}{A}\right)^{\frac{1}{n}} + \left[\left(\frac{Z}{A}\right)^{\frac{2}{n}} + 1\right]^{\frac{1}{2}}\right\} \tag{2-10}$$

$$Z = \dot{\varepsilon}\exp\left[\frac{Q}{(RT)}\right] \tag{2-11}$$

2.2.2 Modelling of fracture behaviour

A correct description of the material fracture behaviour plays a key role in avoiding the risks and costs of catastrophic failures during the forming processes [2]. As a consequence, the interest on this topic progressively increased and it has become one of the main focuses of the metal forming community [21].

In case of sheet forming processes, the fracture prediction is particularly sensitive [63], [64] because the material formability cannot be easily defined since it depends on many interacting factors [65]. In this context, at both academic and industrial level, the failure is commonly predicted using the phenomelogical method of the Forming Limit Diagrams (FLDs) [22], which were firstly proposed by Keeler and Backofen [66] and then extended by Goodwin [67].

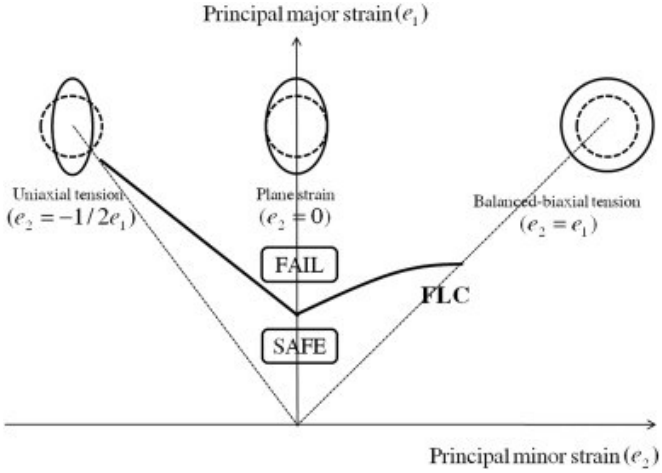

Figure 2-9. Forming Limit Diagram [68].

Figure 2-9 shows an example of Forming Limit Diagram, which indicates the combination of the major (e_1) and minor (e_2) strains that can be applied to a metal

sheet without failure. The threshold between the "safe" and "fail" region is defined by the forming limit curve, which is related to the onset of localized necking, as reported in the ISO 12004 standard [69].

However, the use of this method to predict the sheet formability in a wide range of process conditions, which are typical of sheet forming processes carried out at elevated temperature, requires great experimental efforts because the FLDs depend on different factors, namely sheet thickness, lubrication, temperature and strain rate [48], as represented in Figure 2-10.

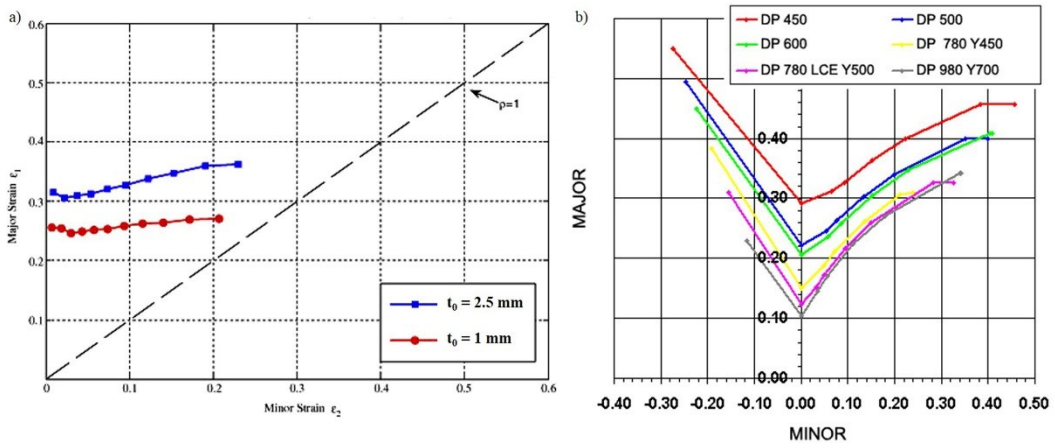

Figure 2-10. a) Effect of sheet thickness on low carbon steel FLDs [70]. b) FLDs sensitivity to temperature for Dual Phase (DP) steels [71].

Therefore, the necessity to overcome this disadvantage is pushing the researchers to provide alternative methods, based on fracture criteria [58], using either coupled or uncoupled approaches. While the coupled criteria link the progressive material damage with the material flow stress, the uncoupled approaches neglect the yield surface sensitivity to the damage evolution [72]. However, even though the coupled criteria consider the physical phenomenon of the ductile fracture, the complexity and difficulty in calibration limit their use, especially in case of industrial applications [23]. On the other hand, the simple formulation and the user-friendly calibration of the uncoupled criteria contribute to their wide spread [72].

Among the uncoupled approaches, the most widely used models are those of Cockcroft and Latham [73], Brozzo [74], Oyane [75] and Johnson and Cook [40], whose formulations derive from energy considerations [58]. These models are generally characterized by a formulation that predicts the fracture onset when a damage parameter reaches a critical value, being the damage variable a function of

different factors, such as the equivalent plastic strain, tensile stress and hydrostatic stress [72]. Because the hydrostatic stress, σ_m[1], was found to influence the nucleation and growth of the voids [76]–[78], controlling therefore the material ductility [72], it was introduced in the damage function through the stress triaxiality, η[2], which is the ratio between the hydrostatic stress and the Von Mises equivalent stress, $\bar{\sigma}$[3]. The stress triaxiality was observed to influence also the fracture mechanisms [79]–[81], thus it was recognized to significantly affect the fracture occurrence [82]. Fracture criteria based on the stress triaxiality are those developed by Oyane [75] and Johnson-Cook [40].

However, when the forming processes are carried out at elevated temperature, where the material is strongly influenced by both the temperature and strain rate, the fracture occurrence depends also on these parameters, besides the stress triaxiality. In this context, while the Oyane criterion [75] was recently modified introducing a function of the temperature and strain rate to be applied in hot rolling conditions [83], where the influence of the stress triaxiality was proved to be high [84], the Johnson-Cook criterion [40] already includes the temperature and strain rate effects, through the introduction of two separate terms in its formulation. Moreover, the Johnson-Cook fracture criterion was found to have good prediction capabilities over the positive range of the stress triaxiality values [23], which can be advantageous in predicting the fracture occurrence in sheet forming processes where the complementary effects of tensile and in-plane stresses lead to fracture [85]. However, the Johnson-Cook criterion does not consider the effect of the Lode parameter, ξ, related to the third invariant (J_3) of the deviatoric stress tensor S ($J_3 = \det(S)$), which was recently recognized to play a significant role in the description of the ductile failure behaviour [23], [86]–[89], since, together with the stress triaxiality, allows predicting the fracture occurrence in more complex stress states [24].

Wilkins et al. [90] was the first to propose the fracture occurrence at room temperature as a function of both the stress triaxiality and Lode parameter, assuming a separable dependency of the fracture locus on these two parameters [91], as represented by Eq. (2-12).

[1] $\sigma_m = (\sigma_1 + \sigma_2 + \sigma_3)/3$, being σ_i the principal stresses.
[2] $\eta = \sigma_m/\bar{\sigma}$
[3] $\bar{\sigma} = \sqrt{(\sigma_1 - \sigma_2)^2 + (\sigma_2 - \sigma_3)^2 + (\sigma_3 - \sigma_1)^2}/\sqrt{2}$, being σ_i the principal stresses.

$$\bar{\varepsilon}_F = h_1(\eta) \cdot h_2(\xi) \quad . \tag{2-12}$$

The same approach was used in later applications [86], [88], until Wierzbicki and Xue [92] proposed a new model, as an extension of the Wilkins' one, which considered a non-separable form (Eq. (2-13)) but symmetric 3D fracture locus as a function of the stress triaxiality and Lode parameter, still at room temperature.

However, because both the separable form and the symmetry of the fracture locus were considered too restrictive assumptions, Bai and Wierzbicki [91] postulated a non-separable and asymmetric form of the fracture locus, where the effect of the Lode angle parameter (namely, the normalized Lode angle) was represented as a parabolic function. The resulting 3D fracture locus in the space of equivalent plastic strain, stress triaxiality and Lode parameter is reported in Figure 2-11.

$$\bar{\varepsilon}_F = f(\eta, \xi) \quad . \tag{2-13}$$

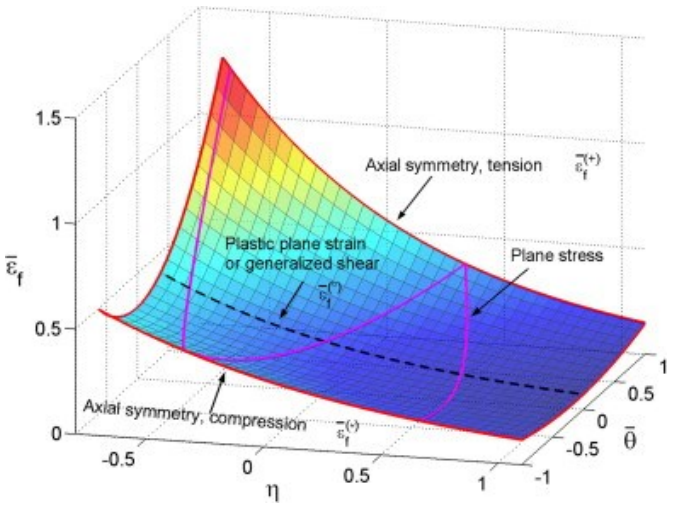

Figure 2-11. The newly 3D fracture locus postulated by Bai and Wierzbicki in a non-separable and asymmetric form [91].

The coupled effect of the stress triaxiality and Lode parameter was first studied in case of bulk materials, as for example in the work by Xue [86]. In this paper [86], the author proposed a damage plasticity model, in which the evolution of damage was considered a non-linear process, while the material deterioration was included on the material strength by a weakening factor [86]. Bulk samples were taken as a reference also by Wierzbicki et al. [93] to compare the relative performances of seven different fracture criteria, with the aim of providing some guidelines for the

FE codes users as to which fracture criterion is suitable for a particular application and how to calibrate a given material for fracture.

However, more recently, the interest on the investigation of the ductile fracture dependence on both stress triaxiality and Lode parameter has been shifted to the case of sheet metal forming. Qian et al. [23], identifying a negligible effect of the Lode parameter on the fracture locus, applied the Johnson-Cook fracture criterion to describe the fracture behaviour of aluminium alloy sheet deformed at room temperature. Continuum damage models were instead used in [87] and [24] for the characterization of the ductile fracture of aluminium alloy and steel sheets, respectively.

As concerns the investigated material, despite the wide use of Ti6Al4V for many applications, only few papers are devoted to the characterization of its fracture behaviour [2], [78], [94], [95]. In particular, among these papers, the research by Giglio et al. [78] focused on the fracture calibration of Ti6Al4V using the Bao-Wierzibicki [81] framework, which, however, is based on the stress triaxiality but does not consider the effect of the Lode parameter. Whereas, the coupled effect of stress triaxiality and Lode parameter on the fracture behaviour of Ti6Al4V alloy was investigated in a more recent study [2], through the calibration of the modified Mohr Coulomb and Lemaitre's damage models.

At present, all the aforementioned papers are devoted to the analysis of the Ti6Al4V failure behaviour at room temperature. On the contrary, a comprehensive evaluation of the influence of the stress triaxiality and Lode parameter on the material ductility in a wide range of temperatures, relevant for sheet forming operations carried out at elevated temperatures, is still missing.

Therefore, the aim of the research is to present a new model that can accurately predict the ductility of Ti6Al4V sheets deformed at different temperatures and strain rates, considering also the effect of the stress state, characterized by both the stress triaxiality and the Lode parameter.

2.3 Biological issues for biomedical applications

Beyond the analysis of the effects of the process parameters on the material microstructure and ductility, which are respectively related to the final mechanical properties and geometric accuracy of the formed part, the use of Ti6Al4V for

biomedical applications requires also the investigation of other issues relevant to the biological interaction of the biomedical implant with the human body.

It is well known that an implant should guarantee a life-long anchorage with the surrounded bone, for which it is essential a mechanically-solid interface resulting from the osseointegration process [25]. Indeed, a successful osseointegration, involving a complex sequence of biological phenomena such as absorption of proteins and adhesion of osteoblasts, leads to the formation of bone tissue and creates a strong mechanical interaction at the native bone tissue-implant interface [96], thus avoiding the formation of fibrous tissue [25] that is responsible for the encapsulation of the implant [97] and its subsequent failure [98].

The biological events are demonstrated to be strongly affected by the implant surface characteristics [26], e.g. surface roughness, chemical composition and wettability [25], [97], [99]. Indeed, based on these properties, the cell processes, which are controlled by the cells capability to perceive the physic-chemical properties of their surroundings [100], can be promoted or hindered, thus deciding for the success or failure of the implant, respectively. A schematic diagram of the interactions between the surface properties and biological events are reported in Figure 2-12.

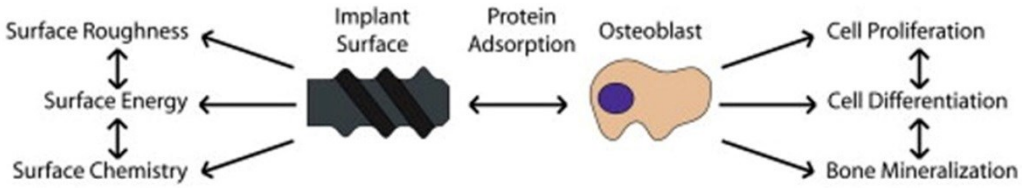

Figure 2-12. Schematic diagram representing the interactions between the surface properties and the biological phenomena [96].

Consequently, the following review focuses on the methods applied to modify the surface characteristics, but also on the description of the role of each surface property, i.e. surface roughness, chemical composition and wettability, on the biological phenomena.

2.3.1 Surface treatments

Different surface treatments are currently used to modify the surfaces of titanium and titanium alloys, as they are acknowledged as the most widely used biomaterials in the field of orthopaedic and oral implantology [101].

A detailed description of the different methods is reported in the following sections.

2.3.1.1 Acid etching

The acid etching category includes a large variety of treatments: they usually imply the immersion of the metallic sample into an acid solution, as illustrated in Figure 2-13, and creates new roughness configurations over the original one.

Figure 2-13. Immersion of the component in the acid solution. The magnetic plate assures the mixing and the heating.

It is worthwhile mentioning that titanium and titanium alloys exhibit different reactivity, which, on turn, depends on the nature of the acidic mixture [101]. Indeed, because titanium alloys react with oxygen creating an oxide layer that reduces its chemical reactivity, only few acids are recommended, such as sulfuric acid (H_2SO_4), hydrochloric (HCl) and hydrofluoric (HF) acids.

In particular, Ban et al. [102] reported that the rate of Ti etching strongly depended on the acid type and its concentration, but also on the temperature of the treatment and its duration.

For cpTi, it was found that the surface roughness increased with the acid temperature and etching time [102], as reported in Figure 2-14. The same dependency on the solution temperature and time was identified also for the loss of weight (Figure 2-14), which was related through a strong linear relation with the surface roughness, as represented in Figure 2-15, suggesting that the higher the loss

of weight the higher the obtained roughness. To note that the initial period in which no weight changes were observed (Figure 2-14) may represent the time required to dissolve the passive oxide layer and expose the metallic Ti to the acid [102].

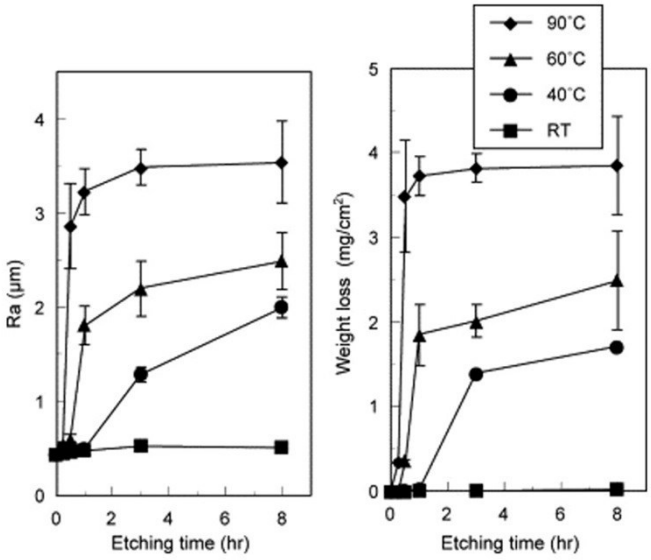

Figure 2-14. Surface roughness R_a and weight loss of cpTi after etching in 48% H_2SO_4 at RT–90°C for 0.25–8 h [102].

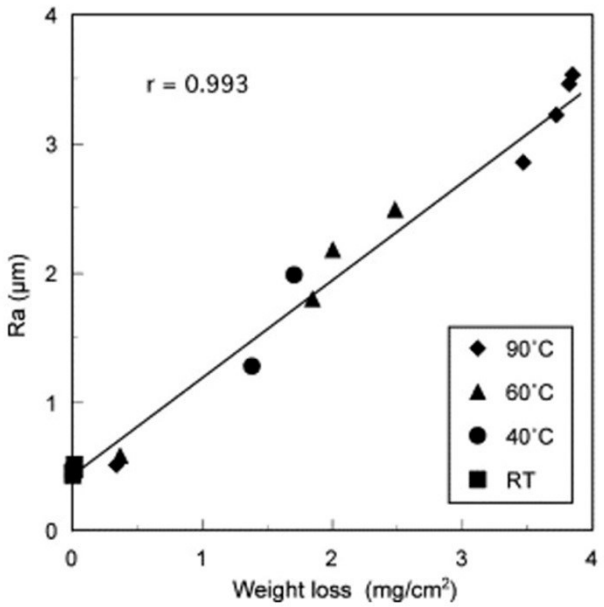

Figure 2-15. Relation between surface roughness and weight loss of cpTi after etching in 48% H_2SO_4 at RT–90°C for 0.25–8 h [102].

2.3.1.2 Blasting process

The blasting process is a low cost method to modify the surface part, which requires abrasive particles to be forced against the surface by a dragging liquid. This is usually compressed by air that, flowing through an ejector, sucks particles up and

carries them. Due to the dynamic of the contact between forced particles and surface, blasting treatment can produce high roughness values and induce mechanical constraints on the metallic surface [101].

The severe plastic deformation, resulted by the impact of the ceramic particles with the surface, leaves a rough surface, whose characteristics are strongly influenced by the size and the shape of the particles [4], [99]. In particular, Lieblich et al. [4] reported that round particles produce a more local homogeneous deformation without grinding down the material, unlike larger particles characterized by edge-like faceted surfaces.

However, beside roughnening, the blasting process can lead to a contamination of the metallic surface, because the temperature increase at the surface, due the high deformation rate and the multiple impacts, favours the surface softening and the particles embedment [4].

Therefore, the blasting material should be chemically stable, biocompatible and should not hamper the osseointegration of titanium implants [99]. Various ceramic paricles are usually applied for sand blasting, such as alumina (Al_2O_3) and titanium dioxide (TiO_2), but another possibility is using a biocompatible, osteoconductive and resorbable blasting material, such as hydroxyapatite [103], [104], which can enrich the metallic surface in calcium (Ca) and phosphorous (P) [101].

According to [99], alumina (Al_2O_3) is frequently used as a blasting material and produces surface roughness varying with the granulometry of the blasting media. An example of a surface blasted with Al_2O_3 particles is reported in Figure 2-16a. However, the blasting material is often embedded into the implant surface and residue remains even after ultrasonic cleaning, acid passivation and sterilization. Alumina is insoluble in acid and is thus hard to remove from the titanium surface. In some cases, these particles have been released into the surrounding tissues and have interfered with the osseointegration of the implants. Moreover, this chemical heterogeneity of the implant surface may decrease the excellent corrosion resistance of titanium in a physiological environment.

Titanium oxide particles is often used for dental implants and, when they are characterized by an average size of 25 μm, a moderately rough surface in the 1–2 μm range can be produced [99]. An example of a titanium oxide-blasted surface is shown in Figure 2-16b. The research work by Ivanoff et al. [105], using micro implants in humans, demonstrated that TiO_2 blasted implants assured a significant

improvement for bone-to-implant contact in comparison with the one resulted for machined surfaces. Similar results were found also by Wennerberg et al. [106], where significant higher removal torque was needed to unscrew screws blasted using TiO_2 particles and screws blasted with Al_2O_3 compared with screws characterized by a turned surface.

Finally, according to [99], calcium phosphate particles lead to a clean, textured, pure titanium surface, being the material resorbable. However, LeGuénnec et al. [99] reported that some experimental studies demonstrated for these surfaces a higher bone-to-implant contact compared to machined surfaces, but similar to that observed with other blasting surfaces when osseointegration is achieved.

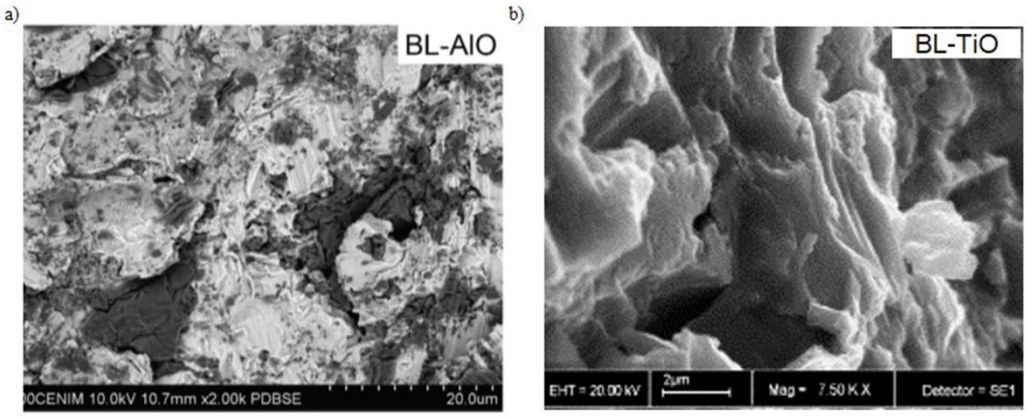

Figure 2-16. a) Backscattered Electron (BE) image of the surface modified with alumina (Al_2O_3) [4]. b) SEM micrograph of a TiO blasted surface [courtesy of Astratech TiOblast^{TM}, France] [99].

2.3.1.3 Electrochemical methods

The electrochemical processes are carried out immersing the metallic part in an electrolytic solution and connecting it to the positive pole of an electrical circuit. Varying the values of the process parameters, different surface roughness can be produced [101]. Many methods were originally set for the electrochemical production of aluminium and they were successively extended to the treatments of titanium based materials [101].

In the category of electrochemical treatments, Bagno et Di Bello [101] reported three different methods, which are electro-erosion, electro-polishing and anodization. The first method leads to a local melting of the metallic material, while the second one provides for the dissolution of surface defects, with a smoothing effect on micrometric scale. Finally, the third treatment (anodic oxidation) allows

the oxide layer to grow from the usual 5-10 nm of atmospheric oxidation up to 40 μm.

The same authors [101] underlines also that, in the case of titanium based substrates, the electrochemical methods can be applied to obtain a wide range of surface properties with a variety of finishing degrees, thanks to the opportunity of a fine tuning of the process conditions.

A combination of acid etching and electrochemical process, i.e. anodization treatment, was applied on pure Ti sheet by Jiang et al. [107], to construct a hierarchical micro–nano structured titania layer and mimic the multi-level bone structure.

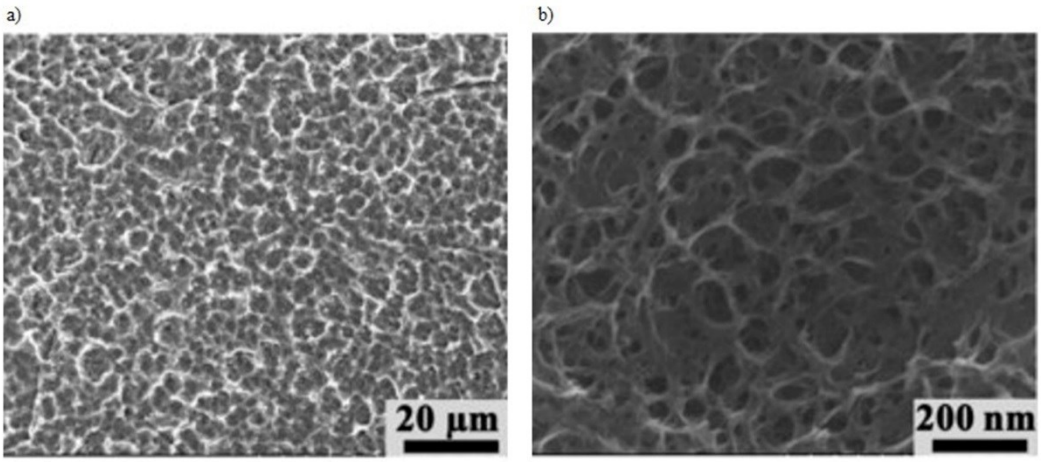

Figure 2-17. SEM micrographs of micro-nano structured surface [107].

This micro–nano structured surface, which is represented in Figure 2-17, resulted from the acid etching in a mixture of H_2SO_4 and HCl followed by the anodization process in a NaOH solution. It was found to be characterized by a higher wettability compared to the nano structured surface, which was obtained through the application of the sole anodization process. Moreover, it was shown that the hierarchical surface was completely covered by a layer of apatite [107], proving the positive effect of the treatment on the material bioactivity, which is the bone-bonding ability of a material [108].

According to Kokubo et Takadama [108], the in vivo bone bioactivity of a material can be predicted examining the ability of apatite to form on its surface during a Simulated Body Fluid (SBF) test, which consists in the immersion of the samples in a solution with ion concentrations nearly equal to those of human blood plasma. The solution, according to [109], can be prepared by dissolving the

following analytical reagents in 1 l of distilled water: 1.5881 g of NaCl, 0.0709 g of $NaHCO_3$, 0.0492 g of $NaHPO_4 \cdot 7H_2O$, 0. 0617 g of $MgCl_2 \cdot 6H_2O$, 0.0746 g of KCl, 0.0171 g of $CaSO_4 \cdot 2H_2O$ and 0.0403 g of $CaCl_2$.

To simulate the biological environment, the SBF tests are performed maintaining the temperature constant at 37°C, while the solution is usually refreshed to keep constant the ions concentration [107].

2.3.1.4 Biochemical treatments

In the analysis of the methods used to modify the surface properties, the biochemical treatments have to be mentioned since they have been recently addressed by an increasing interest, as reported by Puleo et Nanci [110].

According to Dettin et al. [111], these approaches involve implant surface treatments with biologically active substances, which are normally present on cell membrane and extra-cellular matrix, such as adhesion molecules and/or growth factors.

This strategy allows obtaining a bioactive surface able to induce specific cell and tissue responses or, in other words, to control the tissue-implant interface with molecules directly delivered at the interface, which are recognized by the biological environment [111].

Based on [101], the three methods available for the biochemical treatment of a metallic surface are listed in the following.

- Physic-chemical adsorption of the active molecule on the surface. It is the easiest and cheapest method, since it is performed immersing the sample into a bioactive peptide containing solution, but, on the other hand, it does not allow to control the deposition, as represented in Figure 2-18a.
- Covalent binding. In this method, the bioactive peptide is covalently bind to the surface, exploiting the chemical functionalities already present on the metallic surface (Figure 2-18b).
- Enrichment of a biocompatible and bio-resorbable carrier. This method allows controlling with high accuracy the amount of peptide added to a carrier material, which is used to coat the implant surface (Figure 2-18c). Controlling the degradation rate of the carrier, it is possible to guide the release of the peptide in the biological environment.

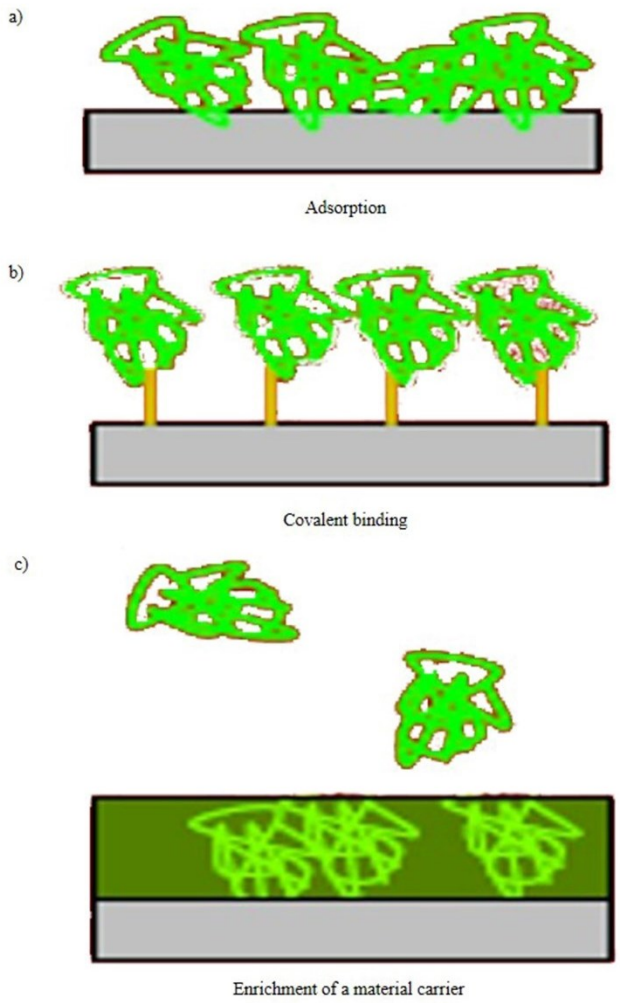

Figure 2-18. Schematic representation of the methods available for the biochemical treatments: a) physic-chemical adsorption, b) covalent binding, c) enrichment of a biocompatible and bio-resorbable carrier.

2.3.1.5 Thermal treatment

The thermal treatment was found to favour the bone-implant interaction by promoting the formation of a layer of titanium dioxide [112], which is characterized by a bioactive behaviour [109].

The role of TiO_2 in the formation of an apatite layer on the treated surface in the simulated body fluids is schematically represented in Figure 2-19. As described by Liu et. al. [113], the Ti-OH groups, formed on the surface after soaking in SBF, are negatively charged and hence combine selectively with the positively charged Ca^{2+} ions in the fluid to form calcium titanate. As the calcium ions accumulate on the surface, the surface gradually gains an overall positive charge. As a result, the positively charged surface combines with negatively charged phosphate ions to

form amorphous calcium phosphate, which spontaneously transforms into apatite since it is the stable phase in the body environment.

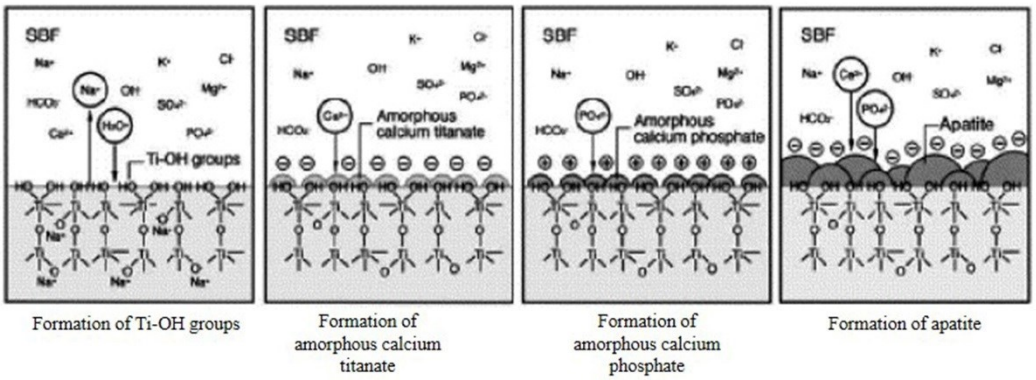

Figure 2-19. Schematic representation of the formation of apatite in simulated body fluids [113].

However, according to [113], [114], the TiO_2 has a positive effect on the implant bioactivity if it is in form of anatase, while an increasing content of the other allotrope, i.e. rutile, could reduce it.

As a consequence, the thermal treatment is usually performed at 450°C for 2 h, triggering the formation of TiO_2 in form of anatase, since an increase of the annealing temperature promotes the transformation of TiO_2 into rutile, as demonstrated by the X-Ray Diffraction (XRD) analyses performed by Lai et al. [112], whose results are reported in Figure 2-20.

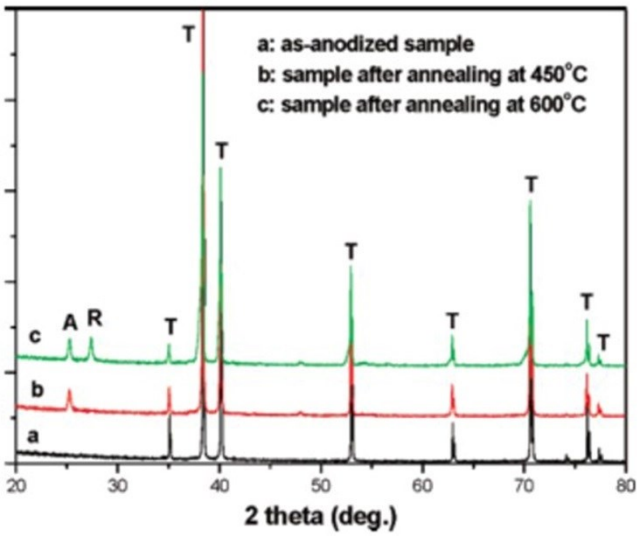

Figure 2-20. XRD patterns of the anodized Ti sample with and without annealing (thermal treatment). A, R, and T represent anatase, rutile, and titanium, respectively [112].

2.3.2 Surface characteristics

As previously described, the material surface characteristics play a key role in controlling the interaction of the biomedical implant with the biological environment. Therefore, the specific role of surface roughness, chemical composition and wettability has to be accurately described.

2.3.2.1 Surface roughness

The surface roughness is shown to give favourable results in vitro, in vivo and clinically [96], by increasing the surface area available for the bone-implant mechanical interaction [4], thus triggering the osseointegration process.

However, even though the surface roughness improves the biological interactions between the bone and the implant, its results can be different varying the scale of the surface irregularities [97].

It was found that micro-scale surfaces maximize the mechanical coupling between the bone and the implant in the early phases in the areas of low quality bone, nano-scale surfaces promote the protein absorption and polymerization, and the adhesion of the osteoblasts that increases the integration between the components [115], [116], while nano + micro-scale surfaces should combine these positive aspects [107] allowing a long-term success of the implant [109].

2.3.2.2 Chemical composition

The surface chemical composition was demonstrated to have effect on the bioactivity of the implant [109], [117], thus affecting the biochemical reactions at the bone-implant interface.

Indeed, as previously described in § 2.3.1.5, the superficial layer of titanium dioxide plays a key role in the formation of apatite, creating an interface layer with characteristics similar to the ones of the bone. Whereas, other chemical elements, as for example growth factors or adhesive proteins, participate in supporting, guiding and controlling cell growth and differentiation, thus enhancing the biochemical phenomena at the base of the implant-bone interaction (§ 2.3.1.4).

2.3.2.3 Wettability

The wettability, used to quantify the material surface energy [118], influences the biological phenomena at the bone-implant interface, and therefore the material bioactivity, with the hydrophilic surfaces promoting the interaction of the surface with the body fluids [119]. The surface hydrophilic or hydrophobic nature is defined

on the basis of the contact angle values, as it can be seen in Figure 2-21. Contact angles lower than 90° identify hydrophilic surfaces (Figure 2-21a), contact angles higher than 90° stand for hydrophobic surfaces (Figure 2-21b).

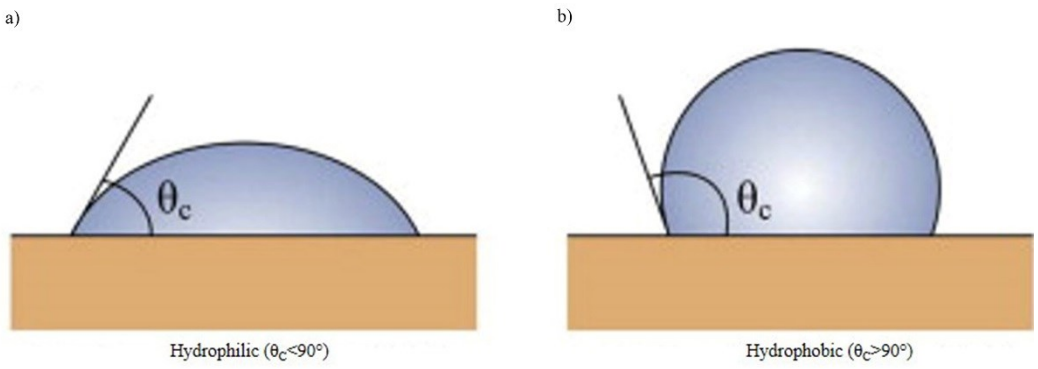

Figure 2-21. Illustration of the contact angle and definition of hydrophilic and hydrophobic surfaces [120].

2.3.3 Biological and forming characteristics

Considering that the production of the biomedical implant involves the two main issues relevant to its surface characteristics and final shape, a process of material design aimed at tailoring its surface properties and a full analysis of this modified material characteristics and performances have to be undertaken. Therefore, beside the investigation of the best surface treatment to modify the surface characteristics enhancing the material bioactivity, which is widely studied in literature as previously described [107], [109], [113], [117], there is the need to investigate the mechanical behaviour of these Ti6Al4V surface treated sheets at elevated temperature in order to determine a proper deformation temperature capable to assure acceptable ductility and, at the same time, to preserve the surface characteristics and material bioactivity.

2.4 Manufacturing processes

The manufacture of biomedical metallic implants can include a series of procedures that depend on different factors, such as the shape and size of the final product, but also the material characteristics and the manufacturing cost.

Different methods can be employed for the manufacturing of biomedical components, i.e. casting, machining, forging and powder metallurgy [3], but for the production of acetabular cups the most widely used are Additive Manufacturing (AM) technologies, which are followed by machining operations [8]. However, the

production of monobloc acetabular cups, consisting of Ti6Al4V shells characterized by high surface-to-thickness ratio and pressed against the polyethylene cup (Figure 1-1b), presents some drawbacks, as the elevated distortion in AM and the significant waste of material in the machining operations to reach the final shape.

The alternative route suggested and investigated within this PhD project is represented by sheet forming processes carried out at elevated temperatures to increase the limited formability of Ti6Al4V at room temperature. However, the proper selection of the sheet forming technique requires an analysis of the existing state of art.

2.4.1 Hot stamping process

Hot stamping process, patented in 1970s by a Swedish company [121], is widely used because it guarantees very high productivity [122]. This process, mostly used for the production of automotive components made of ultra-high strength steel to be applied in the car body-in-white (Figure 2-22) [123]–[125], is a non- isothermal process, where the blank is formed in a single step that combines forming in hot and warming conditions with press hardening between cooled dies [126], as illustrated in Figure 2-23a.

A variation of this process, i.e. the indirect hot stamping, is characterized by a nearly complete cold pre-formed part which is subjected only to a quenching and calibration operation in the press after heating, as shown in Figure 2-23b [122], [127].

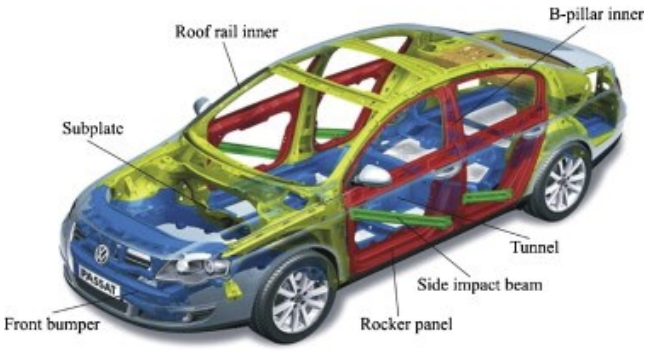

Figure 2-22. Hot stamped parts in a typical middle class car [128].

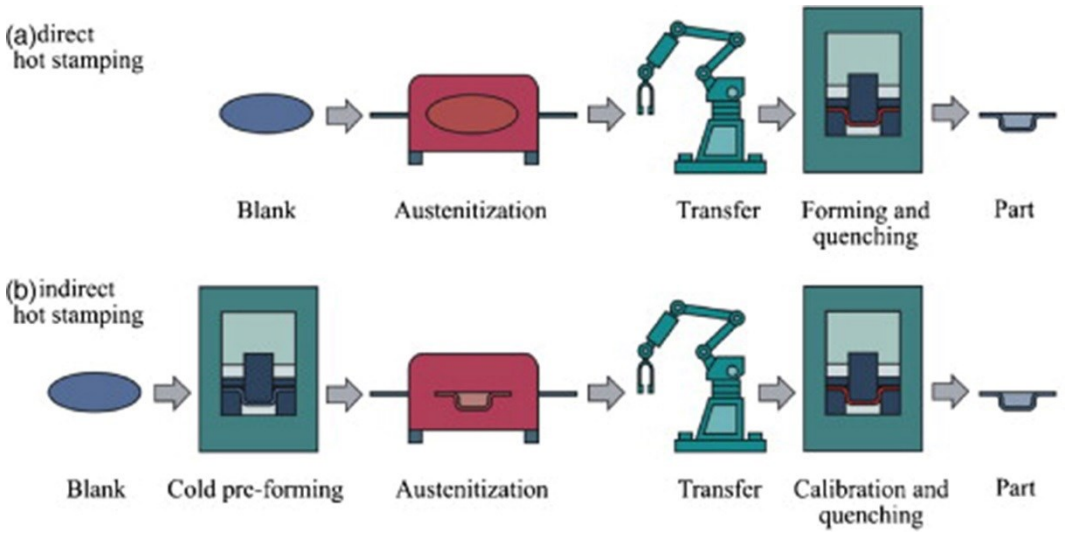

Figure 2-23. a) Direct and b) indirect hot stamping process [122] .

According to [122], the heating phase can be performed exploiting different thermal phenomena, such as radiation in a furnace, induction and conduction. However, because the heating procedure was observed to have a great influence on the part properties, the process time and the cost-efficiency of hot stamping, all these heating methods are required to assure a homogenous blank temperature and a short heating time.

After the heating phase, in the hot stamping process, the blank is transferred as quickly as possible from the heating station to the press, where the forming operations must be completed in the austenitic temperature range. Afterwards, the part is quenched in the closed tool until the entire martensite transformation of the part structure is completed [122].

This fully martensitic structure of the part leads to a tensile strength of up to 1500 MPa and a low elongation of about 5% [122]. However, as reported by Merklein et al. [129], some parts would benefit of regions characterized by a reduced strength but higher ductility in order to enhance their crashworthiness, as the case of the B-pillar automotive component (Figure 2-22). To achieve this, according to [122], the manufacturing of a single part with tailored properties can be carried out applying different process control strategies or using tailor welded blanks, as described in Figure 2-24.

Another advantage of the hot stamping process is obtaining components with a high shape accuracy, since the material springback is minimized with increasing the forming temperature, as demonstrated by He et al. [130] and shown in Figure 2-25.

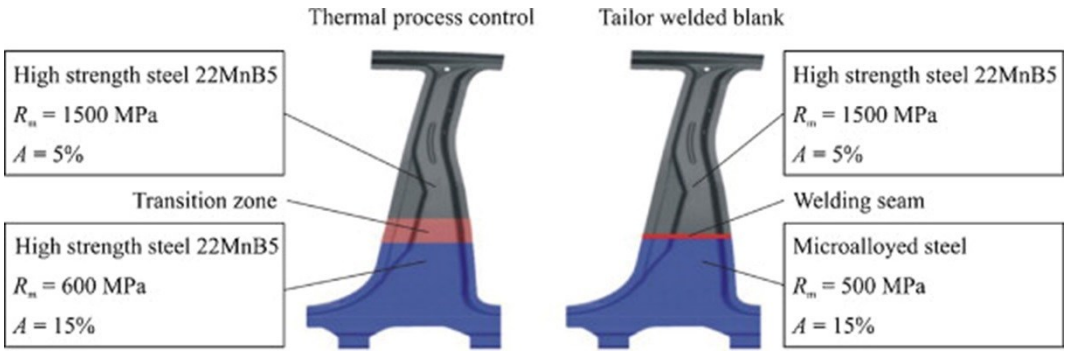

Figure 2-24. B-pillar with tailored properties [122] obtained varying the thermal cycle parameters (left) or using tailor welded blanks (right).

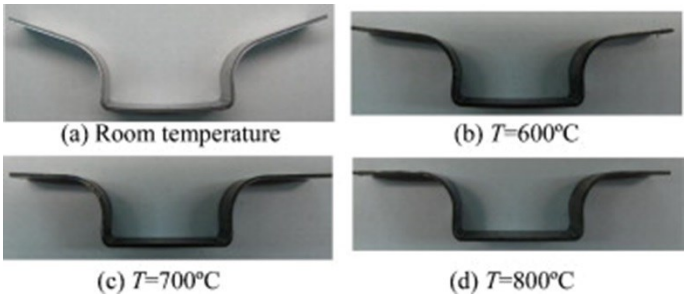

Figure 2-25. Variation in the shape of the side of the hat-shaped bent sheet with the heating temperature: a) room temperature, b) 600°C, c) 700°C and d) 800°C [131].

However, besides the advantageous reduction of springback and the possibility to tailor the mechanical properties of the final component, the hot stamping process needs expensive dies and punches that are specific to the shape of the part being formed.

These drawbacks contribute in limiting the flexibility of the process, which, therefore, results to be adequate only for the mass production [132]. As a consequence, due to the recent diversification of the customer's demand, different manufacturing methods have to be considered for the production of small batches and single products [132].

2.4.2 Incremental Sheet Forming processes

Incremental Sheet Forming (ISF) processes are classified as die-less forming strategies [133], [134] because, unlike conventional sheet metal forming processes, i.e. hot stamping, ISF techniques do not require a dedicated die to operate, thus assuring a high flexibility and a very low set-up cost [135]–[137], while maintaining a relatively low energy demand [138], [139].

This inherent flexibility and negligible tooling cost make incremental forming ideal for small batches [140] and high-customized sheet metal parts, as the case of biomedical implants.

In this context, Ambrogio et al. [141] applied the ISF technique to manufacture an ankle support, starting directly from the analysis of the patient's ankle shape, which was represented in a 3D model by using the reverse engineering approach to assure the best correspondence between the manufactured support and the human body.

Lu et al. [142] applied the ISF process to produce a cranial plate (Figure 2-26a), which is used to repair the deformity of a human skull due to brain tumour or traumatic injuries. The paper demonstrated that a satisfactory cranial shape can be obtained with sufficient accuracy and surface finish (Figure 2-26b), thus indicating the high potential of ISF process in terms of technological advances and economic benefits.

On the other hand, Fiorentino et al. [143] focused the attention on the surface characteristics and biocompatibility of cpTi parts formed by ISF process. It was found that the alkaline (AL) and acid (AC) anodization treatments, applied before the forming process with the aim of modifying the material bioactivity, affected the final surface finish (Figure 2-27) and the cellular growth, being the AL condition the worst case. It is worthwhile noting that the authors accepted the results even if they were not satisfying under a technological point of view, because a rough surface can be a good ground for the strength of cells-prosthesis substrate layer, as previously described in § 2.3.

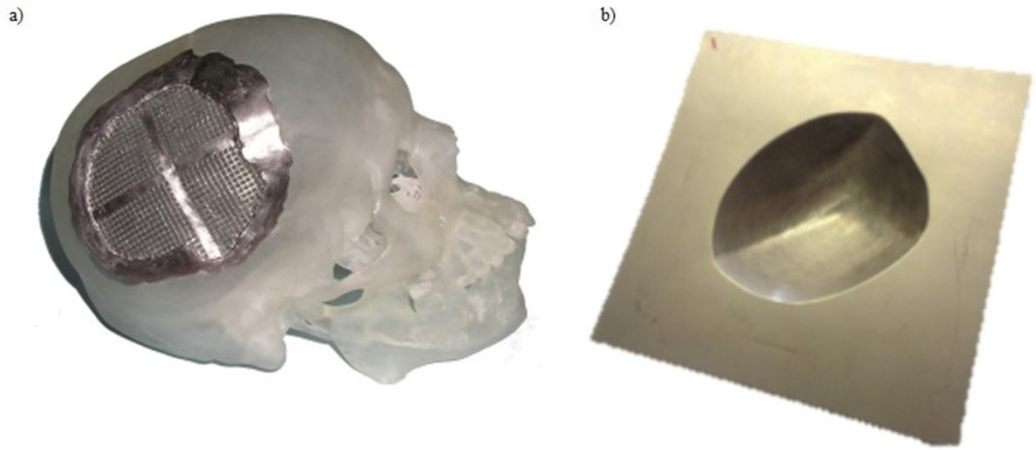

Figure 2-26. a) Cranial plate used in the cranioplasty surgery [144]. b) Cranial plate obtained by Lu et al. applying ISF process [142].

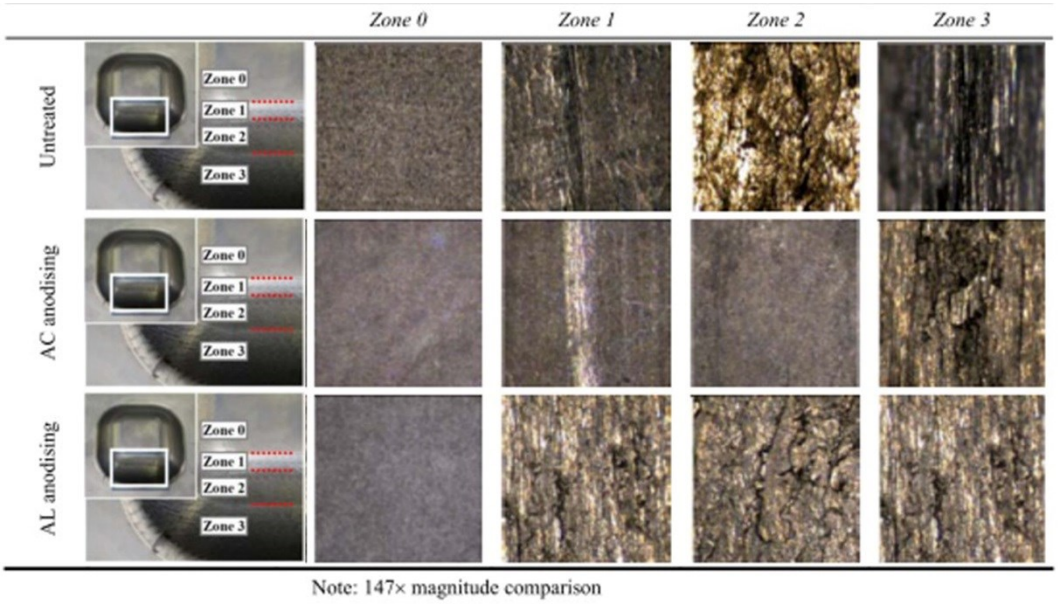

Figure 2-27. Effects of preliminary alkaline (AL) and acid (AC) treatments on the surface of the formed part in different areas, defined in the first column [143].

In ISF processes, the sheet can be locally deformed by one, i.e. Single Point Incremental Forming (SPIF), or more stylus-type tools that move along pre-defined toolpaths [145], as it will be described in the following analysis.

In ISF process, the sheet is placed on a three axes CNC machine table and peripherally clamped during the process, as represented in Figure 2-28.

During the SPIF process, the forming tool, moving from outward to inward and shifting downward as represented in Figure 2-29a along a trajectory generated by a CAD/CAM system on the basis of the part's geometry, locally deforms the sheet [146], [147]. The accumulation of all these local deformations gives the sheet its final shape, as represented in the sequence of the SPIF forming steps reported in Figure 2-29b.

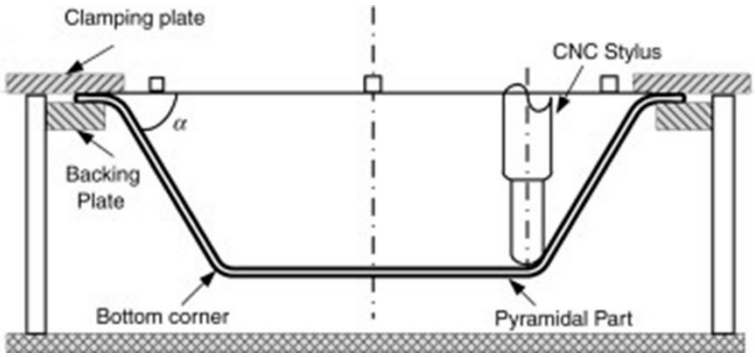

Figure 2-28. Schematic of single point incremental forming setup [148].

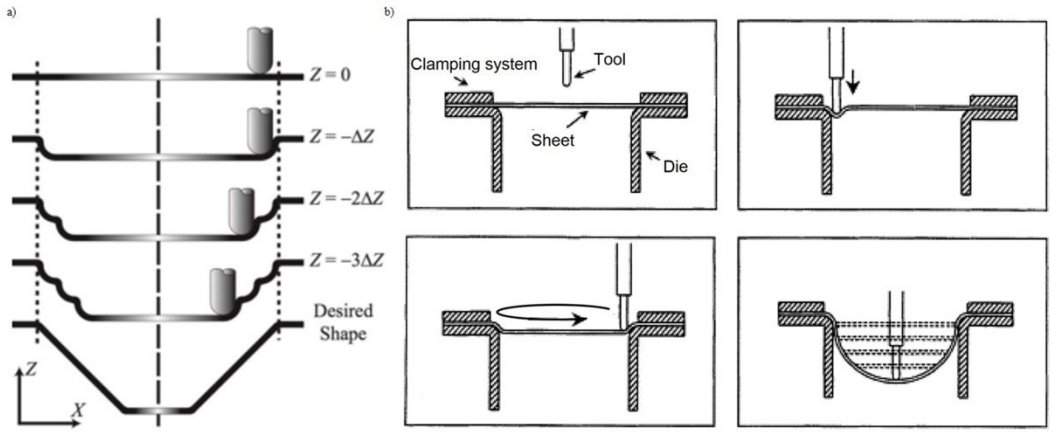

Figure 2-29. a) Toolpath strategy in SPIF [149]. b) Schematic representation of the forming steps in SPIF [150].

SPIF process was found to increase the forming limits compared to conventional processes, providing a different and higher forming limit curve compared to the traditional one [151], [152], as represented in Figure 2-30. Indeed, as reported by Filice et al. [152], because the plastic deformation induced by the small size punch is strongly localized and incrementally progresses as the tool moves along the assigned path, higher strains can be attained in the material before that fracture occurs.

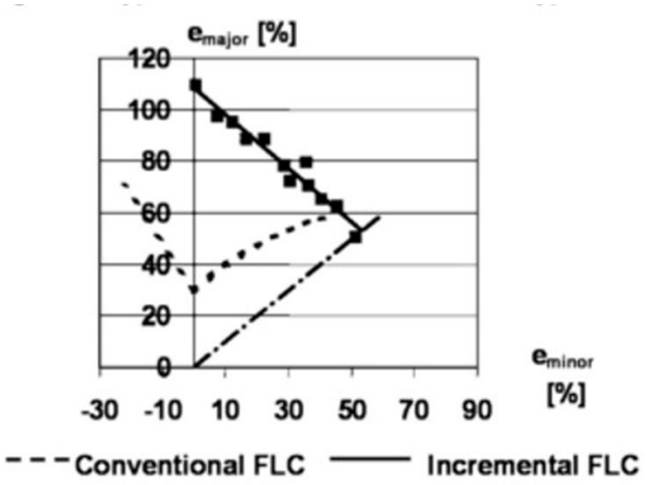

Figure 2-30. AA 1050-0 Forming Limit Diagram for incremental forming processes [152].

To take advantage of this higher formability, it is necessary to understand how to maximize it varying the process parameters, focusing therefore on the analysis of the effect of each working parameter. As a consequence, the review performed by McAnulty et al. [153], based on the analysis of experiments and results from 35 papers, aims at providing evidence to support the hypothesis of an ideal operating range for each parameter and interdependency of parameters. The authors [153]

concluded that, despite most papers concluding that formability increased with thickness, the material thickness should be optimized based on the type of material because very large thicknesses, beyond the values tested in most of the papers, would begin to be too challenging to form due to the large forces required. Moreover, the review [153] reported that the type and thickness of the material should also be a consideration in optimization of tool diameter, in order to achieve maximum formability. However, the authors [153] highlighted conflicting results about the impact of changing the tool diameter, likely due to this parameter affecting the process in a number of ways such as friction conditions, forming force and stress at the tool-sheet interface. The analysis [153] suggested also more research work on the effect of the tool type in order to understand when non-hemispherical tools might be beneficial to formability and other outcomes in SPIF, for example surface finish or forces. Still reporting the authors' conclusions [153], the consensus in the literature for step down (or incremental depth) was that formability improved with decreasing values, but it should be optimized if reduced process time is a requirement. However, the fact that in polymers a too-small step size was found to reduce the formability indicates also a step size sensitivity to the material [153]. In conclusion, the review [153] reported that both feed rate and spindle speed should be optimized depending on the material type, with the former also necessarily requiring a trade off with process time. To note that spindle speed was generally recognized to be a major factor in the heat generated from friction, and if heating benefits are desired, optimization is necessary to prevent surface damage from excessive friction between the tool and sheet [153].

According to Malhotra et al. [154], the choice of appropriate process parameters is supported by a comprehensive physical knowledge of the mechanisms of deformation and fracture, since the formability was observed to be strongly influenced by the combination of global shape and process parameters.

By using a FE model, the authors investigated accurately the deformation mechanics in SPIF, analysing the deformation history in the sections and elements represented in Figure 2-31.

It was found that the local stretching and bending of the sheet around the tool lead the material on the outer side (element 8) to stretch more than the one in the inner side (element 1), thus increasing the plastic strain (ε_p) in the outer surface as it can be observed in Figure 2-32a. Whereas, the shear strains (ε_{zx}, ε_{zy}) were

observed to be higher in the inner surface (element 1 for ε_{zx} in Figure 2-32b), because of the friction determined by the tool motion in the meridional (perpendicular to the toolpath spiral) and circumferential (parallel to the hoop of the toolpath) directions. However, because the tool moves mainly in the circumferential direction, the shear along this direction (ε_{zx}) resulted to be greater than the one in the direction perpendicular to the toolpath motion (ε_{zy}). Moreover, this through-the-thickness shear was found to increase along the toolpath motion with the deformation depth (Figure 2-32b) [154].

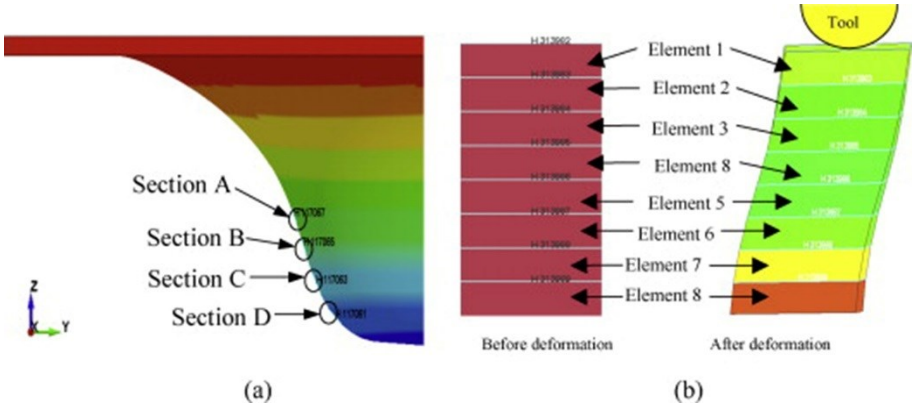

Figure 2-31. a) Schematic of sections A, B, C and D along the component wall at which the deformation history from FEA is examined. b) Nomenclature of elements through the thickness of the sheet [154]: element 1 refer to the inner surface, element 8 to the outer surface.

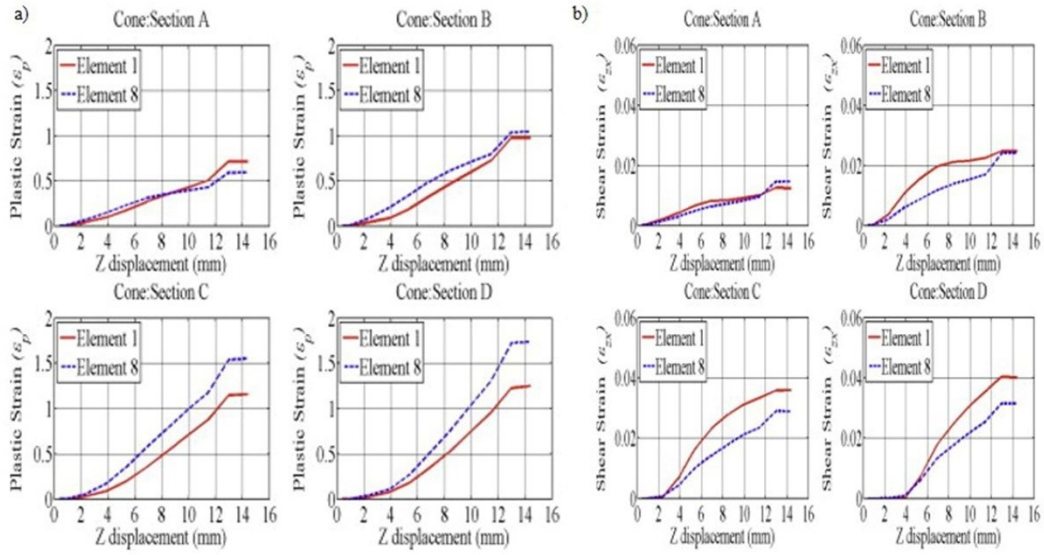

Figure 2-32. Evolution at sections A, B, C, and D for the 70° cone of a) plastic strain ε_p and b) through-the-thickness shear along the toolpath direction, ε_{zx} [154].

These results on the through-the-thickness shear are in agreement with the work by Allwood et al. [155] which proposed that greater shear can enhance

formability, identifying the through-the-thickness shear as the deformation mechanism which reduces the damage accumulation on the inner side of the sheet.

Therefore, based on the analysis by Malhotra et al. [154], the local bending and the through-the-thickness shear were identified as the two mechanisms governing the fracture occurrence and the crack initiation location, since their cumulative effect is to increase the damage accumulation on the outer side of the sheet, causing the fracture to start from this side of the sheet.

The occurrence of the fracture starting from the outer surface correlates well also with the work by Fang et al. [156]. Based on their analytical evaluation of the deformation mechanisms arising in SPIF, it was concluded that the fracture appears in the outer side of the sheet at the transitional zone between the contact area and the formed wall, namely in correspondence of the point "Q" represented in Figure 2-33. Indeed, the research work [156] revealed that the deformation is not limited to the area in contact with the forming tool ("region A" in Figure 2-33), but it occurs also in the neighbouring zone of the wall which was already formed ("region B" in Figure 2-33).

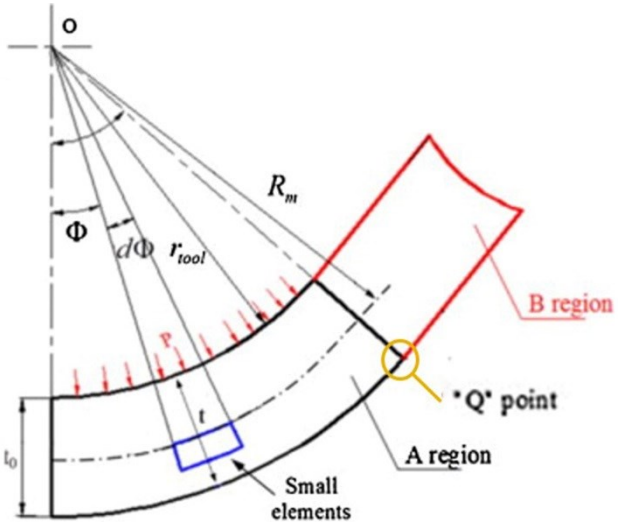

Figure 2-33. a) Schematic representation of a cross section view of SPIF: details of the contact region A and the neighbouring wall of region B. "Q" point represents the transitional point between region A and B [156].

The identification of the "Q" point as the most likely starting point for fracture was supported also by the experimental result of Figure 2-34a, in which the fracture was observed to occur approximately at the transition area between the contact area and the wall [156]. Figure 2-34b shows the detailed location of the fracture by

overlapping the deformation area and the tool behind it, highlighting also the transition dotted line between region A and B.

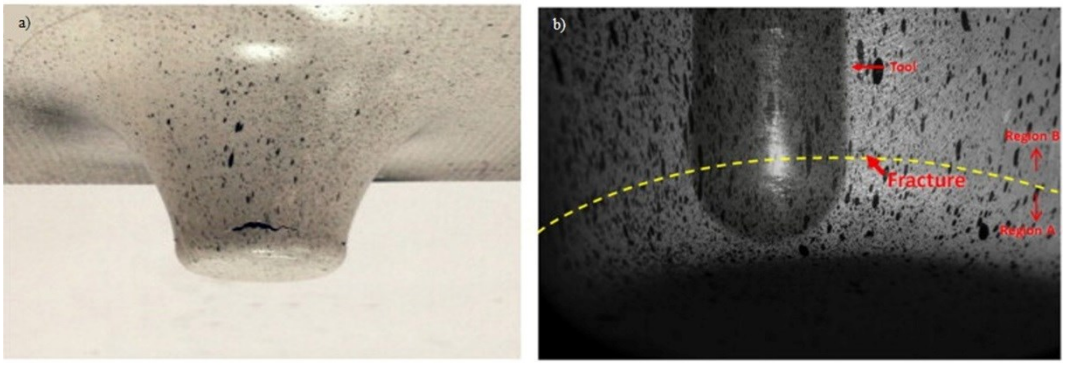

Figure 2-34. a) Fracture in the formed part (aluminium alloy AA1100). b) Overlapped the sheet deformation zone and the tool behind it, highlighting region A and B through the separation dotted yellow line [156].

Moreover, the analysis of the fracture evolution represented in Figure 2-35 led the authors [156] to conclude that the crack in SPIF occurs first along the toolpath horizontal direction (Figure 2-35a). In the following forming steps, the crack was found to be stretched by the meridional tensile stresses, which arise from the downward movement of the tool, and then expanded in the horizontal direction, due to the circumferential movement of the tool.

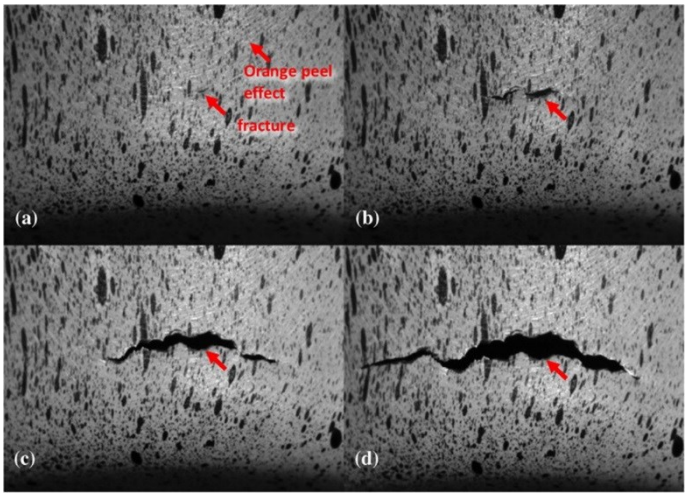

Figure 2-35. Detailed view of the fracture evolution in aluminium alloy AA1100 sheet: a) first pass after fracture, b) second pass, c) third pass, d) fourth pass [156].

In the same paper [156], the investigation of the fracture surface, performed through SEM observations reported in Figure 2-36, revealed the formation of dimples, characteristics of the ductile fracture, but also a shear band in the inner side of the sheet, which was determined by the movement of the tool in the

circumferential direction. According to the authors [156], in agreement with the results of Malhotra et al. [154] and Allwood et al.[155], the suppression of the dimple formation in the inner side determined by the severe shear effect was recognized as the mechanism that hinders the fracture occurrence, proving the propagation of fracture from the outer to the inner side of the sheet.

As the orientation of the dimples can be regarded as the origin of fracture, a further evidence of the fracture initiation on the outer side of the sheet is given by the fact that some dimples were found to be elongated along the perpendicular direction to the sheet thickness and orientated towards the outer surface [156].

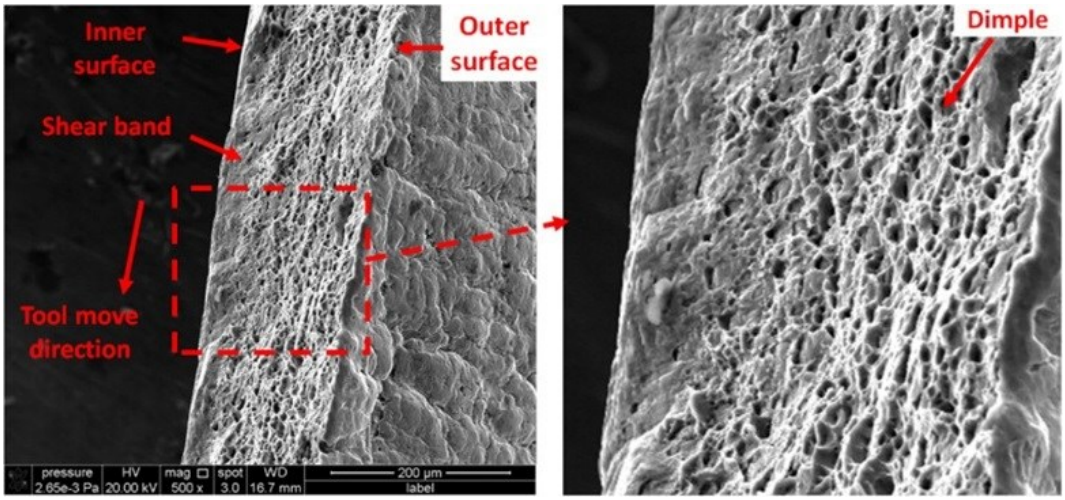

Figure 2-36. Fractographic analysis at SEM at the crack location of aluminium alloy AA1100 sheet formed applying SPIF[156].

During SPIF process, the undesirable local bending that occurs in the region between the forming tool and the fixture (see Figure 2-28) results in a poor geometric accuracy [133]. To alleviate this issue, different variants of ISF have been proposed in recent years.

Among them, Multi-pass Single Point Incremental Forming (MSPIF) strategy allows increasing the maximum formable wall angle [157], [158], forming consecutive, intermediate shapes as represented in Figure 2-37, covering the entire [159] or partial [160] forming areas.

According to Duflou et al. [159], the enlargement of the process window achievable by means of multi-step SPIF can be explained by the straining of horizontal workpiece areas that remain unaffected in conventional toolpath strategies, allowing the production of vertical walls without leading to part failure. Moreover, the resulting thinning of the sheet during multi-step forming can exceed

the maximum thickness reductions observed in single-step processing, implying a further formability shift.

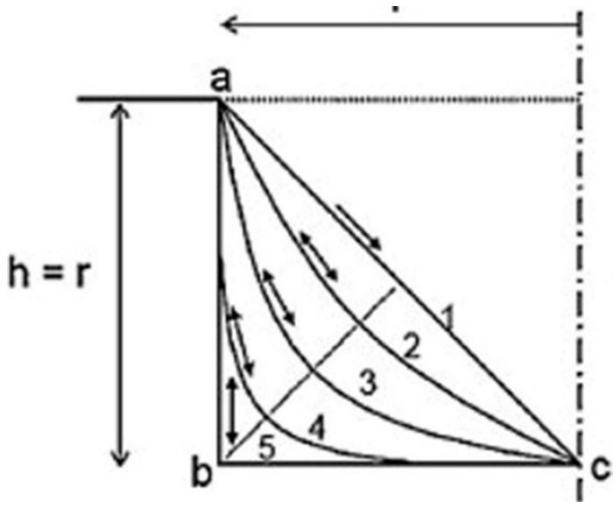

Figure 2-37. Example of Multi-Pass Incremental Forming Strategy used by Skjoedt et al. [161] and reported from [157] .

However, even though geometric improvements were attained according to [133], these efforts in MSPIF still cannot overcome the aforementioned global bending effect, which can be limited by forming the part close to the edge of the forming area.

In this context, a new variant of incremental forming, known as Two Point Incremental Forming (TPIF), emerged. It is based on the use of a partial (Figure 2-38a) or a full die (Figure 2-38b), which, supporting the sheet during the deformation process, allows reducing the global bending effect.

During the TPIF process, the sheet is deformed in two points: while the forming tool pushes the material downward, causing a deformation point on the inner side of the sheet, the partial die generates a counter force, which results in the other deformation point on the outer side of the sheet.

TPIF process was found to reduce the formability limits compared to SPIF, but, on the other hand, it allows forming parts with a higher geometric accuracy, also in case of complex and asymmetric components [134], [162]. However, the use of a partial or total die reduces the inherent flexibility of the incremental forming strategy [133].

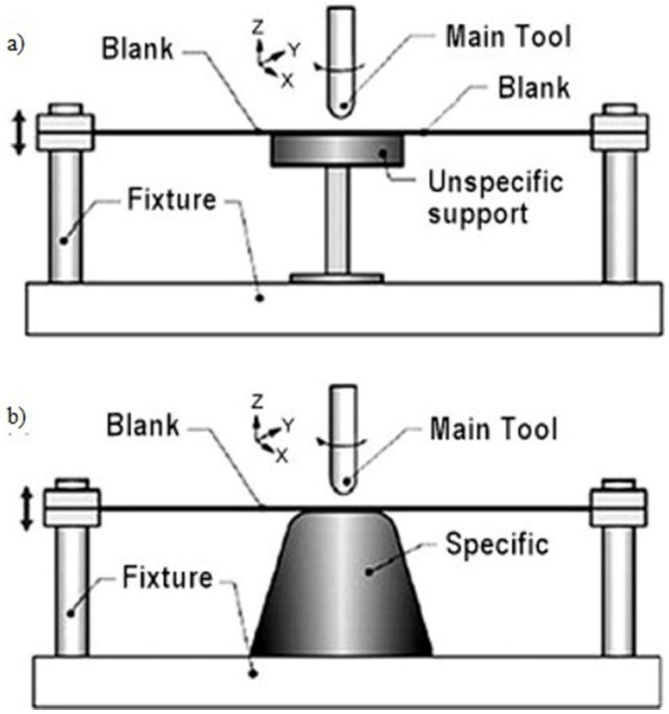

Figure 2-38. TPIF with a) partial die and b) full die [162].

As a consequence, this method was extended leading to another incremental forming strategy, called Double-Sided Incremental Forming (DSIF), in which two moving tools are used in each side of the sheet, as shown in Figure 2-39. In particular, the tool added to the outer side of the sheet (named "supporting" or "bottom" tool) moves along with the forming ("top") tool in the toolpath direction, and, simultaneously, acts as a supporting tool without compromising the die-less nature of the incremental forming process [163]–[165].

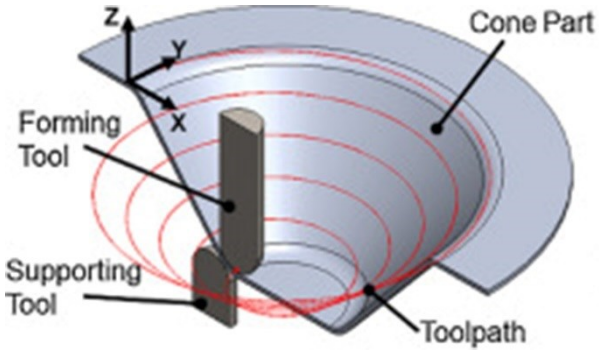

Figure 2-39. Cross section of DSIF with the detail of the two tools and the toolpath [166].

The DSIF forming strategy was found to increase the geometric accuracy compared to SPIF [167], but it still does not give optimum results. This is attributed to the fact that the prediction of the appropriate position of the supporting tool is particularly challenging because it is based on the instant local thickness of the

sheet, which strongly depends on the stretching mechanism operative during the IF process. A slightly off prediction of the sheet thickness in the toolpath generation will cause the loss of contact between the tool and the sheet metal, thus declassing DSIF into SPIF and resulting in a lower geometric accuracy [149], [167]. Because the loss of contact has been frequently observed using the sine law[4] to predict the part's thickness, complicated equipment and compensation algorithm were realized to address this issue in DSIF [166].

Considering the analysis of the deformation mechanism, very few papers are devoted to this topic in DSIF [168]. Among them, Moser et al. [169] evaluated the evolution of the triaxial state of deformation in an innovative part geometry, characterized by convex and concave surfaces, through FEM simulations. It was found that the strain loading path history is strongly influenced by the local curvatures of the part, as the tools approach the material in different ways.

Lu et al. [168] developed an analytical model based on the stress state analysis. According to this, the main difference in the formability limits between SPIF and DSIF comes from the Drop Of the Stress Triaxiality (DOST), which occurs in the part of the sheet compressed by both the tools. Indeed, if the stress triaxiality is used to evaluate the material formability, the fracture occurs when the shaded area in Figure 2-40, representing the integration of the stress triaxiality as a function of the equivalent strain, reaches a critical value. Therefore, if the shaded areas in SPIF and DSIF are the same, the DOST allows DSIF reaching higher value of strains compared to the SPIF process.

The forces related to the bottom tool, generating the DOST, allows delaying the fracture occurrence in DSIF compared to SPIF [168]. In particular, the DOST was found to increase with the application of greater forming forces, thus enhancing the formability by further moving the fracture point toward right, as represented in Figure 2-41a [168].

On the other hand, the DOST was observed to be dependent also on the shift of the supporting tool, which represents the relative position of the two tools in DSIF. Lu et al. [168] explained this effect through the change of the position where

[4] The sine law is defined as:

$$t_F = t_0 \sin(90 - \alpha)$$

where t_F, t_0 and α are the final thickness, the initial thickness and the desired wall angle, respectively.

the DOST occurs, as represented in Figure 2-41b. In detail, it was found that, when the tool shift is applied, the DOST can be reached at a value of the equivalent strain lower that the case without tool shift, thus increasing the forming limit.

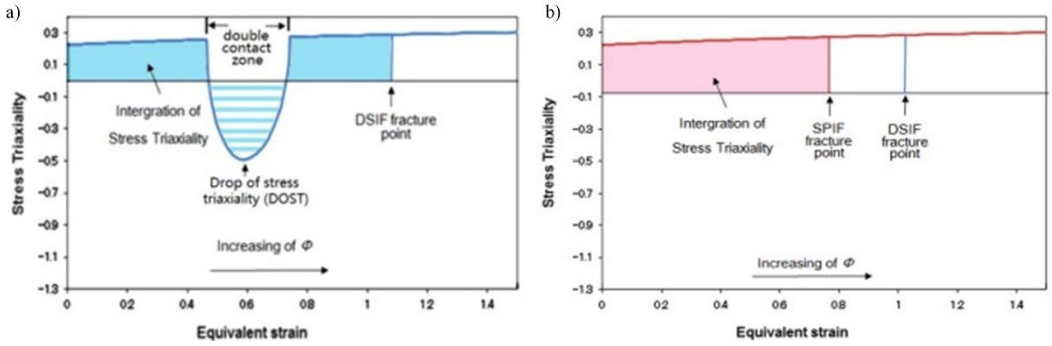

Figure 2-40. Comparison of stress triaxiality between SPIF and DSIF process: a) DSIF; b) SPIF [168].

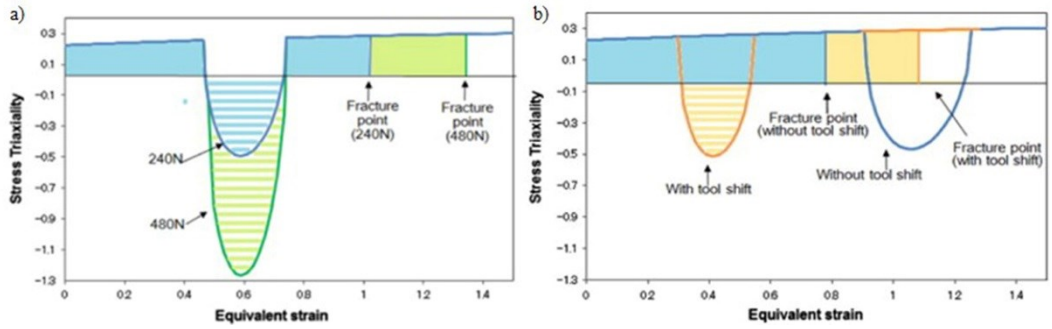

Figure 2-41. Effect on stress triaxiality drop and DSIF formability of a) supporting force and b) tool shift [168].

In the same paper [168], the material deformation behaviour was investigated by analysing the final shapes of the holes (Figure 2-42), which were drilled in the sheet before the DSIF process. Based on these observations, the authors concluded that the major deformation mode in the DSIF process is stretching in the meridional direction, compression in the radial direction and slight through-the-thickness shear in the tool movement direction [168].

The research underlined also that introducing the tool shift and increasing the supporting force have similar effect on increasing the compression, but they do not significantly affect the occurrence of the through thickness shear, as the contact area at the bottom tool side is smaller than that at the top tool side [168]. This result also implies that the top tool still plays the major role than that of the bottom tool in the DSIF material deformation [168].

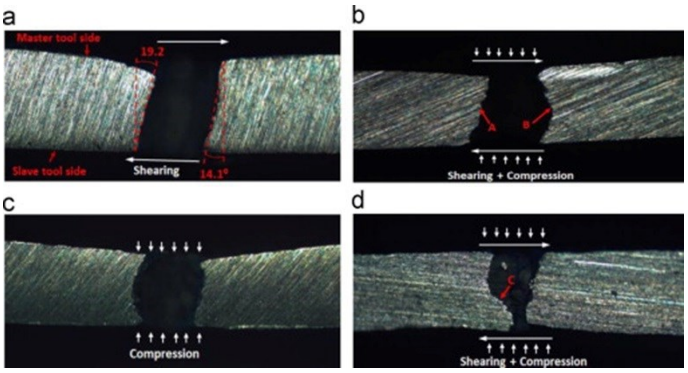

Figure 2-42. Material deformation in tangential cross-section of the hole: a) 240 N without tool shift, b) 240 N with tool shift, c) 480 N without tool shift, d) 480 N with tool shift [168].

As an alternative to the DSIF process, Accumulative Double-Sided Incremental Forming (ADSIF) was proposed by Malhotra et al. [170] by changing the toolpath strategy used in DSIF.

As described in [133], in the conventional DSIF, the tools move in the negative Z-direction by an incremental depth ΔZ, and deform the sheet along a shape-dependent XY-trajectory at that depth. Afterwards, the tools move down by another ΔZ and repeat the process until the tools reach the final depth of the desired geometry (Figure 2-43a). The tools, consequently, move from the outside of the desired geometry to the inside while traveling vertically from the top to the bottom of the component to be formed.

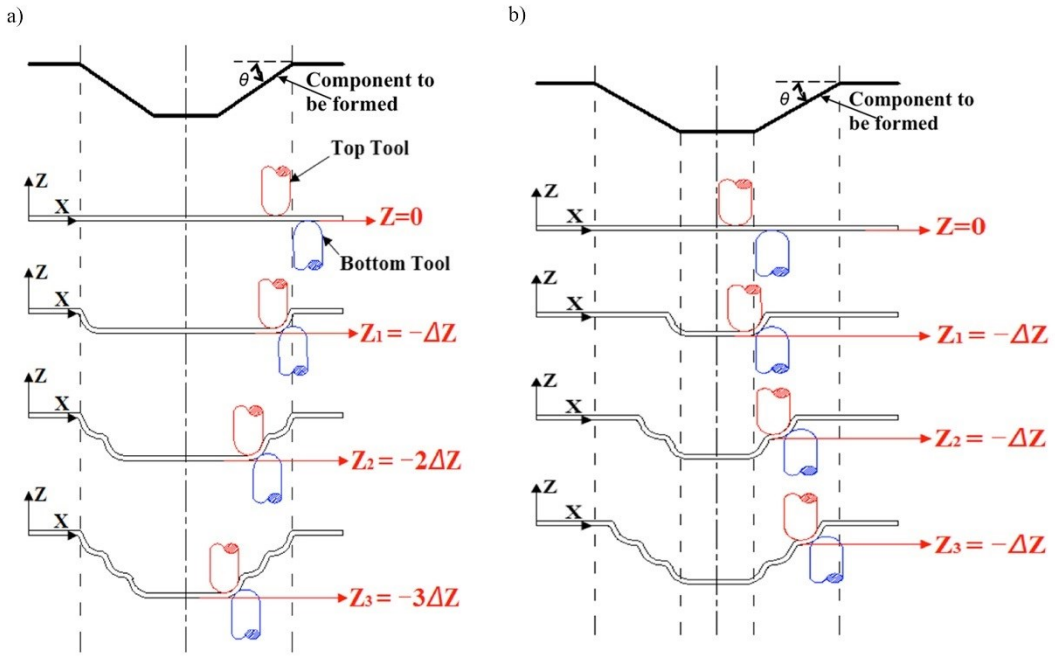

Figure 2-43. a) DSIF and b) ADSIF toolpath strategies [149].

On the contrary, in ADSIF, the tools move from inward to outward, at a given horizontal plane as represented in Figure 2-43b. In details, the tools in ADSIF moves along the shape-dependent loop in circumferential direction to the specified incremental depth ΔZ and then travel outward in the plane of the sheet forming another loop of undeformed material to the subsequent ΔZ, thus causing the previously formed annulus to be moved downward to a new depth that is twice the previous depth [171].

It is important to note that in ADSIF there is no loss of contact between the tool and the sheet because the tools, kept at the same plane and moved toward, always deform the virgin material, thus avoiding the need of predicting the local thickness to position the tool and resolving the issue of loss of contact with the conventional DSIF toolpath strategy.

The ADSIF strategy was found to significantly increase the geometric accuracy, with a lower incremental depth reducing the deviation between the formed part and the desired geometry as represented in Figure 2-44. However, because the smaller incremental depth the higher process time, Ndip-Agor et al. [149] proposed a systematic approach to determine the relative tool position which allows achieving the desired geometric accuracy with a larger incremental depth.

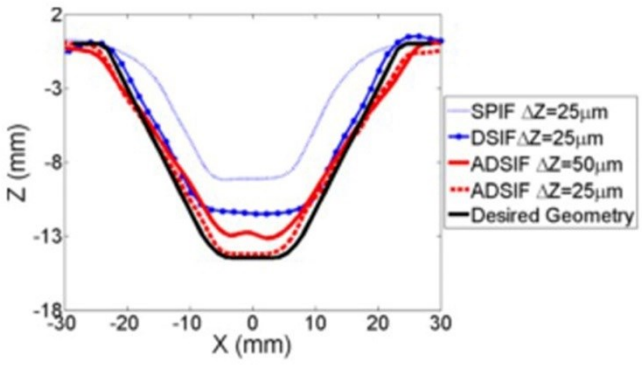

Figure 2-44. Improved geometric accuracy for a 40° cone with ADSIF and the influence of incremental depth in ADSIF on geometric accuracy [133], [170].

Along with the improvements of the geometric accuracy, ADSIF is also characterized by an increased formability compared to SPIF and DSIF [170]. According to the analysis by Smith et al. [171], in which the deformation mechanisms of ADSIF are compared with the ones of SPIF by using FE models, this is attributed to the increased hydrostatic pressure and greater through-the-thickness shear recorded for the ADSIF process. Moreover, the ADSIF process was

demonstrated to have no adverse effects on the fatigue life under cyclic tension [172].

A step forward in the ISF processes is represented by the Mixed Double-Sided Incremental Forming (MDSIF) process, which was recently developed by Zhang et al. [133] through the combination of the DSIF and ADSIF strategies.

As described by the authors [133], in the MDSIF strategy, a part is first formed using ADSIF with a relatively large incremental depth, to ensure that the loss of contact between the supporting tool and the sheet is avoided and to reduce the forming time, respectively. This ADSIF step acts therefore as a rough forming pass to obtain the formed geometry close to the desired geometry. Then, without unclamping the fixture or moving the metal sheet, DSIF is used as the second forming step on the preformed part to fine tune the geometric accuracy of the part.

In MDSIF, according to [133], the first forming step, resulting in a geometry closed to the desired one, allows reducing the forming forces in the second step, because of the smaller plastic deformation needed to reach the final shape. As a consequence, the global bending and the loss of contact between the tools and the sheet due to compliance are reduced, and the geometric accuracy is improved, also for complex shapes characterized by convex and concave surfaces, as reported in Figure 2-45.

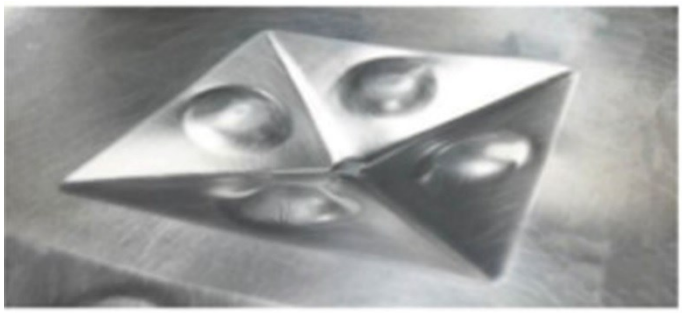

Figure 2-45. Convex-concave aluminium part formed by Zixuan et al. [133] applying Mixed Double-Sided Incremental Forming (MDSIF) technique.

One challenge in all the aforementioned incremental forming techniques is forming workpieces made of lightweight but “difficult-to-form” materials [145], such as Ti6Al4V. Because of its low formability at room temperature [9], [10], a possible solution to form Ti6Al4V sheets using ISF processes is to increase the forming temperature. According to literature, many techniques have been proposed based on the following heating methods:

- Convection: Ji and Park [173] exploited the heat convection using hot air blowers to form magnesium alloy (AZ31) sheet by SPIF at different forming temperatures. Their results shown that the forming limits increased with the temperature (Figure 2-46), as found in other conventional forming processes.

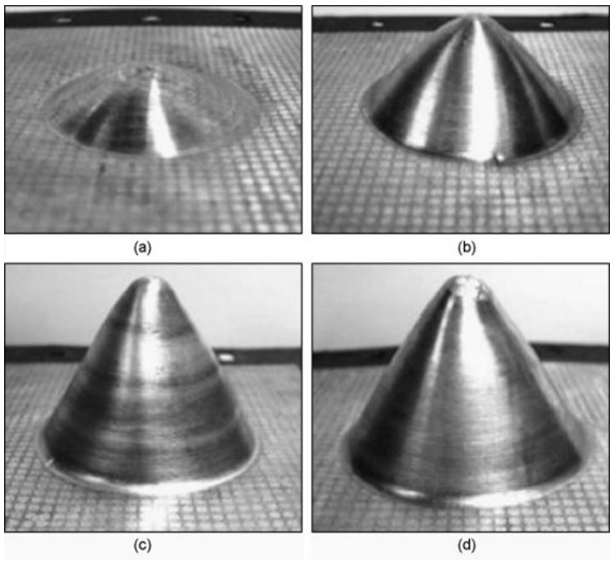

Figure 2-46. Magnesium cones incrementally formed at various temperatures: a) 100°C, b) 150°C, c) 200°C and d) 250°C [173].

- Conduction: Ambrogio et al. [174] designed a heating system to assure a homogeneous temperature of the sheet. A heating band, fixed at the external surface of the die as represented in Figure 2-47, was used to form magnesium alloy (AZ31) sheets, whose maximum formability resulted at 250°C, as found in other conventional forming processes, like deep drawing.

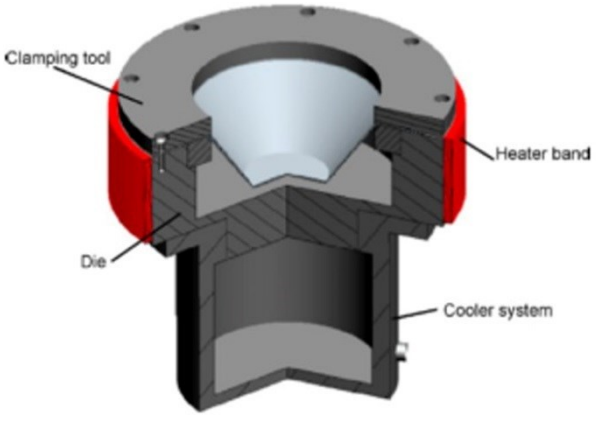

Figure 2-47. Experimental set-up with the detail of the heating band used by Ambrogio et al. [174].

- Friction heat: Ambrogio et al. [175], investigating the high-speed incremental forming (SPIF) of Ti6Al4V, took into account also the heating of the sheet generated by the elevated friction. Recently, a deep analysis of the temperature variation as a function of the applied feed rate and material was performed using an infrared thermo-camera by Ambrogio et Gagliardi [176].
- Electric heating: Fan et al. [177] introduced the use of electric current to heat the metal sheet in incremental forming operations (Figure 2-48). Good results were found in forming difficult-to-form materials, like magnesium and titanium alloys [178].

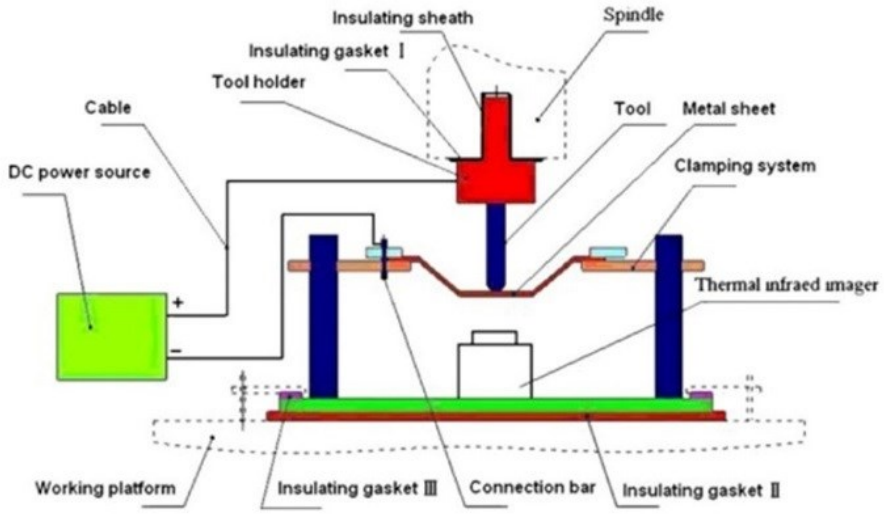

Figure 2-48. Experimental set-up for electric heating of metal sheet in Single Point Incremental Forming (SPIF) [179].

- Radiation: Duflou et al. [180] took advantage of a laser beam to generate a localized heated point, which moves along with the forming tool. This laser-assisted process was found to assure improvements in formability and geometric accuracy, but it is not cost-effective compared to the other variants [145].

Among all these methods, the Electrically-assisted Incremental Sheet Forming process (E-ISF) has the highest potential because it is the most flexible and efficient in terms of equipment cost, but the geometric inaccuracy and the final poor surface quality are the main drawbacks [145]. However, if the surface quality is still a challenge for all the aesthetic purposes, a rough surface is advantageous for biomedical applications, playing a key role in the bone-implant interaction [101],

[117], as previously described in § 2.3. Therefore, for the production of a part made of Ti6Al4V and characterized by a double curvature, as the acetabular cups used in the hip replacement, E-ISF process allows combining the deformation process and the surface modification aimed at increasing the bioactivity of the part.

E-ISF can be classified based on the applied forming strategy, i.e. SPIF and DSIF, but also on the extent of the heated area. Ghiotti and Bruschi [181] proposed a new experimental set-up to combine SPIF strategy and a homogeneous temperature field in the entire blank, while, in Electrically-assisted DSIF (E-DSIF) process [182], where the two tools act as two electrodes, the sheet is locally heated at the tools-sheet contact point. However, in this case, the lack of contact between the bottom tool and the sheet metal, which may occur in DSIF process, can cause the occurrence of sparks, thus damaging both the sheet and the tool.

Therefore, based on the previous analysis, a valid forming strategy to electrically form Ti6Al4V sheets has to take into account the achievements reported in literature related to the two main issues, namely the geometric accuracy and the electric phenomena, such as the sparks formation.

2.5 Summary

The idea of applying sheet forming process for the production of a biomedical component made of Ti6Al4V and characterized by a high surface-to-thickness ratio, as described in the Introduction, requires an investigation of the material characteristics, such as anisotropy, microstructural and mechanical properties, in a wide range of temperatures and moderate strain rates, being the literature more focused on the lower ones, characteristics of the superplastic regime.

With the increasing interest of the academic and industrial communities in the numerical assessment of the manufacturing process for its design and optimization, the PhD project aims at providing the modelling of the material behaviour under different testing conditions, paying attention to the prediction of fracture, which is particularly sensitive in case of sheet forming processes. In this context, the latest achievements and considerations about the fracture criteria have to be taken into account, focusing most on the significant effect of the Lode parameter, which, representing the influence of the deviatoric stress tensor, was recently recognized to play a key role in describing the material fracture behaviour. Moreover, because all the models related to the investigation of Ti6Al4V were found to be focused on

its failure behaviour at room temperature, the analysis of literature suggested to investigate this aspect in a wide range of temperatures.

Moving to the biomedical aspect and the related biological issues of the industrial problem, many methods have been investigated in literature to modify the surface characteristics and trigger the implant's osseointegration, but none of them examines the mechanical and technological properties of the material modified on the surface, thus suggesting the need for further investigations.

Finally, considering the analysis of the papers related to the manufacturing processes, the Incremental Sheet Forming process is chosen to produce the Ti6Al4V shell, since its die-less nature makes this process flexible, cost-efficient and therefore suitable for small volume batches. Among the different heating methods described in literature to increase the forming temperature and therefore the material formability, Electrically-assisted ISF process is shown to combine the deformation process and the surface modification aimed at increasing the bioactivity of the part, thus considering the twofold aspect of the industrial case. Different forming strategies, chosen among the ones described in the review of literature, are considered to increase the geometric accuracy of the final component.

Furthermore, the analysis of ISF process in literature revealed that the deformation mechanics, which strongly influences the material formability and therefore the fracture phenomenon, were widely studied in case of SPIF, but in a limited manner in the variants using two moving tools, as the case of DSIF technique, thus suggesting the need to provide a deeper understanding of the relations between the DSIF process mechanics and the fracture occurrence.

3 Chapter

Material characterization

This chapter focuses on the investigation of the microstructural and mechanical properties of Ti6Al4V sheets under testing conditions similar to the ones experienced during the deformation process carried out at elevated temperature.

The material characterization investigates the material plastic and anisotropic behaviour, as well as the post-deformation properties, i.e. micro-hardness, crystallographic and microstructural features, as a function of the process parameters, namely temperature and strain rate.

The chapter is divided into two main parts: while the first describes the experimental set-up and procedures for the different tests and analyses performed, the second reports the related results, paying attention to the correlation between the Ti6Al4V mechanical properties and microstructural characteristics.

3.1 Material & methods

3.1.1 Material

The material characterization was performed on samples extracted from a 1 mm thick Ti6Al4V sheet, which was purchased by Titanium Consulting & Trading™.

Table 3-1. Ti6Al4V chemical composition [wt%].

Chemical composition [wt%]				
Al	Fe (max)	O (max)	Ti	V
6	0.2	0.2	Balance	4

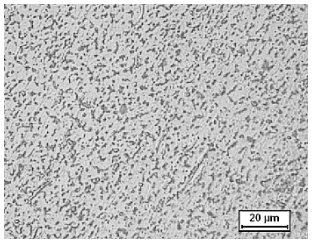

Figure 3-1. Microstructure of the as-received Ti6Al4V sheet.

The material chemical composition provided by the supplier is reported in Table 3-1, while the microstructure in the as-received condition can be observed in the optical micrograph of Figure 3-1. Comparing this micrograph with the ones available in literature [183], the as-received material reveals an equiaxed $\alpha + \beta$ microstructure (the α phase is the white background, while the black spots are the β phase). The α and β phases coexist until the β-transus temperature, which is equal to 995 ± 15°C, according to [28], [12].

3.1.2 Thermal tests

The thermal tests allow evaluating the influence of the thermal cycle parameters, namely heating system, temperature, soaking time and cooling rate, on the Ti6Al4V micro-hardness and microstructural characteristics. The thermal tests were carried out using two heating technologies, namely furnace and induction.

- The *"furnace tests"* were performed introducing the samples in the chamber of Nabertherm N 7/H furnace, which was previously heated at the testing temperature. After the specific soaking time at the fixed constant temperature, which was controlled through a k-type thermocouple spot-welded on the sample central zone, the samples were removed to cool them down in calm air or water.
- The *"induction tests"* were performed on the universal MTS^{TM} testing machine, which was equipped with an induction heating system, as depicted in Figure 3-2a and Figure 3-2b. As in the furnace tests, the temperature was controlled by a k-type thermocouple spot-welded in the sample central area (Figure 3-2c) during all the thermal phases, namely heating, soaking and cooling. In the induction tests, in addition to the cooling conditions of calm air and water, two intermediate cooling rates were investigated, controlling the temperature descent either through the inductor or by using an air nozzle.

The experimental plan for the thermal tests is reported in Table 3-2. After the thermal tests, the samples micro-hardness and microstructure were investigated following the experimental procedures that will be described in § 3.1.4.

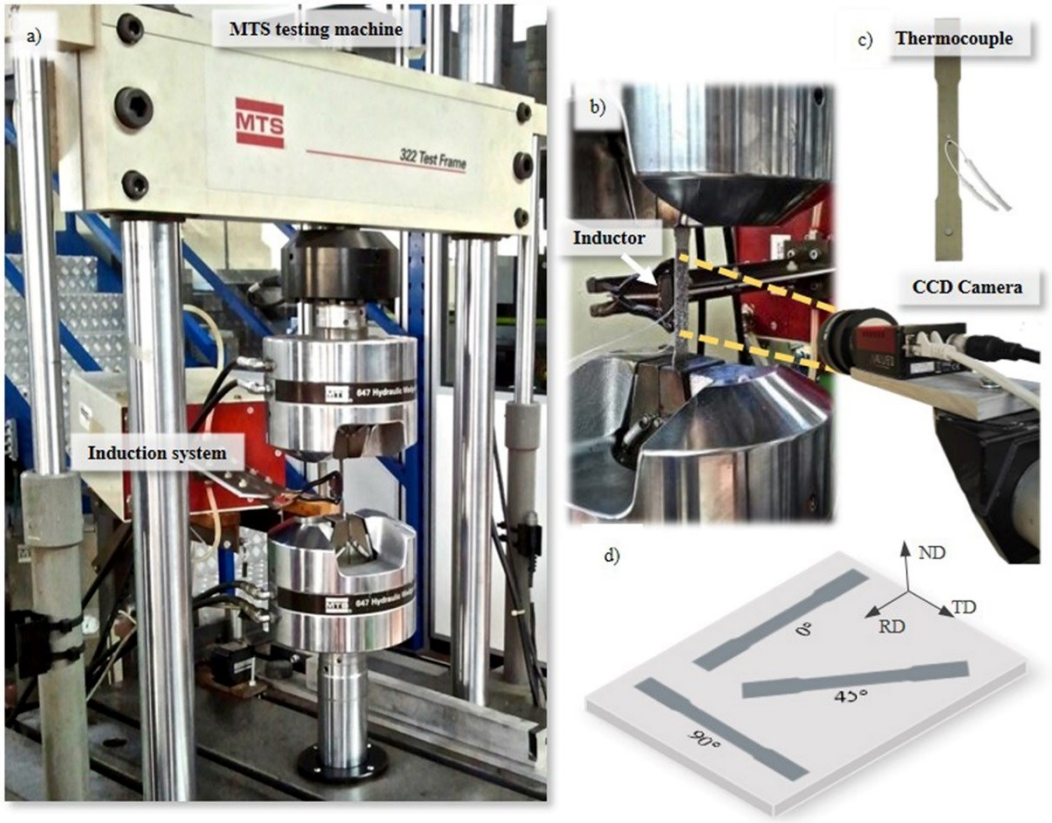

Figure 3-2. a) 5t MTS™ testing machine. b) Detail of the induction heating system and CCD camera. c) Detail of the K-type thermocouple spot-welded on the sample centre area. d) Orientations of the tensile samples with respect to the reference system.

Table 3-2. Experimental plan for the thermal tests.

Heating technology	**Temperature**		**Soaking time**				**Cooling rate**			
	[°C]		**[s]**				**[°C/s]**			
Furnace	600	800	30	90	180	300	Air	Water		
Induction	600	800	30	90	180	300	Air	Water	10	1

3.1.3 Tensile tests

To characterize the material behaviour and properties at elevated temperatures and different strain rates, tensile tests were performed on the universal 5t MTS™ testing machine (Figure 3-2a), equipped with the same induction heating system used for the thermal tests. Because of the intrinsic material anisotropy, which stems from the rolling process, but also from the asymmetry of the material crystallographic elementary cell [48], the tests were carried out on samples cut along different orientations (θ) with respect to the rolling direction, namely at 0°,

45° and 90° as represented in Figure 3-2d. The geometry of the samples is reported in Figure 3-3a.

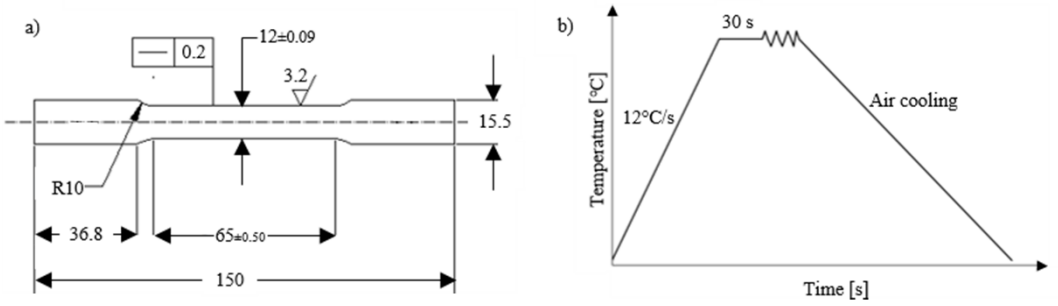

Figure 3-3. a) Geometry of the tensile specimen (dimension in [mm]). b) Experimental procedure for the tensile tests at elevated temperatures.

The tests were performed in a wide range of temperatures, spanning from room temperature to 900°C, while the nominal strain rates were set at 0.1 s^{-1} and 1 s^{-1}, as summarized in the experimental plan of Table 3-3.

During the tensile tests, the sample was heated up to the target temperature, which was monitored by a k-type thermocouple, applying a constant heating rate of 12°C/s. After a soaking time of 30 s, which allowed the homogenization of temperature and microstructure, the samples were strained until fracture, maintaining the temperature of the gauge length constant. To note that the specimen gauge length is equal to 65 mm for the room-temperature tests, whereas, for the tests at higher temperatures, it is fixed at 15 mm, the latter identified on the basis of the recordings of an infrared thermo-camera. After the end of the test, the fractured samples were left cooling in calm air. The experimental procedure is schematically illustrated in Figure 3-3b.

Table 3-3. Experimental plan for the tensile tests.

Temperature [°C]							**Strain [-]**	**Strain rate [s^{-1}]**	**Orientation [-]**
25	200	400	600	700	800	900	ε_F	0.1	0°,45°,90°
25	200	400	600	700	800	900	ε_F	1	0°,45°,90°

The sample deformation of all the tests was recorded through a CCD camera (Figure 3-2b), while its acquisitions were used in the Aramis™ system from GOM to calculate the evolution of the true strain, namely the major (ε_1) and minor (ε_2)

strains. Based on the volume conservation, represented by Eq. (3-1), the true strain on thickness (ε_3) can be calculated and the Lankford coefficients, which are the ratio between the width strain (ε_2) and the thickness one (ε_3) as described in Eq. (3-2), can be obtained for each testing condition ($T, \dot{\varepsilon}$) and orientation (θ) of the sample. The values of the Lankford coefficients for each testing condition were picked out at a fixed value of strain equal to 0.1.

$$\varepsilon_1 + \varepsilon_2 + \varepsilon_3 = 0 \tag{3-1}$$

$$r_\theta\ (T, \dot{\varepsilon}) = \frac{\varepsilon_2}{\varepsilon_3} \tag{3-2}$$

Gathering all the r_θ values for each orientation, the average normal anisotropy, $\bar{R}$, which determines the thinning behaviour of sheet metals during stretching [48], can be expressed as a function of temperature and strain rate through Eq. (3-3),

$$\bar{R}\ (T, \dot{\varepsilon}) = \frac{r_0(T, \dot{\varepsilon}) + 2r_{45}(T, \dot{\varepsilon}) + r_{90}(T, \dot{\varepsilon})}{4}, \tag{3-3}$$

where r_0, r_{45} and r_{90} are the Lankford coefficients related to the three orientations represented in Figure 3-2d.

3.1.4 Post thermal and mechanical tests analyses

After the tensile tests, the true strains at fracture, which can be considered as an index of the material ductility, were calculated as a function of temperature and strain rate through Eq. (3-4),

$$\varepsilon_F(T, \dot{\varepsilon}) = \ln\frac{A_0}{A_F}, \tag{3-4}$$

where A_0 is the sample initial cross-section area and A_F the fractured one. Following the procedure reported in [184], the sample fracture area was measured through Scanning Electron Microscopy, SEM (Fei Quanta 450™, Figure 3-4a), placing the fracture surface perpendicular to the electron beam. The analysis of the fracture surface using SEM allows evaluating also any possible change in the fracture mode as a function of the testing parameters.

To verify any possible influence of the testing parameters on the material mechanical properties after the thermal and tensile tests, the micro-hardness of all the samples was measured by using a micro-durometer Leitz (Figure 3-4b). The indenter's imprints were placed along a line in the centre of the TD-ND section of the 0° samples (Figure 3-2d), whose surfaces were previously prepared through

mechanical polishing. The distance between each imprint was fixed equal to 130 μm, the mass used during the test was 200 gr while the indentation lasted 30 s.

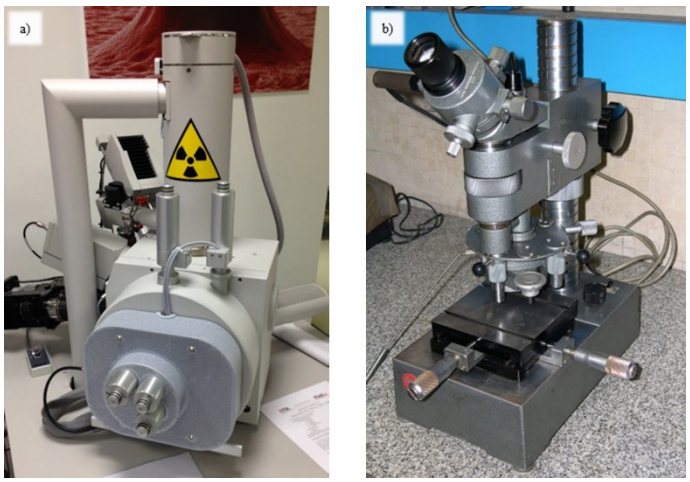

Figure 3-4. a) FEI Quanta 450™ Scanning Electron Microscope (SEM). b) Micro-durometer Leitz.

The material microstructural characteristics, after the thermal and mechanical tests, were investigated on the 0° samples surfaces perpendicular to the RD direction (Figure 3-2d) by means of Optical Microscopy, OM (Leica MEF4U™), and SEM. With this aim, the surfaces were previously prepared through mechanical polishing and chemical etching with the Kroll reagent.

The crystallographic texture of the deformed samples was investigated through the Electron Back Scattered Diffraction (EBSD) analysis, which was performed using the probe installed inside the FEI Quanta 450™ SEM. The investigation was carried out on the longitudinal section of the 0° samples, which refers to the RD-TD plane in Figure 3-2d. In this case, after a mechanical polishing up to a surface finish of 0.05 μm, using first papers and then cloths lubricated with a solution of silica and hydrogen peroxide, the samples were finished with a vibratory polishing using an acid solution containing 0.02 μm colloidal silica. Afterwards, the results were elaborated using the licensed software OIM Analysis by EDAX.

3.2 Results

3.2.1 Thermal tests

3.2.1.1 Micro-hardness analysis

The micro-hardness analysis performed on the samples after the thermal tests allows investigating the micro-hardness sensitivity to the thermal testing parameters, as it can be observed in Figure 3-5. Figure 3-5a represents the micro-

hardness sensitivity to the soaking time, with values relevant to samples heated in furnace at 600°C and cooled down in calm air. As it can be seen, the micro-hardness increases as the soaking time passes from 90 to 180 s, while it remains nearly constant passing to 300 s. A slight increase of the micro-hardness can be noticed also for the samples heated by induction technology passing from 30 to 90 s of soaking time. Figure 3-5b shows that the heating temperature does not modify the micro-hardness, as well as the influence of the cooling rate (Figure 3-5c) and heating technology is not significant, since the maximum percentage differences are always below 6.4%. Therefore, it can be stated that, besides the soaking time, the influence of the thermal process parameters on the sample properties is negligible.

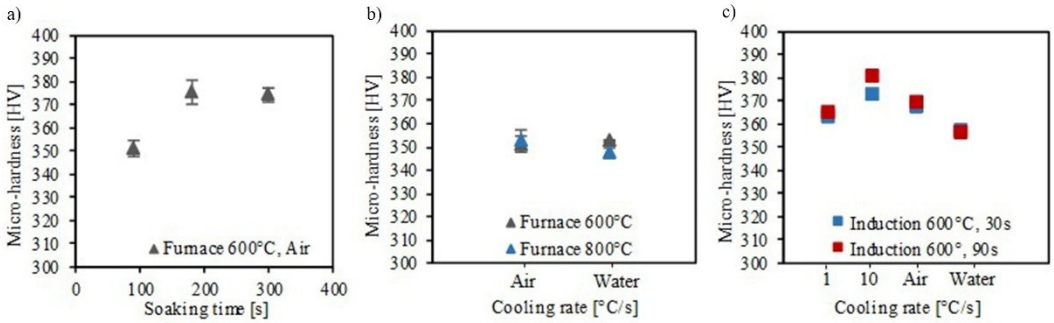

Figure 3-5. Micro-hardness sensitivity to a) soaking time, b) heating temperature and c) cooling rate.

3.2.1.2 Microstructural analysis

The micrographs of the thermally treated samples are reported in Figure 3-6.

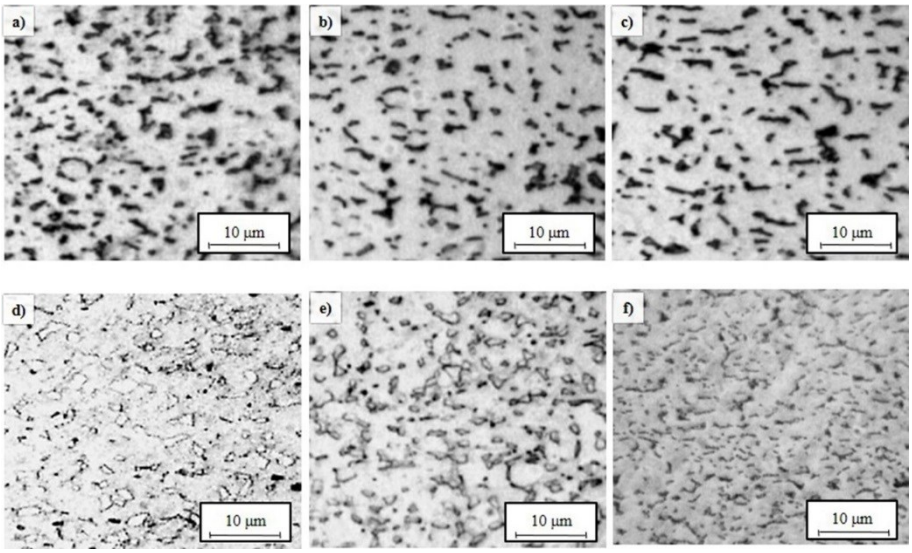

Figure 3-6. Optical micrographs. a, b, c) Furnace, 600°C, soaking time respectively 90, 180, 300s, air cooling. d) Furnace, 800°C, 90s, water cooling. e) Furnace, 800°C, 90s, air cooling. f) Induction, 600°C, 90s, air cooling.

Figure 3-6 shows that the microstructure remains equiaxed $\alpha + \beta$ [183] without any differences as a function of the soaking time (Figure 3-6 a, b, c), cooling rate (Figure 3-6 a, d), heating temperature (Figure 3-6 a, e) and heating technology (Figure 3-6 a, f).

3.2.2 Tensile tests

3.2.2.1 Flow stress

The Ti6Al4V flow stress curves, resulted from the tensile tests performed on 0° samples at different temperatures (25°C-900°C) and strain rates (0.1 s^{-1} and 1 s^{-1}), are shown in Figure 3-7a and Figure 3-7b.

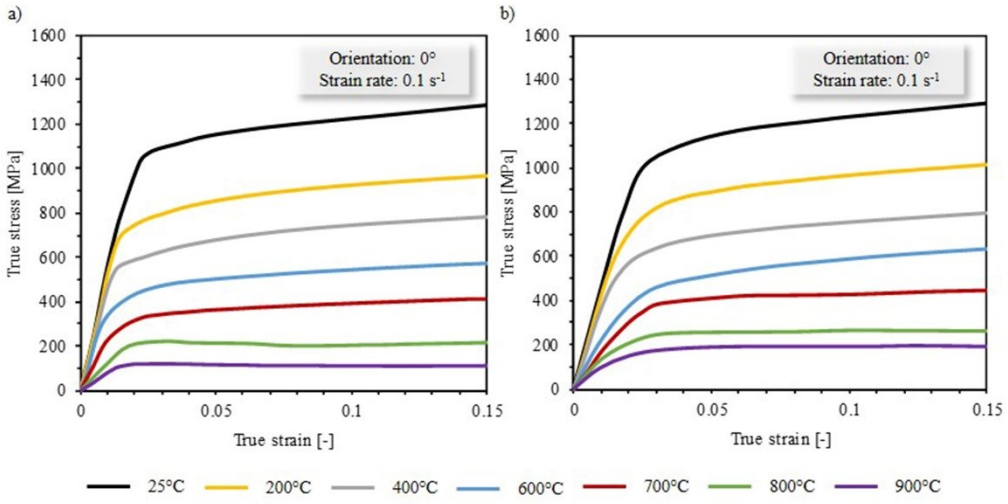

Figure 3-7. Ti6Al4V true stress-true strain curves for 0° samples at different temperatures (25°C-900°C) and strain rates set at a) 0.1 s^{-1} and b) 1 s^{-1}.

As expected, the flow stress decreases with increasing temperature and decreasing strain rate. It is worth to note that, for both the strain rates, the same dependency on temperature can be identified also for the strain hardening, as witnessed by the progressive flattening of the curves, which was found also in [185]. This is more evident as the temperature reaches 800°C and the reason can be attributed to one of the two possible microstructural phenomena, dynamic recrystallization (DRX) and dynamic recovery (DRV), which can occur when the Ti6Al4V sheets are deformed in $\alpha + \beta$ phase at elevated temperature [36], [186].

The data obtained from tensile tests carried out on samples cut along different orientations with respect to the rolling direction allow evaluating the effect of the cutting direction on the flow stress behaviour. By analysing the flow stress sensitivity to the rolling direction at three different temperatures, the 0° samples have higher values of flow stress compared to the other samples. Furthermore, at

fixed strain values of 0.1, 0.15 and 0.20, the percentage variation between the maximum and the minimum values of the flow stress at each temperature raises as the temperature increases, suggesting a different influence of the rolling direction on the flow stress as a function of the testing temperature.

3.2.2.2 Material ductility

The measurement of the samples fracture areas through SEM, as reported in the insert of Figure 3-8a, allows calculating the strain at fracture applying Eq. (3-4), thus obtaining an index of the material ductility under different testing conditions.

Figure 3-8a represents the strain at fracture sensitivity to temperature for the 0°, 45° and 90° samples deformed at 0.1 s^{-1}. For each rolling direction, the same tendency in the formability increase can be noticed: the strain at fracture starts to rapidly increase when the temperature reaches 600°C, while, below this temperature, the ductility sensitivity to temperature is less pronounced.

The strain rate effect on the strain at fracture can be evaluated in Figure 3-8b for the 0° samples. As it can be observed, the material ductility starts to be significantly affected by the strain rate as the temperature reaches 800°C. In this high temperature range (800°C and 900°C), regardless the sample orientation, the higher the strain rate the lower the strain at fracture.

Both the effects of temperature and strain rate on the material ductility can be attributed to the transformation of the α phase (HCP) to the more ductile and strain rate sensitive β phase (BCC), as represented in Figure 2-3.

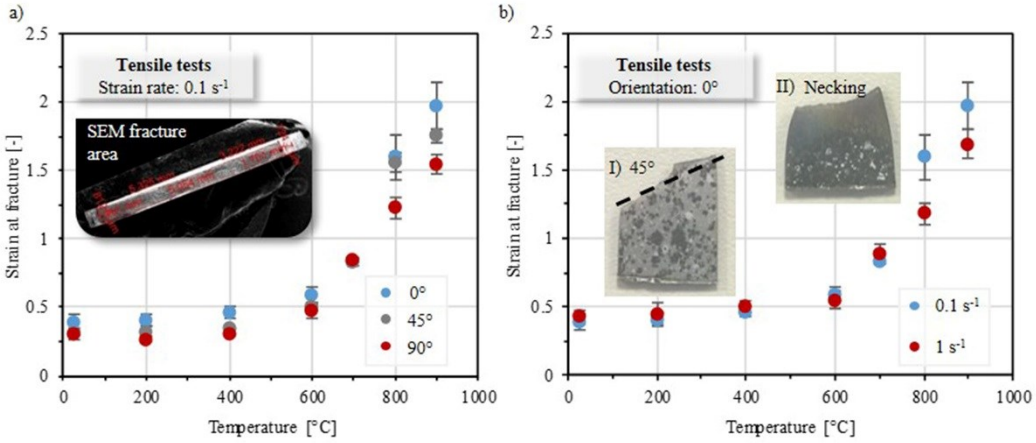

Figure 3-8. a) Strain at fracture sensitivity to temperature and rolling direction ($\dot{\varepsilon} = 0.1$ s^{-1}); detail of the sample fracture area measured through SEM observation. b) Strain at fracture sensitivity to temperature and strain rate for 0° samples; detail of two broken samples: I) 45° fracture surface and II) necking.

Regarding the sensitivity to the rolling direction, the strains at fracture calculated for the 90° samples are always lower than the 0° and 45° samples for each value of temperature (Figure 3-8a) and strain rate considered in this study.

The observation of the broken samples and the analysis of the fracture surfaces allow investigating the fracture phenomenon and its sensitivity to the process parameters. Starting with the macro-observation of the broken samples, it can be noted that their morphology is affected by the testing temperature regardless the strain rate, as it can be observed in the inserts of Figure 3-8b. Indeed, while the samples deformed below 600°C (Figure 3-8b-I) show a fracture surface at 45° with respect to the loading direction and a slight necking, for temperatures higher than 600°C, the fracture surface at 45° disappears and the necking is progressively more evident with the temperature increase (Figure 3-8b-II).

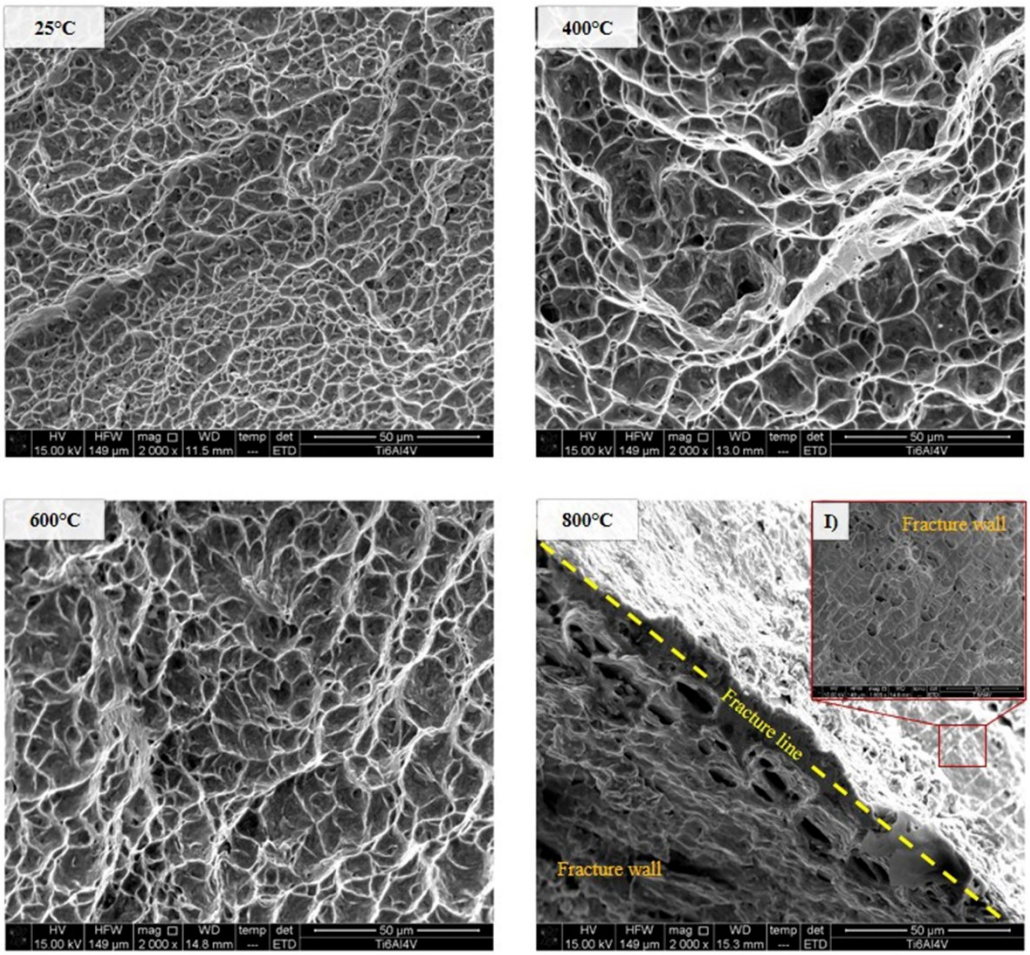

Figure 3-9. Fracture surfaces at different testing temperatures ($\dot{\varepsilon} = 1\ s^{-1}$). I) Detail of the fracture wall at 800°C ($\dot{\varepsilon} = 1\ s^{-1}$).

Passing to the micro-level of the fracture surfaces investigation, the SEM images reported in Figure 3-9 reveal that, in the range between room temperature

and 600°C, the characteristics dimples of the fracture surfaces are almost the same, being the fracture surface characterized by essentially 100% dimpled ductile rupture [187]. The same result can be identified also for the highest temperature based on the characteristic but more elongated dimples observed in the fracture wall (insert in Figure 3-9, 800°C). This is because the fracture surface in this case became a fracture line due to the significant necking that occurred during the test.

3.2.2.3 Micro-hardness analysis

The micro-hardness average values of the 0° samples reported in Figure 3-10a show that the thermo-mechanical processing can affect this property as a function of the testing temperature: in fact, the micro-hardness values slightly decrease passing from the 25°C-400°C to temperatures over 600°C. However, the analysis of Figure 3-10b, which represents the percentage differences between the hardness of the tested samples and the one of the as-received Ti6Al4V sheets, shows that these differences are always below 7.5%, suggesting that the thermo-mechanical processing does not significantly affect the samples post-deformation mechanical characteristics. To note that the high values of Ti6Al4V micro-hardness before and after the deformation process is an advantage in blocking the dislocation movements and retarding the following crack propagation [4].

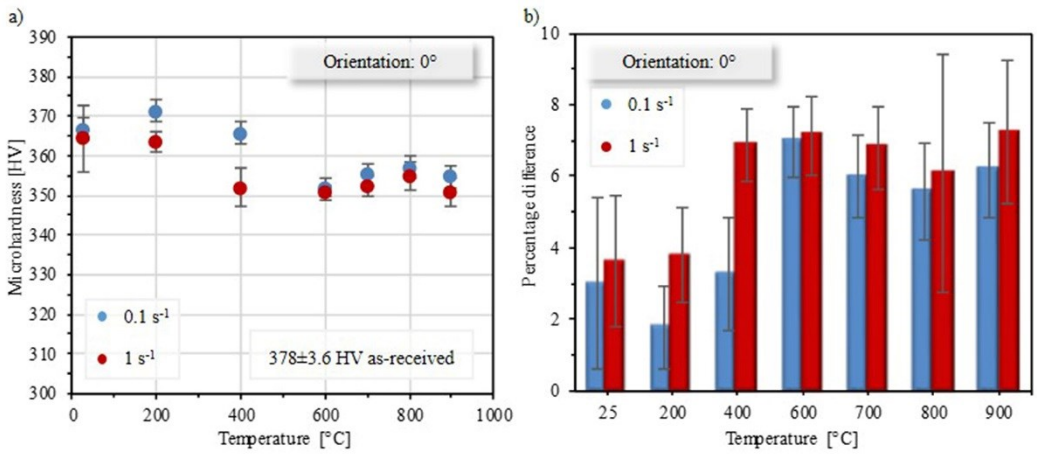

Figure 3-10. a) Micro-hardness sensitivity to temperature and strain rate. b) Percentage difference between the micro-hardness of the tested samples and the one of the as-received Ti6Al4V sheet.

Regarding the strain rate effect on the micro-hardness (Figure 3-10a), it can be considered negligible because the percentage difference between the hardness values at different strain rate for each temperature is always below 4%.

3.2.2.4 Anisotropy

The average normal anisotropy, $\bar{R}$, resulting from Eq. (2-5) as a function of temperature and strain rate, is reported in Figure 3-11a. While the $\bar{R}$ sensitivity to the strain rate can be considered negligible, as the percentage differences are always lower than 12%, the effect of temperature on $\bar{R}$ is noticeable, suggesting further evaluations. Considering that a value of normal anisotropy equal to 1 means an isotropic behaviour of the material, the resulting data reveal a progressive increase of the material isotropic characteristics from RT to 600°C, whereas, above 600°C, the material anisotropic characteristics are recovered.

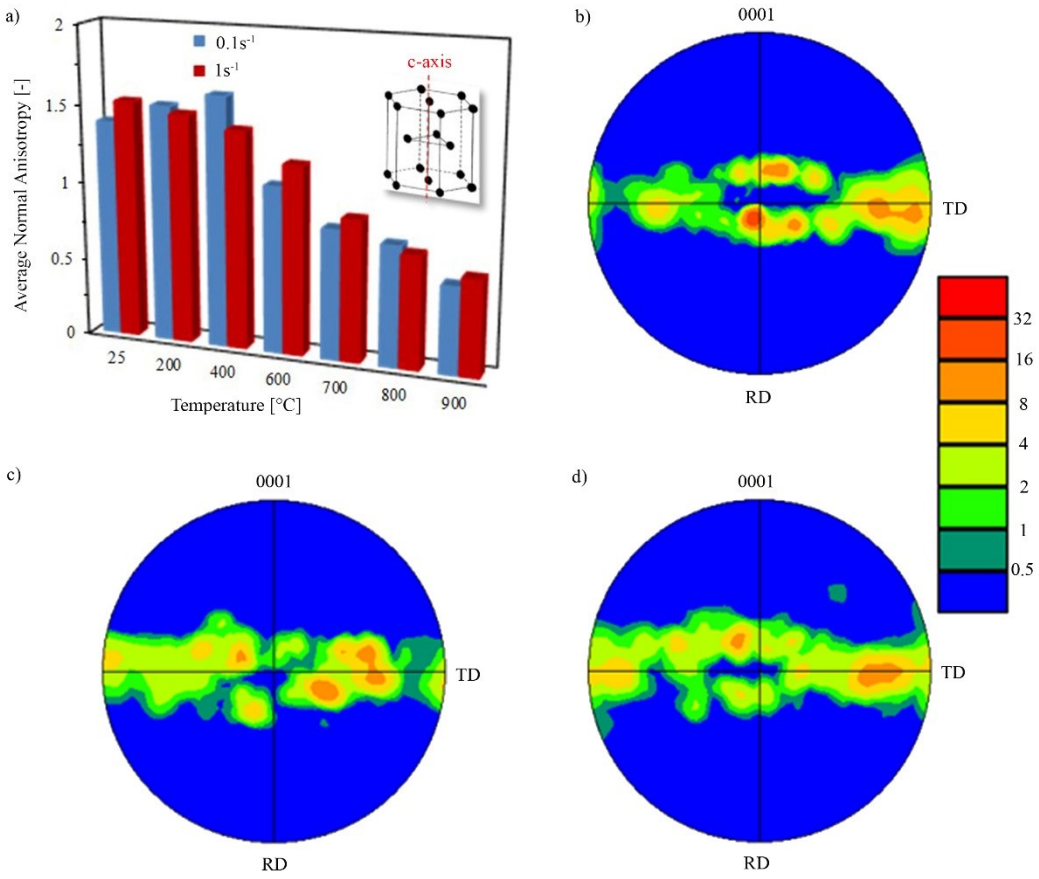

Figure 3-11. a) Ti6Al4V average normal anisotropy, $\bar{\boldsymbol{R}}$, as a function of the temperature and strain rate with the detail of the $\boldsymbol{\alpha}$ hexagonal cell. EBSD pole figures at b) 25°C, c) 600°C, d) 800°C ($\dot{\boldsymbol{\varepsilon}} = 1\ s^{-1}$).

The reason of this inversion in the material anisotropic behaviour can be found in the different texture characteristics of the material as a function of temperature, which were investigated through the EBSD analyses. Figure 3-11b, Figure 3-11c and Figure 3-11d show the texture plots (pole figures) for the RD-TD plane (Figure 3-2d) of the samples deformed at 1 s^{-1} at 25, 600 and 800°C, respectively.

At 25°C (Figure 3-11b), a $(0001)_\alpha$ accumulation along the TD direction and near the centre exists, suggesting that the c-axis of the Ti6Al4V α hexagonal cell (insert in Figure 3-11a) is perpendicular to the RD direction (T-texture), which coincides with the loading direction. Increasing the testing temperature to 600°C (Figure 3-11c), the $(0001)_\alpha$ strong accumulation near the centre disappears and a new agglomeration becomes visible along the diagonals, indicating a rotation of the α hexagonal cells and a progressive alignment of the c-axis with the loading direction. On the other hand, shifting to higher temperatures (800°C), this alignment is still visible, but there is also the restoration of the T-texture, as witnessed by the $(0001)_\alpha$ accumulation at the poles of the TD direction in Figure 3-11d.

The variation of the texture as a function of the temperature is in agreement with the results reported by Nakai et al. [14], in which the T-texture of the Ti9 titanium alloy was found to decrease with increasing temperature.

3.2.2.5 Microstructural analysis

The optical micrographs reported in Figure 3-12 for the 0° samples reveal that the deformed microstructure is the same equiaxed $\alpha + \beta$ type of the as-received material (Figure 3-1) [183], regardless the testing condition. Therefore, the thermo-mechanical process, to which the Ti6Al4V sheets were subjected, did not affect the material microstructural morphology, as no microstructural transformation were identified in the optical micrographs.

However, it is worth to note that a microstructural refinement was observed for both the strain rates passing from the low and medium temperature range to the high one, namely 800°C (Figure 3-12, 800°C). As a proof of this, the EBSD quantitative grain size distribution, reported in Figure 3-13a, shows a greater amount of grains with an ASTM number higher than 17, which is characteristic of smaller grains, for the sample deformed at 800°C compared to the others strained at 25°C and 600°C. In the insert of Figure 3-13a, reported as an example, the EBSD map of the sample deformed at 800°C and 1 s^{-1} highlights in red the α grains with an ASTM number greater than 18.

For the same sample, the presence of small grains (2-5 μm) is proved also by the EBSD phase and grain boundaries map reported in Figure 3-13b. It shows the presence of small grains (Grain 1), which are characterized by a lower

misorientation value compared to the one resulted for the coarse grain (Grain 2), as it can be seen in the chart reported in Figure 3-13b-II.

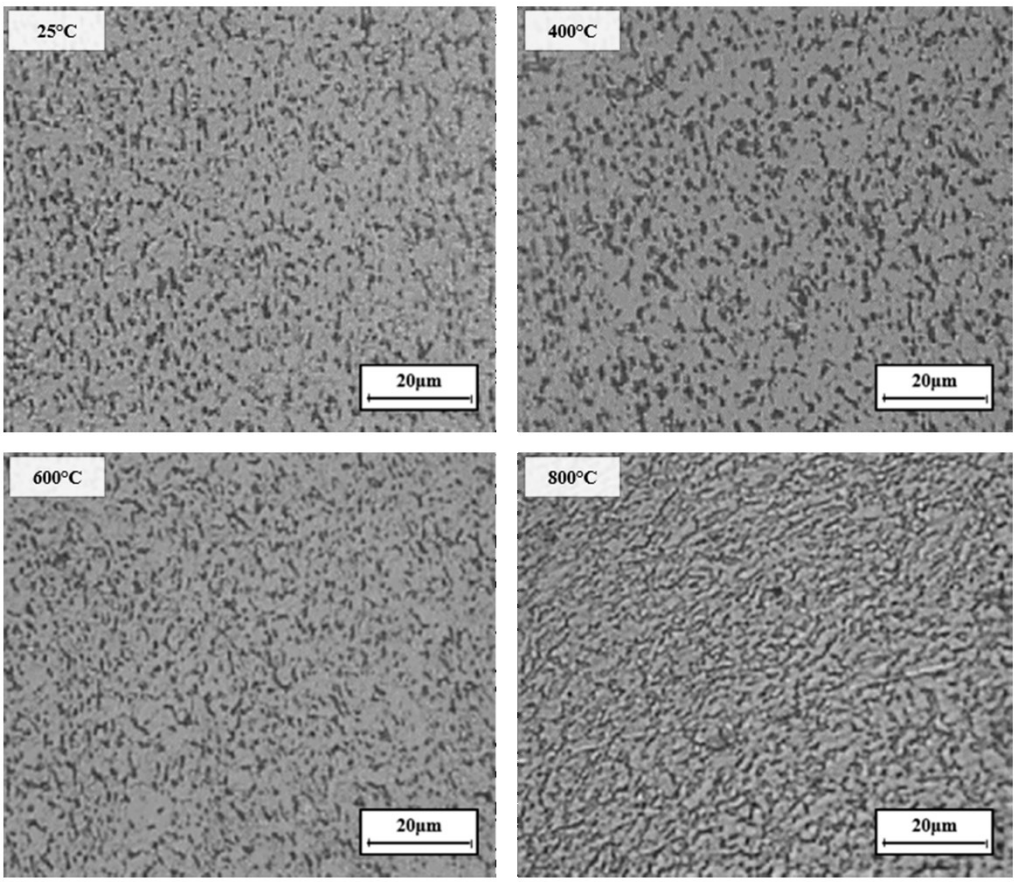

Figure 3-12. Microstructures of the Ti6Al4V samples deformed at different temperatures ($\dot{\varepsilon} = 0.1$ s^{-1}).

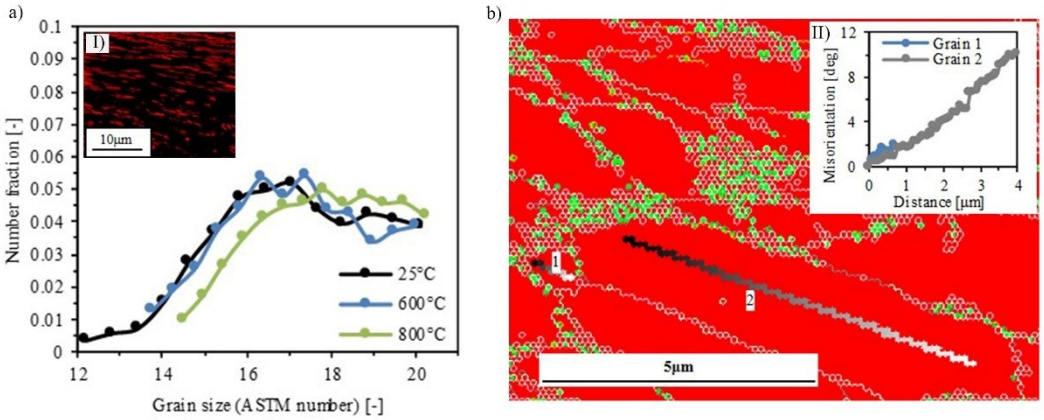

Figure 3-13. a) Ti6Al4V grain size distribution as a function of the testing temperature ($\dot{\varepsilon}$= 1 s^{-1}) and I) the EBSD phase map of α grains (in red) with an ASTM number greater than 18 (800°C and 1 s^{-1}). b) EBSD phase (α in red, β in green) and boundaries map (800°C and 1 s^{-1}) and II) misorientation lines for 1: small and 2: coarse grains.

This microstructural refinement is an evidence of the dynamic recrystallization and recovery, which were hypothesized to take place on the basis of the flattening of the flow stress curves (§ 3.2.2.1) and that can occur when the Ti6Al4V sheets are deformed in $\alpha + \beta$ phase at elevated temperature [36], [186].

3.2.2.6 Highlights

Based on the previous discussion of the results obtained from the tensile tests, the following points can be highlighted.

- The flow stress decreased with increasing temperature and decreasing strain rate. Moreover, the strain hardening was found to decrease with the temperature increase, as witnessed by the progressive flattening of the curves, which was observed to become more pronounced as the temperature reached 800°C.
- The Ti6Al4V ductility, evaluated in terms of strain at fracture, was found to increase starting from 600°C, while the effect of the strain rate became more significant in the higher temperature range. Both the effects were attributed to the increase of the more ductile and strain rate sensitive β phase fraction as a function of temperature.
- All the samples showed a ductile fracture characterized by a growing necking, more pronounced with the temperature increase.
- The micro-hardness of the strained samples was slightly affected by the previous thermo-mechanical processing, even if the differences with the as-received condition were considered negligible.
- As regards the anisotropic characteristics, Ti6Al4V appeared to be isotropic at 600°C, whereas, at lower and higher temperatures, the material showed its characteristic anisotropic behaviour. This change in the material behaviour was explained with the variation of the texture identified through the EBSD analyses: at 600°C the c-axis of the hexagonal cells was found to be aligned with the loading direction, while at lower and higher temperatures the T-texture was more pronounced.
- The optical micrographs resulted for the strained samples revealed that neither the temperature nor the strain rate affects the as-received equiaxed $\alpha + \beta$ microstructure. However, the microstructure refinement above 800°C and the presence of small grains free of misorientation, highlighted

also by the EBSD results, were considered an evidence of the occurrence of dynamic recrystallization and recovery.

3.3 Summary

Chapter 3 offers an overview of the Ti6Al4V behaviour in a wide range of temperatures and different strain rate, highlighting the relations between the microstructural and mechanical properties. The main conclusions of Chapter 3 can be listed in the following.

- The heating technology, the heating temperature and cooling rate neither affect the micro-hardness nor the alloy microstructure, which remains an equiaxed $\alpha + \beta$ one.
- The material ductility was found to rapidly increase from 600°C and the strain rate effect to become more pronounced in the high temperature range. These effects were attributed to the transformation of the α phase (HCP) to the more ductile and strain rate sensitive β phase (BCC).
- 600°C was observed to be the temperature that marks the inversion in the material anisotropic behaviour. This phenomenon was ascribed to the variation of the crystallographic textures as a function of the deformation temperature.
- The equiaxed $\alpha + \beta$ microstructure was not affected by the thermo-mechanical process, as any microstructural transformation was observed.

4 Chapter
Material modelling

This chapter describes the research work related to the modelling of the material behaviour, whose importance has increased with the interest on the use of FE models.

In the chapter, the material rheology is described using Johnson-Cook and Arrhenius-type models, because of their simplicity in calibration, while great efforts are dedicated to the identification of a new model able to describe the ductility of Ti6Al4V sheets deformed in a wide range of temperatures and stress states. The project aims at including in the new model not only the effects of the process parameters, such as temperature and strain rate, but also the influence of the stress state in terms of both stress triaxiality and Lode parameter, whose coupled effect represents the main novelty in the description of the ductile fracture behaviour, according to the most recent literature.

4.1 Material rheology

The Ti6Al4V flow stress behaviour under tensile conditions and moderate strain rates was modelled applying two empirically-based constitutive models, namely the Johnson-Cook and Arrhenius-type models, since the review of literature has shown that Ti6Al4V under tensile conditions has been mostly investigated at very low strain rates typical of the superplastic regime (§ 2.2.1). The Johnson-Cook model is simple, characterized by a limited number of material constants and widely applied to take into account the effect of temperature and strain rate [40]. On the other hand, the Arrhenius-type model requires a more complex procedure for the identification of its constants, but it allows a more effective coupling of the effect of strain rate and temperature on the flow stress through the Zener-Hollomon parameter [60].

Both the models were elaborated to predict the plastic flow stress, thus neglecting the elastic behaviour, for the 0° samples deformed at strain rates of 0.1

s^{-1} and 1 s^{-1} in the temperature range from 600 to 900°C. This temperature range was chosen since it assures a significant enhancement of the material ductility, as shown in Figure 3-8b.

4.1.1 Johnson-Cook model

The Johnson-Cook (J-C) flow stress model is expressed as:

$$\sigma = (A + B\varepsilon^n)(1 + C \ln \dot{\varepsilon}^*)(1 - T^{*m}) , \tag{4-1}$$

where σ is the equivalent stress, ε the equivalent plastic strain, A the material yield strength in the reference testing conditions, B and n represent the strain hardening, C the strain rate strengthening and m the thermal softening [60]. Therefore, in Eq. (4-1), the expressions into brackets give the stress sensitivity to strain, strain rate and temperature, respectively.

$\dot{\varepsilon}^*$ is the dimensionless strain rate and can be written as

$$\dot{\varepsilon}^* = \frac{\dot{\varepsilon}}{\dot{\varepsilon}_{ref}} , \tag{4-2}$$

where $\dot{\varepsilon}$ is the strain rate while $\dot{\varepsilon}_{ref}$ is the reference strain rate. T^*, in Eq. (4-1), represents the homologous temperature and can be defined as

$$T^* = \frac{T - T_{ref}}{T_m - T_{ref}} , \tag{4-3}$$

in which T is the testing temperature, T_{ref} the reference testing temperature, and T_m the material melting temperature, which is fixed at 1650°C. The reference testing conditions were set at a temperature of 600°C and a strain rate of 1 s^{-1}, while the material yield strength, under such conditions, was $A = 460$ MPa. The choice of 600°C as reference temperature was based on the rapid increase of the β phase fraction (Figure 2-3) and material ductility (Figure 3-8b) above this temperature.

The procedure used to identify the material constants of Eq. (4-1), in agreement with [60], will be described in the following.

In the reference conditions, where $\dot{\varepsilon}^*$ becomes unity and T^* becomes zero, Eq. (4-1) results to be:

$$\sigma = (A + B\varepsilon^n) . \tag{4-4}$$

Applying the natural logarithm on both sides of Eq. (4-4), it is arranged into

$$\ln(\sigma - A) = \ln B + n \ln \varepsilon . \tag{4-5}$$

A linear regression analysis of $\ln(\sigma - A)$ versus $\ln \varepsilon$ is carried out to determine B and n, which are the intercept and the slope of the linear fitting line in Figure

4-1a, respectively. They are calculated out to be 1400.38 MPa and 1.231, respectively.

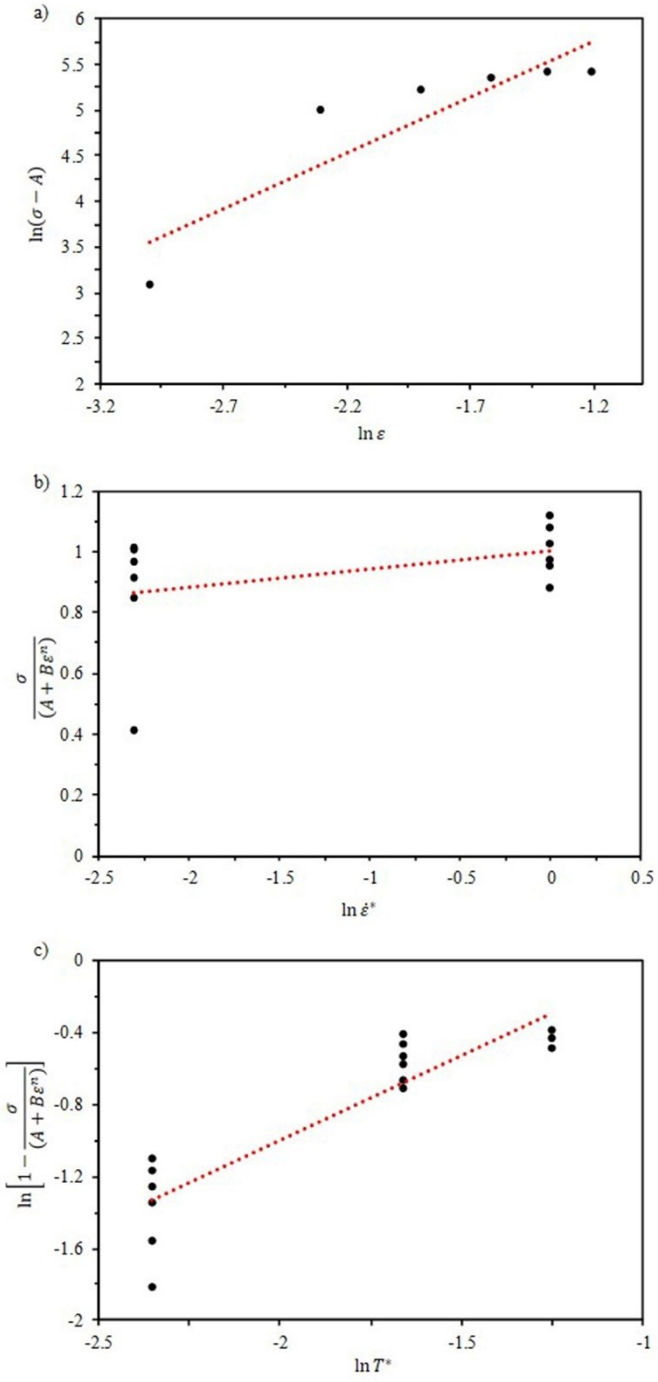

Figure 4-1. Data fitting for the identification of the J-C model material constants.

At the reference temperature of 600°C, the J-C model (Eq. (4-1)) can be written as

$$\frac{\sigma}{(A + B\varepsilon^n)} = 1 + C \ln \dot{\varepsilon}^* . \tag{4-6}$$

The constant C can be calculated as the slope of the linear fitting of $\frac{\sigma}{(A+B\varepsilon^n)}$ versus $\ln \dot{\varepsilon}^*$ (Figure 4-1b) and it comes out to be 0.0625.

Finally, the calculation of the constant m is fulfilled considering the reference strain rate and re-arranging Eq. (4-1) as follows:

$$\ln\left[1-\frac{\sigma}{(A+B\varepsilon^n)}\right] = m \ln T^* . \tag{4-7}$$

The slope of $\ln\left[1-\frac{\sigma}{(A+B\varepsilon^n)}\right]$ versus $\ln T^*$ (Figure 4-1c) corresponds to the average constant m that resulted to be 0.9483. Figure 4-1c shows also that the thermal softening increase occurs as the temperature raises, but it is much more pronounced passing from 700°C to 800°C than from 800°C to 900°C, which suggests a more pronounced thermal softening effect starting from 800°C in accordance with the progressive flattening of the flow stress curves, highlighted in the analysis of the material flow stress behaviour (§ 3.2.2.1).

All the calculated constants for the J-C model are summarized in Table 4-1, while the resulting J-C model for Ti6Al4V sheet is expressed in Eq. (4-8).

Table 4-1. Material constants of the J-C model in the temperature range of 600°C-900°C.

A	***B***	***n***	***C***	***m***
[MPa]	**[MPa]**	**[-]**	**[-]**	**[-]**
460	1400.38	1.231	0.062	0.948

$$\sigma = (460 + 1400{,}38 * \varepsilon^{1{,}231}) \cdot (1 + 0{,}062 * ln\,\dot{\varepsilon}) \cdot \left[1-\left(\frac{T-600}{1650-600}\right)^{0{,}948}\right]. \tag{4-8}$$

4.1.2 Arrhenius-type model

The Arrhenius-type constitutive model is expressed as

$$\sigma = \frac{1}{\alpha}\ln\left\{\left(\frac{Z}{A}\right)^{\frac{1}{n}} + \left[\left(\frac{Z}{A}\right)^{\frac{2}{n}} + 1\right]^{\frac{1}{2}}\right\}. \tag{4-9}$$

Z is the Zener-Hollomon parameter, which is defined as

$$Z = \dot{\varepsilon}\exp\left[\frac{Q}{(RT)}\right], \tag{4-10}$$

where Q is the activation energy for the hot deformation, R the universal gas constant, T the absolute temperature, $\dot{\varepsilon}$ the strain rate. The model can be also expressed as:

$$\dot{\varepsilon} = A_3\,[\sinh(\alpha\sigma)]^{n_2} \exp\left[\frac{-Q}{RT}\right], \qquad \text{for all } \sigma \qquad (4\text{-}11)$$

$$\dot{\varepsilon} = A_1\sigma^{n_1} \exp\left[\frac{-Q}{RT}\right], \qquad \alpha\sigma < 0.8 \qquad (4\text{-}12)$$

$$\dot{\varepsilon} = A_2 \exp(\beta\sigma) \exp\left[\frac{-Q}{RT}\right], \qquad \alpha\sigma > 1.2 \qquad (4\text{-}13)$$

where A_3, α, n_2, Q are the material constants. The procedure for their identification [188], reported as an example in the following, refers to a true strain of 0.18.

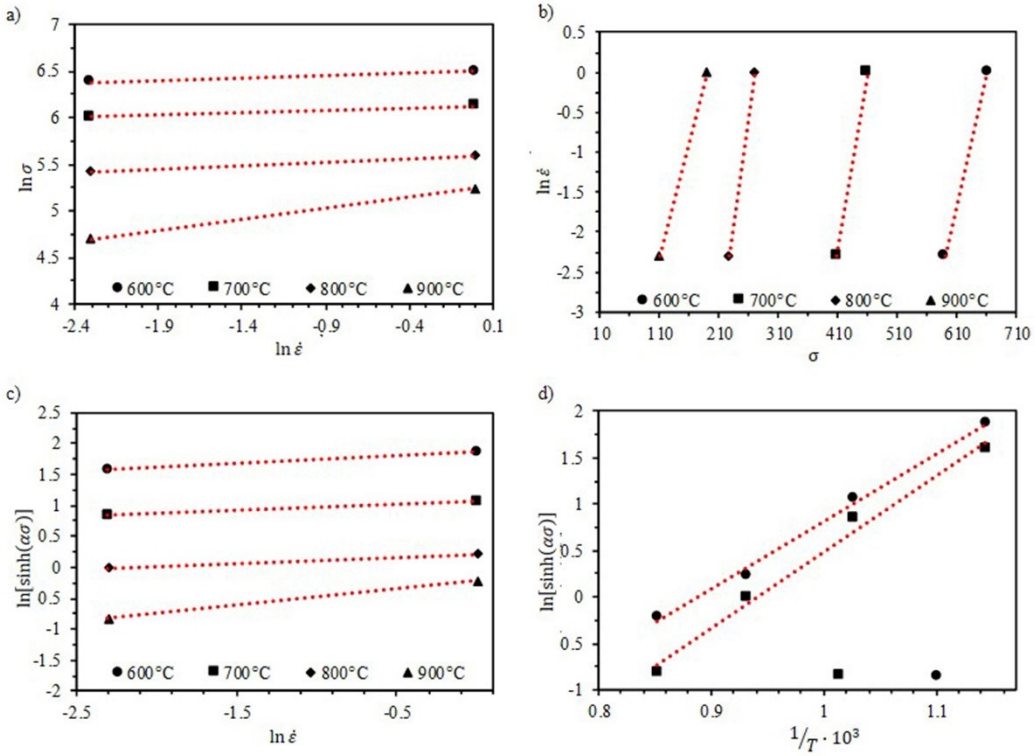

Figure 4-2. Arrhenius-type model. a) Relationship between ln $\boldsymbol{\sigma}$ and ln $\dot{\boldsymbol{\varepsilon}}$ to calculate $\boldsymbol{1/n_1}$. b) Relationship between ln $\dot{\boldsymbol{\varepsilon}}$ and $\boldsymbol{\sigma}$ to calculate $\boldsymbol{\beta}$. c) Relationship between $\boldsymbol{ln}\,[\boldsymbol{sinh}(\boldsymbol{\alpha\sigma})]$ and ln $\dot{\boldsymbol{\varepsilon}}$ to calculate $\boldsymbol{n_2}$. d) Relationship between $\boldsymbol{ln}\,[\boldsymbol{sinh}(\boldsymbol{\alpha\sigma})]$ and $\boldsymbol{1/T}$ to calculate $\boldsymbol{Q}$.

The constant α is the product between $1/n_1$ and β, which can be calculated taking the natural logarithm of both sides of Eq. (4-12) and Eq. (4-13), respectively, and re-arranging the resulting equations, as follows.

$$\frac{1}{n_1} = \frac{\partial \ln \sigma}{\partial \ln \dot{\varepsilon}}_{T} \qquad (4\text{-}14)$$

$$\beta = \frac{\partial \ln \dot{\varepsilon}}{\partial \sigma}_{T} \qquad (4\text{-}15)$$

Based on Eqs. (4-14) and (4-15), $1/n_1$ and β, which represent the slopes of the linear fitting lines in the $\ln \sigma$ versus $\ln \dot{\varepsilon}$ and $\ln \dot{\varepsilon}$ versus σ plots, respectively (Figure 4-2a and Figure 4-2b), resulted to be 0.103 MPa·s and 0.039 $MPa^{-1} \cdot s^{-1}$.Therefore, α is calculated out to be 0.004.

Afterwards, applying the natural logarithm to Eq. (4-11), the resulting equation can be written as

$$\ln [\sinh(\alpha\sigma)] = \frac{1}{n_2} \ln \dot{\varepsilon} - \frac{1}{n_2} \ln A_3 + \frac{Q}{n_2 RT}, \tag{4-16}$$

and $1/n_2$ results to be the average slope of the linear fitting line of $\ln [\sinh(\alpha\sigma)]$ versus $\ln \dot{\varepsilon}$ at constant temperature (Figure 4-2c). Therefore, n_2 resulted to be 6.964.

Considering the strain rate constant, Eq. (4-16) can be re-arranged as follows:

$$Q = \frac{n_2 R \, \partial \ln[\sinh(\alpha\sigma)]}{\partial(\frac{1}{T})}, \tag{4-17}$$

where Q represents the slope of the linear fitting lines of $\ln [\sinh(\alpha\sigma)]$ versus $1/T$ (Figure 4-2d) and resulted to be 448.124 KJ/mol.

Finally, the value of $\ln A_3$ can be obtained considering Figure 4-2c and Eq. (4-16): the interception of this equation is indeed equal to $(-\ln A_3/n_2 + Q/n_2 RT)$ and $\ln A_3$ was calculated out to be 47.618.

Because the material constants change as a function of the strain, their values were calculated for different strains, as reported in Figure 4-3, applying the same procedure previously described for a strain of 0.18. To take into account this dependency in the constitutive equation, the material constants are assumed to be polynomial functions of the strain, as reported in the following equations,

$$\alpha = C_1 \varepsilon^2 + C_2 \varepsilon + C_3, \tag{4-18}$$

$$n_2 = C_1 \varepsilon^2 + C_2 \varepsilon + C_3, \tag{4-19}$$

$$Q = C_1 \varepsilon^2 + C_2 \varepsilon + C_3, \tag{4-20}$$

$$\ln A_3 = C_1 \varepsilon^2 + C_2 \varepsilon + C_3, \tag{4-21}$$

whose coefficients are reported in Table 4-2.

Once the model constants α, n_2, Q and A_3 were identified for each value of strain at different strain rates and temperatures, the flow stress can be calculated applying Eq. (4-9).

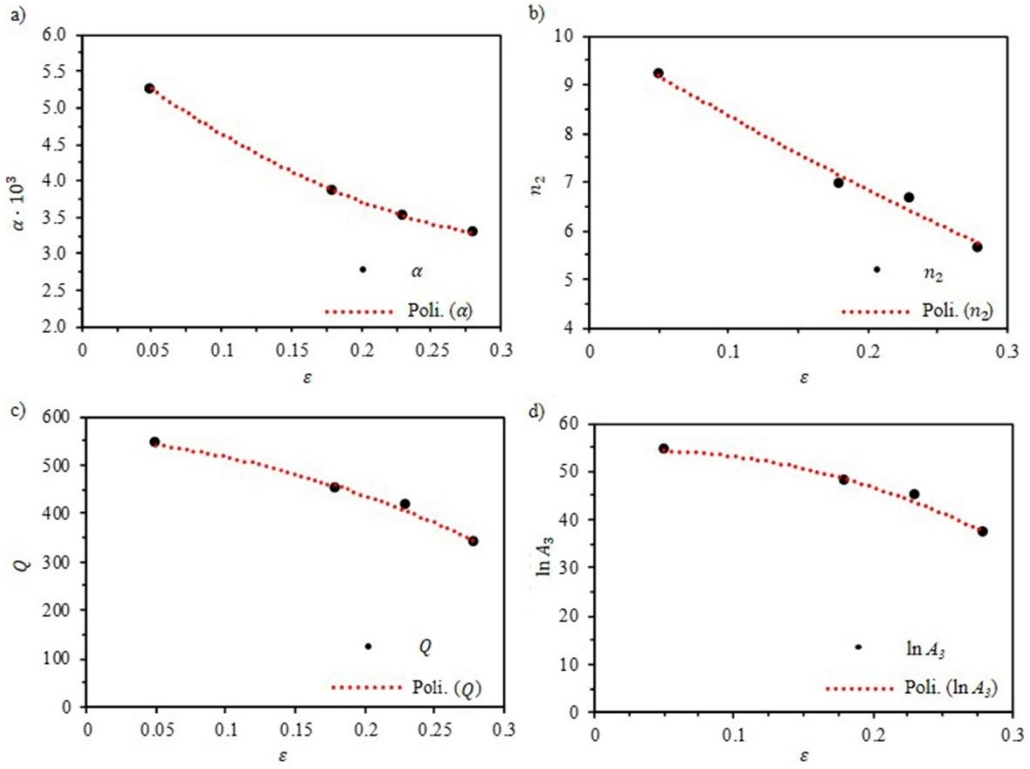

Figure 4-3. Material constants of the Arrhenius-type model as a function of the strain: a) $\boldsymbol{\alpha}$, b) $\boldsymbol{n_2}$, c) $\boldsymbol{Q}$ and d) $\boldsymbol{ln\ A_3}$.

Table 4-2. Coefficients of the polynomial functions for $\boldsymbol{\alpha}$, $\boldsymbol{n_2}$, $\boldsymbol{Q}$ and $\boldsymbol{ln\ A_3}$ of the Arrhenius-type model.

Coefficients	**α**	**n_2**	**Q**	**$\ln A_3$**
	[-]	**[-]**	**[KJ/mol]**	**[-]**
C_1	0.0207	7.967	-2061.6	-284.31
C_2	-0.015	-17.600	-182.1	20.166
C_3	0.006	10.043	554.89	53.97

4.1.3 Discussion

The comparison between the experimental data and the stress values predicted at both strain rates applying J-C (Eq. (4-1)) and Arrhenius-type (Eq. (4-9)) models with the material constants of Table 4-1 and Table 4-2, respectively, are reported in Figure 4-4. As it can be seen in Figure 4-4a and Figure 4-4b, the J-C model agrees well with the experimental data only when the testing conditions are close to the reference ones, in accordance with [40]. Figure 4-4c and Figure 4-4d shows that Arrhenius-type model guarantees a good fit up to 800°C, but increasing the

temperature to 900°C, the percentage difference rises to a maximum value of 30%, which is still acceptable compared to the higher differences characterizing the J-C model.

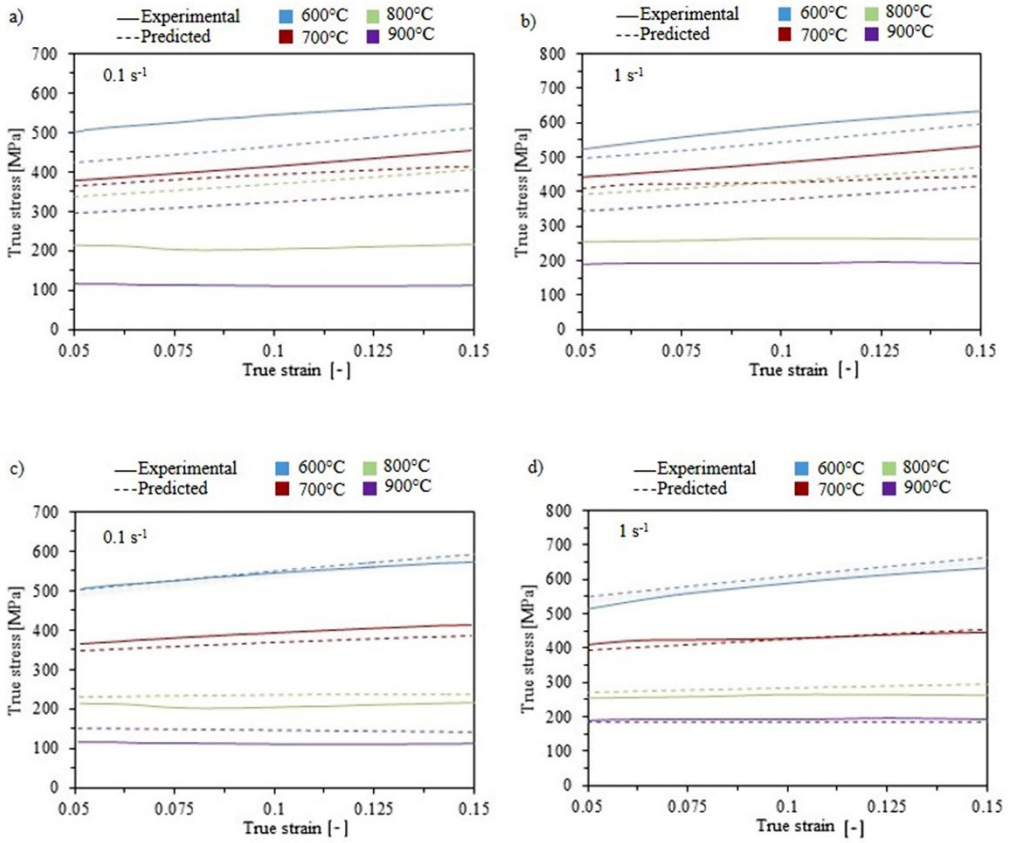

Figure 4-4. True stress-true strain curves: experimental and predicted data at different strain rates based on a), b) the J-C model and c), d) the Arrhenius-type model.

The accuracy of the two constitutive models employed in predicting the flow stress behaviour can be analysed evaluating two statistical parameters, namely the coefficient of determination (R^2) and the Average Absolute Relative Error ($AARE$), which are calculated by using the statistical software R©. R^2 (Eq. (4-22)) quantifies the accuracy of the linear relationship between the experimental and the predicted values, while AARE (Eq. (4-23)) indicates the predictability of a numerical model [60].

$$R^2 = 1 - \frac{\sum_{i=1}^{i=N}(\sigma_{exp_i} - \sigma_{p_i})^2}{\sum_{i=1}^{i=N}(\sigma_{exp_i} - \bar{\sigma}_{exp})^2} \tag{4-22}$$

$$AARE = \frac{1}{N}\sum_{i=1}^{i=N}\left|\frac{\sigma_{exp_i} - \sigma_{p_i}}{\sigma_{exp_i}}\right| \cdot 100 \tag{4-23}$$

Their values were calculated out to be respectively 0.74 and 53.55% for the J-C model, 0.98 and 8.05% for the Arrhenius-type one. The high value of R^2 obtained for the Arrhenius-type model agrees with the good linear fitting in Figure 4-5b. Moreover, the lower value of $AARE$ resulted for the Arrhenius-type model confirms its better predictability compared to the one of the J-C model.

The greater accuracy of the Arrhenius-type model compared to the J-C one at high temperature is attributed to the coupled effect of temperature and strain rate on the flow stress expressed through the Zener-Hollomon [40], [189].

Based on these considerations, the Arrhenius-type model guarantees a greater accuracy in predicting the Ti6Al4V flow stress behaviour between 600 and 900°C at strain rates of 0.1 s^{-1} and 1 s^{-1} then the J-C model.

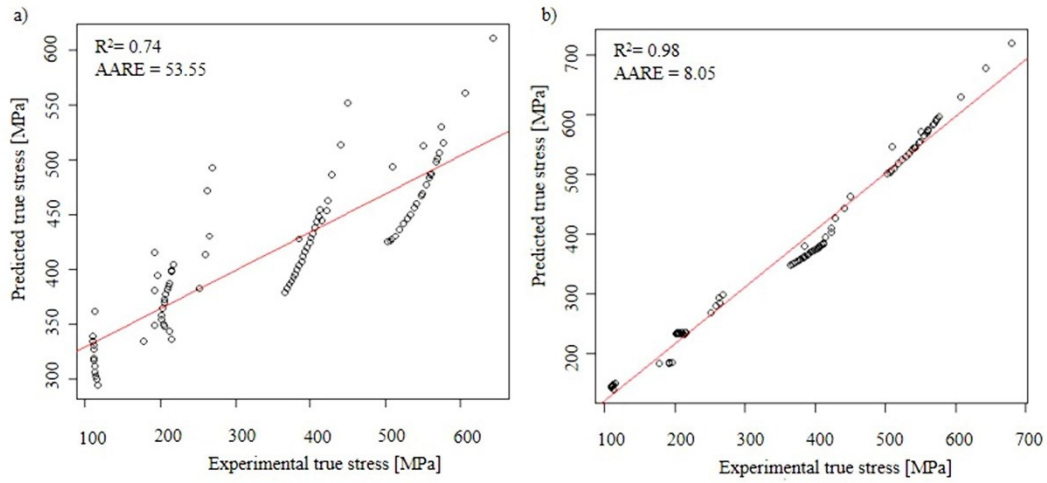

Figure 4-5. Linear relationship between the experimental and predicted data obtained by using a) the Johnson-Cook model, and b) the Arrhenius-type model, with indication of the $\boldsymbol{R^2}$ and $\boldsymbol{AARE}$ statistical parameters.

4.2 Formability modelling

At present, despite the wide use of Ti6Al4V for many applications, the few papers devoted to the characterization of its fracture behaviour refer to room temperature conditions (§ 2.2.2). However, because the elevated temperature ductility of sheet material is being exploited to generate geometries that are difficult to form at room temperature, a comprehensive evaluation of the stress state effect, in terms of both stress triaxiality and Lode parameter, on the material ductility in a wide range of testing conditions, relevant for sheet forming operations carried out at elevated temperatures, is still missing.

Therefore, the aim of the research is to present a new model that can accurately predict the ductility of Ti6Al4V sheets deformed at different temperatures and

strain rates, and incorporating the effect of the stress state by including both the stress triaxiality and the Lode parameter. Based on the Johnson-Cook (J-C) strain fracture criterion [40] that takes into account the temperature and strain rate effects, the proposed new model introduced the Lode effect and a polynomial dependency of the material ductility on the temperature, as a consequence of the experimental evidences. In the new formulation, it was considered that the temperature dependent phase transformations significantly affect the ductility of the dual phase (α/β) titanium alloy. This strong dependence on temperature was incorporated in the new formulation of the J-C model using higher order polynomial of temperature.

The model was applied to 1 mm thick Ti6Al4V sheets deformed in a wide range of temperatures, spanning from room temperature to 900°C, at different strain rates.

In the following, the theoretical background and the approach used to develop the new model are first described in § 4.2.1, followed by the description of the experimental tests and related numerical modelling in § 4.2.2 and § 4.2.3, respectively. The paragraph § 4.2.4 describes the stress states arising in the tests as a function of stress triaxiality and Lode parameter. Finally, while § 4.2.5 presents the calibration of the proposed new model, the following § 4.2.6 focuses on its validation.

4.2.1 Development of the J-C based model

In the literature review (§ 2.2.2), it has been shown that the fracture strain is strongly influenced by stress triaxiality and Lode parameter during plastic deformation. The stress triaxiality is a dimensionless pressure defined as

$$\eta = \frac{-p}{\bar{\sigma}} = \frac{\sigma_m}{\bar{\sigma}}, \tag{4-24}$$

where σ_m is the hydrostatic pressure and $\bar{\sigma}$ the Von Mises equivalent stress, which are represented by Eqs. (4-25) and (4-26), respectively, considering σ_i as the principal stresses.

$$p = -\sigma_m = -\frac{1}{3}(\sigma_1 + \sigma_2 + \sigma_3) \tag{4-25}$$

$$\bar{\sigma} = \sqrt{3J_2} = \frac{1}{\sqrt{2}}\sqrt{(\sigma_1 - \sigma_2)^2 + (\sigma_2 - \sigma_3)^2 + (\sigma_3 - \sigma_1)^2} \tag{4-26}$$

The stress triaxiality represents the stress state corresponding to the points of the conical surface, being OO' the axis perpendicular to the π plane in Figure 4-6a.

However, according to the geometrical definition of the stress triaxiality, it is necessary to introduce another stress parameter, namely the Lode angle θ shown in Figure 4-6b, in order to uniquely define the material stress state for each value of η. The Lode effect can be expressed through the Lode angle θ or the Lode parameter ξ, which are associated to the third deviatoric stress invariant J_3 in Eq. (4-27).

$$\xi = \cos(3\theta) = \frac{27}{2}\frac{J_3}{\bar{\sigma}^3} \tag{4-27}$$

As the Lode angle ranges from 0 to $\pi/3$, the Lode parameter ξ ranges from -1 to 1. Therefore, each stress state can be uniquely identified by the aforementioned set of parameters (η, ξ).

In the special case of plane stress condition, the stress triaxiality and the Lode parameter are related to each other through

$$\xi = -\frac{27}{2}\eta\left(\eta^2 - \frac{1}{3}\right) \tag{4-28}$$

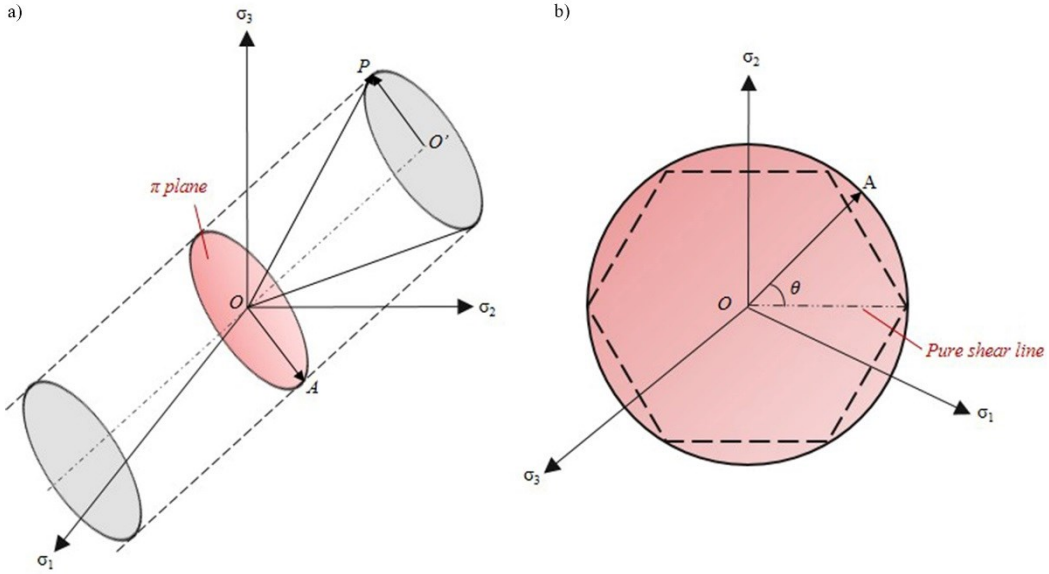

Figure 4-6. a) Stress state in the space of principal stresses and b) geometrical representation of the Lode angle $\boldsymbol{\theta}$ on the $\boldsymbol{\pi}$ plane.

The equivalent strain at fracture, ε_F, is widely used to characterize ductile fracture and damage in engineering materials. McClintock [190] developed a plastic strain based criterion by the behaviour of cylindrical holes under prescribed state of principal stresses, while Rice and Tracey [76] developed a stress triaxiality η based function to predict the growth and linking of spherical holes during deformation. They used an exponential function to relate the strain at fracture to the stress triaxiality:

$$\varepsilon_F(\eta) = D_1 \cdot e^{-D_2 \cdot \eta}\,, \tag{4-29}$$

where D_1 and D_2 are material constants. Johnson and Cook [40] extended this concept to develop a damage criterion that included the effects of strain rate and temperature on material ductility using the separable function approach,

$$\varepsilon_F = [D_1 + D_2 \cdot e^{D_3 \cdot \eta}] \cdot [1 + D_4 \cdot \ln \dot{\varepsilon}^*] \cdot [D_5 \cdot T^* + 1]\,, \tag{4-30}$$

$$\varepsilon_F = [f(\eta)] \cdot [g(\dot{\varepsilon}^*)] \cdot [h(T^*)]\,, \tag{4-31}$$

where $f(\eta)$, $g(\dot{\varepsilon}^*)$ and $h(T^*)$ are functions of the stress triaxiality, strain rate and temperature respectively.

As done in the J-C flow stress constitutive equation (Eq. (4-1)), the strain rate and the temperature effects [40], [60] are represented by the dimensionless parameter $\dot{\varepsilon}^*$ and the homologous temperature T^*, which are expressed in Eqs. (4-2) and (4-3), respectively.

At the reference testing strain rate and temperature, called in the following reference conditions, where $\dot{\varepsilon}^*$ becomes unity and T^* becomes zero, the strain at fracture is then a function of the stress triaxiality only,

$$\varepsilon_F = [D_1 + D_2 \cdot e^{D_3 \cdot \eta}]\,. \tag{4-32}$$

Since the material stress state depends also on the Lode parameter, its effect on the strain at fracture has to be included along with stress triaxiality according to Eq. (4-33),

$$\varepsilon_F = f(\xi, \eta)|_{T_{ref}, \dot{\varepsilon}_{ref}}\,. \tag{4-33}$$

This is referred to as the fracture locus identified at the reference conditions. Consequently, the fracture locus becomes a function of the stress state unambiguously defined by a 3D surface in the $(\xi, \eta, \varepsilon_F)$ space. The addition of the term related to the Lode parameter represents the main novelty of the proposed model, which is now capable to cover the whole range of the stress states.

On the basis of the procedure used to identify the material constants of the original J-C model [40], [184], Eq. (4-33) is modified to introduce the strain rate and temperature effects, by varying them individually as follows:

$$\frac{\varepsilon_F(\xi, \eta)}{f(\xi, \eta)} = g(\dot{\varepsilon}^*)|_{T_{ref}}\,, \tag{4-34}$$

$$\frac{\varepsilon_F(\xi, \eta)}{f(\xi, \eta)} = h(T^*)|_{\dot{\varepsilon}_{ref}}\,. \tag{4-35}$$

Therefore, the functional representation of the proposed new model is reported in Eq. (4-36).

$$\varepsilon_F = f(\xi,\eta)\cdot g(\dot{\varepsilon}^*)\cdot h(T^*) \quad . \tag{4-36}$$

In the following sections, the functions of this ductile fracture model will be derived.

4.2.2 Experimental plan to determine elevated temperature ductility

Several types of tests were performed to investigate the ductile fracture behaviour of Ti6AlV, in form of 1 mm thick annealed Ti6Al4V sheets (§ 3.1.1), under various loading conditions. The experimental plan was specifically designed to cover different stress states, each of which corresponds to well-defined values of the stress triaxiality and Lode parameter. Based on the stress state in the (η,ξ) 2D diagram [2], [91], the tests can be divided into three categories: (i) uni-axial tensile tests carried out on both smooth and notched samples, characterized by positive values of both the stress triaxiality and Lode parameter, (ii) pure shear tests with loading conditions close to the origin of the coordinate system of the (η,ξ) diagram, (iii) equi-biaxial plane stress tension tests (Nakajima) characterized by a positive value of the stress triaxiality and a negative one of the Lode parameter. In this way, the aforementioned tests allow covering the whole range of the Lode parameter, spanning from -1 to 1, without assuming any symmetry of the facture locus as a function of Lode parameter.

The tests conducted at varying stress state at the reference conditions allowed calibrating the fracture locus of Eq. (4-33). On the other hand, the tensile tests on smooth samples, carried out in a wide range of temperatures, spanning from 25 to 900°C, at the reference strain rate, were used to calibrate Eq. (4-35), whereas the tensile tests under different strain rates at the reference temperature allowed calibrating Eq. (4-34). It is worth to underline that the reference conditions in terms of temperature and strain rate were chosen based on the Ti6Al4V behaviour as a function of temperature (§ 2.1.2, § 3.2.2.2).4

A summary of the tests, with the details of the correspondent stress state, testing temperature and strain rate, is reported in Table 4-3.

Table 4-3. Summary and details of the tests used for the model calibration.

Test	Specimen	η	ξ	Temperature [°C]							Strain rate [s^{-1}]
Tensile	Smooth	>0	>0				600				0.1
	Smooth	>0	>0	25	200	400	600	700	800	900	1
	Notch 2 mm	>0	>0				600				1
	Notch 5 mm	>0	>0				600				1
	Notch 10 mm	>0	>0				600				1
Shear	Shear	≈0	≈0				600				1
Equi-biaxial tension	Circular shape	>0	<0				600				1

4.2.2.1 Tensile tests

The tensile tests were performed on samples characterized by different geometries, namely smooth and notched as shown in Figure 4-7, in order to vary both the stress triaxiality and the Lode parameter. These tests were carried out using the same experimental set-up (Figure 3-2) and procedure described in § 3.1.3.

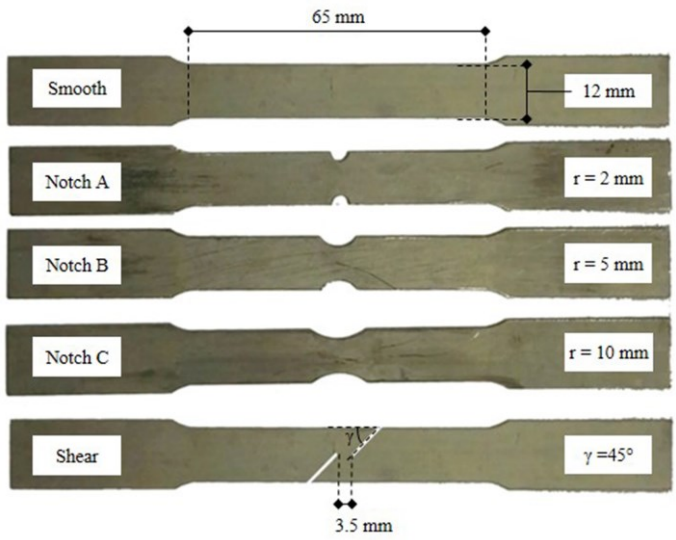

Figure 4-7. Geometry of the samples used for the tensile and shear tests.

Regardless of the sample geometry, the true strain at fracture at varying temperature and strain rate was calculated applying the same procedure given in § 3.1.4.

As done for the calibration of the rheological J-C model (§ 4.1.1), the reference temperature of 600°C was chosen based on the evolution of the β phase fraction

(Figure 2-3) and material ductility (Figure 3-8b) as a function of temperature, while the reference strain rate was set equal to 1 s^{-1}. At these conditions, Figure 4-8 shows the strain at fracture sensitivity to the sample geometry, which corresponds to the different stress states reported in Table 4-3 for the tensile tests samples.

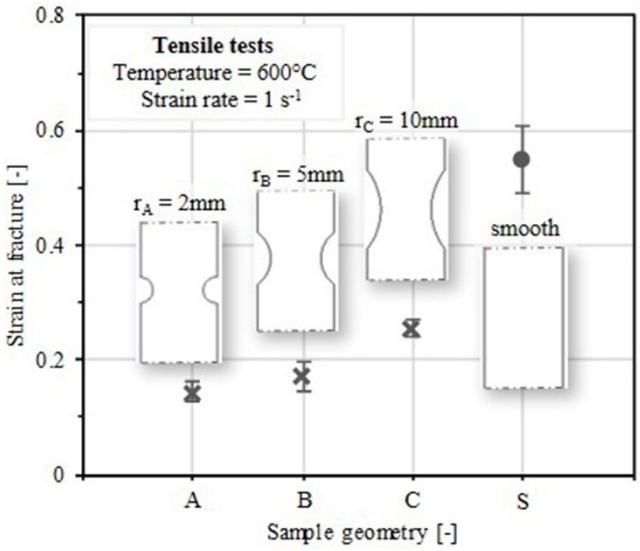

Figure 4-8. Strain at fracture sensitivity to the sample geometry at the reference conditions.

4.2.2.2 Shear tests

The shear tests were carried out on samples with the geometry shown in Figure 4-7, which was designed according to the ASTM B831 standard [191]. The geometry corresponds to a stress state defined by values of the stress triaxiality and Lode parameter close to 0. The tests were performed using the same experimental set-up and applying the same procedure of the tensile tests (§ 3.1.3). The true strain at fracture under shear loading conditions was calculated on the basis of the equivalent gamma strain measured by the Aramis™ system till fracture.

4.2.2.3 Equi-biaxial plane stress tension tests

To reproduce a stress state characterized by a positive value of the stress triaxiality and a negative value of the Lode parameter, namely equi-biaxial plane stress tension condition [192], a Nakajima-type test was performed at the reference temperature and strain rate (Table 4-3) on a 200 mm *x* 200 mm circular sample, using the experimental set-up and procedure described in [193]. The images recorded by the CCD cameras during the test were used in the Aramis™ system to calculate the evolution of the true strain. The equivalent strain measured by Aramis™ just before the fracture was considered as the material ductility limit.

4.2.3 Numerical modelling

The FE-based models of all the tests carried out in the experimental campaign were developed for the calibration and validation of the new model using the software Forge© by Transvalor. The material flow stress as a function of the temperature and strain rate was described using the Hansel-Spittel (H-S) law, using the formulation with five material constants according to Eq. (4-37):

$$\sigma = Ae^{T \cdot m_1} \varepsilon^{m_2} e^{\frac{m_4}{\varepsilon}} \dot{\varepsilon}^{m_3} , \tag{4-37}$$

where A and m_1 to m_4 are material constants representing the flow stress sensitivity to the strain, strain rate and temperature. The material constants were identified on the basis of the flow stress data resulted from the tensile tests on the smooth samples in the whole range of temperature and strain rate. Because of the different behaviour of the material ductility below and above 600°C (Figure 3-8b), the H-S constants were identified for these two temperature ranges, namely Range A (25°C-600°C) and Range B (600°C -900°C). The value of the material constants are given in Table 4-4 and Table 4-5, respectively, while the comparison between the experimental and predicted flow stress behaviour in both the temperature ranges is shown Figure 4-9a.

Table 4-4. Hansel-Spittel material constants for temperature Range A (25°C-600°C).

A	m_1	m_2	m_3	m_4
1564	-0.001	0.044	0.008	-0.008

Table 4-5. Hansel-Spittel material constants for temperature Range B (600°C-900°C).

A	m_1	m_2	m_3	m_4
10012	-0.004	0.002	0.034	-0.007

To capture the different stress states characteristic of each test, the samples geometry was accurately reproduced in the FE models, as well as the testing parameters. The experimental thermal field of the samples, measured at the end of the soaking time by means of an infrared thermo-camera, was replicated in the FE model, as shown in the example of Figure 4-9b. The mesh size was progressively refined until a further decrease did not lead to a significant variation in the simulation results, but only to a relevant increase in the computation time.

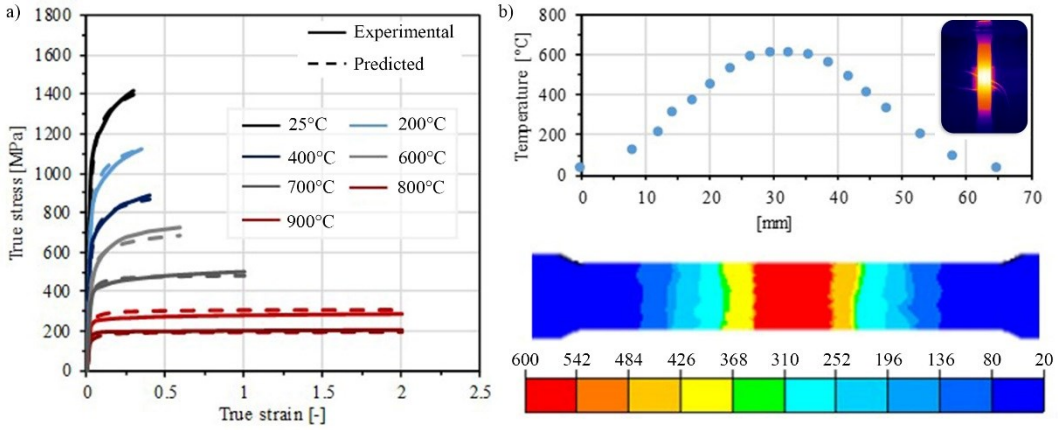

Figure 4-9. a) Comparison between the experimental and predicted flow stress curves at 1 s^{-1}. b) Example of the sample thermal field imposed in the FE model as recorded from the infrared thermo-camera measurements.

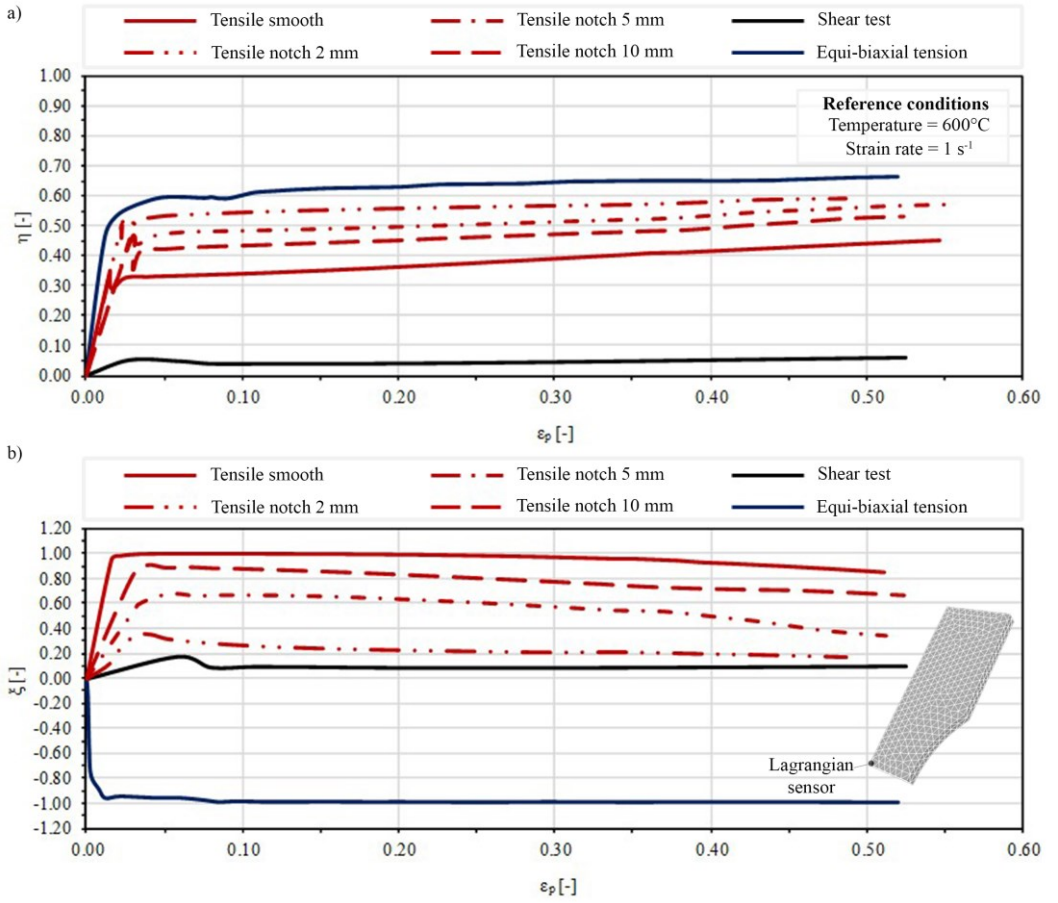

Figure 4-10. a) Stress triaxiality $\boldsymbol{\eta}$, and b) Lode parameter $\boldsymbol{\xi}$ as a function of the equivalent plastic strain at the reference conditions with the detail of the Lagrangian sensor location in the sample neck region.

Figure 4-10 shows the η and ξ evolution as a function of the equivalent plastic strain at the reference conditions for the different test categories and samples geometries. The reported values of η and ξ were recorded by means of a local

Lagrangian sensor placed in the neck zone of the samples (Figure 4-10b), as done in other papers related to the stress state analysis [40], [184], [194].

To calibrate the fracture locus at the reference conditions (Eq. (4-33)), as well as the new model (Eq. (4-36)), each test was summarized as a point in the 3D $(\xi, \eta, \varepsilon_F)$ space, using the average values of the stress triaxiality, η_{av}, and the Lode parameter, ξ_{av}, which were calculated for each test as a function of the equivalent plastic strain until the strain at fracture value according to Eqs. (4-38) and (4-39) [93].

$$\eta_{av} = \frac{1}{\varepsilon_F}\int_0^{\varepsilon_F} \eta \, d\varepsilon_p \tag{4-38}$$

$$\xi_{av} = \frac{1}{\varepsilon_F}\int_0^{\varepsilon_F} \xi \, d\varepsilon_p \tag{4-39}$$

4.2.4 Stress states in terms of triaxiality and Lode parameter

The average values of the stress triaxiality and Lode parameter for each test performed at the reference conditions are reported in Figure 4-11. As foreseen, the tests of Table 4-3 cover the whole possible range of the Lode parameter, namely from -1 to +1, and the positive range of the stress triaxiality, which is typical of sheet forming operations. Moreover, it is worthwhile to note that the points of Figure 4-11 properly belong to the plane stress curve, in agreement with the results reported in [2] for Ti6Al4V sheets deformed at room temperature.

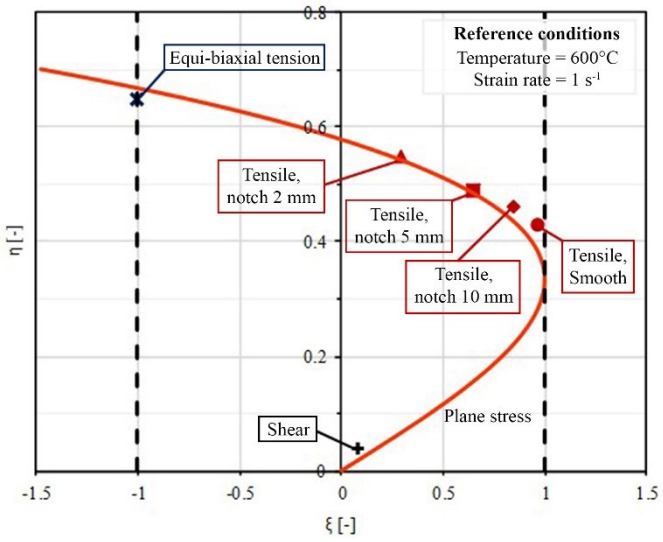

Figure 4-11. η_{av} and ξ_{av} values of the tests of Table 4-3 carried out at the reference conditions. The red solid line represents the plane stress condition expressed by Eq. (4-28).

A further evidence of the different stress states and related fracture mechanisms for each test under the reference conditions is given by the SEM analysis of the samples fracture surfaces (see Figure 4-12).

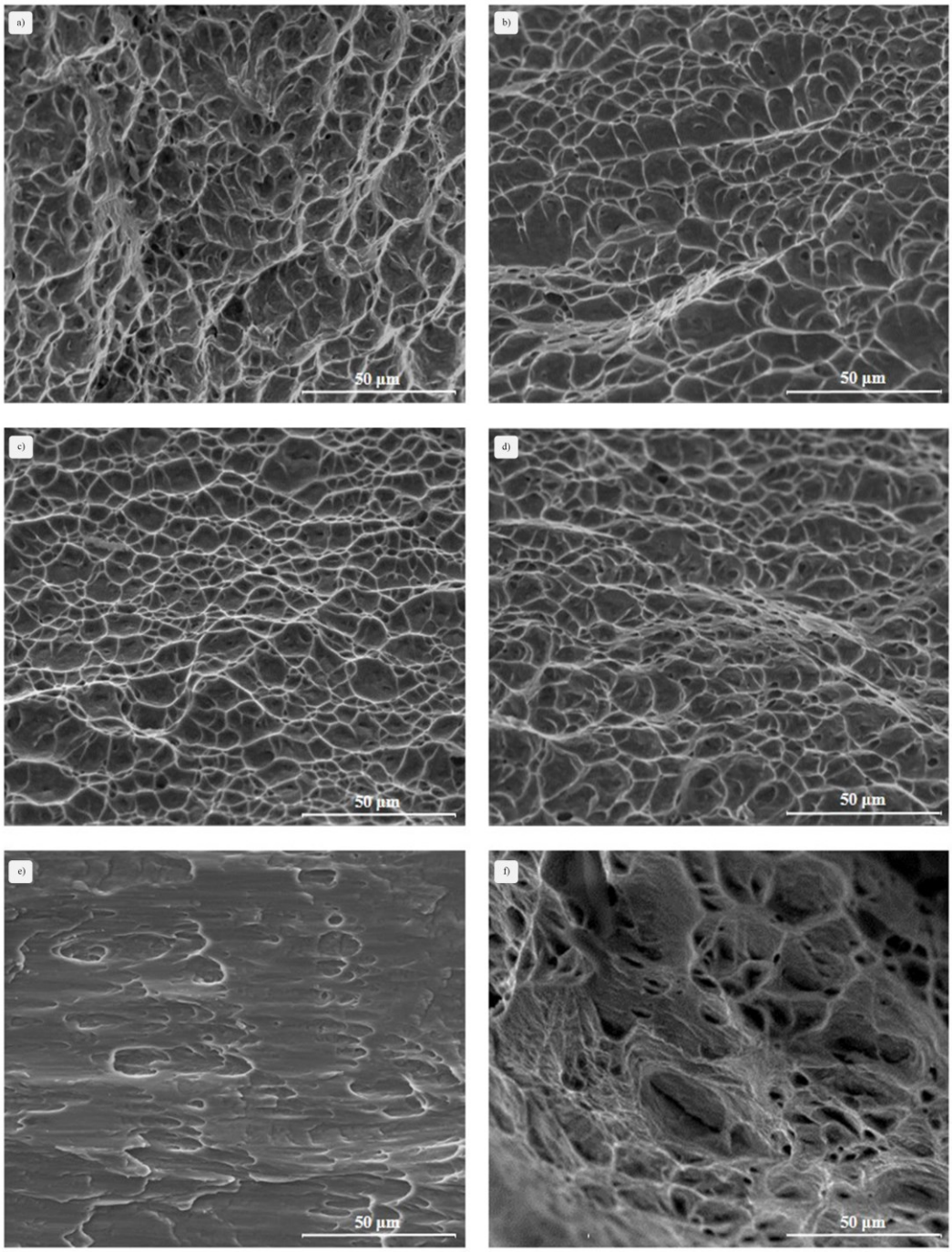

Figure 4-12. SEM images of the fracture surfaces of the specimens deformed at the reference conditions: a) tensile smooth, b) tensile notch 2 mm, c) tensile notch 5 mm, d) tensile notch 10 mm, e) shear, f) equi-biaxial plane stress tension. Magnification: 2000x.

The fracture surfaces of the smooth and notched samples (Figure 4-12a-d) show equiaxed dimples, typical of the occurrence of ductile fracture, and evidence that the tensile stress condition was operative in all these tests [187]. The absence

of micro-cracks in the notched samples (Figure 4-12b-d), the latter being considered as an evidence of the ductility decrease as function of the stress triaxiality increase for Ti6Al4V at room temperature [2], demonstrates the pronounced influence of the testing temperature.

Moreover, the increase of the voids dimensions and the progressive transformation of the sphere-like voids into more ellipsoid-like ones, passing from the higher notch radii (Figure 4-12a and Figure 4-12d) to the smallest one (Figure 4-12b), prove the variation of the stress triaxiality and the Lode parameter as function of the notch radius in Figure 4-11. Indeed, according to [78], the voids dimensions are ruled by the hydrostatic stress, related to the stress triaxiality through Eq. (4-24), and the higher the hydrostatic pressure the larger the voids dimensions. The voids geometry, instead, is influenced by the deviatoric stress tensor [78], represented by the second deviatoric stress invariant J_2, in the Von Mises equivalent stress (Eq. (4-26)), and the third deviatoric stress invariant J_3, expressed in the definition of the Lode parameter (Eq. (4-27)).

The fracture surface of the shear sample (Figure 4-12e) is far different from the ones of the tensile samples (Figure 4-12a-d), being characterized by small, partially formed dimples, as the ones reported in [187] for the shear-band portion of the fracture surface, stretched along the loading direction.

Finally, the significant difference in the voids dimensions detectable in the fracture surface of the Nakajima sample (Figure 4-12f) explains the distance between the average values of the stress triaxiality and Lode parameter of the equi-biaxial tension test and the other tested categories shown in Figure 4-11.

4.2.5 Calibration of the new ductility model

4.2.5.1 3D fracture locus in the reference conditions

To identify the fracture locus function of the stress triaxiality and Lode parameter, according to Eq. (4-33) at the reference conditions identified in § 4.2.2.1, the Curve Fitting Toolbox of the Matlab™ software was used to best fit the points in the $(\xi, \eta, \varepsilon_F)$ space. First, a hyperbolic cylindrical surface (Eq. (4-40)) was considered as the initial surface for the optimization process, similarly to the procedure followed by Bai and Wierzbicki in [91].

$$\varepsilon_F = f(\xi, \eta) = \frac{\xi^2}{A} - \frac{\eta^2}{B} - C \tag{4-40}$$

Because the goodness of the fit was very low on the basis of the output statistical parameters, namely the Sum of Squares due to Error (SSE) and the correlation coefficient R^2, different other formulations were tested, among which the following equation, representing the 3D fracture locus at the reference conditions, was found to give the best performance in terms of fitting of the experimental data:

$$\varepsilon_F = f(\xi,\eta) = \left[\left(\frac{\xi^4}{A^2} - \frac{(B + C\cdot e^{D*\eta})^4}{E^2} - F\right)\cdot e^{(\xi^4-\eta^4)}\right]. \qquad (4\text{-}41)$$

The material constants of Eq. (4-41) were identified through a non-linear regression analysis by minimizing the difference between the $(\xi, \eta, \varepsilon_F)$ points and the resulting 3D surface. Their values are reported in Table 4-6, as well as the values of the statistical fitting parameters: R^2 close to 1 and SSE close to 0 suggest the good predictability of the model. The good accuracy of the proposed equation is witnessed also by the average error between the predicted and experimental data, which is reduced from 23.5% using the hyperbolic cylinder of Eq. (4-40) to 8.2% of Eq. (4-41).

Table 4-6. Material constants of the 3D fracture locus at the reference conditions.

a	b	c	d	e	f	SSE	R^2
2.9010	-0.1096	-0.2589	0.6638	-1.256	-0.1537	0.0043	0.9759

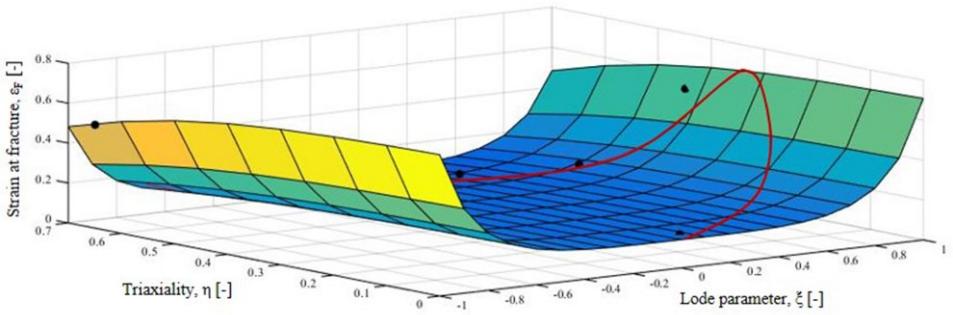

Figure 4-13. 3D fracture locus of the Ti6Al4V identified at the reference conditions (600°C and 1 s^{-1}). The red solid line represents the plane stress condition (Eq. (4-28)). The black points refer to the experiments of Table 4-3.

It should be noted that that the proposed fracture locus is a non-separable form in η and ξ, as assumed in [91], and it does not assume any symmetry with respect to the Lode parameter, providing the most generalization in representing the effect

of the stress state on the strain at fracture. The geometrical representation of the resulting 3D surface is shown in Figure 4-13.

At the reference conditions, the proposed fracture locus, which considers the effects of both the stress triaxiality and Lode parameter, is represented by Eq. (4-42).

$$\varepsilon_F = f(\xi,\eta) = \left[\left(\frac{\xi^4}{2.901^2} - \frac{(-0.1096 - 0.2589 \cdot e^{0.6638*\eta})^4}{-1.256^2} + 0.1537\right) \cdot e^{(\xi^4-\eta^4)}\right]. \quad (4\text{-}42)$$

4.2.5.2 Strain rate and temperature effects on the 3D fracture locus

The temperature and strain rate effects were introduced in the 3D fracture locus of Eq. (4-42), following the approach described in § 4.2.1, in order to obtain a fracture criterion suitable for processes performed at elevated temperatures.

Considering a linear dependency of the strain at fracture sensitivity to the strain rate, as assessed in the original J-C fracture model (Eq. (4-30)), Eq. (4-34), which defines a general relationship between the strain at fracture and the strain rate, becomes

$$\frac{\varepsilon_F(\xi,\eta)}{f(\xi,\eta)} = [1 + D_4 \cdot \ln \dot{\varepsilon}^*]|_{T_{ref}}\,, \quad (4\text{-}43)$$

where $f(\xi,\eta)$ is represented by Eq. (4-42). The material constant D_4 is therefore identified considering the experimental data at the reference temperature of 600°C and different strain rates. It is calculated as the slope of the linear fitting of the curve $\varepsilon_F(\xi,\eta)/f(\xi,\eta)$ versus $\ln \dot{\varepsilon}^*$, as shown in Figure 4-14a.

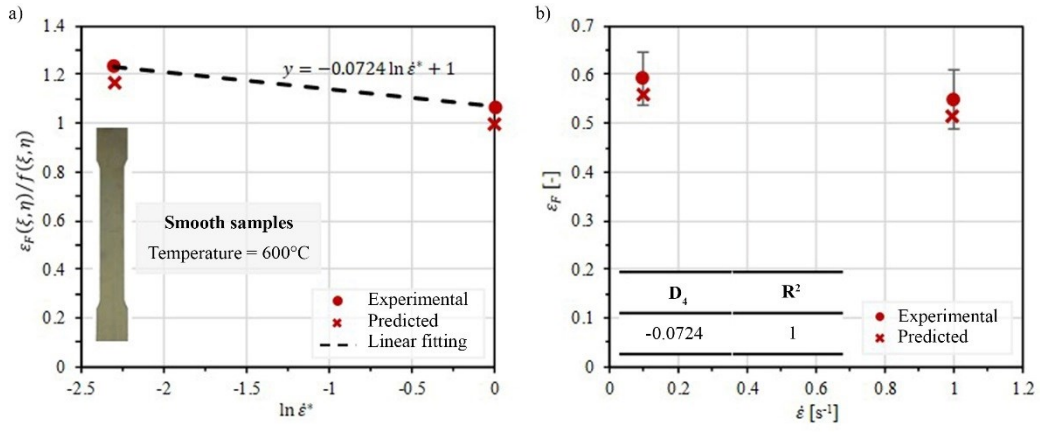

Figure 4-14. a) Strain at fracture-to-fracture locus vs natural logarithm of $\dot{\boldsymbol{\varepsilon}}^*$, and b) comparison between the experimental and predicted strains at fracture as a function of the strain rate at the reference temperature.

The value of the constant D_4 , equal to -0.0724, and the comparison between the experimental results and predicted data, calculated using Eq. (4-43) with the fracture locus of Eq. (4-42), are given in Figure 4-14b, showing a good fitting on the basis of the resulting value of the correlation coefficient R^2.

The effect of the temperature, which is considered linear in the original J-C fracture criterion according to Eq. (4-30), was modified on the basis of the Ti6Al4V ductility characteristics at varying temperature, as shown in Figure 3-8b. Since the strain at fracture as function of the temperature is not constant (Figure 3-8b), three temperature ranges were separately considered for the identification of the material constants, defining the fracture locus sensitivity to temperature: Range A, from 25 to 600°C, Range B, from 600 to 900°C, and finally Range C, which covers the whole range of temperatures. As reported in Eq. (4-35) and § 4.2.2, the material constants giving the temperature effect through the homologous temperature, T^*, are identified on the basis of the data obtained at the reference strain rate and different temperatures.

Within Range A, the relationship between the strain at fracture-to-fracture locus ratio and the homologous temperature was considered linear, as in the original J-C fracture model; therefore, Eq. (4-35) becomes:

$$\frac{\varepsilon_F(\xi,\eta)}{f(\xi,\eta)} = [D_5 \cdot T^* + 1]|_{\dot{\varepsilon}_{ref}} . \tag{4-44}$$

According to Eq. (4-44), the material constant D_5 is identified as the slope of the linear fitting interpolating the points in the $\varepsilon_F(\xi,\eta)/f(\xi,\eta)$ versus T^* chart, as shown in Figure 4-15a. D_5 resulted to be equal to 0.7323, while the comparison between the experimental data and the calculated strains at fracture are reported in Table 4-7. Based on the value of the correlation coefficient close to 1 (R^2 equal to 0.939), and an average error of 5.1% in the prediction of the strains at fracture, it can be stated that Eq. (4-44) allows predicting the experimental results with a good accuracy.

On the other hand, based on the experimental results of Figure 4-15b, a polynomial relationship between the strain at fracture-to-fracture locus ratio and the homologous temperature was adopted within Range B, according to Eq. (4-45):

$$\frac{\varepsilon_F(\xi,\eta)}{f(\xi,\eta)} = \left[D_I \cdot T^{*2} + D_{II} \cdot T^* + D_{III}\right]\Big|_{\dot{\varepsilon}_{ref}} . \tag{4-45}$$

Therefore, the material constants, D_I, D_{II} and D_{III}, defining the temperature effect in the high temperature range, refer to the polynomial fitting in Figure 4-15b, while the comparison between the strains at fracture predicted using Eq. (4-45) and the experimental data are reported in Table 4-7. The value of the correlation coefficient equal to 0.975 and an average error of 9.1% suggest again a good predictability of the proposed model.

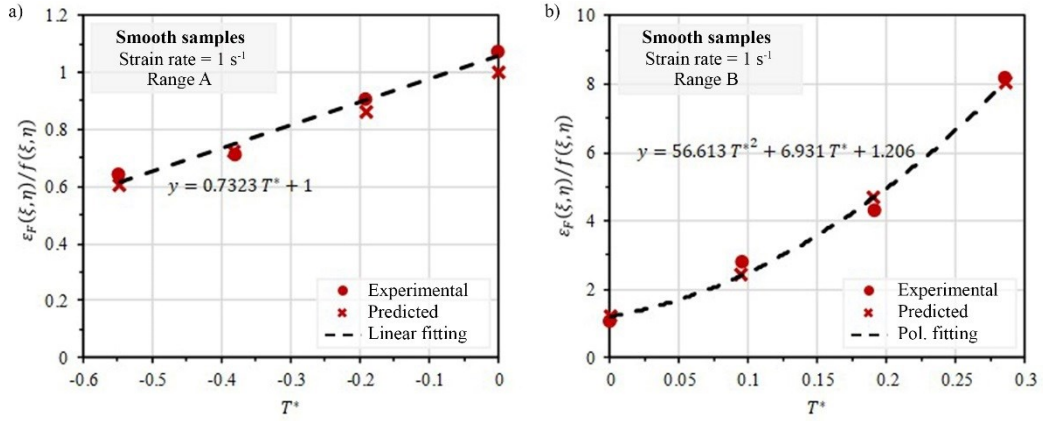

Figure 4-15. Strain at fracture-to-fracture locus ratio as a function of the homologous temperature within a) Range A, (25°C-600°C), and b) Range B, (600°C-900°C), at the reference strain rate.

Table 4-7. Comparison between the experimental and predicted strains at fracture at the reference strain rate in Range A (25°C -600°C) and Range B (600°C -900°C).

Range A			**Range B**		
Temperature [°C]	**Experimental ε_F [-]**	**Predicted ε_F [-]**	**Temperature [°C]**	**Experimental ε_F [-]**	**Predicted ε_F [-]**
25	0.426	0.396	600	0.549	0.620
200	0.449	0.457	700	0.889	0.759
400	0.503	0.479	800	1.179	1.292
600	0.549	0.514	900	1.689	1.660

The last range to consider in the analysis of the strain at fracture sensitivity to temperature is Range C, spanning from 25 to 900°C. As it can be observed in Figure 4-16a, the relationship between the strain at fracture-to-fracture locus ratio and the homologous temperature is represented by a fourth degree polynomial function, which was identified by minimizing the difference between the experimental and fitted data using the Matlab™ software. Therefore, in Range C, the temperature

effect on the strain at fracture, which was generally represented through Eq. (4-35) in § 4.2.1, is defined as Eq. (4-46) at the reference strain rate.

$$\frac{\varepsilon_F(\xi,\eta)}{f(\xi,\eta)} = \left[D_A \cdot T^{*4} + D_B \cdot T^{*3} + D_C \cdot T^{*2} + D_D \cdot T^{*} + D_E\right]\Big|_{\dot{\varepsilon}_{ref}} \qquad (4\text{-}46)$$

The comparison between the experimental and the predicted strains at fracture, calculated out through Eq. (4-46) using the resulting material constants (Figure 4-16a), are reported in Figure 4-16b: as it can be seen, the experimental and predicted values almost overlap suggesting the good accuracy of the model, demonstrated also by the high value of the correlation coefficient, reported in Figure 4-16b.

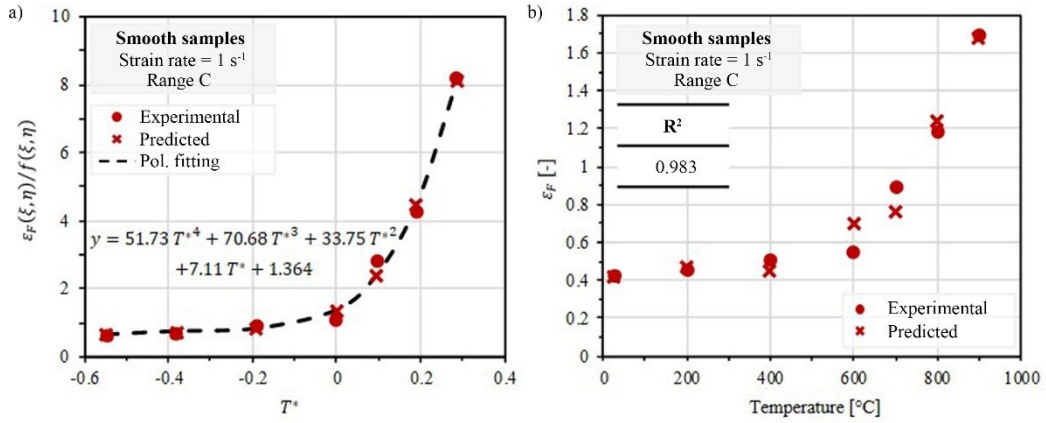

Figure 4-16. a) Strain at fracture-to-fracture locus ratio versus the homologous temperature, and b) comparison between the experimental and predicted strains at fracture in Range C (25°C-900°C) at the reference strain rate.

The average error of the model proposed for the Range C (Eq. (4-46)) is equal to 8.3%. However, it must be noted that the higher percentage difference between the experimental and predicted values of the strain at fracture at 600°C (see Figure 4-16b) compared to the fitting obtained using Eq. (4-45) can be attributed to the change of the slope in the evolution of the strain at fracture as a function of the temperature (Figure 3-8b).

Nevertheless, even if the average error found for the model using Range C lies in between the ones resulted for Range A and Range B, Eq. (4-46) was chosen to describe the influence of the temperature in the proposed ductility model, whose final equation is expressed as:

$$\varepsilon_F = \left[\left(\frac{\xi^4}{2.901^2} - \frac{(-0.1096 - 0.2589 \cdot e^{0.6638*\eta})^4}{-1.256^2} + 0.1537\right) \cdot e^{(\xi^4 - \eta^4)}\right] \cdot [1 - 0.0724 \cdot \ln \dot{\varepsilon}^*] \cdot \left[51.73 \cdot T^{*4} + 70.68 \cdot T^{*3} + 33.75 \cdot T^{*2} + 7.11 \cdot T^* + 1.364\right] \quad (4\text{-}47)$$

4.2.6 Validation of the new ductility model

The predictability of the new ductility model, expressed by Eq. (4-47), was verified on the basis of the data obtained under testing conditions different from the ones used in the calibration procedure. With this aim, the strains at fracture resulted from seven tensile tests performed on smooth samples in the whole temperature range and one shear test at 400°C, all of them carried out at 0.1 s^{-1} as summarized in Table 4-8, were used.

Table 4-8. Summary and details of the tests used for the model validation.

Test	Specimen	η	ξ	Temperature [°C]	Strain rate [s^{-1}]
Tensile	Smooth	>0	>0	25 200 400 700 800 900	0.1
Shear	Shear	≈0	≈0	400	0.1

Figure 4-17 shows the comparison between the experimental and the predicted strains at fracture in tensile and shear conditions at 0.1 s^{-1} and different temperatures.

In tensile condition, the correlation coefficient, defining the accuracy in the prediction of the modified criterion, resulted to be 0.991 in the whole temperature range. However, considering separately the two ranges of the low (25°C -600°C) and elevated (600°C-900°C) temperatures, the correlation index of the latter is higher than the one calculated for the 25°C-600°C range. This can be attributed to the fact that the model overestimates the strains at fracture as lower strain rates induces higher ductility, while, in the high temperature range, where the effect of the strain rate is more pronounced, the accuracy of the model predictions increases.

In shear condition at 400°C and 0.1 s^{-1}, the new formulation of the model guarantees a good accuracy since the percentage difference between the experimental and the predicted strain at fracture is very low, equal to 0.7%, as it can be observed in Figure 4-17.

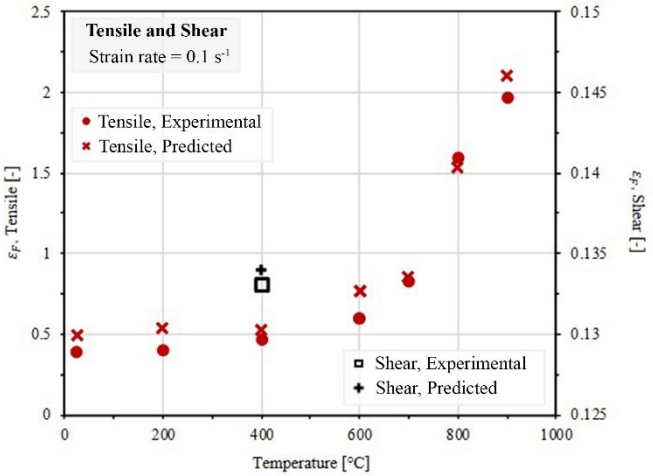

Figure 4-17. Comparison between the experimental and predicted strains at fracture as function of the temperature resulted from the tensile and shear tests performed at 0.1 s^{-1}.

4.2.7 Highlights

Based on the discussion reported in the previous sections, the following points can be highlighted.

- The combinations of the stress triaxiality (η) and Lode parameter (ξ) values, which were identified at the reference conditions and reported in the (ξ, η) space, proved that the proposed experimental program covered a wide range of stress states typical of the sheet forming operations. The analysis of fracture surfaces, showing different dimensions and shapes of the dimples, confirmed that different stress states (identified as (ξ, η) points) were developed in each test.
- The Lode and stress triaxiality parameters were implemented in the J-C model at the identified reference conditions. The proposed fracture locus was a non-separable fourth order polynomial form in η and ξ parameters. It did not assume any symmetry with respect to the Lode parameter. This model adequately fitted the test data in the (ξ, η) test space.
- The effect of the strain rate was considered linear as assessed in the original J-C fracture criterion. It was found to adequately predict the effect of the strain rate in the 0.1 to 1s^{-1} range.
- The temperature effect was analysed in the three temperature ranges, identified according to the evolution of the transformation controlled material ductility in terms of the change in strain at fracture with the temperature. The linear relationship characterizing the strain at fracture

sensitivity to temperature in the low temperature range (Range A, 25°C-600°C) was modified into a polynomial function in the high temperature one (Range B, 600°C -900°C), where the ductility started increasing rapidly above 600°C. Range C covered temperature from room temperature to 900°C. In this range, a better description of the temperature effect was modelled using a fourth order polynomial function.

- A significant difference between experimental and predicted data was found at 600°C, which can be attributed to the change of slope in the evolution of the strain at fracture as function of the temperature.
- The proposed model was validated using the values of the strain at fracture resulted from tensile and shear tests performed at 0.1 s^{-1} and not used for the criterion calibration. Generally, a good predictability was shown, except for the temperature of 600°C.

4.3 Summary

Chapter 4 gives an overview on the research work carried out to develop numerical models able to describe the material behaviour, in terms of flow stress behaviour and material ductility. Based on the reported results, the following main conclusions can be pointed out.

- At elevated temperature and strain rate, the Arrhenius-type model was found to guarantee a better accuracy in predicting the flow stress behaviour of the Ti6Al4V sheets compared to the J-C one, as proved by the values of $R^2$and $AARE$ calculated out for each model. The greater accuracy of the Arrhenius-type model was attributed to the coupled effect of temperature and strain rate on the flow stress, which is expressed through the Zener-Hollomon parameter.
- A new model based on the Johnson-Cook strain fracture criterion was proposed for the prediction of the ductility in Ti6Al4V titanium alloy sheets deformed in a wide range of temperatures at different strain rates. Besides the influence of the stress triaxiality, temperature and strain rate, the new model added the effect of the Lode parameter through a non-separable form in η and ξ, thus providing the most generalization in representing their effect on the strain at fracture and covering the whole range of possible stress states a sheet can be subjected to during forming

operations. Generally, a good predictability was shown in different testing conditions, except for the temperature of 600°C, at which the material ductility was demonstrated to start increasing.

5 Chapter

Surface modification for biomedical applications

This chapter is devoted to the twofold aspect of the industrial case, namely the biomedical and forming issues, to determine the proper process conditions capable to preserve the surface characteristics relevant to the osseointegration process and, at the same time, to assure acceptable ductility.

Therefore, Chapter 5 focuses on the methods aimed at tailoring the surface characteristics to enhance the material bioactivity, but also on the investigation of the behaviour of these Ti6Al4V surface treated sheets at elevated temperature.

In the following, the different methods applied to modify the surface topography of Ti6Al4V sheets are described and the resulting surface characteristics, together with the analysis of the material bioactivity, are accurately investigated. Furthermore, the effect of the forming process on the material bioactivity, but also the sensitivity of the material behaviour to the surface treatment are evaluated.

5.1 Material & methods

5.1.1 Material

The samples to be surface treated and later on tested at elevated temperature were extracted from the 1 mm thick Ti6Al4V sheet (§ 3.1.1) along its rolling direction (Figure 3-2d). The as-received microstructure of the sheet consists of equiaxed $\alpha + \beta$ (Figure 3-1, [183]), while the as-received surface roughness is equal to 0.719 ± 0.009 μm.

5.1.2 Surface treatments

Six different surface treatments were considered, which modify the as-received sheet surface through three different methods, namely acid etching, acid etching

followed by anodization, and etching in a hydrothermal reactor. The details of the six treatments are reported in Table 5-1, where they are named from A to E, being G the as-received sample.

Table 5-1. Details of the surface treatments.

Treatment	Surface treatment #1	Surface treatment #2
A	Etching 48%H_2SO_4+18%HCl at 75°C for 2 h	—
B	Etching 48%H_2SO_4+18%HCl at 75°C for 1 h	—
C	Etching 48%H_2SO_4+18%HCl at 75°C for 1 h	Anodization 5M NaOH at 15 V for 2 h
D	Etching 48%H_2SO_4+18%HCl at 90°C for 2 h	—
E	Etching 48%H_2SO_4+18%HCl at 90°C for 1 h	—
F	Anodization 10M NaOH at 100°C for 2 h	Etching 5% HNO_3 at 25°C for 6 h
G	As-received	—

The treatments A, B, D and E are based on acid etching with the same reagent, but they are performed at different etching temperatures and times. The treatment C provides anodization after the etching, in order to assure a nano-textured surface on the micro-substrate obtained by the acid etching [107]. The treatment F, which is etching in a hydrothermal reactor, would assure a micro-nano surface characterized by an improved wettability [115]. These treatments were chosen since, according to literature, they assured good values of roughness and bioactivity [107], [115].

Before being treated, the samples were ultrasonically washed in acetone and distilled water for 10 minutes, and then weighed with a high precision scale (sensibility 0.01 mg). After the surface treatment, the samples were rinsed with distilled water and weighed again in order to analyse the loss of weight due to the process. Afterwards, all the samples were cut into two parts, one of which was thermally treated in a Nabertherm™ N7/H furnace at 450°C for two hours, with the aim of evaluating any possible difference between the sole etched surface and the thermally treated one (in the following they will be called "Before-TT" and "After-TT" samples, respectively). According to literature [112], the thermal treatment should promote the formation of the TiO_2 in form of anatase on the sample surface, which favours the interaction between the implant and the body.

5.1.3 Surface characterization and biological test

The surface morphology obtained with the previously described surface treatments was first analysed using the Fei Quanta 450™ SEM (Figure 3-4a), while the chemical composition was investigated through maps and spectrums obtained through the Energy Dispersive Spectroscopy (EDS) analysis, which was performed using the probe installed inside the SEM. The surface roughness and topography were evaluated through a SensoFar Plu-Neox™ 3D profiler (Figure 5-1a). The roughness parameter R_a was calculated as an average of 5 measurements for each sample. The surface characterization was performed before and after the thermal treatment, thus studying its influence on the surface characteristics.

The Simulated Body Fluids (SBF) test was used to evaluate the formation of calcium phosphate on the samples surfaces, and therefore the material bioactivity [108]. The samples that underwent the complete modification process (surface modification plus thermal treatment) were immersed into the SBF solution for 7 days at 37°C, using the experimental set-up depicted in Figure 5-1b. The solution was prepared following the instructions and formula available in literature [109] and, in order to keep constant the ions concentration, was changed every two days.

After the SBF test, the samples were analysed through EDS to evaluate their chemical composition. The treatment that assured the best bioactivity was chosen considering that the higher the percentage of Ca and P the higher the apatite formation and, therefore, the material bioactivity [108].

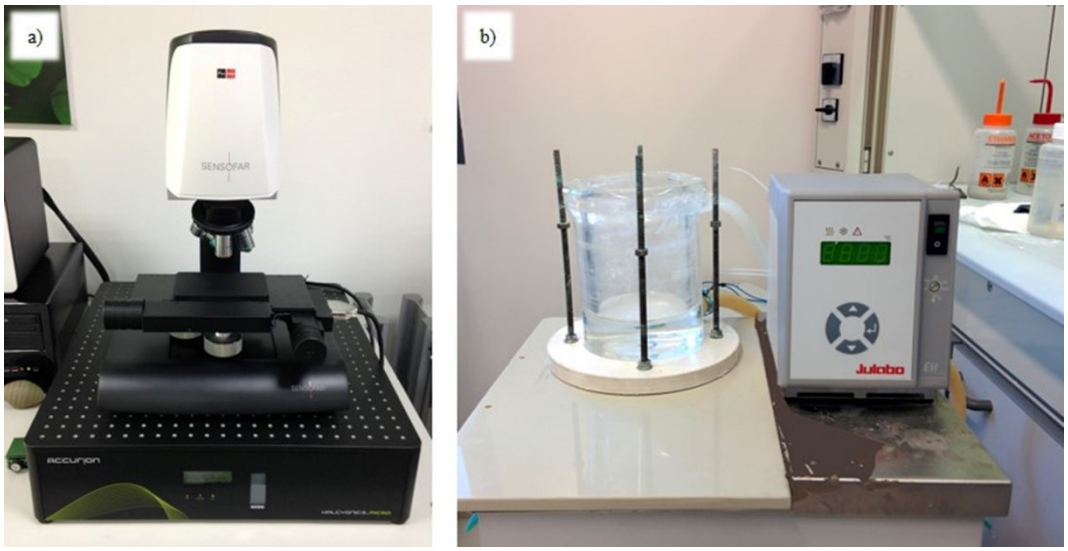

Figure 5-1. a) SensoFar Plu-Neox™ 3D profiler. b) Experimental set-up for the Simulated Body Fluids (SBF) test.

5.1.4 Tensile tests on samples modified on the surface

The samples subjected to the surface treatments that, according to the results of the surface characterization (§ 5.2.1, § 5.2.2), assured the best performances in terms of roughness and bioactivity were tested at elevated temperatures under tensile conditions on the MTS™ testing machine, represented in Figure 3-2, following the same experimental procedure described in § 3.1.3.

The tests were performed at 400°C, 600°C and 700°C, besides room temperature, at a nominal strain rate of 0.1 s^{-1}, which, according to the data resulted from the tensile tests carried out on the untreated (virgin material) Ti6Al4V samples (§ 3.2.2), assures higher ductility and lower flow stress. The value of 700°C as the maximum testing temperature was chosen to limit the formation of TiO_2 in form of rutile on the sample surface that could lower the material bioactivity, as described in the literature review (§ 2.3).

5.1.5 Post-deformation analyses

The flow behaviour and ductility at elevated temperature of the surface treated samples were compared with the ones of the untreated samples (§ 3.2.2) in order to evidence a possible influence of the surface treatments. As it was done in the analysis of the untreated material, the ductility of the Ti6Al4V samples modified on the surface was investigated evaluating the strains at fracture, which were calculated following the procedure described in § 3.1.4.

To evaluate the effect of the tensile test parameters on the microstructural and mechanical properties of the thermo-electro-chemical modified samples, optical and scanning electron microscopy investigation, as well as the micro-hardness analysis, were carried out following the experimental procedures reported in § 3.1.4.

The topography of the sample surface nearby the fracture zone was analysed by means of the SensoFar Plu-Neox™ 3D profiler and the surface chemical composition evaluated through the EDS analysis, starting from the fracture surface along the sample longitudinal direction.

An X-Ray Diffraction (XRD) analysis was also carried out on the samples surface to evaluate the possible formation of rutile [113], the allotrope of TiO_2 that can lower the material bioactivity. The XRD patterns were collected using a Philips PW 1710™ diffractometer (Cu K-alfa radiation) in a 2θ range from 20° to 50° on the heated part of the longitudinal surface of the sample.

Finally, to investigate the effect of the tensile test parameters on the material bioactivity, the SBF tests were performed also on the strained samples.

5.2 Results

5.2.1 Surface characteristics

The results of the 3D profiler analysis show that the roughness of all the treated samples is always higher than the one of the as-received sheet, as it can be observed in Figure 5-2, suggesting the positive effect on the roughness increase of all the surface treatments.

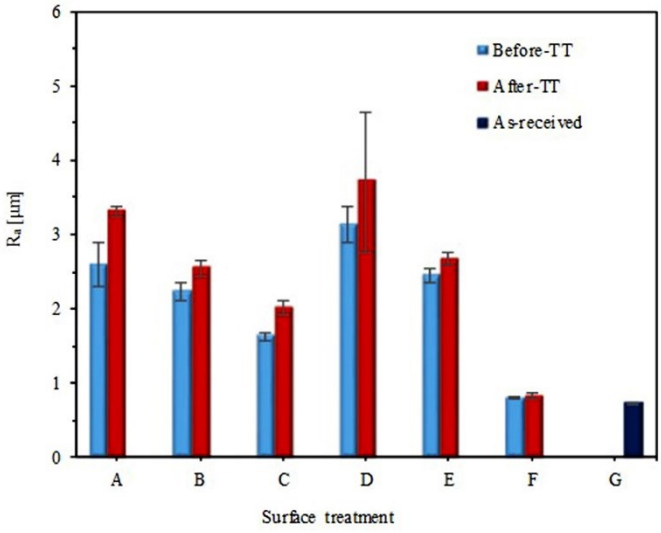

Figure 5-2. Comparison of surface roughness between different surface treatments and before and after the thermal treatment.

Based on the reported experimental values, the minimum increase of roughness results to be 50%, excluding the sole treatment F that causes a slighter increase of 11%. Figure 5-2 also shows that the thermal treatment after the surface modification further promotes the surface roughness increase.

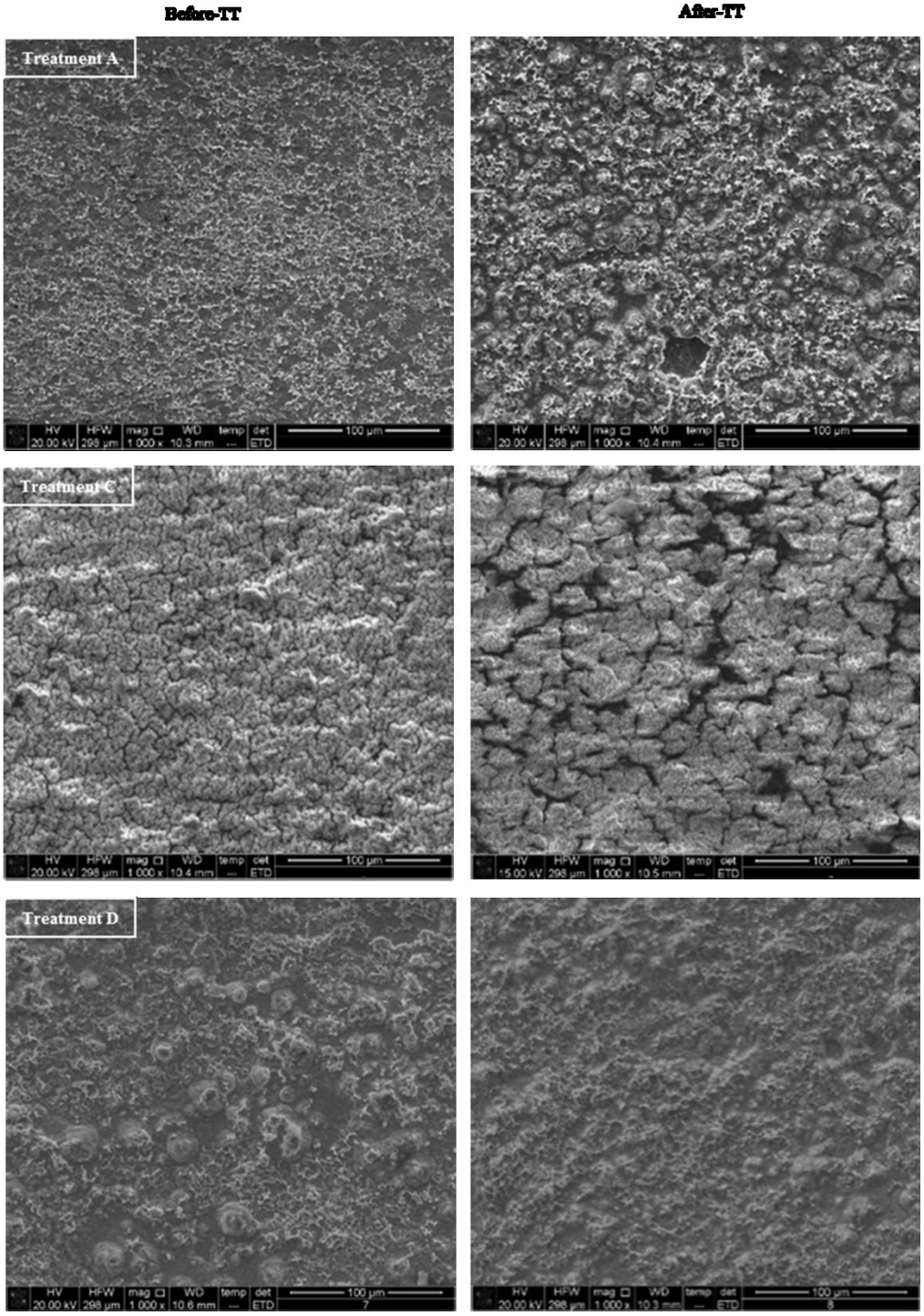

Figure 5-3. SEM images before and after the thermal treatment for different surface treatments.

An example of the difference in the surface roughness before and after the thermal treatment can be seen in the SEM images of Figure 5-3: the formation of TiO_2, favoured by the thermal treatment [112] and confirmed by the EDS analysis, provokes indeed an enhancement of the surface roughness. Moreover, the SEM images acquired before and after the thermal treatment witness that each treatment assures a uniform surface appearance of the surface for all the investigated samples.

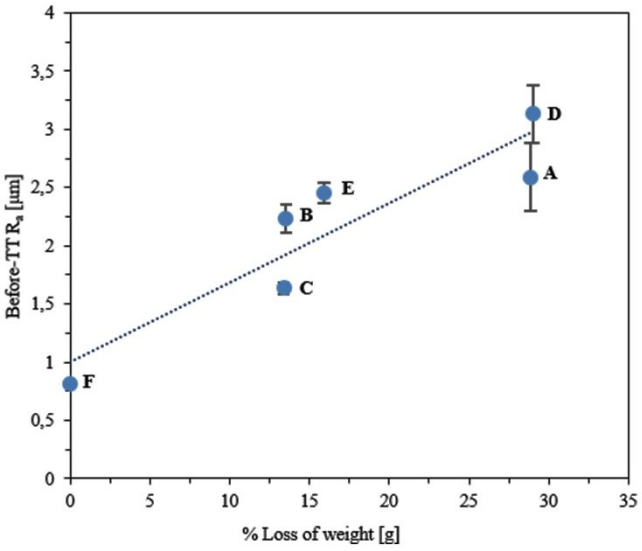

Figure 5-4. Before-TT roughness as a function of the percentage of weight loss.

Figure 5-4 shows the linear relationship between the surface roughness before the thermal treatment and the loss of weight due to the applied surface treatments: the higher the obtained roughness the higher the loss of weight, whose maximum corresponds to a resulting thickness of 0.7 mm.

Moreover, the effect of the etching time and etching temperature on the loss of weight can be evaluated for the acid etching treatments A, B, D and E. It was found that the effect of the etching time is more significant than the one of the etching temperature: passing from 75°C to 90°C for an etching time of 1 h, the percentage variation is 15%, while the increase of the etching time from 1 h to 2 h at 75°C produces a percentage variation of the weight loss of 53%. The same trend can be observed also for the roughness: by increasing the etching temperature for an etching time of 2 h, the percentage variation is 17%, while, maintaining the temperature at 90°C and rising the etching time, the percentage difference increases up to 21%. Therefore, the time has a greater effect than the temperature on both the loss of weight and roughness, with its impact on the weight loss more significant than the one it has on the surface roughness.

Based on the evaluation of the surface characteristics (Figure 5-2), the surface treatments that assure the highest values of roughness are treatments A and D: therefore, they will be considered as possible treatments to be applied to the samples for the following tensile tests.

5.2.2 Apatite deposition

To identify the surface treatments assuring the most significant bioactivity in terms of presence of calcium phosphate, which spontaneously transforms into apatite in contact with the body fluids in the biological environment [113], the samples immersed in SBF for 7 days were successively analysed through EDS. The resulting Ca and P percentages, calculated through the images analysis, are reported in Figure 5-5. An example of the resulting maps of the Ca and P distribution of the sample subjected to treatment D is reported in Figure 5-6. As it can be noticed, the areas covered with Ca coincide with the ones characterized by the presence of P, suggesting the formation of calcium phosphate.

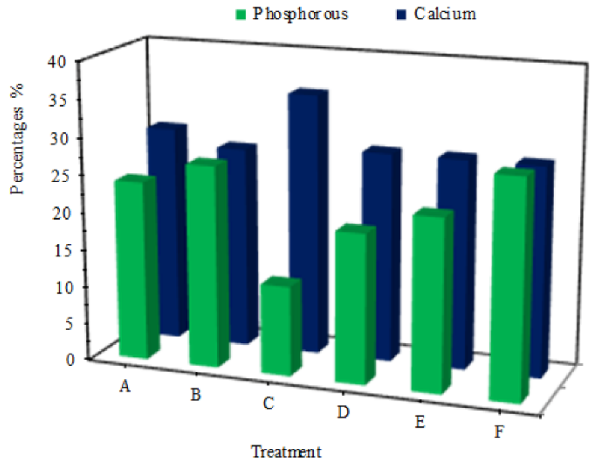

Figure 5-5. Percentages of Ca and P for all the surface treated samples resulted from the EDS analysis.

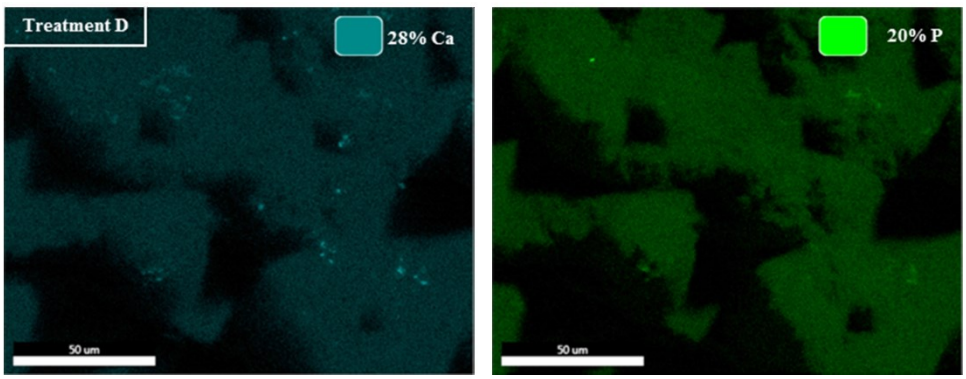

Figure 5-6. Example of EDS maps of the Ca and P distribution elements percentages in case of treatment D.

Figure 5-5 highlights that the highest percentages of Ca and P can be found when the treatment F is applied. However, based on the reported results, the treatment F is excluded from the next considerations as it assures a good bioactivity in terms of percentages of Ca and P, but, on the other hand, a too low roughness (Figure 5-2). The treatment A was preferred over B, as well as D was preferred over E, since the treatments A and D assure higher values of roughness (Figure 5-2) and good bioactivity (Figure 5-5). Finally, the treatment C was considered to evaluate the effect of a surface treatment different from the simple acid etching, even if it shows a medium roughness and a gap between the percentages of Ca and P.

In conclusion, considering these results in terms of bioactivity and the ones obtained in § 5.2.1 for the roughness characteristics, the treatments A, C and D were chosen as the best candidates to be applied to the samples for the tensile testing at elevated temperature, as they assure a good compromise between surface topography and bioactivity.

5.2.3 Comparison between treated and untreated samples

Figure 5-7 shows the Ti6Al4V flow stress sensitivity to the testing temperature and surface treatment: as resulted for the untreated samples, the higher the temperature the lower the flow stress, whereas, except at 600°C, the flow stress of the as-received material is always lower than the ones of the treated samples. As regards the flow stress sensitivity to the surface treatment, its effect on the flow stress can be considered negligible.

Figure 5-8 reports the strain at fracture sensitivity to the testing temperature: regardless the sample surface conditions, the strain at fracture starts increasing significantly when the temperature reaches 600°C, while, below this temperature, the ductility increase due to temperature is less pronounced. The ductility of the as-received material is always higher than the one of the treated samples, with a maximum difference of 39.9% and 32.4% respectively at 400°C and 600°C. The surface treatment influences the true strain at fracture, especially at 600°C, at which the treatment A assures the best performance in terms of ductility comparable to that of the untreated material.

Therefore, it can be stated that the temperature has a significant effect on both the flow stress and strain at fracture, while the surface conditions affect only the material ductility, as its influence on flow stress can be considered negligible.

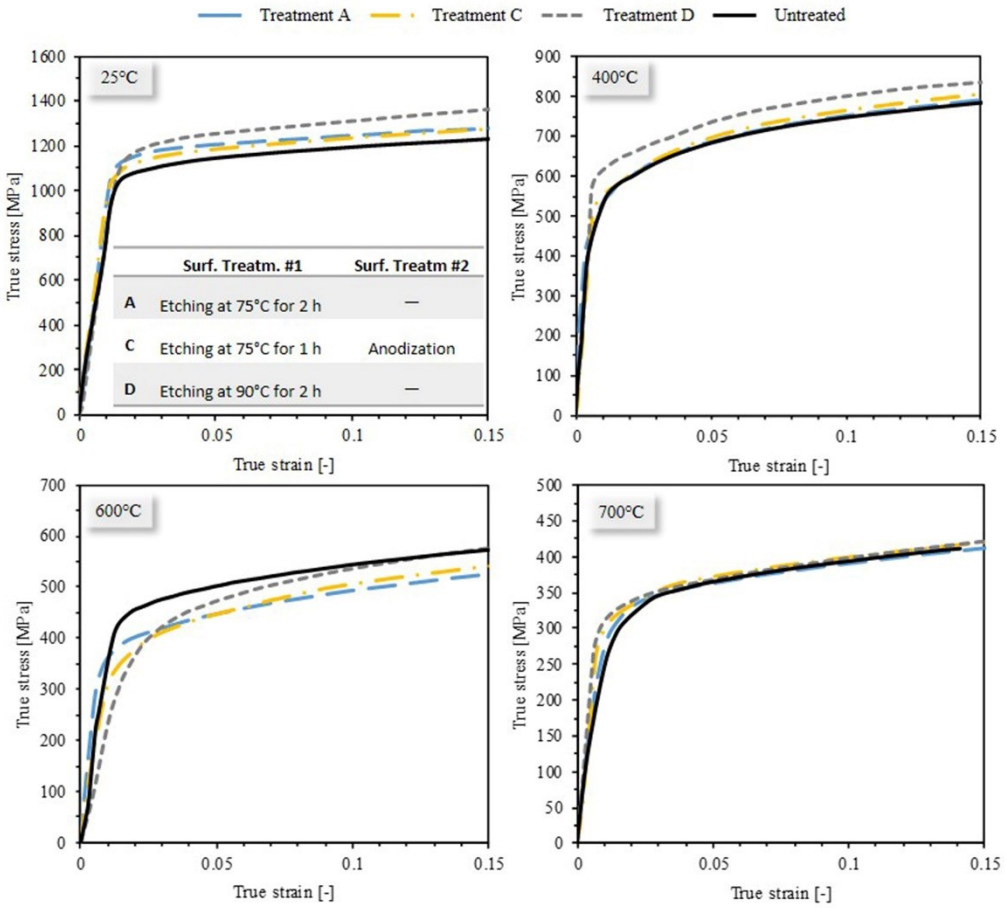

Figure 5-7. Ti6Al4V flow stress sensitivity to the testing temperature and surface treatment. The table in the upper right corner reports a summary of the surface treatments considered (see Table 5-1 for all the details).

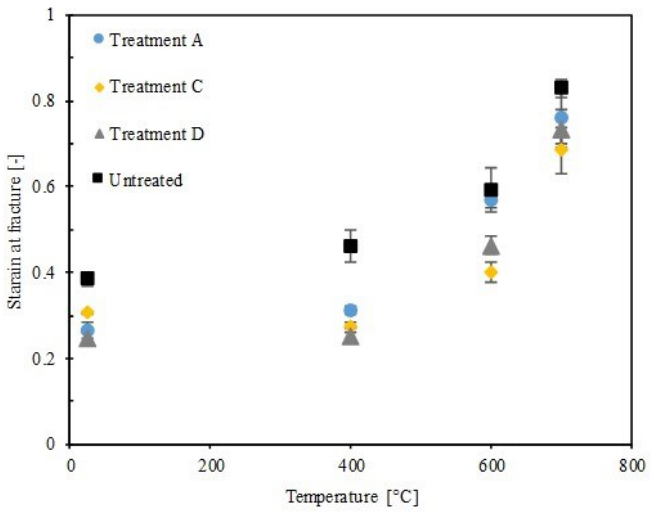

Figure 5-8. True strain at fracture sensitivity to the testing temperature and surface treatment.

5.2.4 Post-deformation characteristics

All the treated samples deformed till fracture were analysed through optical and scanning electron microscopy to investigate the microstructural characteristics as a function of the testing temperature and surface treatment. Figure 5-9 shows as example the optical micrographs of the samples subjected to the treatment D and deformed at the different testing temperatures.

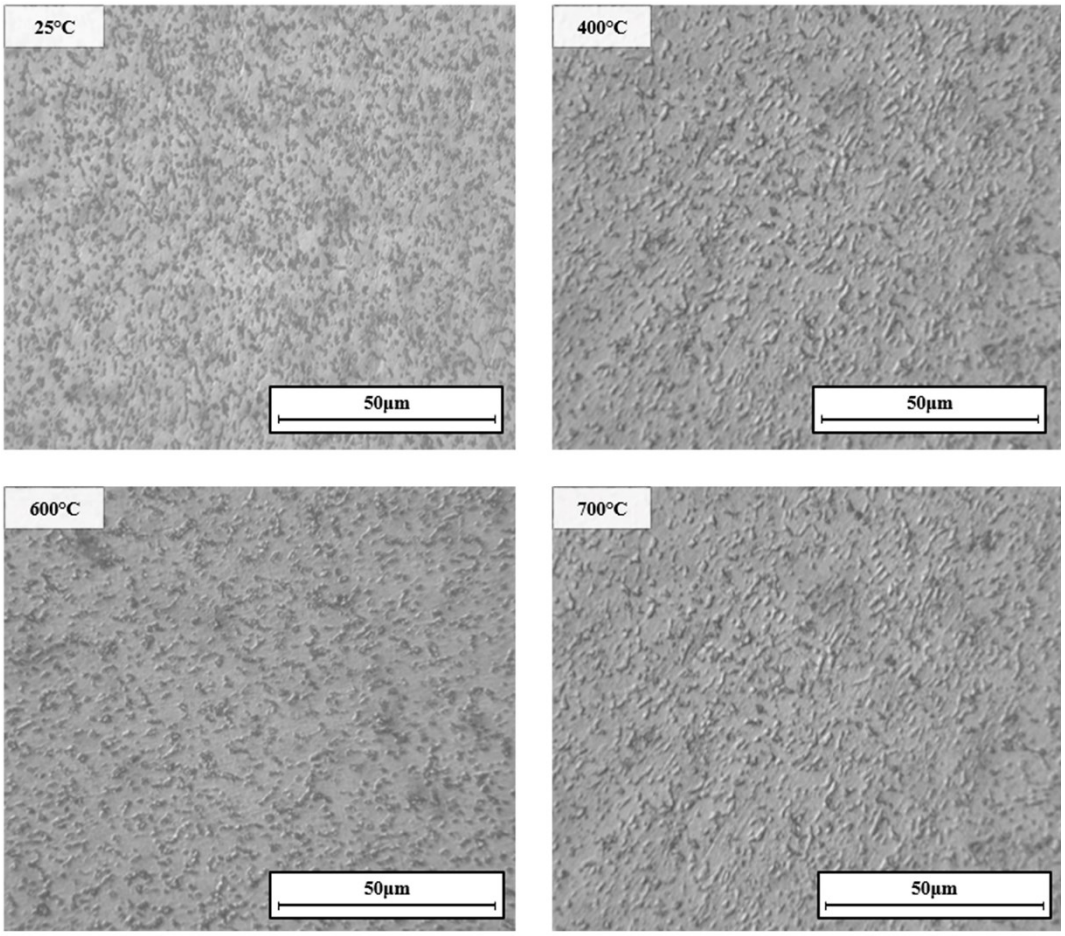

Figure 5-9. Microstructures of the samples treated with the surface treatment D (Table 5-1) and deformed at (a) 25°C, (b) 400°C, (c) 600°C and (d) 700°C.

All the deformed samples show an equiaxed $\alpha + \beta$ microstructure [183], as it is the one in the as-received condition (Figure 3-1). The influence of the testing temperature on the microstructural characteristics is negligible, since no evident microstructural modifications can be seen in comparison with the microstructure of the as-received sheet (Figure 3-1). This result, in the low and medium temperature range (25°C-700°C), correlates well with the conclusions reported for the untreated material (§ 3.2.2.5). In addition, a negligible influence of the surface treatment was found, proving that neither the surface treatment nor the deformation in the

investigated temperature range modify the initial material structure. Consequently, the testing temperature, the surface treatment and the mechanical process are parameters that do not significantly affect the material microstructural characteristics.

The micro-hardness measurements of the deformed samples are reported in Figure 5-10: it is evident that the surface treatments do not affect the material micro-hardness, being the percentage differences between the micro-hardness of the treated and untreated samples lower than 5%. Moreover, the percentage difference between the micro-hardness of the treated samples and the one of the as-received Ti6Al4V sheet is always lower than 7.5%, therefore implying that the thermo-mechanical processing does not significantly affect the samples post-deformation mechanical characteristics. A slight sensitivity to the testing temperature, as found for the untreated material (§ 3.2.2.3), can be appreciated for each surface treatment, even if cannot be considered significant being less than 9.6%. All these results prove that neither the surface treatment nor the thermo-mechanical processing significantly affect the material mechanical properties in terms of micro-hardness.

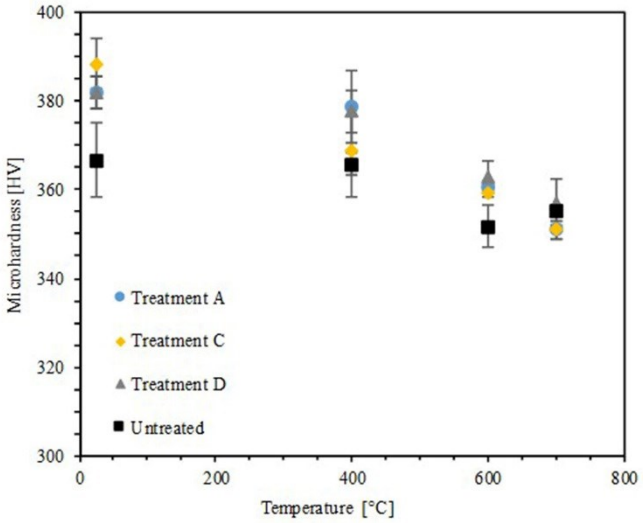

Figure 5-10. Micro-hardness sensitivity to the testing temperature and surface treatment.

To analyse the effect of the thermo-mechanical process on the surface roughness, the post-deformation surface roughness was measured by means of the SensoFar™ profiler in proximity of the fracture surface.

The 3D maps, reported as an example in Figure 5-11, offer an overview of the surface topography of samples subjected to the treatments A, C and D and deformed at 600 and 700°C.

Analysing the resulting S_a values, it can be stated that the treatment D assures the highest values for both the samples strained at 600°C and 700°C, while the treatment A offers the lowest ones.

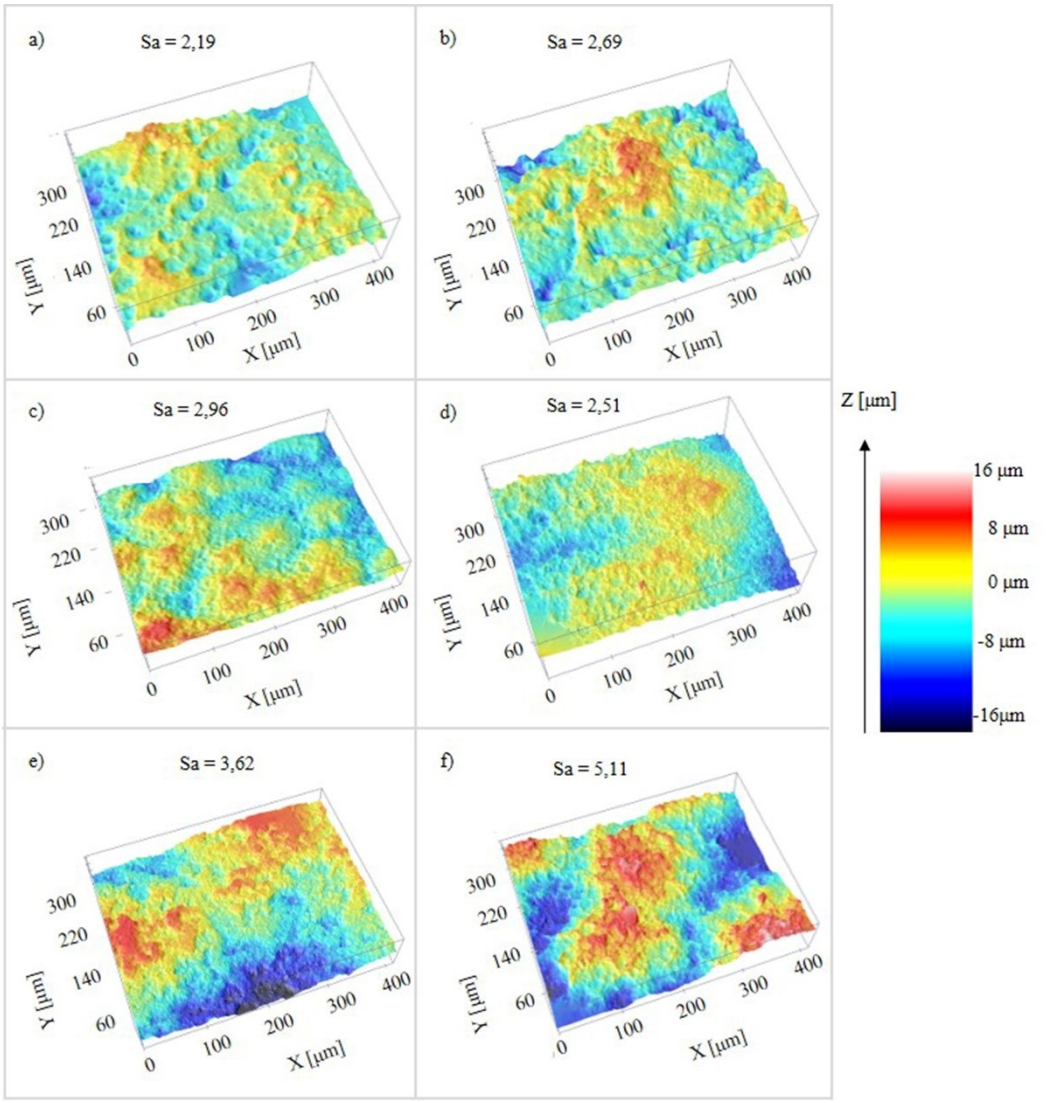

Figure 5-11. a), b), c) Topography of samples deformed at 600°C and submitted to treatment A (S_a = 2.19), C (S_a = 2.69) and D (S_a = 2.96), respectively. d), e); f) Topography of samples deformed at 700°C and submitted to treatment A (S_a = 2.51), C (S_a = 3.62) and D (S_a = 5.11), respectively.

The resulting values of the post-deformation roughness are shown in Figure 5-12 as a function of the strain at fracture, testing temperature and surface treatment, allowing the identification of the surface roughness sensitivity to the thermo-mechanical process, testing temperature and applied surface treatment.

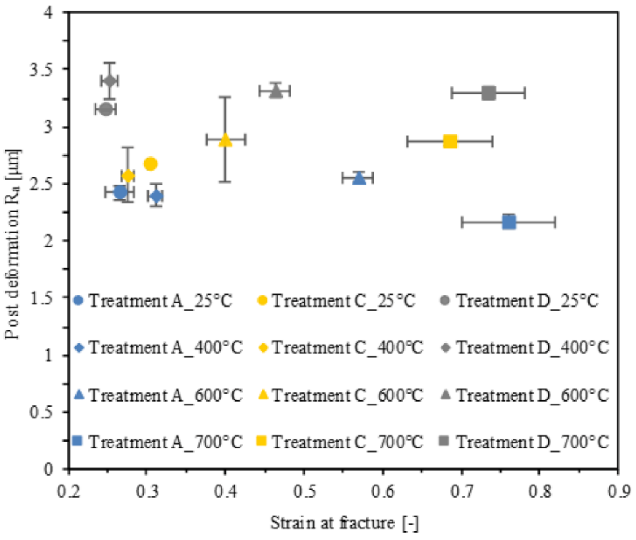

Figure 5-12. Post-deformation roughness (R_a) versus true strain at fracture as a function of the testing temperature and surface treatment.

The roughness sensitivity to the mechanical process can be evaluated comparing the R_a values obtained after the thermal treatment (Figure 5-2) and after the tensile test performed at 25°C (Figure 5-12). Considering the results obtained for the treatments A, C and D summarized in Figure 5-13, the values differ of 22% on an average.

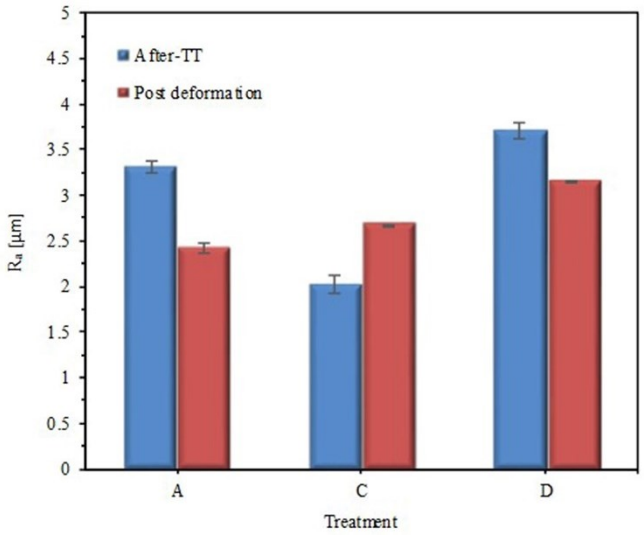

Figure 5-13. After-TT and post-deformation (room temperature) roughness values.

Considering the samples deformed at elevated temperature, the roughness sensitivity to the thermo-mechanical process can be evaluated through the comparison of the R_a values measured in proximity of the fracture surface (deformed area) and near the clamping area, which is not interested by the deformation process (undeformed zone). These values differ among each other for

an average difference of 9%. These differences can be attributed to the fact that the treatments were performed in different batches, but, considering the thermo-mechanical process, they can be read as a result of the variation of the surface top layer due to the stretching experienced by the sample during the tensile test.

From Figure 5-12 it can be also noted that the sensitivity of surface roughness to the testing temperature can be considered negligible since the percentage difference is maximum 10%, regardless the surface treatment.

On the other hand, the roughness sensitivity to the surface treatment after deformation is more pronounced, as a maximum percentage difference of 30% can be seen between the treatment A and the treatment C at 600°C; the treatment D is the one that assures the highest value of surface roughness after deformation, regardless the testing temperature.

Summarizing these results, the surface roughness sensitivity to the mechanical process can be considered negligible, as well as the one to the testing temperature, whereas the influence of the surface treatment is more pronounced.

Figure 5-12 summarizes the surface and ductility characteristics allowing the identification of the deformation temperature and the surface treatment that offer the best balance between ductility and biomedical requirements. Based on these results, it can be concluded that treatment D assures the highest values of the roughness after deformation at elevated temperature, while a temperature of 600°C guarantees an enhanced ductility compared to room temperature, still maintaining low the presence of TiO_2 in form of rutile on the surface [113]. This is proved by the XRD analysis carried out on the heated part of the strained samples whose patterns are reported in Figure 5-14. The rutile peaks in the patterns related to 600°C are lower than the ones obtained for the samples deformed at 700°C for all the treatments with the exception of treatment C for which the principal and the second rutile peaks are nearly the same.

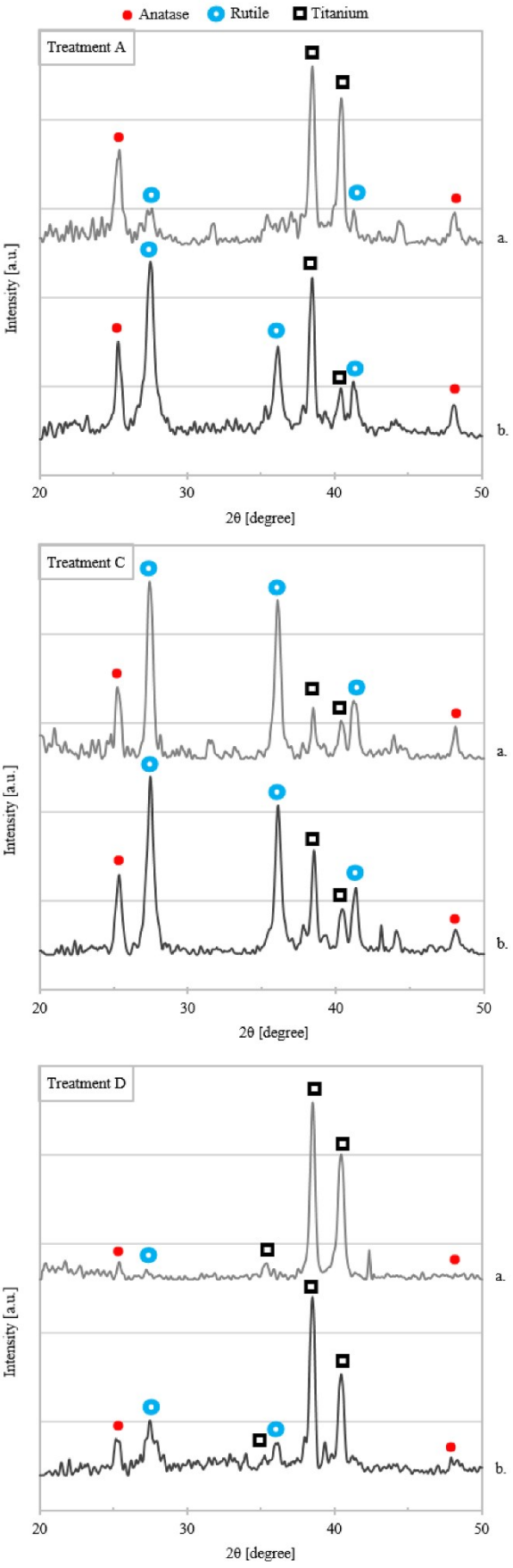

Figure 5-14. XRD patterns of samples subjected to treatments A, C and D. The curves a. and b. refer to samples deformed at 600°C and 700°C respectively.

Finally, the bioactivity of a sample surface treated by using the treatment D and deformed at 600°C was investigated through a SBF test of 7 days in order to investigate the bioactivity sensitivity to the thermo-mechanical process. The surface chemical composition of the sample after the SBF test was investigated through the EDS analysis (Figure 5-15): it reveals that the oxygen percentage on the surface increased compared to the one obtained for the correspondent sample modified on the surface, while the percentages of Ca and P are nearly constant (compare with Figure 5-6). Therefore, it can be stated that the bioactivity of the sample is not influenced by the deformation, suggesting the possibility to perform the surface treatment before the forming operations.

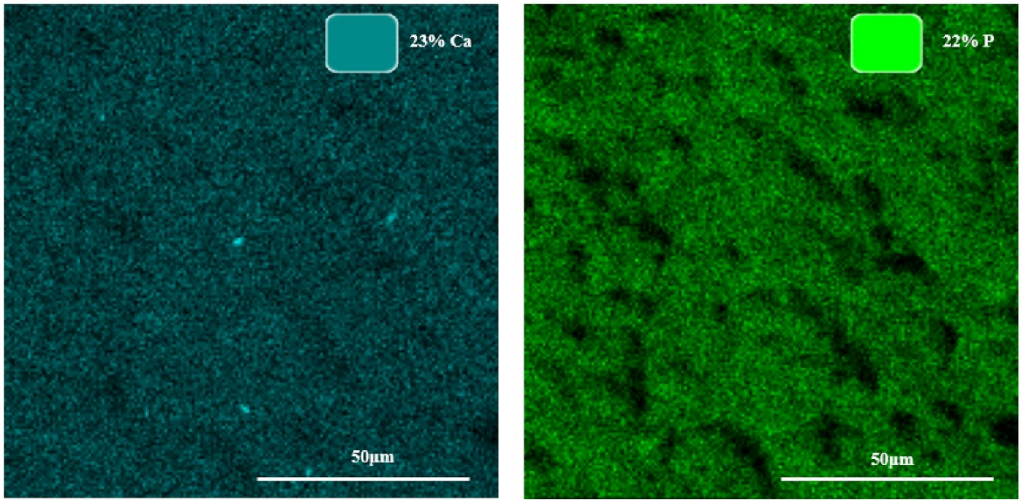

Figure 5-15. EDS maps of the Ca and P distribution for the sample surface treated with treatment D and deformed at 600°C.

5.3 Summary

Chapter 5 offers an overview of the analyses performed to investigate the effects of the surface treatments on the material roughness and bioactivity, but also on the mechanical behaviour of this thermo-electro-chemical modified Ti6Al4V sheets. The analyses allowed the identification of the deformation temperature and the surface treatment that offer the best balance between ductility and biomedical requirements. Based on the reported results, the main highlights of Chapter 5 can be listed in the following.

- The applied surface treatments enhanced the surface roughness that was further increased by the following thermal treatment. The obtained roughness was proportional to the loss of weight and both these parameters were influenced by the etching time and temperature. The higher the

etching time and temperature the higher the roughness and loss of weight, being the etching time influence more pronounced.

- The tensile tests carried out at elevated temperature on the surface treated samples showed that both the temperature and surface treatment influenced the strain at fracture, which however was found to rapidly increase starting from 600°C as observed for the untreated material.
- Neither the surface treatment nor the thermo-mechanical processing affected the material micro-hardness and microstructure, which remained an equiaxed $\alpha + \beta$ one for all the testing conditions.
- The SBF tests revealed that the material bioactivity was not influenced by the deformation at elevated temperature, since the percentages of Ca and P were nearly constant.
- Samples deformed at 600°C after being treated with the treatment D, namely chemical etching at 90°C for 2 h, was found to assure at 600°C the best balance between high roughness, good bioactivity and increased ductility compared to room temperature.

6 Chapter

Incremental Sheet Forming process

This chapter reports the experimental procedures and results related to the production of a prototype of the Ti6Al4V acetabular cup applying the Incremental Sheet Forming process, which, according to literature (§ 2.4.2), is suitable for small volume batches and high-customized sheet metal parts. Considering the different variants of the process and the improvements achieved in the geometric accuracy using two moving forming tools (§ 2.4.2), the ADSIF strategy and the mixed approach, based on the combination of the ADSIF and DSIF techniques, were applied. To face the challenge of the limited formability of Ti6Al4V at room temperature, all the processes were electrically-assisted, thus exploiting the increase of temperature by the Joule effect and the related enhancement of the material ductility demonstrated in Chapter 3.

In addition, the investigation of the fracture phenomenon in the DSIF process aims at providing a deeper understanding of the relations between the process mechanics and the fracture occurrence.

All the activities were performed in collaboration with the Northwestern University, where I spent three months as a visiting PhD student.

6.1 Manufacturing of the Ti6Al4V acetabular cup

As described in Chapter 2, the Electrically-assisted Incremental Sheet Forming (E-ISF) process can be used to exploit the increase of the material ductility at elevated temperatures, but it results in low geometric accuracy. Moreover, with the application of the DSIF forming strategy, the loss of contact that may occur between the sheet and the tools, which act as electrodes, can cause the occurrence of sparks.

Therefore, to overcome the issue of the limited geometric accuracy inherent to the E-ISF process and the spark phenomenon in E-DSIF, two spark-free approaches were proposed based on the ADSIF technology and the tool-gap compensation

algorithm developed to avoid the loss of contact in DSIF. Note that in ADSIF, the tools, deforming the virgin material, are always in contact with the sheet, thus eliminating the spark problem. Specifically, the two proposed methods are the Electrically-assisted Accumulative Double-Sided Incremental Forming (E-ADSIF) and the Electrically-assisted Mixed Double-Sided Incremental Forming (E-MDSIF), respectively.

6.1.1 Material & methods

The material used in the following tests was extracted from a 0.5 mm thick Ti6Al4V sheet in annealed conditions. Its microstructure in the as-received condition consists of equiaxed $\alpha + \beta$ [183], as shown in Figure 6-1a.

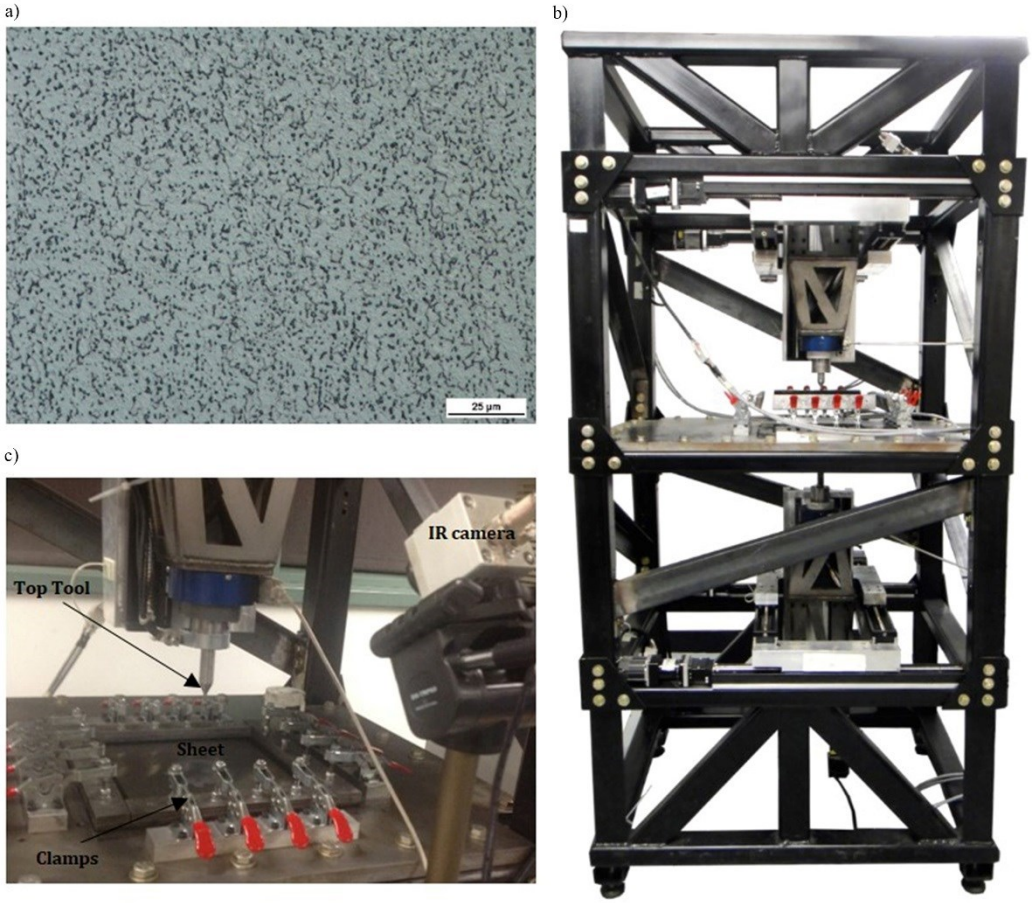

Figure 6-1. a) Microstructure of 0.5 mm thick Ti6Al4V sheet in the as-received condition. b) DSIF machine at Northwestern University and c) details of the DSIF clamping system and the experimental set-up.

The experimental tests were performed on the custom-built DSIF machine housed at Northwestern University (Figure 6-1b). The Ti6Al4V sheets (320 mm x 320 mm) were isolated at the edges with temperature-resistant insulator tape (-18°C to 105°C), and then clamped by using a proper clamping system as shown in Figure

6-1c. Two hemispherical tools made of tool steel (60 HRC) with diameter of 5 mm were used as "Top tool" (Figure 6-1c) and "Bottom tool" (not shown in the figure, blocked by the sheet metal). The D and S parameters, which define the position of the bottom tool with respect to the top tool during the forming process [133], were set at 2.5 and 0.43 mm, respectively, as seen in Figure 6-2. The tools moved along spiral toolpaths with a constant incremental depth of 0.1 mm. The tool speed was set as 10 mm/s. The forming forces were recorded by two multi-axis load cells.

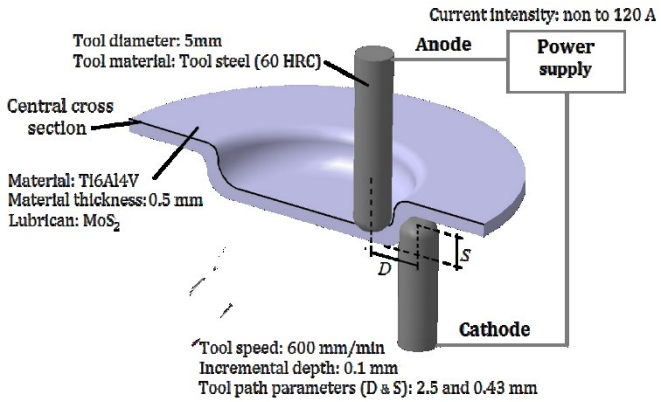

Figure 6-2. Sketch of the experimental set-up used for E-ISF process and working parameters.

To electrically assist the forming process, a continuous current power supplier (Dynatronix, model LFP12-300) was integrated to the experimental set-up, as depicted in Figure 6-2, creating a closed circuit. In all the experiments, the electricity was applied after the contacts between the sheet and the forming tools were made initially in order to avoid electric arcs that could damage both the sample and the tools. Polymeric matrixes were utilized to isolate the tools from the DSIF machine.

To analyse how the electricity affects the material formability and geometric accuracy, the experiments were first carried out without electricity at room temperature ("Base line"), and then with different current intensities, spanning from 40 A to 120 A in the E-ADSIF cases. The E-MDSIF process was performed using the best current value obtained from the E-ADSIF cases. The results from E-ADSIF and E-MDSIF using the same current value were then compared in terms of geometric accuracy and post-deformation material properties. To reduce the friction during the forming phase, MoS_2 powder was used as lubricant at the tool-sheet interfaces, avoiding the occurrence of sparks [179].

Following the approach used in [176], the surface temperature was measured using an infrared (IR) thermo-camera (Micro-Epsilon, model TIM160 Imager), placed as depicted in Figure 6-1c, with a temperature range from -20°C to 900°C. The Ti6Al4V emissivity in the testing conditions was set at 0.75 after a calibration process, which consisted in the comparison between the temperature values recorded by the IR camera and the ones resulted from a thermocouple placed on the sheet.

The part geometry to be tested in this work is a part with a total depth of 20 mm and a double curvature with wall angles of 20° and 50°, respectively, as shown in Figure 6-3. The double-curvature shape is characteristic of the acetabular cups used in the hip replacement and described in the Introduction.

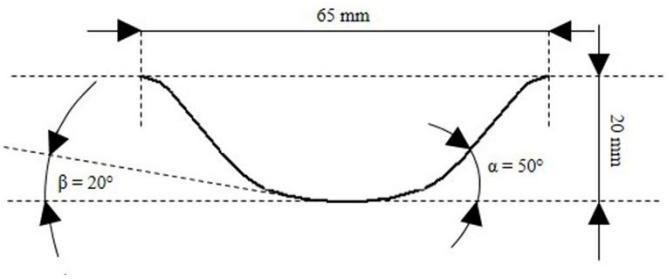

Figure 6-3. CAD drawing of the part examined (desired geometry).

The geometric accuracy was evaluated by comparing the resulting geometries of the formed parts, measured with a non-contact 3D laser scanner (Minolta, model VIVID 900), with respect to the desired one. After being scanned, the formed parts were cut at the central cross section (Figure 6-2) to allow more characterization work, namely the surface roughness, the microstructures and the micro-hardness. The average surface roughness of the as-received material and the formed parts (both internal and external surfaces), R_a, was measured with an optical surface profiler (Alicona, InfiniteFocus). The micro-hardness tests were performed on a micro-durometer (Struers, model Duramin 5) and the reported results are the average values acquired along the thickness and far enough from the edges of the samples. The microstructures of the specimens revealed using the Kroll's reagent were analysed along the thickness with an optical microscope (Nikon, model Optiphot-10). They were evaluated to examine any effect on the microstructural features that could be associated to the applied electric configurations.

6.1.2 Results

6.1.2.1 Geometric accuracy

The geometries of the formed parts are compared with the desired one in Figure 6-4, while Table 6-1 reports the values of the parameters used to characterize the geometric accuracy. It was evaluated considering the resulting two wall angles, the achieved depth and the fracture occurrence.

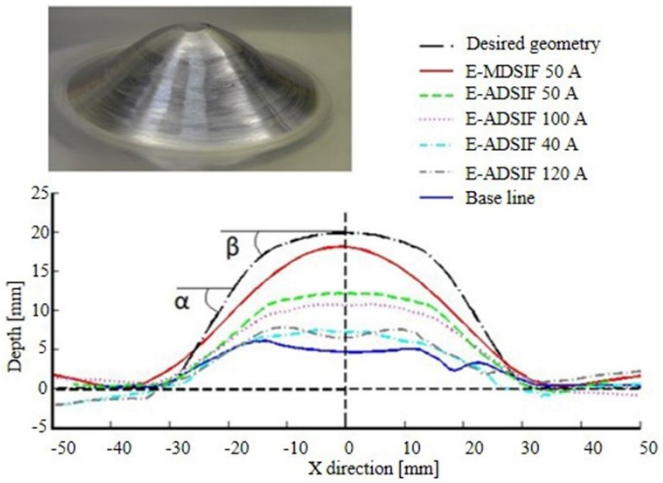

Figure 6-4. Formed part geometry for each configuration.

Table 6-1. Geometric accuracy for each configuration.

Part	*I* [A]	Depth [mm]	α [º]	β [º]	Fracture
Desired	-	20	50	20	-
Base line	-	4.58	20.45	-	Yes
E-ADSIF	40	7.20	24.44	3.27	Yes
	50	12.02	35.88	10.84	No
	60	7.88	19.13	2.73	No
	100	10.58	29,48	8.33	No
	120	6.48	24.72	-	Yes
E-MDSIF	50	18.02	36.80	11.9	No

First, among all the E-ADSIF cases, the forming heights were increased from the base line case (0 A), to 40 A and then 50 A cases, but decreased in the 100 A and 120 A cases. The progressive wear of the tools, linked to the rise of temperature

resulting from the increase of the current intensity, develops a negative effect on the material. Figure 6-4 shows that the best geometrical approximation compared to the desired shape was achieved when a current intensity of 50 A was applied.

According to Figure 6-4 and Table 6-1, the E-MDSIF outperforms all the E-ADSIF cases significantly, reaching the highest values of total depth and wall angles. This could be attributed to the fact that the material is first moved from the inner to the outer circumference in E-ADSIF and then redistributed during E-DSIF.

6.1.2.2 Forming forces and temperatures

The forming forces of the top and bottom tools along the x, y and z directions, named F_x, F_y and F_z, respectively, were elaborated to calculate an average total forming force for each tool by using the following equation:

$$F_T = \frac{1}{T}\int_0^T \sqrt{{F_x}^2 + {F_y}^2 + {F_z}^2} \cdot dt\,, \tag{6-1}$$

where F_T is the average total forming force and T is the period of time of the forming process.

To estimate how the temperature, generated by the Joule effect, influences the forming forces, a normalized forming force, F_N, is calculated by dividing the average forming forces, F_T, of the E-ADSIF with the ones acquired during the "base line" experiment. The values of F_N for both the bottom and the top tool are reported in Figure 6-5. These results indicate that the E-ADSIF decreases the forming forces needed. This force reduction is attributed to the increase of the forming temperature, which results from the application of electricity. The effect of temperature on flow stress reduction of Ti6Al4V in a wide range of temperatures was reported in Chapter 3. The maximum decrease of forming forces was calculated when a current intensity of 100 A was applied and was found equal to 14.5%, while the minimum, namely 3%, was observed at 40 A. Nevertheless, a decrease of about 8% was found when the process was assisted with 120 A. Therefore, it seems that above 100 A, the temperature becomes a drawback for further reduction of forming forces. This could be explained by the significant wear of the tools observed due to the resulting high temperature when higher current intensities were applied (insert in Figure 6-5). Material oxidation at that temperature value can also be a factor in the increase of forming force.

The measured temperatures reported in Figure 6-5 refer to the surroundings of the tool-sheet contact area, as the localized heating zone was blocked by the tools

in the view of the IR camera. Therefore, to estimate the temperature right under the sheet-tool contact area, an approach similar to the one used in [195] was applied. This instantaneous temperature was roughly estimated assuming an adiabatic condition and the cross section of the contact area circular with a radius of 0.25 mm, as resulted from experimental observations. Therefore, the instantaneous rise of temperature by the Joule effect at the sheet-tool contact is estimated to be:

$$\Delta T = (c \cdot \rho)^{-1} \cdot \gamma \cdot (\frac{I}{\pi \cdot r^2})^2 \cdot t\,, \tag{6-2}$$

where I is the current intensity, r the radius of the cross sectional area, t the time (0.05 s, estimated from the applied tool speed), γ ($1.78 \cdot 10^{-6}$ Ω m), c (526 J/(kg·°C)) and ρ ($4.43 \cdot 10^3$ kg/m^3) are the electrical resistivity, specific heat and density, respectively. The temperatures estimated at the tool-sheet contact area through Eq. (6-2) result to be much higher than the measured value of the surroundings. Note that heat loss was not considered in the estimated temperature, but according to [175] the heat is quickly dissipated in the sheet due to irradiation, heat conductivity and its dispersion into surrounding. However, the sheet temperature was always lower than the alloy β-transus one as it is demonstrated in the following section.

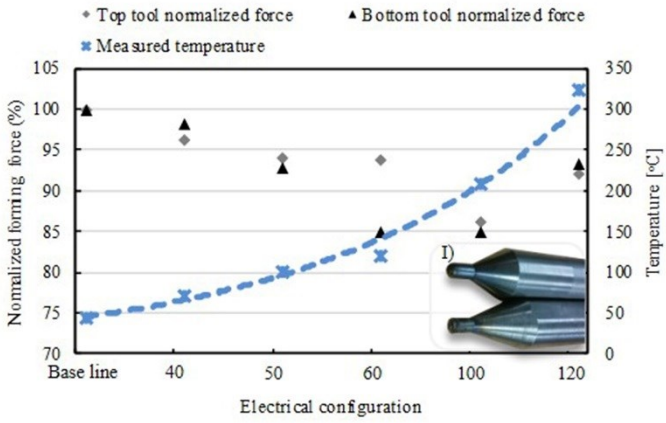

Figure 6-5. Top and bottom tool normalized forces and associated measured temperatures. I) Detail of the wear of the tools at 120 A.

6.1.2.3 Post-deformation analyses

The results of the surface analysis, microstructural observations and micro-hardness measurements are shown in Figure 6-6, Figure 6-7 and Figure 6-8 as a function of the current intensity and forming strategy. The average values of the

surface roughness (R_a) and micro-hardness, along with their standard deviations, are calculated from at least 15 measurements along the specimen.

Figure 6-6 shows that even the sole ADSIF process ("Base line") allows increasing the surface roughness compared to one of the as-received sheet, but the application of the electricity makes this effect more significant, especially in case of the internal surface. Indeed, a higher current intensity triggers the oxidization process on both internal and external surfaces, but the higher forming pressure applied by the top tool increases the mechanical effect on the internal surface, i.e., removing the oxide layer, and at the same time increasing the average roughness [196]. Concerning the effect of various forming strategies, the E-MDSIF, namely E-ADSIF followed by E-DSIF in the second step, resulted in the highest values of the surface roughness, thus making the E-MDSIF strategy suitable for the production of biomedical applications.

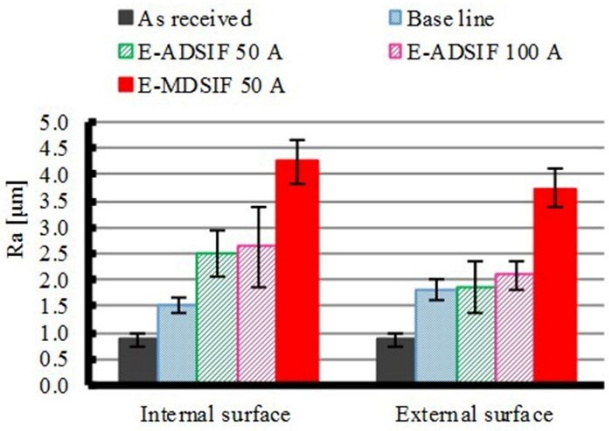

Figure 6-6. Surface roughness, R_a, as a function of the different manufacturing configurations.

The micrographs reported in Figure 6-7 show the same equiaxed α + β microstructure of the as-received sheet [183], proving that, for current intensities lower than 100 A, the forming temperature did not exceed the β-transus temperature (approx. 995°C [12], [28]). The "Base line" specimen shows several cracks along the profile of the internal surface orientated from the top to the bottom (Figure 6-7-I). These cracks were found in the middle part of the specimen, where the wall angle is 50°. In this particular region, the material, hardened by the previous plastic deformation, experiences a stretching mechanism. This stretch along with the reduction of the sheet thickness could be one of the reasons for the onset of these cracks. On the contrary, no cracks were found in the electrically-formed specimens

because the thermal contribution affects the material by releasing its internal stresses, similar to an annealing process (Figure 6-7-II).

The annealing effect also explains why the micro-hardness drops at the case of 100 A after the initial increases from the as-received, to "Base line", and to E-ADSIF 50A (Figure 6-8). Note that the initial increase, was due to the repeated bending and unbending [171] at the local area. Interestingly, comparing the E-ADSIF to E-MDSIF, both performed at 50 A, there exists a slightly positive increase of micro-hardness due to the two forming steps used in the MDSIF strategy.

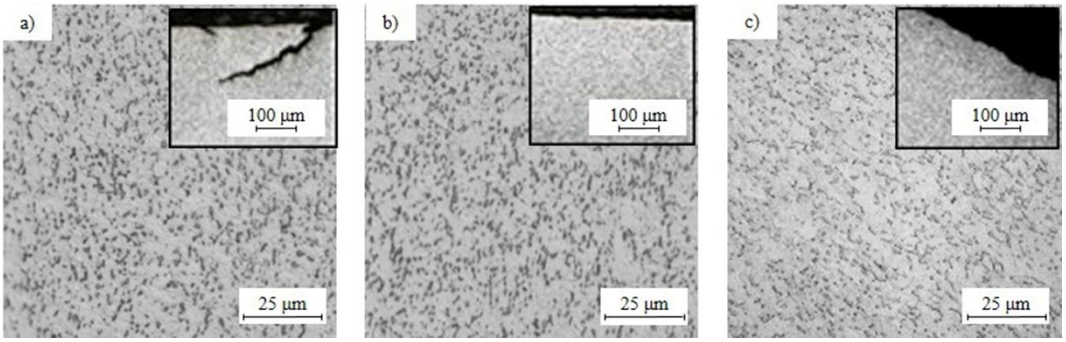

Figure 6-7. Microstructure for a) base line, b) E-ADSIF 100 A, c) E-MDSIF 50 A samples.

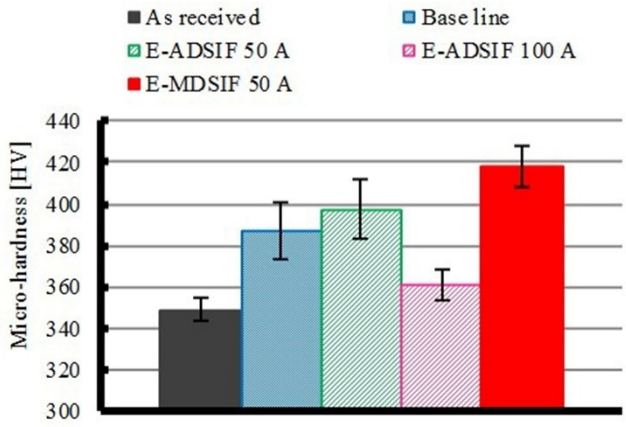

Figure 6-8. Material micro-hardness as a function of forming process and current intensity.

6.1.3 Highlights

Based on the previous results the following points can be highlighted:

- The forming forces were reduced when the ADSIF process was electrically assisted: higher current intensities decreased the forming forces, though at 120 A non-desired thermal effects were observed.
- E-MDSIF greatly enhanced the geometric accuracy compared to the ADSIF process performed with and without electricity.

- The thermal softening from the Joule effect prevented surface defects from crack propagation that could bring an early fracture or future fatigue failure.
- The E-MDSIF process did not affect the material microstructure and it proved to increase the material micro-hardness, as well as the surface roughness, which is related to the osseointegration of the implant.

6.2 Post-process surface treatments

Based on the results reported in Chapter 5, treatment D was found to assure the best balance between high roughness, good bioactivity and ductility. However, considering the twofold aspect of the industrial case, the effect of the surface treatment on the final component, and especially on its final shape, has to be evaluated.

With this aim, the part produced through E-MDSIF process was subjected to the acid etching and thermal treatment of the surface treatment D (refer to Table 5-1), and then analysed in terms of surface properties and geometric accuracy.

The surface topography was investigated by means of the Sensofar 3D optical profiler (Figure 5-1a), while the final shape was examined through Computed Tomography (CT) metrology, which is a non-destructive technology able to measure as well the inner as the outer geometry of a complex component, performing dimensional (size, thickness, deviation from the nominal geometry) and material quality control (defects and porosity) simultaneously [197], [198].

To evaluate how the surface treatment affects the final shape of the part and its surface roughness, the CT and surface analyses were first performed on the part produced through E-MDSIF process ("Pre-treatment"), and then on the parts obtained after the acid etching ("Post-etching") and thermal treatment ("Post-thermal") related to the surface treatment D of Table 5-1.

The surface characteristics of the "Pre-treatment" part are the ones reported in Figure 6-6 for the E-MDSIF case, while its shape, resulted from the CT scan, is reported in Figure 6-9a. The red zone observed in the 3D map of the thickness distribution (Figure 6-9b) identifies the area of the part characterized by the minimum thickness. This is the proof of the thinning occurring during the incremental forming process in the radial (i.e. parallel to thickness) direction, which, according to literature, is the result of the tensile stresses operative in the

meridional direction [168]. As it can be seen more in details in Figure 6-10, the thickness (t) in this red area ranges from 0.32 to 0.343. To note that the final thickness predicted by the sine law[4], considering a wall angle of 50° (Figure 6-3) and an initial thickness of 0.5 mm, is equal to 0.321, which is in the range resulted from the CT analysis.

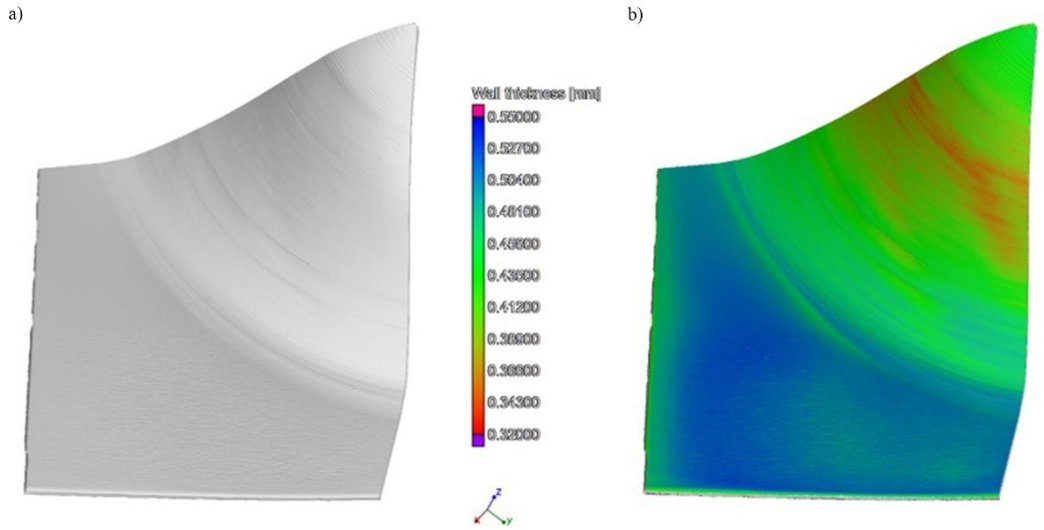

Figure 6-9. Results of the CT scan of the "Pre-treatment" part: a) 3D volume part; b) 3D map of the thickness distribution.

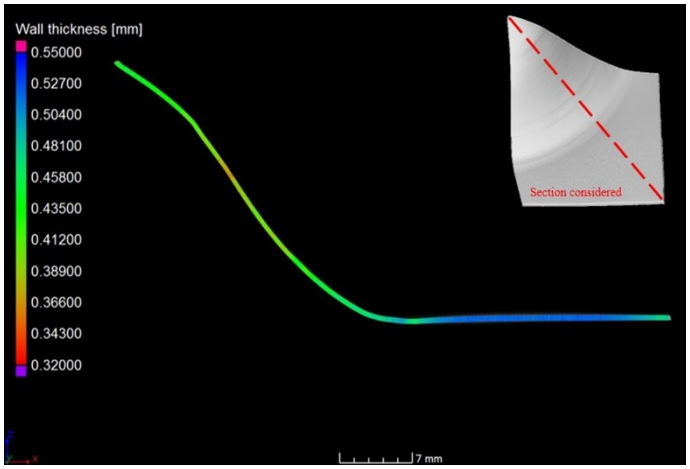

Figure 6-10. 2D thickness distribution for the "Pre-treatment" part, highlighting the section considered for the analysis in the volume part.

A comparison between the 3D thickness maps related to the "Pre-treatment" and "Post-etching" parts, reported in Figure 6-9b and Figure 6-11a respectively, shows that the red area characterized by the minimum thickness in the "Post-etching" part is larger than the one observed in the "Pre-treatment" specimen.

This qualitative result is supported by the calculation performed by the CT software, which counts the total area of the part characterized by each value of

thickness. Indeed, as it can be observed in Figure 6-12, the shift towards left of the peak related to the thickness of 0.5 mm observed for the "Post-etching" curve demonstrates that this part is characterized by lower values of thickness compared to the "Pre-treatment" part. Therefore, based on these results, the thinning due to the manufacturing process is worsened by the strong erosive effect of both the acids used in the etching solution, namely H_2SO_4 and HCl.

On the other end, the overlap of the curves related to the "Post-etching" and "Post-thermal" specimens in Figure 6-12 reveals that the thermal treatment does not have significant effects on the thickness distribution.

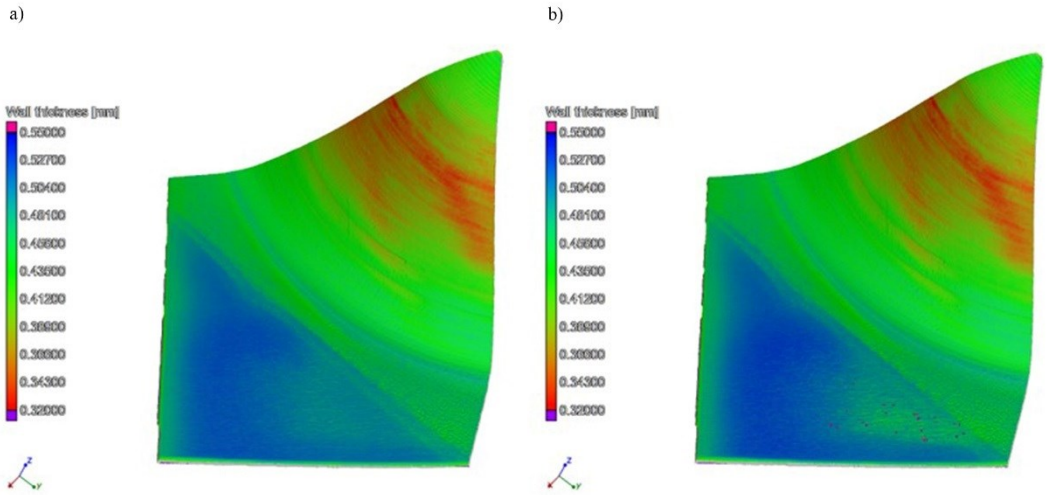

Figure 6-11. 3D maps of thickness distribution after the a) acid etching ("Post-etching") and b) thermal treatment ("Post-thermal") related to the surface treatment D of Table 5-1.

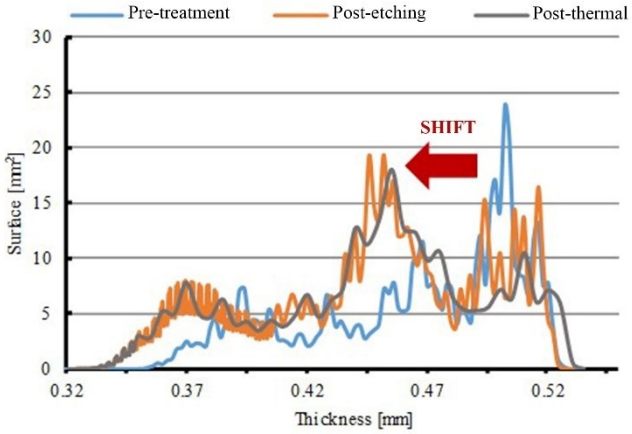

Figure 6-12. Total surface of the part counted for each value of thickness, considering the three cases. The shift represents the thinning due the acid etching.

The erosive effect of the acid solution influences also the surface topography, by decreasing the surface roughness of the "Post-etching" part compared to the base line resulted from the manufacturing process ("Pre-treatment"), as it can be

observed in Figure 6-13. To note that the value of R_a resulting for the "Post-etching" part is similar to the one resulted from the application of the etching treatment on the as-received sheet (Treatment D-"Before-TT" in Figure 5-2, § 5.2.1). However, as it was found in the analysis of the surface treatments effects in § 5.2.1, the thermal treatment assures an increase of the surface roughness (Figure 6-13), reaching values similar to the ones obtained from the manufacturing process, both in the internal and external surfaces.

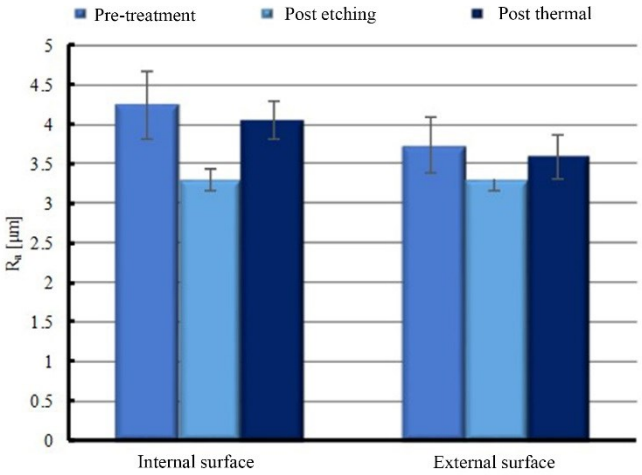

Figure 6-13. Surface roughness, R_a, after the manufacturing process ("Pre-treatment"), the acid etching ("Post-etching") and the thermal treatment ("Post-thermal").

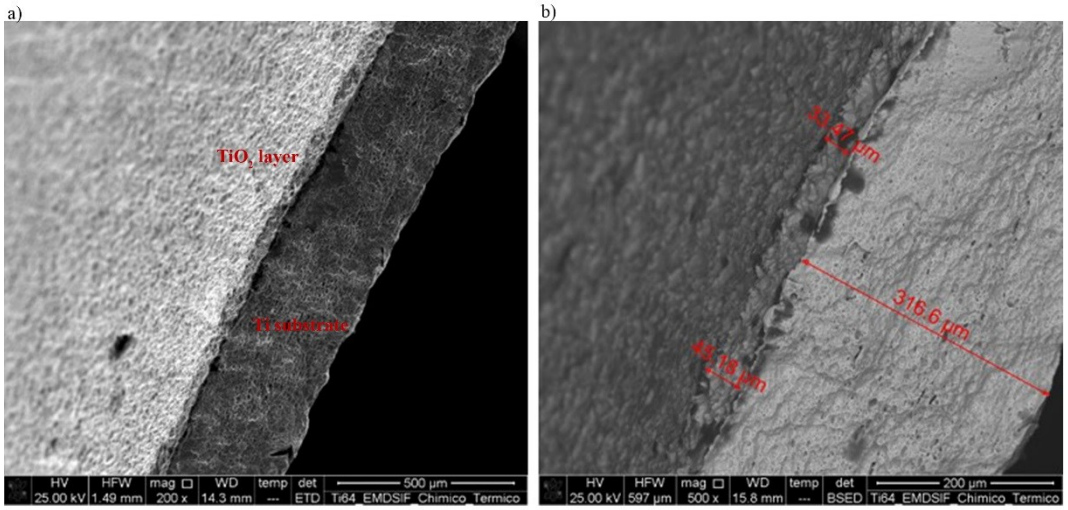

Figure 6-14. a) SEM and b) BSED images of the "Post-thermal" part, showing the TiO_2 layer on Ti6Al4V substrate with the related measured thicknesses.

The formation of the titanium dioxide layer after the thermal treatment can be clearly observed in Figure 6-14a and Figure 6-14b, which resulted from the SEM and BSED (Back Scattered Electron Detector) observations of the "Post-thermal" part, respectively. Based on the value of the thickness measured for the TiO_2 layer

in Figure 6-14b, it is worth to note that the thermal treatment allows the oxide layer to grow from the usual 5-10 μm of atmospheric oxidation [101] up to 40 μm. On the other hand, the minimum value of thickness measured for the substrate in the BSED image of the "Post-thermal" part can be considered in agreement with the results obtained from the CT analysis.

To investigate the final wettability of the component, six drop tests were performed on the flat area of the "Post-thermal" part [199], as it is highlighted in Figure 6-15.

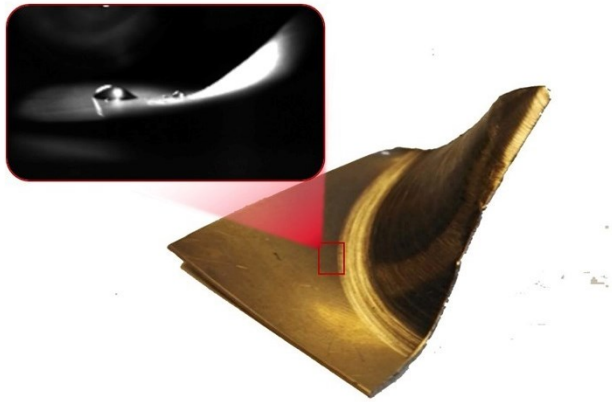

Figure 6-15. "Post-thermal" part and detail of the water droplet to investigate the contact angle of the treated surface.

Table 6-2. Measured values of the right and left contact angles.

Test	Right contact angle [°]	Left contact angle [°]
1	75.67	82.61
2	62.03	73.68
3	63.30	53.48
4	76.62	63.35
5	63.11	63.35
6	74.37	59.43
Average	**69.18**	**65.98**
Standard deviation	**7.03**	**10.47**

From the resulting water droplets, the correspondent right and left contact angles were measured. Based on these values, reported in Table 6-2, the average contact angle resulted to be 67.58° with a standard deviation of 8.67°, thus proving the hydrophilic nature of the titanium dioxide layer. Therefore, the thermal

treatment, assuring a good wettability of the surface, increases the capability of the part to interact with the body fluids in the biological environment.

However, beside the advantageous increase of wettability thanks to the TiO_2 layer, the thermal treatment shows a critical drawback, namely the distortion of the shape, as it is highlighted from the results of the CT scans illustrated in Figure 6-16. Indeed, while Figure 6-16a reveals a neglecting effect of the acid etching on the final shape, being the "Pre-treatment" and "Post-etching" parts overlapped, Figure 6-16b, comparing the "Post-etching" with the "Post-thermal" parts, shows a distortion in the upper part of the cup due to the thermal treatment.

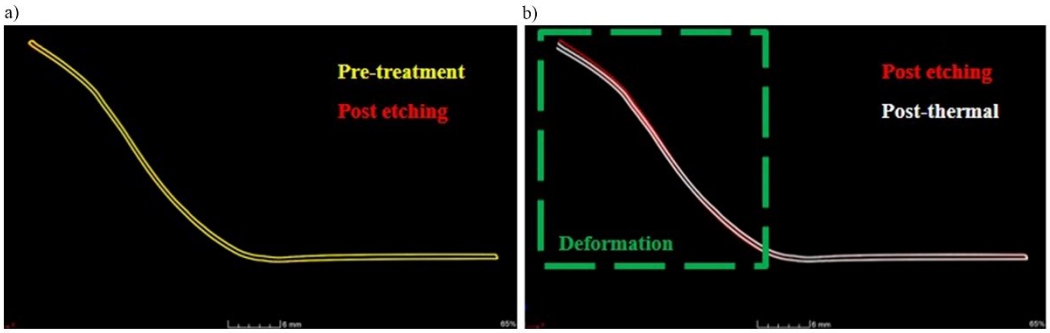

Figure 6-16. CT scan results for the shape analysis: a) comparison between the "Pre-treatment" and "Post-etching" parts; b) comparison between the "Post-etching" and "Post-thermal" parts.

In conclusion, these analyses confirm the positive effect of the surface treatment D on the bioactivity of the part, assuring a good wettability through the TiO_2 layer and an increase of the surface roughness, even though the acid etching slightly reduces the surface roughness determined from the scraping effect of the two tools during the E-MDSIF forming process. However, the thermal treatment that allows creating the TiO_2 layer results in the deformation of the part final shape, which therefore turns out to be the main drawback of this strategy.

6.3 Fracture characterization in DSIF process at elevated temperature

The incremental and localized nature of the incremental deformation process, which depends on different factors, namely the tool motion, material properties, lubrication and thermal effects, results in a complex material deformation behaviour [156], which was widely studied in case of SPIF [154], [156], [171], [200], but in a limited manner for DSIF, as reported in § 2.4.2 and highlighted in § 2.5.

Since the deformation mechanics strongly influences the material formability [154], as demonstrated in SPIF application cases where the damage accumulation

was proved to be dominated by local bending and through-the-thickness shear (§ 2.4.2) [200], the following research work, developed in collaboration with the Northwestern University, aims at providing a deeper understanding of the relations between the DSIF process mechanics and the fracture occurrence, the latter examined through fractographic observations.

With this aim, the fracture surfaces of Ti6Al4V parts, manufactured through E-DSIF, were investigated through Scanning Electron Microscopy (SEM) and then examined to evaluate their sensitivity to the applied current intensity. The fracture characteristics were also analysed in comparison with the ones resulting from tests carried out under similar process conditions but characterized by simpler stress states, namely uni-axial tensile and pure shear loading conditions. Furthermore, an accurate analysis of the stress state operative in the DSIF forming strategy was performed to identify the fracture mode controlling the fracture occurrence, pointing out its origin point.

6.3.1 Material & methods

The E-DSIF tests were performed using the same Ti6Al4V sheets and experimental set-up described in § 6.1.1, except for the two hemispherical-ended tools that, in this case, are made of tungsten carbide (WC).

For these tests, the relative position of the tools is schematically shown in Figure 6-17. In DSIF, the squeeze factor s represents the magnitude of squeezing between the tools within the local area, while the surface normal of this area is used to locate the tip of the bottom tool with respect to the top tool. In these experiments, s was set as 0.8 because it was able to ensure the contact between the bottom tool and the sheet metal. The tools travelled along a pre-defined spiral toolpath at a speed of 10 mm/s, with an incremental depth of 0.1 mm.

Based on the previous results reported in § 6.1, three values of the current intensity, namely 50 A, 87.5 A and 100 A, were applied to evaluate the effect of electricity on the fracture occurrence when forming a part characterized by a double-curvature shape, as the one represented in Figure 6-3.

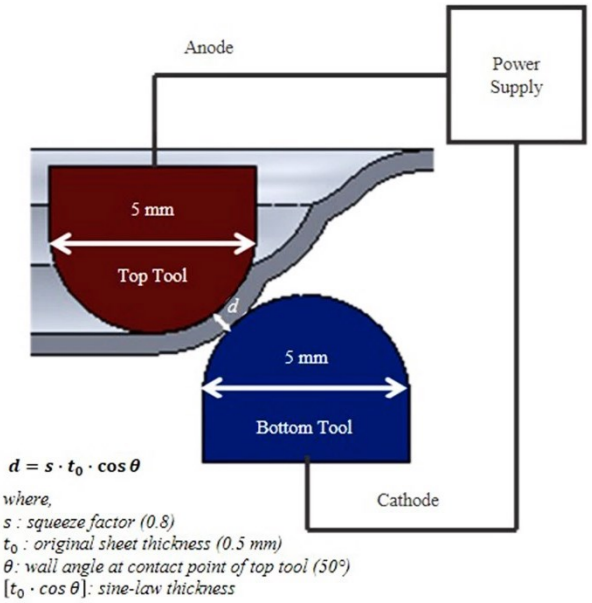

Figure 6-17. Relative position of the tool in the schematic configuration of the experimental set-up.

The forming process stopped at the moment when fracture occurred. The formed parts were taken out of the clamps and their geometries were digitized using a Romer Absolute Arm with an integrated laser scanner. The deepest position, namely the total depth of each formed part was recorded and compared to evaluate the material formability under different current density.

To investigate the effect of the stress mechanics on the material failure behaviour, the uni-axial tensile and pure shear tests, characterized by simpler stress states compared to DSIF forming strategy, were performed straining the samples until fracture. The tensile and shear tests were carried out using the same experimental set-up and applying the same procedures described in § 3.1.3 and § 4.2.2.2, respectively. A summary of all the experiments, with the details of the process parameters, is reported in Table 6-3.

Table 6-3. Summary of the experiments and process parameters.

Test	**I**			**Temperature**			**Strain rate**	**Strain**
	[A]			**[°C]**			**[s^{-1}]**	**[-]**
E-DSIF	50	87.5	100	-	-	-	-	Fracture
Tensile	-	-	-	200	600	800	0.1	Fracture
Shear	-	-	-	200	600	800	0.1	Fracture

To carry out the fractographic analysis, the fracture surfaces of all the samples were observed using the SEM microscopy. During these analyses, the samples were placed in order to have the fracture area perpendicular to the SEM electron beam.

To compare the fracture surfaces resulted from the E-DSIF experiments with the ones of the tensile and pure shear tests, the E-DSIF amperage had to be linked with the testing temperature achieved in the other tests. To address this issue, a qualitative comparison between the sheet colours was applied, identifying the chromatic analogies between the samples deformed in the E-DSIF and tensile experiments, as represented in the example of Figure 6-18. The amperage equal to 50 A was related to 200°C since none of the samples present any colour difference compared to the as-received condition (Figure 6-18); on the other hand, the amperage equal to 87.5 A, where a brown colour with some few light blue hints was found on the sheet because of the higher temperature, was linked to 600°C. Finally, the highest amperage of 100 A was associated with the highest temperature, as, in both cases, the sheet was brown with a wide blue area.

Figure 6-18. Qualitative chromatic comparison between the samples obtained from the tensile and E-DSIF tests performed at 200°C and 50 A, respectively. The red box represents the area heated by the induction system during the tensile tests.

6.3.2 Characterization of the E-DSIF fractures

Figure 6-19 shows an overview of the fracture surfaces of the E-DSIF samples, deformed at different current intensities.

The first row of Figure 6-19 shows the fracture surface of the sample deformed by applying the lowest current intensity, namely 50 A, which is characterized by the shortest forming depth, as it can be observed in Table 6-4, where the values of the total depths were calculated out from the results of the laser scans reported in Figure 6-20. In the zoom of the red boxes, two different areas can be identified based on

their characteristics: one half of the fracture surface, related to the inner surface of the sheet, shows dimples similar to the ones of the ductile fracture under tensile stresses [187], while the other half, relevant to the outer surface (the surface in contact with the bottom tool), presents small, partially formed dimples typical of the shear conditions [187]. At the inner side of the part, the top tool pushes the material downward making the tensile stress predominant, while, at the outer side, the circumferential movement of the bottom tool and the related shear effect generate the shear-type surface fracture.

Moving to the sample deformed by applying the medium amperage value, namely 87.5 A, which allows increasing the part achievable forming depth compared to the previous test (Table 6-4, Figure 6-20), the analysis of the fracture surface evidences three areas, named A, B and C as reported in Figure 6-19 (87.5 A), because different characteristics along the sample were identified. Indeed, as it can be seen in the second row of Figure 6-19, Area A has an aspect typical of the shear ductile fracture [187], where the partially formed dimples point towards the outer surface, Area B shows dimples similar to the ones of the ductile fracture under tensile stresses, while Area C shows a faceted surface, typical of brittle fracture. Considering that the ductile-type and brittle fracture surfaces are placed one after the other in the circumferential direction, it can be stated that the fracture starts as ductile, and then propagates along the toolpath in the horizontal direction until the laceration of the sample, provoking a brittle fracture. This is in agreement with [156], where, in SPIF experiments, the fracture is first stretched due the meridional tensile stresses, which are operative also in DSIF strategy [168] because of the downward tools movement, and then expanded in the horizontal direction of the toolpath. It is worth to underline that the sample deformed by applying 50 A does not present any brittle fracture, as the total forming depth was so low, namely the fracture occurred so early to prevent any laceration of the sample.

Similar characteristics of shear conditions, in terms of small, partially formed dimples orientated towards the outer surface, were found also in the E-DSIF 100 A sample, as it is highlighted in the third row of Figure 6-19. This analogy in the fracture surface features is associated to the fact that, compared to the E-DSIF test carried out at 50 A, the increase of the total forming depth recorded for the test at 100 A (Table 6-4, Figure 6-20) is similar to the one resulted for the E-DSIF 87.5 A sample.

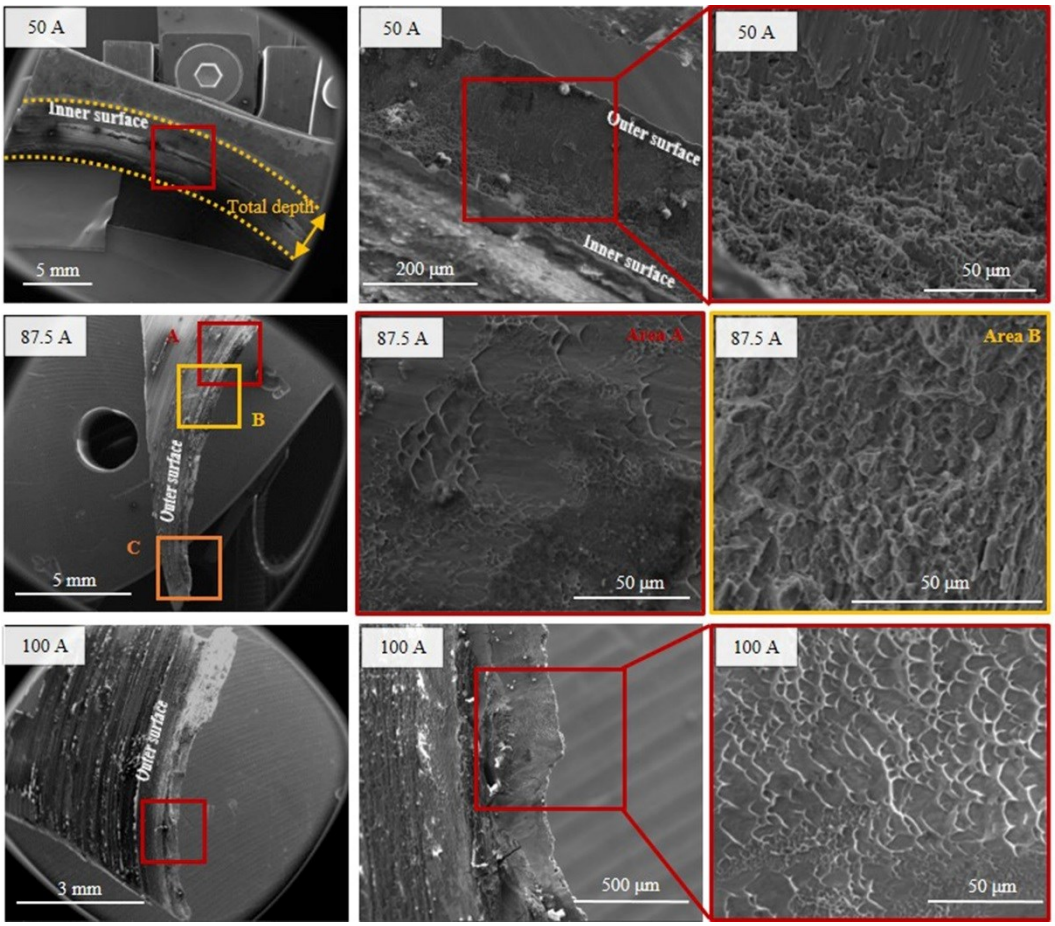

Figure 6-19. SEM images of the E-DSIF samples at 50 A, 87.5 A and 100 A, specifying the inner and outer surfaces of the sheet, and some details of the fracture surfaces.

Table 6-4. Total depths obtained from laser scans.

E-DSIF	Total depth [mm]
E-DSIF 50 A	1.8
E-DSIF 87.5 A	7.9
E-DSIF 100 A	8.4

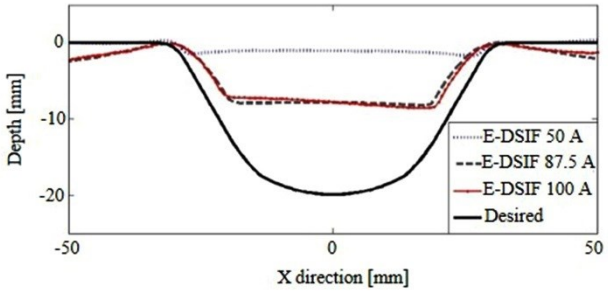

Figure 6-20. Results of the laser scan.

The characteristics found in the E-DSIF fracture surfaces are in agreement also with the results obtained from the tensile and shear tests, which are reported in Figure 6-21, performed under different testing conditions (see Table 6-3).

As it can be noticed, the fracture surfaces of the specimens subjected to the uni-axial tensile stress at 200°C and 600°C are characterized by essentially 100% dimpled rupture. The same result can be identified at the highest temperature based on the characteristic dimples that can be observed in the fracture wall. This is because the fracture surface in this case became a fracture line (Figure 6-21, 800°C) due to the significant necking that occurred during the test.

On the other hand, the fracture surfaces of the shear tests are characterized by dimples that, after being formed, are dragged because of the load applied during the tests. In shear conditions, no significant differences can be noted at varying testing temperature.

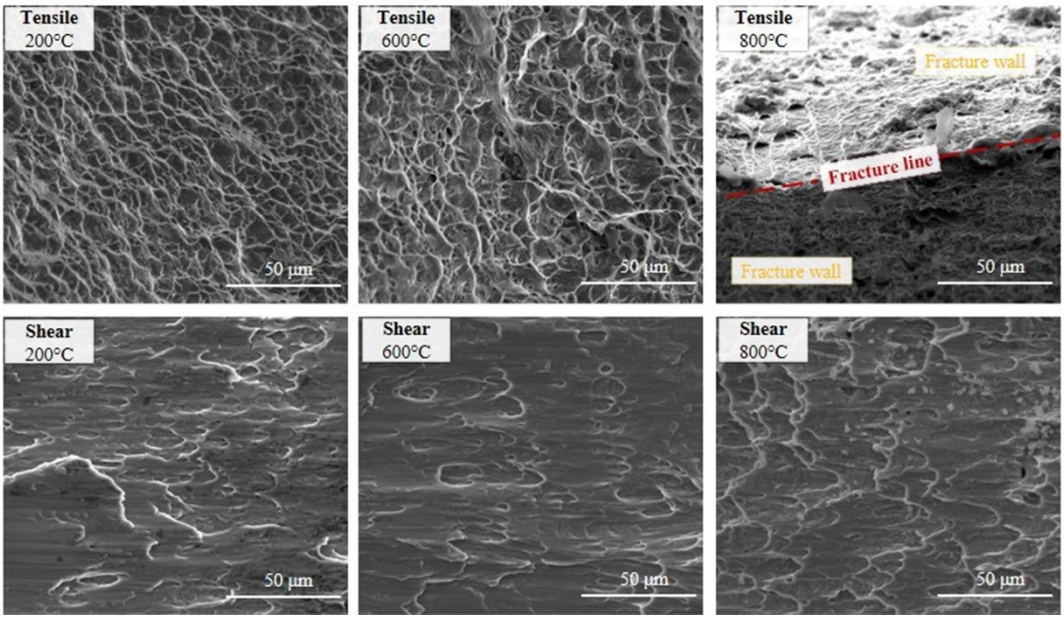

Figure 6-21. Fracture surfaces from tensile and shear tests at the testing conditions reported in Table 6-3.

6.3.3 Correlation between the E-DSIF fracture surfaces and the stress state

Based on the analytical model proposed by Lu et al. [168] for the DSIF process, the deformation area in the E-DSIF can be split into three zones, as represented in Figure 6-22a. Zone I is the portion of the sheet that first comes into contact with the top tool; Zone II is the one that squeezes between the two tools; Zone III is related to the part of the material that has been already formed by the two tools, but still in contact with only the top tool. Therefore, Zone I and Zone III are characterized by

tensile stresses in the meridional direction, since the material is in contact only with the top tool, without any squeezing effect from the bottom tool [168], while Zone II is a compressive area because of the pressure applied by the bottom tool in the radial direction.

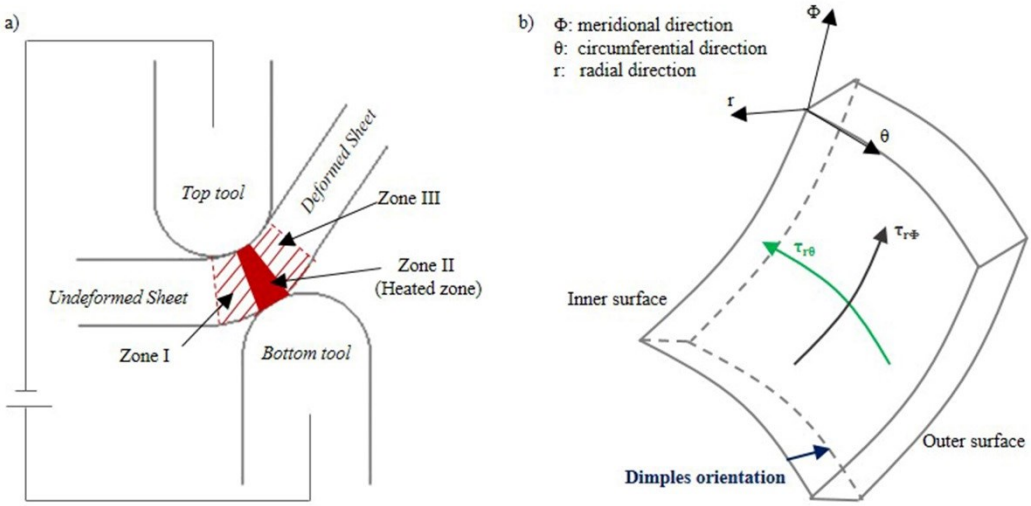

Figure 6-22. a) Deformation zones in the E-DSIF process; b) shear stress components in a small element through the thickness and detail of the dimples orientation.

According to [168], the pressure in Zone II postpones the fracture occurrence thanks to the Drop Of Stress Triaxiality[5] (DOST) phenomenon, meaning that the fracture is not likely to initiate in this compressive area. Moreover, considering that in the E-DSIF process the tools-sheet contact area (Zone II) is heated through the Joule effect, which leads to an increase of the material ductility as proved in Chapter 3, it is even less likely that the fracture starts in Zone II. On this basis, it can be assumed that the fracture starts in the area of the sheet that has been already formed (Zone III in Figure 6-22a), which is characterized by a lower temperature and a reduced resistant section resulted from the thinning in the radial direction. This is related to the negative strain in the radial direction that, considering the volume conservation, resulted from the fact that convex shapes, such as the desired geometry in this study, lead to positive strain loading paths in the major (ε_1) versus minor (ε_2) true strains space, as reported in [201]. Based on the stress state analysis, the thinning is caused by the tensile stress operated in the meridional direction.

[5] It means that the critical value of the integration of stress triaxiality along the equivalent strain in DSIF is reached at a higher value of strain compared to the one in SPIF (§ 2.4.2) [168].

Zone III, which is in contact with only the top tool as in SPIF [154], beside the tensile stresses, is subjected also to bending around the tool, causing the material at the outer surface to stretch more compared to the material at the inner surface, thus resulting in a higher plastic strain on the outer surface. In the same zone, the friction at the tool-sheet contact along the meridional and circumferential directions results in $\tau_{r\Phi}$ and $\tau_{r\theta}$ tangential stresses, respectively, as represented in Figure 6-22b, the latter being more significant because the tool moves mainly in the circumferential direction [168]. Moreover, considering the E-DSIF process, the friction is amplified with the increase of the current amperages, since the oxide layer triggered by the electrical heating hinders the movement of the top tool, leading to an increase of the $\tau_{r\theta}$. Because this through-the-thickness shear was recognized as the mechanism that allows increasing the forming limits in incremental forming operations [154], [155], its effect on the inner surface leads to a lower ductility on the outer surface of the sheet, thus raising the damage accumulation on this side.

Therefore, since both the local bending and through-the-thickness shear intensifies the damage on the outer surface, it can be concluded that the fracture starts from this side, as it was found for SPIF [154].

Summarizing all the aforementioned aspects, it can be stated that the fracture in E-DSIF occurs by progressive thinning of the sheet under tension, starting from the outer surface. Consequently, considering the conventional classification of the fracture modes [187], the fracture in E-DSIF can be classified as Mode I, or tearing. To note that tearing is considered as the conventional fracture mode also in SPIF [201], [202].

A further proof of the fracture by tearing in E-DSIF is given by the orientation of the dimples, which was identified in § 6.3.2. Indeed, as the dimples in the tearing fracture surfaces point towards the origin of fracture [187], the dimples in the E-DSIF fracture surfaces are orientated towards the outer side (Figure 6-19), which was demonstrated to be the starting point of fracture because of its higher damage.

6.3.4 Highlights

Based on the previous results, the following highlights can be pointed out.

- Small, partially formed dimples characteristics of the shear stress state were observed in all the fracture surfaces of the E-DSIF parts. Moreover, the dimples were found to point towards the outer surfaces at the higher

current intensities, where similar fracture surfaces and comparable total forming depth were observed.

- The presence of ductile and brittle fracture surfaces along the sample in the horizontal direction suggested that the fracture started as a ductile crack and then propagated in the same direction until the laceration of the sample.
- The analysis revealed that the fracture was not likely to occur in the compressive area of the sheet between the two tools, because the pressure applied by the bottom tool was demonstrated to postpone it. Moreover, the contact area between the two tools was heated through the Joule effect, thus increasing the material ductility.
- The fracture in E-DSIF was supposed to occur by progressive thinning of the sheet under tension in the part of the sheet already formed and in contact with only the top tool, starting from the outer surface. Indeed, in this zone, the damage accumulation is higher on the outer surface, because of the cumulative effect of local bending and through-the-thickness shear.
- The fracture in E-DSIF was classified as Mode I, or tearing. As the dimples in the tearing fracture surfaces pointed towards the origin of fracture, the dimples in the E-DSIF fracture surfaces orientated towards the outer side, as shown by the SEM analysis, further proved the aforementioned fracture mode.

6.4 Summary

Chapter 6 gives an overview of the results related to the application of the Incremental Sheet Forming (ISF) strategies to manufacture the Ti6Al4V shell of the acetabular cup, investigating therefore the feasibility of producing these biomedical parts through non-conventional forming processes.

In addition, a deeper analysis of the process, focusing on the DSIF strategy, was performed to offer a correlation between the deformation mechanics and the fracture occurrence, providing an update of the literature related to this topic.

Based on the reported results, the main conclusions of Chapter 6 can be listed in the following.

- The Electrically-assisted Mixed Double-Sided Incremental Forming (E-MDSIF) process, which combines the ADSIF and DSIF forming strategies with the electrical current, was proved to be a possible strategy to manufacture patient-specific biomedical products using Ti6Al4V sheets. Indeed, the E-MDSIF process was shown to improve the material formability and the geometric accuracy compared to other ISF processes, but also the surface roughness, which plays a key role in the osseointegration process. However, the still great difference between the formed part and the real acetabular cup requires future investigation and optimization of the process.
- The investigation of the fracture phenomenon in Electrically-assisted Double-Sided Incremental Forming, together with the analysis of the stress states arising in the part during the process, enabled the identification of the relations between the DSIF process mechanics and the fracture occurrence. The fracture in E-DSIF was supposed to occur by progressive thinning of the sheet under tension in the part of material already formed by both the tools and still in contact with the top tool, starting from the outer surface. Therefore, the fracture in E-DSIF was classified as Mode I, or tearing.

7 Chapter
Conclusions

The main objective of this thesis was the application of sheet forming processes at elevated temperatures to produce the Ti6Al4V shell of the acetabular cup used in the hip replacement. To this aim, the research work was divided into three main topics, namely (i) Material behaviour, (ii) Material modelling and (iii) Manufacturing process.

The first one offered an overview of the Ti6Al4V behaviour, providing the relations between the mechanical and microstructural properties in a wide range of temperatures and different strain rates, which are the two main important parameters affecting the material when the forming processes are carried out at elevated temperatures. The results revealed a drastic increase of the material ductility starting from 600°C, which were related to the transformation of the α phase to the more ductile β phase. However, considering also the biomedical requirements related to the role of the surface characteristics in governing the biological phenomena and the osseointegration process at the bone-implant interface, it was demonstrated that the forming temperature does not have to exceed 700°C to preserve the material bioactivity enhanced by the applied chemical and thermal surface treatments. Furthermore, 600°C was observed to mark an inversion in the material anisotropic behaviour, which was attributed to the variation of the texture as a function of temperature, being the T-texture more pronounced below and above the aforementioned temperature. The DRX and DRV phenomena, which can occur when deforming Ti6Al4V in the $\alpha + \beta$ phase, were identified to explain the microstructural refinement and the reduction of the strain hardening observed at the highest temperatures.

Focusing on the material modelling, the Johnson-Cook (J-C) and Arrhenius-type models were calibrated to describe the Ti6Al4V flow stress behaviour under tensile conditions at elevated temperatures and moderate strain rates, thus covering the domains that were found to be missing in the literature review. The greater

accuracy resulted for the Arrhenius-type model compared to the J-C one was attributed to the coupled effect of temperature and strain rate on the flow stress expressed through the Zener-Hollomon.

Moreover, a new model based on the J-C fracture criterion was proposed to predict the Ti6Al4V ductility in a wide range of temperatures and stress states. According to the comparison between the experimental and predicted strains at fracture, the model was shown to assure good predictability in a wide range of testing conditions. To note that this model represents a novelty for predicting the ductility of Ti6Al4V sheets deformed in a wide range of temperature, since it includes not only the effect of temperature and strain rate, but also the influence of the stress state through the coupled effect of stress triaxiality and Lode parameter, which was recently recognized to play a key role in describing the material fracture behaviour.

Finally, considering the manufacturing aspect of the project, the feasibility of producing the Ti6Al4V prototype was investigated applying different variants of the incremental forming process. It was found that the combination of electric current and the most recent forming strategy, i.e. Mixed Double-Sided Incremental Forming (MDSIF) in which the part is first formed through Accumulative Double-Sided Incremental Forming (ADSIF) and then fine-tuned with Double-Sided Incremental Forming (DSIF), allows reaching the best results in terms of geometric accuracy and surface roughness, thus positively affecting both the forming and the biological issues of the industrial case. Moving to the investigation of the fracture phenomenon in incremental forming process, the correlation of the fracture surfaces in E-DSIF with the stress state operative in the forming process enabled to demonstrate that the fracture in E-DSIF can be classified as Mode I, with the starting point on the outer surface of the sheet, as similarly found in literature for the Single Point Incremental Forming (SPIF).

References

[1] A. Majorell, S. Srivatsa, and R. C. Picu, “Mechanical behavior of Ti-6Al-4V at high and moderate temperatures-Part I: Experimental results,” *Mater. Sci. Eng. A*, vol. 326, no. 2, pp. 297–305, 2002.

[2] N. Allahverdizadeh, A. Gilioli, A. Manes, and M. Giglio, “An experimental and numerical study for the damage characterization of a Ti-6AL-4V titanium alloy,” *Int. J. Mech. Sci.*, vol. 93, pp. 32–47, 2015.

[3] A. L. Jardini, M. A. Larosa, R. M. Filho, C. A. D. C. Zavaglia, L. F. Bernardes, C. S. Lambert, D. R. Calderoni, and P. Kharmandayan, “Cranial reconstruction: 3D biomodel and custom-built implant created using additive manufacturing,” *J. Cranio-Maxillofacial Surg.*, vol. 42, no. 8, pp. 1877–1884, 2014.

[4] M. Lieblich, S. Barriuso, M. Multigner, G. Gonzalez-Doncel, and J. L. Gonzalez-Carrasco, “Thermal oxidation of medical Ti6Al4V blasted with ceramic particles: Effects on the microstructure, residual stresses and mechanical properties,” *J. Mech. Behav. Biomed. Mater.*, vol. 54, pp. 173–184, 2016.

[5] M. Mitsuishi, J. Cao, P. Bártolo, D. Friedrich, A. J. Shih, K. Rajurkar, N. Sugita, and K. Harada, “Biomanufacturing,” *CIRP Ann. - Manuf. Technol.*, vol. 62, no. 2, pp. 585–606, 2013.

[6] M. Koike, K. Martinez, L. Guo, G. Chahine, R. Kovacevic, and T. Okabe, “Evaluation of titanium alloy fabricated using electron beam melting system for dental applications,” *J. Mater. Process. Technol.*, vol. 211, no. 8, pp. 1400–1408, 2011.

[7] P. Thomsen, J. Malmström, L. Emanuelsson, M. René, and A. Snis, “Electron beam-melted , free-form-fabricated titanium alloy implants : Material surface characterization and early bone response in rabbits,” *J Biomed Mater Res B Appl Biomater*, vol. 90, no. 1, pp. 35–44, 2009.

[8] A. Bordin, S. Bruschi, A. Ghiotti, and P. F. Bariani, “Analysis of tool wear in cryogenic machining of additive manufactured Ti6Al4V alloy,” *Wear*, vol. 328–329, pp. 89–99, 2015.

[9] F. K. Chen and K. H. Chiu, “Stamping formability of pure titanium sheets,” *J. Mater. Process. Technol.*, vol. 170, no. 1–2, pp. 181–186, 2005.

[10] F. Ozturk, R. E. Ece, N. Polat, A. Koksal, Z. Evis, and A. Polat, “Mechanical and microstructural evaluations of hot formed titanium sheets by electrical resistance heating process,” *Mater. Sci. Eng. A*, vol. 578, pp. 207–214, 2013.

[11] Q. Zheng, T. Shimizu, and M. Yang, “Scale effect on springback behavior of pure titanium foils in microbending at elevated temperature,” *J. Mater. Process. Technol.*, vol. 230, pp. 233–243, 2016.

[12] R. Boyer and G. Welsch, *Materials Properties Handbook : Titanium Alloys*. 1994.

[13] N. Kotkunde, H. N. Krishnamurthy, P. Puranik, A. K. Gupta, and S. K. Singh, “Microstructure study and constitutive modeling of Ti-6Al-4V alloy at elevated temperatures,” *Mater. Des.*, vol. 54, pp. 96–103, 2014.

[14] M. Nakai, M. Niinomi, J. Hieda, K. Cho, Y. Nagasawa, T. Konno, Y. Ito, Y. Itsumi, and H. Oyama, “Reduction in anisotropy of mechanical properties of coilable (α+β)-type titanium alloy thin sheet through simple heat treatment for use in next-generation aircraft applications,” *Mater. Sci. Eng. A*, vol. 594, pp. 103–110, 2014.

[15] R. Ding, Z. X. Guo, and A. Wilson, “Microstructural evolution of a Ti–6Al–4V alloy during thermomechanical processing,” *Mater. Sci. Eng. A*, vol. 327, no. 2, pp. 233–245, 2002.

[16] W. Lee, M. Lin, L. Woei-Shyan, and L. Ming-Tong, “The effects of strain rate and temperature on the compressive deformation behaviour of Ti-6Al-4V alloy,” *J. Mater. Process. Technol.*, vol. 71, no. 2, pp. 235–246, 1997.

[17] J. Luo, M. Li, W. Yu, and H. Li, “The variation of strain rate sensitivity exponent and strain hardening exponent in isothermal compression of Ti-6Al-4V alloy,” *Mater. Des.*, vol. 31, no. 2, pp. 741–748, 2010.

[18] X. Li, G. Guo, J. Xiao, N. Song, and D. Li, “Constitutive modeling and the

effects of strain-rate and temperature on the formability of Ti-6Al-4V alloy sheet," *Mater. Des.*, vol. 55, pp. 325–334, 2014.

[19] M. Vanderhasten, L. Rabet, and B. Verlinden, "Ti-6Al-4V: Deformation map and modelisation of tensile behaviour," *Mater. Des.*, vol. 29, no. 6, pp. 1090–1098, 2008.

[20] V. Velay, H. Matsumoto, V. Vidal, and A. Chiba, "Behavior modeling and microstructural evolutions of Ti–6Al–4V alloy under hot forming conditions," *Int. J. Mech. Sci.*, vol. 108–109, pp. 1–13, 2016.

[21] B. T. Tang, S. Bruschi, A. Ghiotti, and P. F. Bariani, "An improved damage evolution model to predict fracture of steel sheet at elevated temperature," *J. Mater. Process. Technol.*, vol. 228, pp. 76–87, 2015.

[22] M. Merklein, A. Maier, D. Kinnstätter, C. Jaremenko, and E. Affronti, "A New Approach to the Evaluation of Forming Limits in Sheet Metal Forming," *Key Eng. Mater.*, vol. 639, pp. 333–338, 2015.

[23] L. Y. Qian, G. Fang, P. Zeng, and Q. Wang, "Experimental and numerical investigations into the ductile fracture during the forming of flat-rolled 5083-O aluminum alloy sheet," *J. Mater. Process. Technol.*, vol. 220, pp. 264–275, 2015.

[24] B. Ma, Z. G. Liu, Z. Jiang, X. Wu, K. Diao, and M. Wan, "Prediction of forming limit in DP590 steel sheet forming: An extended fracture criterion," *Mater. Des.*, vol. 96, pp. 401–408, 2016.

[25] C. Moerke, P. Mueller, and B. Nebe, "Attempted caveolae-mediated phagocytosis of surface-fixed micro-pillars by human osteoblasts," *Biomaterials*, vol. 76, pp. 102–114, 2016.

[26] F. Lüthen, R. Lange, P. Becker, J. Rychly, U. Beck, and J. G. B. Nebe, "The influence of surface roughness of titanium on β1- and β3-integrin adhesion and the organization of fibronectin in human osteoblastic cells," *Biomaterials*, vol. 26, no. 15, pp. 2423–2440, 2005.

[27] X. Li, Q. Zhou, S. Zhao, and J. Chen, "Effect of pulse current on bending behavior of Ti6Al4V alloy," *Procedia Eng.*, vol. 81, no. October, pp. 1799–1804, 2014.

[28] E. L. Odenberger, J. Hertzman, P. Thilderkvist, M. Merklein, A. Kuppert, T. St??hr, J. Lechler, and M. Oldenburg, "Thermo-mechanical sheet metal forming of aero engine components in Ti-6Al-4V - PART 1: Material characterisation," *Int. J. Mater. Form.*, vol. 6, no. 3, pp. 391–402, 2013.

[29] M. Peters and C. Leyens, "Titan Und Titanlegierungen (German Edition)." 2002.

[30] Dynamet and A Carpenter Company, "Titanium for Medical Applications," *Titanium in Medicine*. [Online]. Available: http://www.cartech.com/globalassets/literature-files/dynamettitaniumformedical.pdf. [Accessed: 01-Aug-2016].

[31] A. K. F. Klocke, D. Welling, J. Dieckmann, "Titanium Parts for Medical Sector Made By Wire-Edm," *1st Int. Conf. Des. Process. Med. Devices*, vol. 49, no. 0, pp. 164–166, 2012.

[32] A. C. Popa, G. E. Stan, M. Enculescu, C. Tanase, D. U. Tulyaganov, and J. M. F. Ferreira, "Superior biofunctionality of dental implant fixtures uniformly coated with durable bioglass films by magnetron sputtering," *J. Mech. Behav. Biomed. Mater.*, vol. 51, pp. 313–327, 2015.

[33] "Introduction – Biomaterials Science: An Evolving, Multidisciplinary Endeavor," in *Biomaterials Science*, 2013, pp. xxv–xxxix.

[34] L. A. Bregagnolo, P. F. Bertelli, M. C. Ribeiro, C. E. Sverzut, and A. E. Trivellato, "Evaluation of in vitro resistance of titanium and resorbable (poly-l-dl-lactic acid) fixation systems on the mandibular angle fracture," *Int. J. Oral Maxillofac. Surg.*, vol. 40, no. 3, pp. 316–321, 2011.

[35] F. H. Froes, "Titanium: Alloying," in *Encyclopedia of Materials: Science and Technology*, 2001, pp. 9361–9364.

[36] F. Warchomicka, C. Poletti, M. Stockinger, and T. Henke, "Microstructure evolution during hot deformation of Ti-6Al-4V double cone specimens," *Int. J. Mater. Form.*, vol. 3, no. 1, pp. 215–218, 2010.

[37] J. W. Elmer, T. A. Palmer, S. S. Babu, and E. D. Specht, "In situ observations of lattice expansion and transformation rates of α and β phases in Ti–6Al–4V," *Mater. Sci. Eng. A*, vol. 391, no. 1, pp. 104–113, 2005.

[38] X. P. Zhang, R. Shivpuri, and A. K. Srivastava, “Role of phase transformation in chip segmentation during high speed machining of dual phase titanium alloys,” *J. Mater. Process. Technol.*, vol. 214, no. 12, pp. 3048–3066, 2014.

[39] X. G. Fan and H. Yang, “Internal-state-variable based self-consistent constitutive modeling for hot working of two-phase titanium alloys coupling microstructure evolution,” *Int. J. Plast.*, vol. 27, no. 11, pp. 1833–1852, 2011.

[40] G. R. Johnson and W. H. Cook, “Fracture characteristic of three metals subjected to various strains, strain rates, temperatures and pressures,” *Eng. Fract. Mech.*, vol. 21, no. 1, pp. 31–48, 1985.

[41] Y. Karpat, “Temperature dependent flow softening of titanium alloy Ti6Al4V: An investigation using finite element simulation of machining,” *J. Mater. Process. Technol.*, vol. 211, no. 4, pp. 737–749, 2011.

[42] A. S. Khan, Y. S. Suh, and R. Kazmi, “Quasi-static and dynamic loading responses and constitutive modeling of titanium alloys,” *Int. J. Plast.*, vol. 20, no. 12, pp. 2233–2248, 2004.

[43] Z. J. Wang and H. Song, “Effect of electropulsing on anisotropy behaviour of cold-rolled commercially pure titanium sheet,” *Trans. Nonferrous Met. Soc. China (English Ed.*, vol. 19, no. SUPPL. 2, pp. s409–s413, 2009.

[44] A. Roth, M. A. Lebyodkin, T. A. Lebedkina, J. S. Lecomte, T. Richeton, and K. E. K. Amouzou, “Mechanisms of anisotropy of mechanical properties of α-titanium in tension conditions,” *Mater. Sci. Eng. A*, vol. 596, pp. 236–243, 2014.

[45] Z. S. Zhu, R. Y. Liu, M. G. Yan, C. X. Cao, J. L. Gu, and N. P. Chen, “Texture control and the anisotropy of mechanical properties in titanium sheet,” *J. Mater. Sci.*, vol. 32, no. 19, pp. 5163–5167, 1997.

[46] S. V. S. N. Murty, N. Nayan, P. Kumar, P. R. Narayanan, S. C. Sharma, and K. M. George, “Microstructure-texture-mechanical properties relationship in multi-pass warm rolled Ti-6Al-4V Alloy,” *Mater. Sci. Eng. A*, vol. 589, pp. 174–181, 2014.

[47] D. Banabic, *Sheet Metal Forming Processes*. 2010.

[48] S. Kalpakjian and S. R. Schmid, *Manufacturing Engineering and Technology*. Pearson.

[49] T. Seshacharyulu, S. C. Medeiros, W. G. Frazier, and Y. V. R. K. Prasad, "Hot working of commercial Ti–6Al–4V with an equiaxed α–β microstructure: materials modeling considerations," *Mater. Sci. Eng. A*, vol. 284, pp. 184–194, 2000.

[50] J. Sieniawski, W. Ziaja, K. Kubiak, and M. Motyka, "Microstructure and Mechanical Properties of High Strength Two-Phase Titanium Alloys," *Titan. Alloy. - Adv. Prop. Control*, pp. 70–80, 2013.

[51] R. Filip, K. Kubiak, W. Ziaja, and J. Sieniawski, "The effect of microstructure on the mechanical properties of two-phase titanium alloys," *J. Mater. Process. Technol.*, vol. 133, no. 1–2, pp. 84–89, 2003.

[52] K. Kubiak and J. Sieniawski, "Development of the Microstructure and Fatigue Strength of Two Phase Titanium Alloys in the Processes of Forging and Heat Treatment," *J. Mater. Process. Technol.*, vol. 78, pp. 117–121, 1998.

[53] N. Kotkunde, A. D. Deole, A. K. Gupta, and S. K. Singh, "Comparative study of constitutive modeling for Ti-6Al-4V alloy at low strain rates and elevated temperatures," *Mater. Des.*, vol. 55, pp. 999–1005, 2014.

[54] W. F. Hosford and R. M. Caddel, *Metal Forming. Mechanics and metallurgy*. 2007.

[55] J. Xiao, D. S. Li, X. Q. Li, and T. S. Deng, "Constitutive modeling and microstructure change of Ti-6Al-4V during the hot tensile deformation," *J. Alloys Compd.*, vol. 541, pp. 346–352, 2012.

[56] J. S. Kim, J. H. Kim, Y. T. Lee, C. G. Park, and C. S. Lee, "Microstructural analysis on boundary sliding and its accommodation mode during superplastic deformation of Ti – 6Al – 4V alloy," vol. 263, pp. 272–280, 1999.

[57] W.-S. Lee and C.-F. Lin, "Plastic deformation and fracture behaviour of Ti–6Al–4V alloy loaded with high strain rate under various temperatures,"

Mater. Sci. Eng. A, vol. 241, no. 1, pp. 48–59, 1998.

[58] S. Bruschi, T. Altan, D. Banabic, P. F. Bariani, A. Brosius, J. Cao, A. Ghiotti, M. Khraisheh, M. Merklein, and A. E. Tekkaya, "Testing and modelling of material behaviour and formability in sheet metal forming," *CIRP Ann. - Manuf. Technol.*, vol. 63, no. 2, pp. 727–749, 2014.

[59] N. Kotkunde, A. D. Deole, A. K. Gupta, S. K. Singh, and B. Aditya, "Failure and formability studies in warm deep drawing of Ti-6Al-4V alloy," *Mater. Des.*, vol. 60, pp. 540–547, 2014.

[60] A. He, G. Xie, H. Zhang, and X. Wang, "A comparative study on Johnson-Cook, modified Johnson-Cook and Arrhenius-type constitutive models to predict the high temperature flow stress in 20CrMo alloy steel," *Materials and Design*, vol. 52. pp. 677–685, 2013.

[61] F. J. Zerilli, R. W. Armstrong, and J. Frank, "Dislocation mechanics based constitutive relations for material dynamics calculations," *J. Appl. Phys.*, vol. 61, 1987.

[62] C. Zener and J. H. Hollomon, "Effect of Strain Rate Upon Plastic Flow of Steel," *J. Appl. Phys.*, vol. 15, no. 1, p. 22, 1944.

[63] C. F. Guzmán, V. Tuninetti, G. Gilles, and A. M. Habraken, "Assessment of Damage and Anisotropic Plasticity Models to Predict Ti-6Al-4V Behavior," *Key Eng. Mater.*, vol. 651–653, pp. 575–580, 2015.

[64] J. Q. Tan, M. Zhan, S. Liu, T. Huang, J. Guo, and H. Yang, "A modified Johnson-Cook model for tensile flow behaviors of 7050-T7451 aluminum alloy at high strain rates," *Mater. Sci. Eng. A*, vol. 631, pp. 214–219, 2015.

[65] D. Banabic, H. J. Bunge, K. Pöhlandt, and A. E. Tekkaya, *Formability of metallic materials*. Berlin/Heidelberg: Springer, 2000.

[66] S. Keeler and W. Backofen, "Plastic instability and fracture in sheets stretched over rigid punches," *ASM Trans. Quart.*, vol. 56, pp. 25–48, 1964.

[67] G. M. Goodwin, "Application of strain analysis to sheet metal problems in the press shop," *SAE Pap.*, no. 680, 1968.

[68] H. J. Bong, F. Barlat, M.-G. Lee, and D. C. Ahn, "The forming limit diagram

of ferritic stainless steel sheets: Experiments and modeling," *Int. J. Mech. Sci.*, vol. 64, no. 1, pp. 1–10, 2012.

[69] ISO12004-2, "Metallic Materials - Sheet and Strip - Determination of Forming Limit Curves - Part 2: Determination of Forming Limit Curves in the Laboratory," no. 40, 2008.

[70] A. Assempour, R. Hashemi, K. Abrinia, M. Ganjiani, and E. Masoumi, "A methodology for prediction of forming limit stress diagrams considering the strain path effect," *Comput. Mater. Sci.*, vol. 45, no. 2, pp. 195–204, 2009.

[71] "ArcelorMittal." [Online]. Available: http://automotive.arcelormittal.com/europe/products/AHSS/DP/EN.

[72] H. Li, M. W. Fu, J. Lu, and H. Yang, "Ductile fracture: Experiments and computations," *Int. J. Plast.*, vol. 27, no. 2, pp. 147–180, 2011.

[73] M. G. Cockcroft and D. J. (Latham, "Ductility and the Workability of Metals.," *J. Inst. Met.*, vol. 96, pp. 33–39, 1968.

[74] P. Brozzo, B. Deluca, and R. Rendina, "A new method for the prediction of formability limits in metal sheets.," *Proc. 7th Bienn. Conf. IDDR* ., 1972.

[75] M. Oyane, "Criteria of ductile fracture strain," *Proc. JSME*, vol. 15, pp. 1507–1513, 1972.

[76] J. R. Rice and D. M. Tracey, "On the ductile enlargement of voids in triaxial stress fields," *J. Mech. Phys. Solids*, vol. 17, no. 3, pp. 201–217, 1969.

[77] A. G. Atkins, "Fracture in forming," *J. Mater. Process. Technol.*, vol. 56, pp. 609–618, 1996.

[78] M. Giglio, A. Manes, and F. Viganò, "Ductile fracture locus of Ti6Al4V titanium alloy," *Int. J. Mech. Sci.*, vol. 54, no. 1, pp. 121–135, 2012.

[79] Y. Bao and T. Wierzbicki, "A Comparative Study on Various Ductile Crack Formation Criteria," *J. Eng. Mater. Technol.*, vol. 126, no. 3, p. 314, 2004.

[80] Y. Bao, "Dependence of fracture ductility on thickness," *Thin-Walled Struct.*, vol. 42, no. 8, pp. 1211–1230, 2004.

[81] Y. Bao and T. Wierzbicki, "On fracture locus in the equivalent strain and stress triaxiality space," *Int. J. Mech. Sci.*, vol. 46, no. 1, pp. 81–98, 2004.

[82] M. Luo, M. Dunand, and D. Mohr, “Experiments and modeling of anisotropic aluminum extrusions under multi-axial loading – Part II: Ductile fracture,” *Int. J. Plast.*, vol. 32–33, pp. 36–58, May 2012.

[83] M. F. Novella, A. Ghiotti, S. Bruschi, and P. F. Bariani, “Modelling of AA6082 ductile damage evolution under hot rolling conditions,” *Procedia Eng.*, vol. 81, no. October, pp. 221–226, 2014.

[84] A. Ghiotti, S. Fanini, S. Bruschi, and P. F. Bariani, “Modelling of the Mannesmann effect,” *CIRP Ann. - Manuf. Technol.*, vol. 58, no. 1, pp. 255–258, 2009.

[85] P. A. F. Martins, N. Bay, A. E. Tekkaya, and A. G. Atkins, “Characterization of fracture loci in metal forming,” *Int. J. Mech. Sci.*, vol. 83, pp. 112–123, 2014.

[86] L. Xue, “Damage accumulation and fracture initiation in uncracked ductile solids subject to triaxial loading,” *Int. J. Solids Struct.*, vol. 44, no. 16, pp. 5163–5181, 2007.

[87] M. Brünig, D. Brenner, and S. Gerke, “Stress state dependence of ductile damage and fracture behavior: Experiments and numerical simulations,” *Eng. Fract. Mech.*, vol. 141, pp. 152–169, 2015.

[88] A. Kamoulakos, P. Culiere, and T. Araki, “Prediction of ductile metal rupture with the e-w model in pamcrash.,” *IBEC Chiba, Japan.*, 2003.

[89] Y. Bai and T. Wierzbicki, “Application of extended Mohr-Coulomb criterion to ductile fracture,” *Int. J. Fract.*, vol. 161, no. 1, pp. 1–20, 2010.

[90] M. L. Wilkins, R. D. Streit, and J. E. Reaugh, “Cumulative-Strain-Damage model of ductile fracture : simulation and prediction of engineering fracture tests, ucrl-53058. Lawrence Livermore National Laboratory, Livermore, CA.,” 1980.

[91] Y. Bai and T. Wierzbicki, “A new model of metal plasticity and fracture with pressure and Lode dependence,” *Int. J. Plast.*, vol. 24, no. 6, pp. 1071–1096, 2008.

[92] T. Wierzbicki and L. Xue, “On the effect of the third invariant of the stress deviator on ductile fracture. Impact and Crashworthiness Laboratory, Ma,”

2005.

[93] T. Wierzbicki, Y. Bao, Y. W. Lee, and Y. Bai, “Calibration and evaluation of seven fracture models,” *Int. J. Mech. Sci.*, vol. 47, no. 4–5 SPEC. ISS., pp. 719–743, 2005.

[94] M. Giglio, A. Manes, and F. Viganò, “Numerical simulation of the slant fracture of a helicopter’s rotor hub with ductile damage failure criteria,” *Fatigue Fract. Eng. Mater. Struct.*, vol. 35, no. 4, pp. 317–327, 2012.

[95] S. Katani, F. Madadi, M. Atapour, and S. Ziaei Rad, “Micromechanical modelling of damage behaviour of Ti-6Al-4V,” *Mater. Des.*, vol. 49, pp. 1016–1021, 2013.

[96] R. A. Gittens, R. Olivares-Navarrete, Z. Schwartz, and B. D. Boyan, “Implant osseointegration and the role of microroughness and nanostructures: Lessons for spine implants,” *Acta Biomater.*, vol. 10, no. 8, pp. 3363–3371, 2014.

[97] L. Bacakova, E. Filova, M. Parizek, T. Ruml, and V. Svorcik, “Modulation of cell adhesion, proliferation and differentiation on materials designed for body implants.,” *Biotechnol. Adv.*, vol. 29, no. 6, pp. 739–67, Jan. 2011.

[98] C. Richard, “Innovative Surface Treatments of Titanium Alloys for Biomedical Applications,” in *Thermec, !nternational Conference on Processing & Manufacturing of advanced materials*, 2016.

[99] L. Le Guéhennec, A. Soueidan, P. Layrolle, and Y. Amouriq, “Surface treatments of titanium dental implants for rapid osseointegration,” *Dent. Mater.*, vol. 23, no. 7, pp. 844–854, 2007.

[100] S. Staehlke, A. Koertge, and B. Nebe, “Intracellular calcium dynamics dependent on defined microtopographical features of titanium,” *Biomaterials*, vol. 46, pp. 48–57, 2015.

[101] A. Bagno and C. Di Bello, “Surface treatments and roughness properties of Ti-based biomaterials,” *J. Mater. Sci. Mater. Med.*, vol. 15, pp. 935–949, 2004.

[102] S. Ban, Y. Iwaya, H. Kono, and H. Sato, “Surface modification of titanium by etching in concentrated sulfuric acid,” *Dental Materials*, vol. 22, no. 12.

pp. 1115–1120, 2006.

[103] A. B. Novaes, S. L. S. Souza, P. T. de Oliveira, and A. M. M. S. Souza, “Histomorphometric analysis of the bone-implant contact obtained with 4 different implant surface treatments placed side by side in the dog mandible.,” *Int. J. Oral Maxillofac. Implants*, vol. 17, no. 3, pp. 377–83, 2002.

[104] M. Piattelli, A. Scarano, M. Paolantonio, G. Iezzi, G. Petrone, and A. Piattelli, “Bone response to machined and resorbable blast material titanium implants: an experimental study in rabbits.,” *J. Oral Implantol.*, vol. 28, no. 1, pp. 2–8, 2002.

[105] C. J. Ivanoff, C. Hallgren, G. Widmark, L. Sennerby, and A. Wennerberg, “Histologic evaluation of the bone integration of TiO2 blasted and turned titanium microimplants in humans.,” *Clin. Oral Implants Res.*, vol. 12, no. 2, pp. 128–134, 2001.

[106] A. Wennerberg, T. Albrektsson, B. Andersson, and J. J. Krol, “A histomorphometric and removal torque study of screw-shaped titanium implants with three different surface topographies.,” *Clin. Oral Implants Res.*, vol. 6, no. 1, pp. 24–30, Mar. 1995.

[107] P. Jiang, J. Liang, and C. Lin, “Construction of micro-nano network structure on titanium surface for improving bioactivity,” *Appl. Surf. Sci.*, vol. 280, pp. 373–380, 2013.

[108] T. Kokubo and H. Takadama, “How useful is SBF in predicting in vivo bone bioactivity?,” *Biomaterials*, vol. 27, no. 15, pp. 2907–2915, 2006.

[109] P. S. Vanzillotta, M. S. Sader, I. N. Bastos, and G. De Almeida Soares, “Improvement of in vitro titanium bioactivity by three different surface treatments,” *Dent. Mater.*, vol. 22, no. 3, pp. 275–282, 2006.

[110] D. . Puleo and A. Nanci, “Understanding and controlling the bone–implant interface,” *Biomaterials*, vol. 20, no. 23, pp. 2311–2321, 1999.

[111] M. Dettin, M. T. Conconi, R. Gambaretto, A. Bagno, C. Di Bello, A. M. Menti, C. Grandi, and P. P. Parnigotto, “Effect of synthetic peptides on osteoblast adhesion,” *Biomaterials*, vol. 26, no. 22, pp. 4507–4515, 2005.

[112] Y. Lai, C. Lin, J. Huang, H. Zhuang, L. Sun, and T. Nguyen, "Markedly controllable adhesion of superhydrophobic spongelike nanostructure TiO2 films," *Langmuir*, vol. 24, no. 8, pp. 3867–3873, 2008.

[113] X. Liu, P. Chu, and C. Ding, "Surface modification of titanium, titanium alloys, and related materials for biomedical applications," *Materials Science and Engineering: R: Reports*, vol. 47, no. 3–4. pp. 49–121, 2004.

[114] N. Drnovšek, K. Rade, R. Milačič, J. Štrancar, and S. Novak, "The properties of bioactive TiO2 coatings on Ti-based implants," *Surf. Coatings Technol.*, vol. 209, pp. 177–183, 2012.

[115] L. Lin, H. Wang, M. Ni, Y. Rui, T.-Y. Cheng, C.-K. Cheng, X. Pan, G. Li, and C. Lin, "Enhanced osteointegration of medical titanium implant with surface modifications in micro/nanoscale structures," *J. Orthop. Transl.*, vol. 2, no. 1, pp. 35–42, 2014.

[116] M. Trevoux and A. Behlouli, "De la biofonctionnalité des implants dentaires," *Implantol. Rev.*, vol. Nov., pp. 141–149, 2010.

[117] Y. Li, S. Zou, D. Wang, G. Feng, C. Bao, and J. Hu, "The effect of hydrofluoric acid treatment on titanium implant osseointegration in ovariectomized rats," *Biomaterials*, vol. 31, no. 12. pp. 3266–3273, 2010.

[118] C. N. Elias, Y. Oshida, J. H. C. Lima, and C. A. Muller, "Relationship between surface properties (roughness, wettability and morphology) of titanium and dental implant removal torque," *J. Mech. Behav. Biomed. Mater.*, vol. 1, no. 3, pp. 234–242, 2008.

[119] R. A. Gittens, R. Olivares-Navarrete, A. Cheng, D. M. Anderson, T. McLachlan, I. Stephan, J. Geis-Gerstorfer, K. H. Sandhage, A. G. Fedorov, F. Rupp, B. D. Boyan, R. Tannenbaum, and Z. Schwartz, "The roles of titanium surface micro/nanotopography and wettability on the differential response of human osteoblast lineage cells.," *Acta Biomater.*, vol. 9, no. 4, pp. 6268–77, Apr. 2013.

[120] K. Jiao and X. Li, "Effect of surface dynamic wettability in proton exchange membrane fuel cells," *Int. J. Hydrogen Energy*, vol. 35, no. 17, pp. 9095–9103, 2010.

[121] “Patent GB1490535. Manufacturing ahardenedsteel article, Norrbottens Jaern- verk AB.,” 1977.

[122] H. Karbasian and A. E. Tekkaya, “A review on hot stamping,” *J. Mater. Process. Technol.*, vol. 210, no. 15, pp. 2103–2118, Nov. 2010.

[123] T. Altan and A. E. Tekkaya, *Sheet metal forming: processes and applications*. 2012.

[124] G. Quan, Z. Zhan, L. Zhang, D. Wu, G. Luo, and Y. Xia, “A study on the multi-phase transformation kinetics of ultra-high-strength steel and application in thermal-mechanical-phase coupling simulation of hot stamping process,” *Mater. Sci. Eng. A*, vol. 673, pp. 24–38, 2016.

[125] R. Neugebauer, T. Altan, M. Geiger, M. Kleiner, and A. Sterzing, “Sheet metal forming at elevated temperatures,” *CIRP Ann. - Manuf. Technol.*, vol. 55, no. 2, pp. 793–816, 2006.

[126] P. F. Bariani, S. Bruschi, A. Ghiotti, and A. Turetta, “Testing formability in the hot stamping of HSS,” *CIRP Ann. - Manuf. Technol.*, vol. 57, no. 1, pp. 265–268, 2008.

[127] K. Zhao, Y. Chang, P. Hu, and Y. Wu, “Influence of rapid cooling pretreatment on microstructure and mechanical property of hot stamped AHSS part,” *J. Mater. Process. Technol.*, vol. 228, pp. 68–75, 2016.

[128] “N. N., 2009, Stahl-Informations-Zentrum. Stahl im Automobil, Leicht und sicher. www.stahl-info.de.” .

[129] M. Merklein, M. Wieland, M. Lechner, S. Bruschi, and A. Ghiotti, “Hot stamping of boron steel sheets with tailored properties: A review,” *J. Mater. Process. Technol.*, vol. 228, pp. 11–24, 2016.

[130] B. He, L. Ying, X. Li, and P. Hu, “Optimal design of longitudinal conformal cooling channels in hot stamping tools,” *Appl. Therm. Eng.*, vol. 106, pp. 1176–1189, 2016.

[131] K. Mori and D. Ito, “Prevention of oxidation in hot stamping of quenchable steel sheet by oxidation preventive oil,” *CIRP Ann. - Manuf. Technol.*, vol. 58, no. 1, pp. 267–270, 2009.

[132] Y. H. Kim and J. J. Park, “Effect of process parameters on formability in incremental forming of sheet metal,” *J. Mater. Process. Technol.*, vol. 130, pp. 42–46, 2002.

[133] Z. Zhang, H. Ren, R. Xu, N. Moser, J. Smith, E. Ndip-Agbor, R. Malhotra, Z. Cedric Xia, K. F. Ehmann, and J. Cao, “A Mixed Double-Sided Incremental Forming Toolpath Strategy for Improved Geometric Accuracy,” *J. Manuf. Sci. Eng.*, vol. 137, no. 5, p. 51007, 2015.

[134] J. Jeswiet, F. Micari, G. Hirt, A. Bramley, J. Duflou, and J. Allwood, “Asymmetric Single Point Incremental Forming of Sheet Metal,” *CIRP Ann. - Manuf. Technol.*, vol. 54, no. 2, pp. 88–114, 2005.

[135] G. Hirt, S. Junk, and N. Witulsky, “Incremental sheet forming: quality evaluation and process simulation,” *Proceeding 7th ICTP Conf. Yokohama*, pp. 925–930, 2002.

[136] J. J. Park and Y. H. Kim, “Fundamental studies on the incremental sheet metal forming technique,” *J. Mater. Process. Technol.*, vol. 140, no. 1–3 SPEC., pp. 447–453, 2003.

[137] J. M. Allwood, G. P. F. King, and J. Duflou, “A structured search for applications of the incremental sheet-forming process by product segmentation,” 2005, vol. 219, no. 2, pp. 239–244.

[138] M. A. Dittrich, T. G. Gutowski, J. Cao, J. T. Roth, Z. C. Xia, V. Kiridena, F. Ren, and H. Henning, “Exergy analysis of incremental sheet forming,” *Prod. Eng.*, vol. 6, no. 2, pp. 169–177, 2012.

[139] K. R. Haapala, F. Zhao, J. Camelio, J. W. Sutherland, S. J. Skerlos, D. A. Dornfeld, I. S. Jawahir, A. F. Clarens, and J. L. Rickli, “A Review of Engineering Research in Sustainable Manufacturing,” *J. Manuf. Sci. Eng. Asme*, vol. 135, no. 4, pp. 1–16, 2013.

[140] R. Sousa, “Incremental Sheet Forming Technologies,” in *Reference Module in Materials Science and Materials Engineering*, 2016.

[141] G. Ambrogio, L. De Napoli, L. Filice, F. Gagliardi, and M. Muzzupappa, “Application of Incremental Forming process for high customised medical product manufacturing,” *J. Mater. Process. Technol.*, vol. 162–163, pp. 156–

162, 2005.

[142] B. Lu, H. Ou, S. Q. Shi, H. Long, and J. Chen, “Titanium based cranial reconstruction using incremental sheet forming,” *Int. J. Mater. Form.*, 2014.

[143] A. Fiorentino, R. Marzi, and E. Ceretti, “Preliminary results on Ti incremental sheet forming (ISF) of biomedical devices: biocompatibility, surface finishing and treatment,” *Int. J. Mechatronics Manuf. Syst.*, vol. 5, no. 1, p. 36, 2012.

[144] “BMi, Biomedical Model Inc.” [Online]. Available: http://www.biomodel.com.

[145] D. K. Xu, B. Lu, T. T. Cao, H. Zhang, J. Chen, H. Long, and J. Cao, “Enhancement of process capabilities in electrically-assisted double sided incremental forming,” *Mater. Des.*, vol. 92, pp. 268–280, 2015.

[146] A. K. Behera, B. Lauwers, and J. R. Duflou, “Tool path generation framework for accurate manufacture of complex 3D sheet metal parts using single point incremental forming,” *Comput. Ind.*, vol. 65, no. 4, pp. 563–584, 2014.

[147] G. Hirt, J. Ames, M. Bambach, R. Kopp, and R. Kopp, “Forming strategies and Process Modelling for CNC Incremental Sheet Forming,” *CIRP Ann. - Manuf. Technol.*, vol. 53, no. 1, pp. 203–206, 2004.

[148] A. K. Behera, J. Verbert, B. Lauwers, and J. R. Duflou, “Tool path compensation strategies for single point incremental sheet forming using multivariate adaptive regression splines,” *Comput. Des.*, vol. 45, no. 3, pp. 575–590, 2013.

[149] E. Ndip-Agbor, J. Smith, H. Ren, Z. Jiang, J. Xu, N. Moser, W. Chen, Z. C. Xia, and J. Cao, “Optimization of relative tool position in accumulative double sided incremental forming using finite element analysis and model bias correction,” *Int. J. Mater. Form.*, 2015.

[150] T. . Kim and D. . Yang, “Improvement of formability for the incremental sheet metal forming process,” *Int. J. Mech. Sci.*, vol. 42, no. 7, pp. 1271–1286, 2000.

[151] J. Jeswiet and D. Young, “Forming limit diagrams for single-point

incremental forming of aluminium sheet," *Proc. Inst. Mech. Eng. Part B J. Eng. Manuf.*, vol. 219, pp. 359–364, 2005.

[152] L. Filice, L. Fratini, and F. Micari, "Analysis of Material Formability in Incremental Forming," *CIRP Ann. - Manuf. Technol.*, vol. 51, no. 1, pp. 199–202, 2002.

[153] T. McAnulty, J. Jeswiet, and M. Doolan, "Formability in single point incremental forming: A comparative analysis of the state of the art," *CIRP J. Manuf. Sci. Technol.*, 2016.

[154] R. Malhotra, L. Xue, T. Belytschko, and J. Cao, "Mechanics of fracture in single point incremental forming," *J. Mater. Process. Technol.*, vol. 212, no. 7, pp. 1573–1590, 2012.

[155] J. M. Allwood, D. R. Shoulder, and A. E. Tekkaya, "The increased forming limits of incremental sheet forming processes.," *Key Eng. Mater.*, vol. 344, pp. 621–628, 2007.

[156] Y. Fang, B. Lu, J. Chen, D. K. Xu, and H. Ou, "Analytical and experimental investigations on deformation mechanism and fracture behavior in single point incremental forming," *J. Mater. Process. Technol.*, vol. 214, no. 8, pp. 1503–1515, 2014.

[157] D. Xu, R. Malhotra, N. V. Reddy, J. Chen, and J. Cao, "Analytical prediction of stepped feature generation in multi-pass single point incremental forming," *J. Manuf. Process.*, vol. 14, no. 4, pp. 487–494, 2012.

[158] J. Verbert, B. Belkassem, C. Henrard, A. M. Habraken, J. Gu, H. Sol, B. Lauwers, and J. R. Duflou, "Multi-Step toolpath approach to overcome forming limitations in single point incremental forming," *Int. J. Mater. Form.*, vol. 1, no. 1, pp. 1203–1206, 2008.

[159] J. R. Duflou, J. Verbert, B. Belkassem, J. Gu, H. Sol, C. Henrard, and A. M. Habraken, "Process window enhancement for single point incremental forming through multi-step toolpaths," *CIRP Ann. - Manuf. Technol.*, vol. 57, no. 1, pp. 253–256, 2008.

[160] R. Malhotra, A. Bhattacharya, A. Kumar, N. V. Reddy, and J. Cao, "A new methodology for multi-pass single point incremental forming with mixed

toolpaths," *CIRP Ann. - Manuf. Technol.*, vol. 60, no. 1, pp. 323–326, 2011.

[161] M. Skjoedt, N. Bay, B. Endelt, and G. Ingarao, "Multi stage strategies for single point incremental forming of a cup," *Proc. 11th ESAFORM Conf.*, vol. 1, pp. 1199–1202, 2008.

[162] A. Attanasio, E. Ceretti, C. Giardini, and L. Mazzoni, "Asymmetric two points incremental forming: Improving surface quality and geometric accuracy by tool path optimization," *J. Mater. Process. Technol.*, vol. 197, no. 1, pp. 59–67, 2008.

[163] J. Zhang, H. Meier, O. Dewald, and V. Smukala, "Two Point Incremental Forming with Two Moving Forming Tools," in *Sheet Metal 2007*, 2007, vol. 344, pp. 599–605.

[164] G. Hirt, M. Bambach, E. Maidagan, J. Zettler, and P. P. Rodriguez, "A New Incremental Sheet Forming Process Based on a Flexible Supporting Die System," in *Sheet Metal 2007*, 2007, vol. 344, pp. 607–614.

[165] Y. Wang, Y. Huang, J. Cao, and N. V. Reddy, "Experimental Study on a New Method of Double Side Incremental Forming," *Int. Manuf. ing Sci. Eng. Conf. collocated With 3rd JSME/ASME Int. Conf. Mater. Process.*, pp. 601–607, 2008.

[166] N. Moser, Z. Zhang, H. Ren, H. Zhang, Y. Shi, E. E. Ndip-Agbor, B. Lu, J. Chen, K. F. Ehmann, and J. Cao, "Effective forming strategy for double-sided incremental forming considering in-plane curvature and tool direction," *CIRP Ann. - Manuf. Technol.*, vol. 65, no. 1, pp. 265–268, 2016.

[167] R. Malhotra, J. Cao, F. Ren, V. Kiridena, Z. Cedric Xia, and N. Reddy, "Improvement of Geometric Accuracy in Incremental Forming by Using a Squeezing Toolpath Strategy With Two Forming Tools," *J. Manuf. Sci. Eng.*, vol. 133, no. 6, 2011.

[168] B. Lu, Y. Fang, D. K. Xu, J. Chen, S. Ai, H. Long, H. Ou, and J. Cao, "Investigation of material deformation mechanism in double side incremental sheet forming," *Int. J. Mach. Tools Manuf.*, vol. 93, pp. 37–48, 2015.

[169] N. Moser, Z. Zhang, H. Ren, K. Ehmann, and J. Cao, "An Investigation into

the Mechanics of Double-Sided Incremental Forming using Finite Element Methods," *ESAFORM Conf. Nantes Fr. AIP Publ.*, no. (In Press), 2016.

[170] R. Malhotra, J. Cao, M. Beltran, D. Xu, J. Magargee, V. Kiridena, and Z. C. Xia, "Accumulative-DSIF strategy for enhancing process capabilities in incremental forming," *CIRP Ann. - Manuf. Technol.*, vol. 61, no. 1, pp. 251–254, 2012.

[171] J. Smith, R. Malhotra, W. K. Liu, and J. Cao, "Deformation mechanics in single-point and accumulative double-sided incremental forming," *Int. J. Adv. Manuf. Technol.*, vol. 69, no. 5–8, pp. 1185–1201, 2013.

[172] R. Xu, X. Shi, D. Xu, R. Malhotra, and J. Cao, "A preliminary study on the fatigue behavior of sheet metal parts formed with accumulative-double-sided incremental forming," 2014.

[173] Y. H. Ji and J. J. Park, "Formability of magnesium AZ31 sheet in the incremental forming at warm temperature," *J. Mater. Process. Technol.*, vol. 201, no. 1–3, pp. 354–358, May 2008.

[174] G. Ambrogio, L. Filice, and G. L. Manco, "Warm incremental forming of magnesium alloy AZ31," *CIRP Ann. - Manuf. Technol.*, vol. 57, no. 1, pp. 257–260, 2008.

[175] G. Ambrogio, F. Gagliardi, S. Bruschi, and L. Filice, "On the high-speed Single Point Incremental Forming of titanium alloys," *CIRP Ann. - Manuf. Technol.*, vol. 62, no. 1, pp. 243–246, 2013.

[176] G. Ambrogio and F. Gagliardi, "Temperature variation during high speed incremental forming on different lightweight alloys," *Int. J. Adv. Manuf. Technol.*, vol. 76, no. 9–12, pp. 1819–1825, 2014.

[177] G. Fan, L. Gao, G. Hussain, and Z. Wu, "Electric hot incremental forming: a novel technique," *Int J Mach Tools Manuf*, vol. 48, pp. 1688–1692, 2008.

[178] G. Fan and L. Gao, "Mechanical property of Ti-6Al-4V sheet in one-sided electric hot incremental forming," *Int. J. Adv. Manuf. Technol.*, vol. 72, no. 5–8, pp. 989–994, 2014.

[179] G. Fan, F. Sun, X. Meng, L. Gao, and G. Tong, "Electric hot incremental forming of Ti-6Al-4V titanium sheet," *Int. J. Adv. Manuf. Technol.*, vol. 49,

no. 9–12, pp. 941–947, 2010.

[180] J. R. Duflou, B. Callebaut, J. Verbert, and H. De Baerdemaeker, “Laser Assisted Incremental Forming: Formability and Accuracy Improvement,” *CIRP Ann. - Manuf. Technol.*, vol. 56, no. 1, pp. 273–276, 2007.

[181] A. Ghiotti and S. Bruschi, “A novel experimental set-up for warm incremental forming of AZ31B magnesium alloy sheet,” *STEEL Res. Int.*, vol. 81, no. 9, pp. 950–954, 2010.

[182] H. Meier and C. Magnus, “Incremental Sheet Metal Forming with Direct Resistance Heating Using Two Moving Tools,” *Key Eng. Mater.*, vol. 554–557, pp. 1362–1367, 2013.

[183] *Metallography and Microstructures*, vol. 9. The Materials Information Company. ASM International, 2001.

[184] T. Borvik, O. S. Hopperstad, T. Berstad, and M. Langseth, “A computational model of viscoplasticity and ductile damage for impact and penetration,” *Eur. J. Mech. A/Solids*, vol. 20, no. 5, pp. 685–712, 2001.

[185] S. V. Sajadifar and G. G. Yapici, “Workability characteristics and mechanical behavior modeling of severely deformed pure titanium at high temperatures,” *Mater. Des.*, vol. 53, pp. 749–757, 2014.

[186] G. Z. Quan, G. C. Luo, J. T. Liang, D. Sen Wu, A. Mao, and Q. Liu, “Modelling for the dynamic recrystallization evolution of Ti-6Al-4V alloy in two-phase temperature range and a wide strain rate range,” *Comput. Mater. Sci.*, vol. 97, pp. 136–147, 2015.

[187] *Fractography*, vol. 12. The Materials Information Company. ASM International, 2001.

[188] C. Zhang, X. Q. Li, D. S. Li, C. H. Jin, and J. J. Xiao, “Modelization and comparison of Norton-Hoff and Arrhenius constitutive laws to predict hot tensile behavior of Ti-6Al-4V alloy,” *Trans. Nonferrous Met. Soc. China (English Ed.*, vol. 22, no. SUPPL.2, pp. s457–s464, 2012.

[189] W. Song, J. Ning, X. Mao, and H. Tang, “A modified Johnson–Cook model for titanium matrix composites reinforced with titanium carbide particles at elevated temperatures,” *Mater. Sci. Eng. A*, vol. 576, pp. 280–289, 2013.

[190] F. A. McClintock, “A criterion of ductile fracture by the growth of holes,” *J. Appl. Mech.*, vol. 35, pp. 363–371, 1968.

[191] *ASTM B831. Standard Test Method for Shear Testing of Thin Aluminum Alloy Products*. .

[192] C. C. Roth and D. Mohr, “Ductile fracture experiments with locally proportional loading histories,” *Int. J. Plast.*, vol. 79, pp. 328–354, 2016.

[193] P. F. Bariani, S. Bruschi, A. Ghiotti, and F. Michieletto, “Hot stamping of AA5083 aluminium alloy sheets,” *CIRP Ann. - Manuf. Technol.*, vol. 62, no. 1, pp. 251–254, 2013.

[194] Y. Bai, X. Teng, and T. Wierzbicki, “On the Application of Stress Triaxiality Formula for Plane Strain Fracture Testing,” *J. Eng. Mater. Technol.*, vol. 131, no. 2, p. 21002, 2009.

[195] A. J. Sánchez Egea, H. A. González Rojas, D. J. Celentano, and J. Jorba Peiró, “Mechanical and metallurgical changes on 308L wires drawn by electropulses,” *Mater. Des.*, vol. 90, pp. 1159–1169, 2016.

[196] G. Ambrogio, L. Filice, and F. Gagliardi, “Formability of lightweight alloys by hot incremental sheet forming,” *Mater. Des.*, vol. 34, pp. 501–508, 2012.

[197] J. P. Kruth, M. Bartscher, S. Carmignato, R. Schmitt, L. De Chiffre, and A. Weckenmann, “Computed tomography for dimensional metrology,” *CIRP Ann. - Manuf. Technol.*, vol. 60, no. 2, pp. 821–842, 2011.

[198] L. De Chiffre, S. Carmignato, J.-P. Kruth, R. Schmitt, and A. Weckenmann, “Industrial applications of computed tomography,” *CIRP Ann. - Manuf. Technol.*, vol. 63, no. 2, pp. 655–677, 2014.

[199] T. Mekayarajjananonth and S. Winkler, “Contact angle measurement on dental implant biomaterials,” *J. Oral Implantol.*, vol. 25230–6199, no. 4, pp. 230–236, 1999.

[200] K. Jackson and J. Allwood, “The mechanics of incremental sheet forming,” *J. Mater. Process. Technol.*, vol. 209, no. 3, pp. 1158–1174, 2009.

[201] J. M. C. Soeiro, C. M. A. Silva, M. B. Silva, and P. A. F. Martins, “Revisiting the formability limits by fracture in sheet metal forming,” *J. Mater. Process.*

Technol., vol. 217, pp. 184–192, 2015.

[202] T. Madeira, C. M. A. Silva, M. B. Silva, and P. A. F. Martins, “Failure in single point incremental forming,” *Int. J. Adv. Manuf. Technol.*, vol. 80, no. 9, pp. 1471–1479, 2015.